Meshless Hydrodynamic Simulations Of Young Supernova Remnants

Orapeleng Mogawana

26 October 2020

A thesis presented to the University of Cape Town in full fulfilment of the degree: Master of Philosophy in Astronomy

UNIVERSITY OF CAPE TOWN

Supervisor: Assoc. Prof. S. Mohamed[1] and
Co-supervisor: Dr K. van der Heyden [2]

[1]South African Astronomical Observatory
[2]University Of Cape Town

Abstract

The majority of massive stars end their lives by ejecting their outer envelopes in a core-collapse supernova explosion. The collision of their ejecta with the surrounding circumstellar medium results in the formation of supernova remnants that have been detected at all wavelengths, from radio to gamma-rays. For several dozen supernova remnants, very-long-baseline radio interferometers have spatially resolved the interaction region and directly measured the expansion rates of the shocked gas; many show evidence of the interaction of supernova ejecta with the dense slow winds characteristic of the red supergiant progenitors. Understanding the dynamics and morphology of the interaction region, particularly in young supernova remnants leads to estimates of the total mass of the circumstellar medium, as well as its density distribution around the star given the value of the wind velocity.

Here we studied the interaction of the supernova ejecta with different circumstellar environments to investigate the hydrodynamic evolution of young supernova remnants in the Sedov-Taylor phase. We used the massively parallel, multi-physics magneto-hydrodynamics (MHD) and gravity code, `GIZMO`, for our simulations. We chose `GIZMO` for its flexibility in allowing the user to choose different methods to solve the fluid equations, i.e., new Lagrangian Godunov-type schemes, e.g., Meshless Finite Volume (MFV) and Meshless Finite Mass (MFM), as well as various flavors of smoothed particle hydrodynamics (SPH), or Eulerian fixed-grid schemes.

Since the majority of previous studies used the latter, we focused on an extensive comparison of all the meshless methods in solving the Sedov-Taylor blastwave test, a problem for which there is an exact solution. For our given compute resources, we found the parameters (e.g., smoothing length, number of neighbours, artificial viscosity, and particle resolution) for each meshless method that gave the best agreement with the exact solution. We then carried out 2D and 3D simulations of the hydrodynamic interaction of the supernova ejecta with varying density profiles assumed for the circumstellar medium, namely: a $1/r^2$ density

profile, for a typical, spherically symmetric red supergiant stellar wind, and an axisymmetric torus profile, inspired by the observation of a dense, dusty torus of the circumstellar material around the red supergiant, WOH G64 (Ohnaka et al., 2008). Radially assembled Hierarchical Equal Area isoLatitude Pixelization (HEALPix) shells were used to set-up the initial density and velocity profiles for the ejecta, which is marked by a flat inner core and a steeply declining outer edge. The Weighted Voronoi Tessellation code was used to produce the $1/r^2$ and axisymmetric torus density distributions.

We showed that the growth of Richtmyer-Meshkov instabilities in the 2D and 3D $1/r^2$ profiles are visible as early as 20 yrs into the evolution of the remnant and become increasingly unstable up to 100 yr. While 2D simulations of $1/r^2$ profiles show the presence of the Richtmyer-Meshkov instabilities in the hot shell of a contact discontinuity, in 3D we see large bubbles and filamentary structure of the instabilities. Our results for the numerical approaches to simulating the systems for the $1/r^2$ density cases were broadly consistent with previous studies in the literature where stationary grids were used. Two scenarios with different torus-cavity density contrasts were considered in which we found that the instability rolls along the half-opening angle takes $\sim$ 40 yr to develop in the axisymmetric torus with smooth density drop, whereas the axisymmetric torus with steep density drop does not develop any instability rolls up to the end of the simulation. We concluded with a discussion of the implications of our models for the morphology of supernova remnants and their expected levels of multi-wavelength emission.

Acknowledgements

I would like to thank my supervisor Adj. Assoc. Prof. Shazrene S. Mohamed for her guidance, insight and support throughout my research. Thanks also to my co-supervisor Dr. Kurt van der Heyden for his collaboration and many useful discussions and suggestions. I would like to thank the University of Cape Town astronomy department and South African Astronomical Observatory (SAAO) stuff for their support in providing a conducive office space for students and addressing student needs, especially in the unprecedented times of COVID-19. I give my thanks to my family, friends and fellow research student for their support. Thanks to the National Astrophysics and Space Science Program bursary scheme and SAAO postgraduate service work for the financial support throughout my research.

Plagiarism Declaration

I, Orapeleng Mogawana, know the meaning of plagiarism and declare that all of the work in the document, save for that which is properly acknowledged, is my own.

Contents

List of Figures

List of Tables

Chapter 1

Introduction

Changes in the appearance of stars in the night sky, visible to the naked eye, has always inspired curious questions about their nature. Although human beings have observed "new stars", i.e, novae and supernovae (SNe), for millennia, modern supernova (SN) research began after 1934, following a clear distinction between a classical novae and SN by Baade & Zwicky (1934). The death of a massive star is signified by a cataclysmic explosion called a core-collapse SN (CCSN) that can outshine its host galaxy. Massive stars provide most of the light observed from star forming galaxies. mass-loss from these stars determine their structure and evolution (Smith 2014), which in turn have a feedback effect on their respective galaxy environments. Through this feedback, nuclear fusion inside the cores of massive stars and nucleosynthesis during core-collapse in SNe, provide heavy elements that get dispersed into the interstellar medium (ISM), driving galactic chemical evolution (Edmunds 2017). This has implications in other areas of astrophysics such as the metallicity evolution of the universe and arresting star formation in galaxies by pushing hot gas into the galactic halo (Putman et al. 2012).

By exposing the remaining compact objects such as neutron stars and black holes, SNe permit us to probe the interiors of massive stars and study the high energy physics associated with them. They also drive shock fronts through the circumstellar medium (CSM) and ISM for thousands of years after the explosion (Reynolds 2008), allowing us to investigate the underlying mass-loss histories of their progenitors. Despite the advancement made in understanding the variety of observed SNe and their remnants since they were first discovered, there are still gaps in connecting their diversity to their progenitor evolution. For example, Type-IIn SNe have signatures implying that they are interacting with the CSM (Smartt 2015), however it is not well understood when and how the CSM is formed. It is still an open question whether all Type-IIn SNe progenitors are Luminous Blue Variable (LBV) stars, and all Type-IIb SNe progenitors are binary systems (Smartt 2015). These questions can be addressed by using stellar evolutionary tracks and modelling the interaction of a SN ejecta with different CSM density structures during the early phase of the explosion.

1.1 Evolution of massive single stars

Massive stars have initial masses of $\geq 8\,M_\odot$ (Langer 2012). During the main sequence stage they derive their energy almost entirely from the fusion of hydrogen to helium, primarily via the CNO cycle (Levesque 2017). To study the evolutionary tracks of these stars from the main sequence stage up to their deaths, astronomers use the Hertzsprung-Russell (H-R) diagram shown in Fig 1.1. Initial masses of massive stars can be differentiated into two categories: the lower mass and high mass end. For the lower mass end, as hydrogen becomes depleted in the core, the star then fuses hydrogen in a shell around the helium core. Although the latter contracts, the radius of the star increases as the stellar envelope expands and its temperature plummets (Levesque 2017). The luminosity changes slightly, resulting in the star moving to the right, horizontally across the H-R diagram (see Fig 1.1). The star eventually settles at cool effective temperatures ($\sim 3500 - 4500\,K$) and large radii ($\sim 100 - 1000\,R_\odot$), signifying the beginning of the red supergiant (RSG) phase as core helium fusion begins (Levesque 2017).

They lose more than half of their initial mass after evolving off the main sequence, and the RSG phase is responsible for a significant fraction of this mass-loss. At the more massive end, the star exits the RSG phase, evolving leftward on the H-R diagram, as radiatively driven winds completely strip away their outer envelopes to become Wolf-Rayet (WR) stars (Smartt et al. 2002). Tremendous mass-loss via winds and eruptions dominate the evolution of the highest mass stars, e.g., during the LBV phase (Smith et al. 2016).

The weight of the outer layers of a massive star is sufficient to compress the helium core until it reaches a critical temperature hot enough to fuse helium into carbon, oxygen, neon, and magnesium (Janka et al. 2007). The star repeats the process of contracting, heating and fusing the products of helium nuclear burning into silicon, sulfur, calcium, and argon (Thielemann et al. 1996) These elements are heated to higher temperatures and compressed to higher densities, combining to produce an iron core. The element with the highest binding energy per nucleon is iron, and it signals the end stage of nuclear fusion in hydrostatic equilibrium.

1.2 Core-collapse supernova mechanism

Once nuclear fusion in the core ceases, the outward pressure provided by thermal energy released at the core stops, and a star collapses under its own gravity and compresses the core until the electron degeneracy pressure halts the collapse (Ott et al. 2009). Shell burning adds mass to the now degenerate iron core and drives it to exceed the Chandrasekar mass limit of about $1.26\,M_\odot$ (Pols 2011). In low mass cores of RSGs, iron-peak nuclei absorb electrons by electron capture, which result in a decay of the pressure provided by the degenerate electrons. As a consequence, the core becomes unstable leading the star to undergo

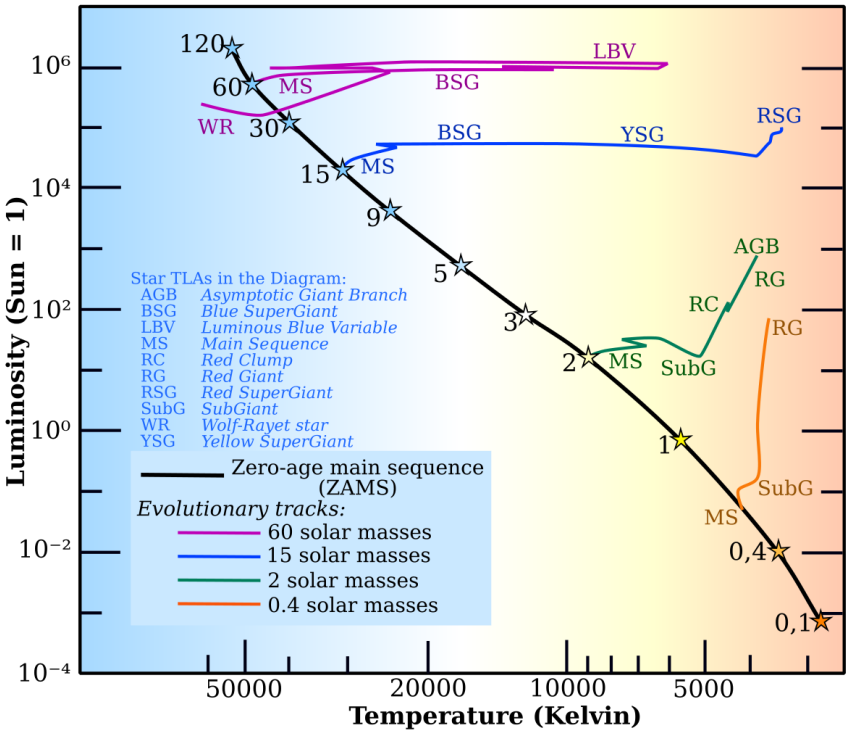

Figure 1.1: Hertzsprung–Russell diagram showing model evolutionary pathways of stars with different initial masses. Figure taken from `https://en.wikipedia.org/wiki/Stellar_evolution`

core collapse. (Ott et al. 2009). Large and hot stellar cores of WR and LBV stars are sufficient to generate gamma-rays that initiate photodisintegration of iron-peak nuclei to alpha particles directly, which accelerates the initial collapse of the degenerate core (Janka et al. 2007). Due to electron capture, protons are converted into neutrons, thereby shifting the nuclei distribution present in the core to be neutron-rich, simultaneously trapping neutrinos in the core.

The core implodes almost instantly until the central subsonically collapsing region of $\sim 0.5\,\mathrm{M}_\odot$ reaches nuclear densities ($\rho = 10^{14}\,\mathrm{g\,cm^{-3}}$) (Janka et al. 2007). The collapse of the now proto-neutron core decelerates rapidly and bounces in response to the neutron degeneracy pressure halting the collapse (Ott et al. 2009). The outer part of the core collapses inward under gravity at supersonic speeds, consequently causing the inner core to rebound into the now in-falling outer core. The result of the core bounce is a hydrodynamic shock, initially propagating outwards in radius while losing energy by dissociating heavy atomic nuclei into nucleons and neutrinos that radiate away from the post-shock region (Ott et al.

2009). Due to energy loses, the shock stalls and turns into an accretion shock at a radius of $\sim 100 - 200\,\mathrm{km}$.

SN models by Janka et al. (2007) show that the compression of the iron-core increases the temperature to about $10^{11}\,\mathrm{K}$, sufficient to generate thermal neutrinos. About $\sim 10^{54}\,\mathrm{erg}$ is converted into a short burst of thermal neutrinos which becomes the primary energy of the SN (Janka et al. 2016). The stalled shock can be revived by the thermal neutrinos streaming away off the newly born neutron star, increasing the pressure behind the shock. This neutrino-driven mechanism re-energizes the stalled shock resulting in a successful explosion.

The neutron star increasingly accumulates mass by accretion of in-falling material until the SN explosion initiates. Depending on the initial mass of the progenitor star, mass below or above $\sim 25\,\mathrm{M}_\odot$, the explosion leaves behind a neutron star, or collapses completely to a black hole, respectively. A fast-moving ejecta is driven into the surrounding CSM, compressing and accelerating the overhead gas and dust which is eventually observed as a SN remnant (SNR) – the subject of this work. Fig. 1.2 shows the variety of the expected deaths of massive stars depending on their initial mass and metallicity. Various factors contribute to the current diversity of observed SNe and their SNRs, and this forms the basis for SN classification.

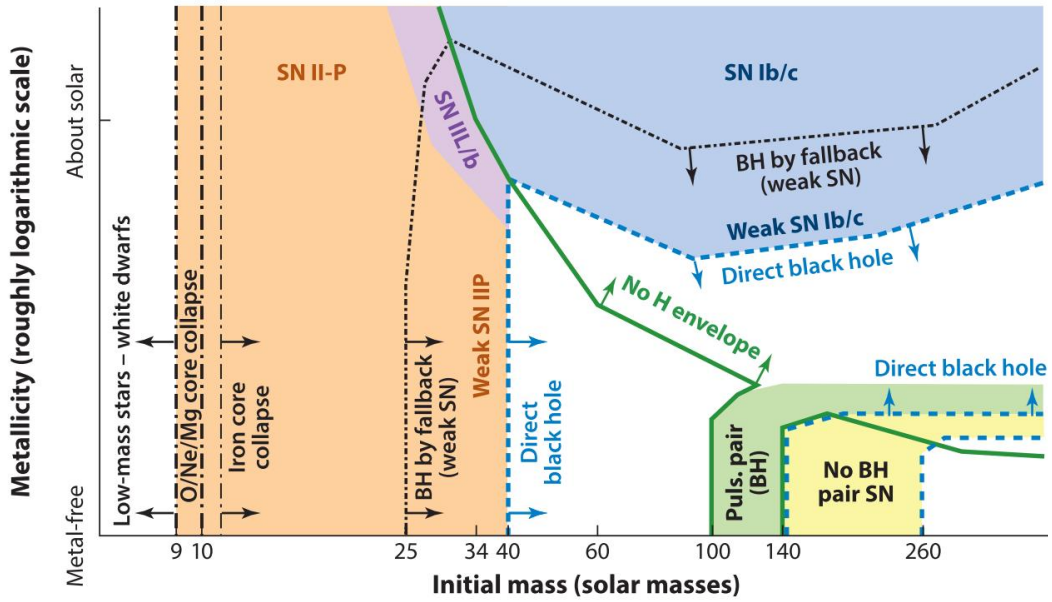

Figure 1.2: Standard expectations of the end stages of single massive stars. Image credit: Adapted from Figure 1 of Smith (2014). Abbreviations: black hole, BH; supernova, SN

1.3 Supernova taxonomy

The type of SN produced by single massive stars depends on the core mass and the presence of the hydrogen envelope moments before explosion (Heger et al. 2003). Observations of SN explosions show that their characteristics vary based on their spectra and light curves. SNe are classified into two basic types, Type-I and Type-II, based on the early time spectra depending on the absence or presence of hydrogen Balmer series emission lines at maximum luminosity, respectively (da Silva 1993, Beswick 2006). These basic categories are further divided into subclasses as shown in Fig. 1.3.

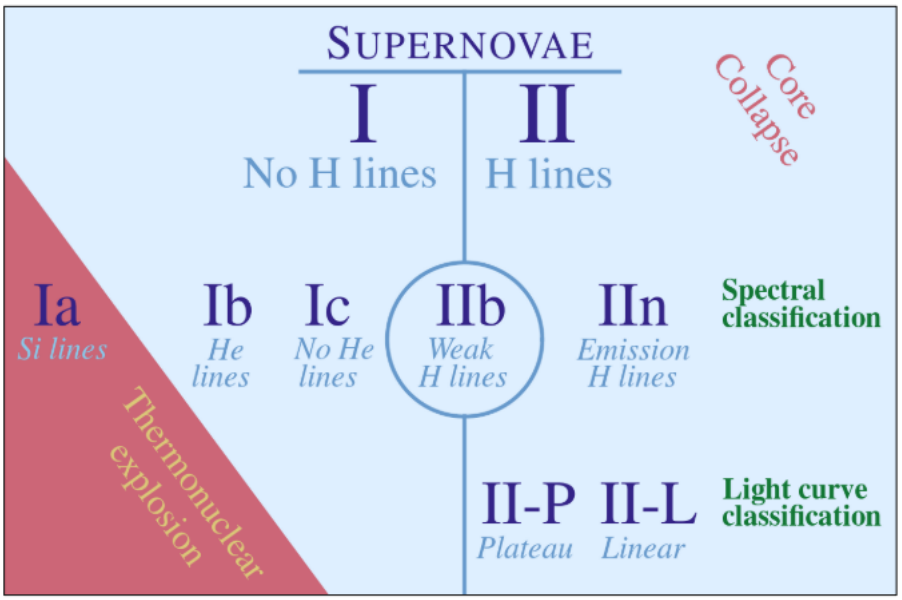

Figure 1.3: Supernova classification diagram. Image credit: Adapted from Figure 3 of Pruzhinskaya & Lisakov (2016).

Type-II SNe are further categorized into subtypes; Type-IIn and Type-IIb based on strong or weak lines of hydrogen emission in their optical spectra, and Type-IIP and Type-IIL based on their photometric visual light curve shape (da Silva 1993). Type-IIP SNe display a constant luminosity for $\sim$ 100 days and so have a prominent plateau in their light curve as shown by red triangles in Fig. 1.4. These are the most common type of CCSN and arise primarily from RSG progenitors (Smartt 2015). The hydrogen in the spectra of Type-IIP is attributed to mass-loss rates not being strong enough to strip away the hydrogen envelope in RSGs prior to their explosion. Type-IIL SNe are spectroscopically very similar to Type-IIP but show a linear decline in their light curves as shown by blue circles in Fig. 1.4. There is no direct evidence for progenitors associated with Type-IIL, however, theoretical model light curves show that mass reduction in the hydrogen-rich envelope of RSGs is a strong contender for transforming the light curve of Type-IIP to a more linear decay (Young 2004).

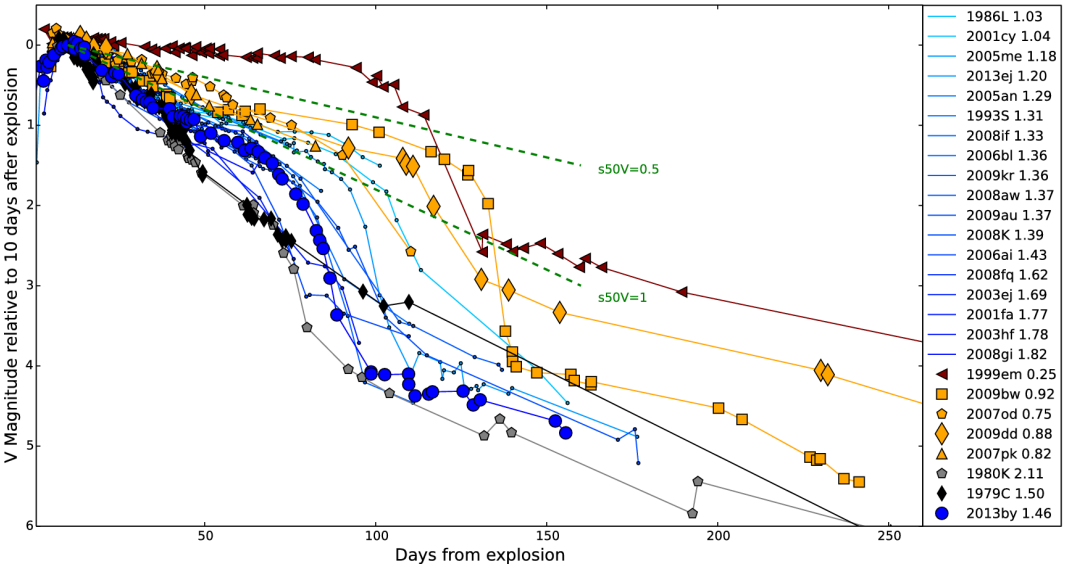

Figure 1.4: Optical light curves of Type-IIP and -IIL SNe in the V-band. Type-IIP SN (red triangles) are shown here undergoing a plateau phase in the first 100 days after explosion and a rapidly declining magnitude of Type-IIL SN (blue circles). Credit: Figure and caption adapted from Figure 8 of Arcavi (2017).

Additionally, Type-IIb SNe are distinct in that they evolve from having an abundance of hydrogen in their early spectra to helium emission lines dominating their spectra near peak luminosity (e.g. SN 2011dh). Evidence of the progenitors of Type-IIb SNe points to yellow supergiants in a binary system (Smartt 2015). Compared to other hydrogen dominated SNe spectra, Type-IIn SNe have strong but relatively narrow hydrogen emission lines as shown in Fig. 1.5. This is attributed to nearby circumstellar material that is photoionized or shock-heated by the SN at early times (Gal-Yam 2017). Observations of optical spectral features corresponding to material velocities of $100\,\mathrm{km\,s^{-1}}$ (Smartt 2015), together with modulated radio emissions which could be the result of a SN ejecta interacting with old shells of regular mass ejections (Kotak & Vink 2006), favour LBVs as progenitors for some Type-IIn SNe.

Type-I SNe are classified into Ia, Ib, and Ic according to their spectroscopic emission lines at maximum luminosity. In terms of their spectral properties, Type-Ia SNe show a dominant signature of silicon (Si II) absorption near peak luminosity and a representative example is SN 2011fe (Gal-Yam 2017). This subclass is widely accepted to arise from a thermonuclear explosion of a carbon-oxygen White Dwarf (WD) when it exceeds the Chandrasekhar mass limit (Hillebrandt & Niemeyer 2000), either from matter accretion in a binary system (Domínguez & Khokhlov 2011) or merger with another WD (Martin et al. 2006). Both these scenarios involve stars of initial mass $(1.8 - 2.2\mathrm{M}_{\odot})$ at low mass range or $(2.2 - 7.5\mathrm{M}_{\odot})$ for intermediate mass range. Type-Ia SNe are important in cosmology since they led to the first evidence for a late-time acceleration in the expansion of the Universe. However, this subclass of SNe will not be the focus of this study.

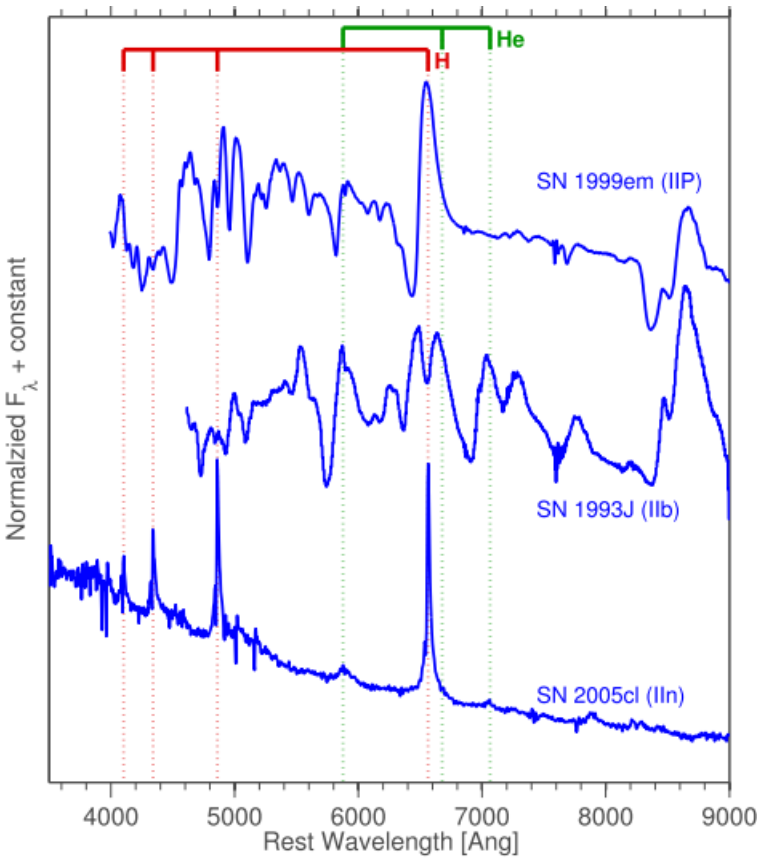

Figure 1.5: Spectra of SN 1999em (Type-IIP), SN 1993J (Type-IIb), and SN 2005cl (Type-IIn). Hydrogen lines, marked with red dashed lines, define all Type-II SNe. Credit: Figure and caption adapted from Figure 17 of Arcavi (2017).

Type-Ib SNe lack hydrogen in their spectra, but are dominated by broad helium lines and while Type-Ic SNe also lack hydrogen, He lines in their spectra are negligible or absent, signaling an example of a massive star with a stripped helium envelope (Beswick 2006). The progenitors of Type-Ib/c are thought to be WR stars, evolved massive stars that have lost their hydrogen envelopes (e.g., WN stars) and also helium envelopes (e.g., WC and WO stars) primarily through radiatively pressure-driven winds, episodic mass-loss and/or interaction with a binary companion (Smartt 2015). Most Type-Ib and Ic SNe are radio luminous and rapidly turn-on/turn-off at radio frequencies, peaking at centimetre wavelengths on comparable timescales to their optical emission peak (Beswick 2006).

The radio emission from CCSNe is synchrotron in origin, arising from relativistic electrons accelerated at the shock fronts (Chevalier & Fransson 2003). Radio light curves from Type-II SNe display very varied properties as shown is Fig. 1.6, including wide variations in luminosity and timescales for the truly peculiar SNe with a flatter spectral index and slower turn-on

(Weiler et al. 1986). Since the CSM is steadily expanding and becomes less dense and opaque at large radii, the radio light curve of a CCSN initially rises at higher frequencies following the explosion before rising at lower frequencies where the material is more transparent to low energy radiation as shown in Fig. 1.6 (Beswick 2006). Chevalier (1982a,b) advocates for relativistic electrons accelerated by enhanced magnetic fields as a necessary condition for synchrotron emission at radio wavelengths and this can be seen by the radio emission arising from the SN blastwave interacting with a relatively high density CSM. Thus, the radio luminosity, L, is related to the average CSM density ρ according to:

$$\rho \propto \frac{\dot{M}}{\upsilon_{\rm w}}, \tag{1.1}$$

via the relation

$$L \propto \left(\frac{\dot{M}}{\upsilon_{\rm w}}\right)^{\eta}, \tag{1.2}$$

where $\upsilon_{\rm w}$ is the wind velocity and η is a constant that governs the deceleration parameter, m, for the SN blastwave and spectral energy index, γ, of relativistic particles (Weiler et al. 2004). This relationship between radio luminosity and density of the CSM is one of several ways to probe the mass-loss histories of massive stars. The wide explosion diversity observed in properties of CCSNe is the consequence of different progenitor masses, metallicities, and mass-loss rates in massive stars. Since this diversity in progenitor mass traces the mass-loss histories of these massive stars which is established in the CSM density structure, we study the interaction of the SN ejecta with different CSM density environments to attempt to connect the evolution of massive stars with their deaths as SNe during the Sedov-Taylor phase of the SNR.

1.4 Circumstellar environments of the progenitor

The vast majority of the progenitors of CCSN progenitors are in the mass range $8 - 25\,M_{\odot}$ (Smith 2014). Single stars with initial masses in this range are predicted to evolve through the RSG phase before they reach the end stages of their evolution as core-collapse SNe (CCSNe). The RSG phase is signified by an enhanced mass-loss rate and luminosity of the star (Beasor & Davies 2017). The mass-loss rate, $\dot{M}$, depends on the average gas density, $\rho(r)$, at a radial distance, r, at which the outflow wind velocity has reached, $\upsilon_{\rm w}$, according to,

$$\dot{M} = 4\pi r^2 \rho(r) \upsilon(r). \tag{1.3}$$

While the driving mechanism for these stellar winds remains uncertain, they set up a circumstellar density environment that imprints the history of the massive star's evolution. Puls et al. (2015) briefly outline the possible stellar mass-loss mechanisms in very massive stars, including dense slow moving winds from RSGs and fast radiative line-driven winds from WR and LBV stars.

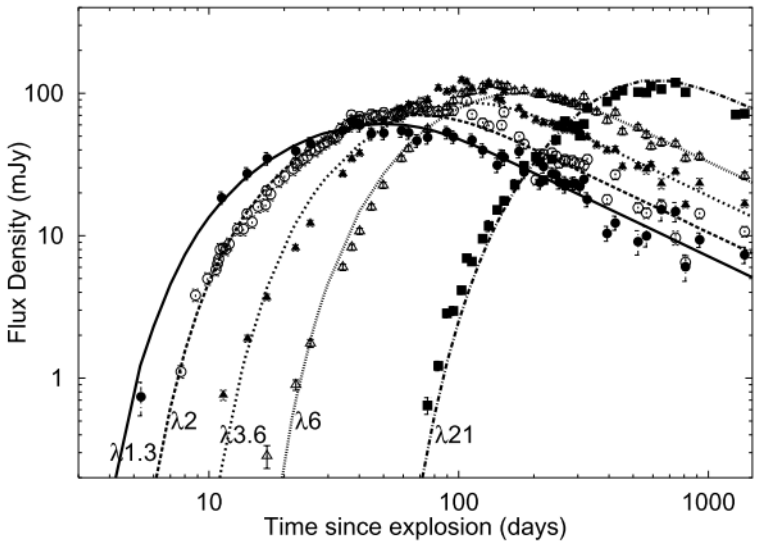

(a)

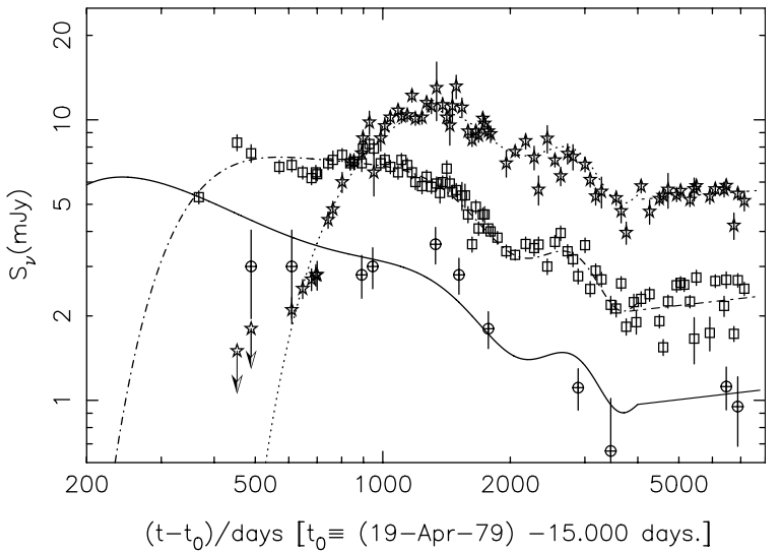

(b)

Figure 1.6: (a) Typical core-collapse radio light curves (SN 1993J) at $\lambda = 1.3$cm (filled circles), $\lambda = 2$cm (open circles), $\lambda = 3.6$cm (filled triangles), $\lambda = 6$cm (open triangles), and $\lambda = 21$cm (filled squares), from measurements made using the VLA . The solid, and other dashed lines represent the best fit model. Credit: figure and caption taken from Figure 1 of Pérez-Torres et al. (2001). (b) Unusual Type-II SN (SN 1979C) at $\lambda = 2$cm (crossed circles), $\lambda = 6$cm (open squares), and $\lambda = 20$cm (open stars). The radio light curves steadily exhibit a sinusoidal behaviour between 1000 and 4000 days. The lines represent the best fit models. Credit: Figure and caption taken from Figure 2(a) of Weiler et al. (2004).

Studying the evolution of SNRs may offer hints pertaining to the progenitor systems of

the various CCSN types observed in the universe. The standard single massive star evolution model described in section 1.1 has shifted in the past decade because a high fraction of massive stars are found in binaries (Sana et al. 2012). Due to the dynamical process of mass-loss and metallicity, rotation in massive stars and mass transfer in binary interactions, complex aspherical circumstellar environments can result from the RSG phase (Langer 2012). Circumstellar environments of RSGs require highs spatial resolution observations in the mid-infrared wavelengths in order to effectively study their dynamical process. Ohnaka et al. (2008) used MID-infrared Interferometric instrument (MIDI) at the Very Large Telescope Interferometer (VLTI) with the help of the Infrared Spectrograph (IRS) aboard the Spitzer space telescope to study the environment of WOH G64, and revealed that it exhibits silicate features in self-absorption. This means that the material enveloping the central object is dusty and optically thick, indicating heavy mass-loss. Different SN progenitors set up different CSM environments, hence, we want to use SNR signatures to determine the stellar histories. The Sedov-Taylor phase is a very important stage in young SNRs and can be modelled using the Sedov-Taylor blastwave solution.

1.5 Sedov-Taylor blastwaves

In 1950, Taylor (1950) used dimensional analysis to determine an approximation of the relationship between the energy of a powerful point explosion and the flow in front of a supersonic, uniformly expanding spherical pressure wave. Sedov (1959) independently derived a self-similar solution for the evolution of a strong spherical shock due to a point release of a large amount of thermal energy. They treated the point explosion as a localized instantaneous release of energy and assumed that the blastwave propagates through a cold uniform ambient medium that behaves as an ideal polytropic fluid (Book 1994). This solution became known as the Sedov-Taylor blastwave solution due to its widespread use throughout the 1950s and beyond. It has been applied as a method for describing one of the major phases of SN evolution, and provides a clear analytical profile that SN simulations can be compared to.

The advantage of the Sedov-Taylor solution is its self-similarity. This means it can be characterized in terms of a dimensionless variable, β, in a coordinate system where the solution is stationary. In other words, this property ensures that the Sedov-Taylor solution is valid regardless of the physical size of the expansion, and is constant when expressed in terms of β. Sedov (1959) proved that one can derive an analytical solution to certain one-dimensional (1D) problems of unsteady motion of a compressible fluid using dimensional analysis.

The analysis involves determining the relationship between several dependent variables and the fundamental parameters pertaining to the problem. In the Eulerian framework, the ba-

sic physical variables involved when solving a 1D unsteady motion problem are the density, ρ, velocity, v, and pressure, p. The 1D characteristic parameters involved are the linear coordinate, $\mathbf{r}$, and time, t, together with the constants that enter the problem, and the initial and boundary conditions of the problem. A solution that depends on the independent variables of the problem has a good chance of harbouring several arbitrary constants. The requirement for self-similar motion is that the problem contains only two characteristic parameters with independent dimensions (Sedov 1959). The full derivation of the self-similar motion in strong shocks is outlined in A.1. Whereas SNRs undergo various dynamical phases during their evolution, we use the self-similarity of the Sedov-Taylor blastwave to model the hydrodynamic evolution of young SNR during the Sedov-Taylor phase.

1.6 Supernova remnants

A SNR forms when the material ejected by a SN explosion interacts with the CSM. Woltjer (1972) schematically categorized the evolution of this interaction into four distinct phases describing the dynamical evolution of a SNR. Still in use today, these phases are defined as (Dubner & Giacani 2015):

- **Free Expansion** - Sometimes called the *ejecta-dominated phase*, the shock wave created by the initial SN explosion expands radially outwards into the CSM at high velocities, compressing the circumstellar gas that has accumulated behind the blastwave. The reverse shock forms behind the contact discontinuity, a turbulent layer distinguishing the shocked ejecta from the shocked circumstellar gas. When the mass of the compressed circumstellar gas behind the forward shock equals the ejecta mass, the SNR transitions to the next phase of the evolution.

- **Sedov-Taylor Phase** - Sometimes called the *adiabatic expansion phase*, here the SNR owes its expansion to the thermal pressure of a shell of hot compressed gas. The temperature inside the SNR is extremely high, making energy lost through radiation negligible. Since the CSM is flash ionized, no recombination takes place, and the gas is only cooled by adiabatic expansion. The SNR continues to expands and cool until it reaches a critical temperature of about 10^6 K, where recombination occurs and energy losses via radiation start to dominate, signaling the end of the Sedov-Taylor phase.

- **Snow Plough Phase** - The Sedov-Taylor phase concludes by slowing down the expansion. This is caused by the decreasing thermal pressure in the post-shock region due to effective radiative cooling. The SNR has now entered the sometimes called *radiative phase*, where the mass of the accumulated circumstellar gas exceeds the ejecta mass. Rayleigh-Taylor and Richtmyer-Meshkov instabilities set in, breaking the SNR shell into individual pieces and leading to the final phase of evolution.

- **Dispersion** - The CSM is not stationary, but has random motions of the order 10 km/s. The SNR expansion velocity decreases to values typical of the CSM, and

eventually loses its identity by dispersing into the CSM.

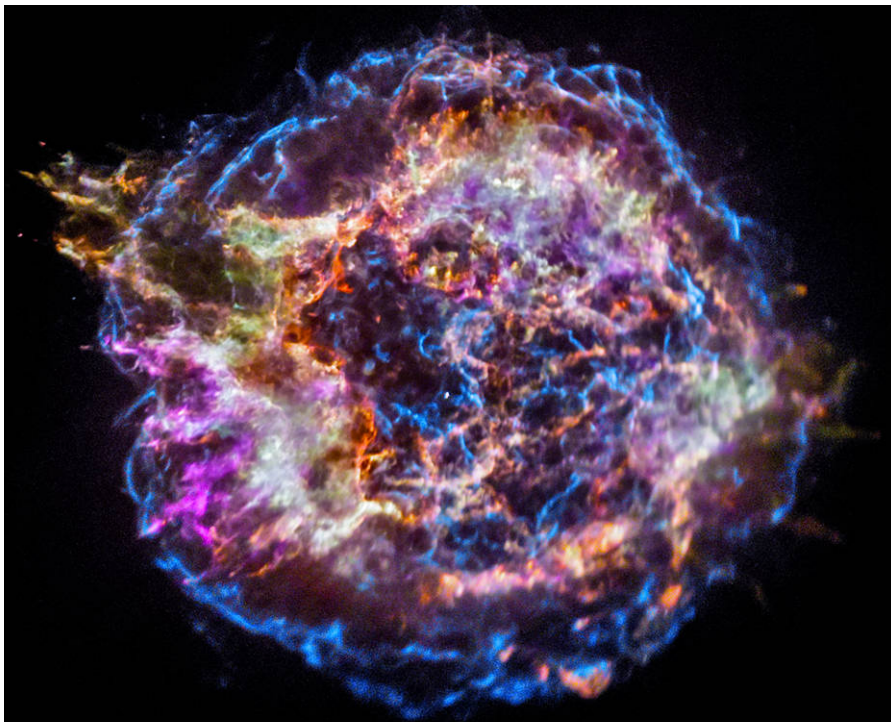

Figure 1.7: This composite image reveals the elementary nature of Cassiopeia A, a remnant of Tycho's CCSN 3C 10 (SN 1572) using three different wavelengths. In red is the Infrared data from the Spitzer Space Telescope; yellow for visible light from the Hubble Space Telescope; and green and blue represents the hard and soft X-ray data from the Chandra X-ray Observatory. Image credit: Figure and Caption adapted from `https://www.nasa.gov/chandra`. Editor: Lee Mohon.

This SNR evolution scheme is an oversimplification of a complex dynamical evolution of the remnant. Distinct phases maybe short-lived, occur simultaneously at different parts of the same remnant, or may not occur at all (Jones et al. 1998). A good example of a dynamically complex SNR is the intensively studied Cas A SNR shown in Fig. 1.7. An idealized picture of a SNR follows a uniform spherically symmetric SN ejecta expanding into a uniform CSM. In this work, we are only concerned with the first two stages; ejecta-dominated and Sedov-Taylor stages. During these phases, SNRs are commonly classified as non-radiative because radiative losses are dynamically insignificant (Franco et al. 1994). The ejecta-dominated stage is initialized the instant the stellar envelope erupts from the progenitor immediately after a SN explosion. The initial expansion velocity of the ejecta is several times great than the sound speed in the CSM, which results in a formation of a leading blastwave shock. This leading blastwave shock compresses and heats up the CSM as it propagates radially outwards.

The compressed accumulated gas behind the forward shock exerts some force back on the

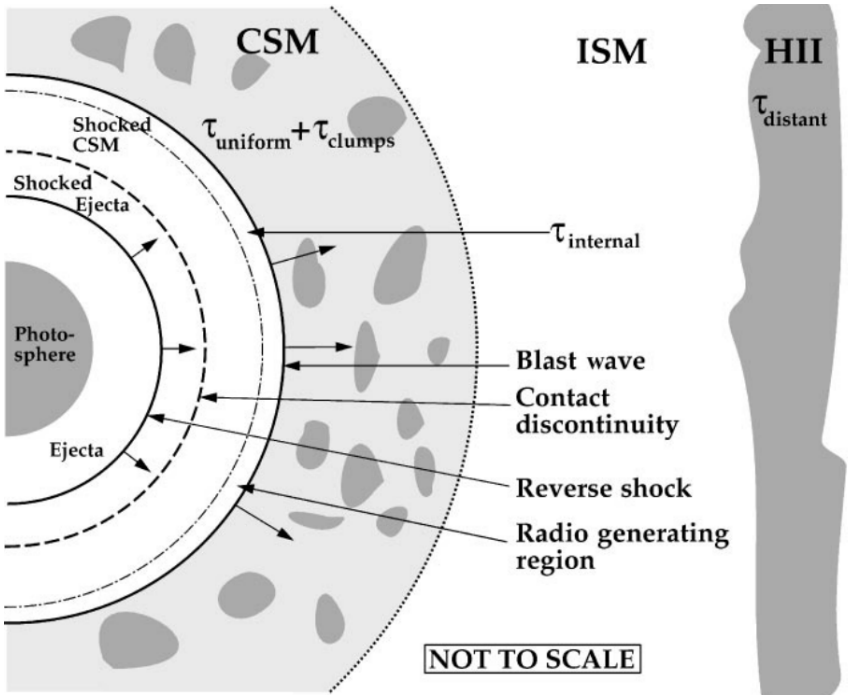

Figure 1.8: A schematic diagram showing the SN shock structure in the interaction region as well as the backdrop of the CSM and ISM (interstellar medium). Credit: Figure and caption taken from Weiler et al. (2002).

freely expanding ejecta, compressing, decelerating and heating it up in the process and forming a reverse shock as a result. Due to the difference in densities of the different regions of the interaction region, a thin contact discontinuity layer forms, that separates a cool, dense, shocked ejecta material from a hot, tenuous, shocked CSM (Truelove & McKee 1999). The reverse shock accelerates the freely expanding unshocked ejecta inward (Chevalier 1977), and relative to the stationary CSM, the velocity of the shocked ejecta retains a resultant outward radial velocity below the shocked value. The reverse shock communicates the existence of the CSM to the ejecta, causing the ejecta to decelerate (Jones et al. 1998). The pressure gradient between the reverse and the forward shock further decelerates the shocked ejecta (Truelove & McKee 1999). A schematic diagram in Fig 1.8 illustrates the various parts of the SNR and its shock structure.

At early times of the ejecta-dominated stage when the reverse shock velocity is still insignificant, the ejecta is modelled as a spherical piston expanding into the CSM (Sedov 1959). At late-times of the Sedov-Taylor stage, when most of the ejecta energy has been used up by work done during expansion, the flow is said to be adiabatic (Truelove & McKee 1999). The system will evolve self-similarly in each limiting case and the deviation from free expansion is the first step towards a non-self-similar evolution (Truelove & McKee 1999).

It is commonly assumed that the Sedov-Taylor stage applies when the mass of the shocked

CSM, $M_{\mathrm{sh\_csm}}$, is much larger than the mass of the ejecta, M_{ej}. In the self-similar ejecta dominated and Sedov-Taylor limits, the radius, R, of the shocked shell material evolves as $R \propto t^m$, where m is a constant called the expansion parameter (Truelove & McKee 1999). During non-self-similar periods of expansion, m, depends on time and it is simply defined as a ratio of the instantaneous and average velocities of the leading forward shock, $\frac{\dot{R}}{(R/t)}$. For newborn remnants in free expansion, the expansion parameter is unity and varies to $\frac{2}{5}$ for older remnants in the late Sedov-Taylor stage (Truelove & McKee 1999). In the late Sedov-Taylor phase, the ejecta is interacting with enough swept up material such that an interaction shell has formed (see Fig. 1.8). This interaction shell is a source of a wide range of electromagnetic radiation observed in SNRs.

1.7 Previous studies and outline

Truelove & McKee (1999) provided analytic and numerical models of the subsequent evolution of a SNR from the early ejecta-dominated phase through to the late Sedov-Taylor phase and demonstrated that the analytic solutions for the motions of both the reverse shock and forward shock are in good agreement with numerical simulations which is valuable for describing the evolution of young remnants. Whalen et al. (2008) performed one-dimensional hydrodynamic models of Type II SNe ($15\,\mathrm{M}_{\odot}$), hypernovae ($40\,\mathrm{M}_{\odot}$), and pair-instability SNe ($260\,\mathrm{M}_{\odot}$) interacting with ionized (H II) and neutral ISM. Their findings suggest that SNe in H II regions first undergo adiabatic expansion and then radiate strongly during interaction with gas from the halo, while SNe in nearly neutral interstellar medium lose most of their initial kinetic energy as X-rays, the ejecta reaches radii of $10 - 20\,\mathrm{pc}$ due to the stored momentum in the system. van Veelen et al. (2009) performed two-dimensional simulations of a SNR in which the SN ejecta interacts with a smooth and clumpy CSM while using WR progenitors of different WR life times. They examined the morphology and kinematics of the remnant for a CSM structure shaped by a spherically symmetric RSG wind of a single massive star with initial mass $20\,\mathrm{M}_{\odot}$. They compared their results with the observations of Cas A, and concluded that the reverse shock radius and shock velocity match the observed values. With the availability of a new class of Lagrangian meshless methods, here we perform 3D hydrodynamic simulations of SN ejecta interacting with different CSM density profiles.

We present a similar study to that of van Veelen et al. (2009), this time focusing on the comparison and morphology of the interaction of SN ejecta with $1/r^2$ and asymmetric torus CSM density profiles using meshless numerical methods. In chapter 2, we discuss the numerical framework of all the meshless methods we employ for modelling the hydrodynamics of the SNR. Chapter 3 focuses on the Sedov-Taylor blastwave tests we performed to determine the parameter space for each method that is in agreement with the Sedov-Taylor blastwave exact solution and discuss the findings for each test. In chapter 4, we compare the simulation results of all methods for hydrodynamic simulations of the SN ejecta interacting with

the $1/r^2$ and asymmetric torus CSM density profiles. We discuss the growth of Richtmyer-Meshkov instabilities and implications of our models for the morphology and observational properties of SNRs. In chapter 5, we present our summary and conclusion for this study, as well as outline work we plan to do in the future.

Chapter 2

Methodology: Computational Hydrodynamics

2.1 Ideal gases

The equation of state (EOS) relates two or more state variables which describe the state of matter and the ideal gas equation is one of the simplest forms. Since most real gases behave like ideal gases, although not perfectly, this can be a good assumption for many astrophysical systems, particularly if densities are low and temperatures high as is often found in stars and circumstellar environments. In an ideal gas, particles move freely, they rarely collide with each other and are smaller than the mean-free path between collisions by several orders of magnitude. The ideal gas EOS relates the absolute gas pressure, P, to absolute temperature, T, and particle number density, n, by

$$P = nk_BT, \tag{2.1}$$

where k_B is the Boltzmann constant relating temperature to energy (given by $k_B = \frac{R}{N_A}$, where N_A is the Avogadro's constant and R is the universal gas constant). We can rewrite this EOS as,

$$P = \frac{\rho k_B T}{\mu m_p} \tag{2.2}$$

where μ represents the mean molecular weight of the gas, m_p is the mass of a proton and ρ is the mass density of the gas. For polytropic fluids, that is fluids that behave according to

$$PV^\gamma = C, \tag{2.3}$$

where P is the gas pressure, C is a constant and V is the volume of the region containing the gas, the polytropic EOS takes the following form:

$$P = (\gamma - 1)\rho\epsilon \tag{2.4}$$

where γ is the adiabatic index of the gas and ϵ is the specific internal energy. The governing equations of fluid dynamics should account for the EOS when they are established.

2.2 Equations of hydrodynamics

The state of a fluid in motion, whose thermodynamic properties are known can be explicitly expressed in terms of velocity($\mathbf{v}$), density (ρ), and pressure (P) as a function of position (r) and time (t). These functions are fundamentally described by a set of differential equations that define the general laws of conservation of mass, momentum and energy.

2.2.1 Equations of hydrodynamics in Eulerian form

Using the Eulerian framework, one can calculates a derivative at a fixed point in space and time, thus, the partial derivative with respect to time at an arbitrary point in space is used, denoted by $\frac{\partial}{\partial t}$. The continuity equation describes how mass is conserved in a hydrodynamic system, that is, the change in density in a given volume element is entirely due to the inflow or outflow of mass through volume ∂V,

$$\frac{\partial \rho}{\partial t} + \nabla \bullet (\rho \mathbf{v}) = 0. \tag{2.5}$$

The conservation of momentum equation considers the rate of change of total momentum of a fluid inside the volume V,

$$\rho \left[\frac{\partial \mathbf{v}}{\partial t} + \mathbf{v} \bullet \nabla \mathbf{v} \right] = -\nabla P + \rho \mathbf{f}, \tag{2.6}$$

where $\mathbf{f}$ represents external forces; it is also known as Euler's equation. The conservation of energy describes the change in specific internal energy (ϵ) of a given particle when work is done on the particle by its surrounding medium and external energy sources (Q),

$$\frac{\partial}{\partial t}\left(\frac{1}{2}\rho \mathbf{v}^2 + \rho\epsilon \right) = -\nabla \bullet \left[\left(\rho\epsilon + \frac{\rho \mathbf{v}^2}{2} + P \right) \right] + \rho Q. \tag{2.7}$$

The aforementioned hydrodynamic equations can be numerically solved for each fluid particle provided the initial state of the flow and fluid EOS are known (Teyssier 2015). Equation 2.5-2.7 are the conservative form of Euler equations and this allows the computational volume to be discretized into fixed volume elements where the changes in the conserved quantities (mass, linear momentum, and total energy) are obtained by taking the summation of the

net fluxes across cell interfaces (Teyssier 2015).

2.2.2 Equations of hydrodynamics in Lagrangian form

The Lagrangian form of the Euler equations are simpler to derive and can be used to design Lagrangian codes as in the case of Smoothed Particle Hydrodynamics (SPH) discussed in the following section. In the Lagrangian description, derivatives are evaluated in a coordinate system that changes with a moving fluid element. Total or material derivatives ($\frac{\mathbf{D}}{\mathbf{D}t}$) are used to describe the rate of change of time of any fluid property, therefore, the derivative with respect to time in the Lagrangian coordinates is equivalent to $\frac{\mathbf{D}}{\mathbf{D}t} = \frac{\partial}{\partial t} + \mathbf{v} \bullet \nabla$. Solving the equations of hydrodynamics reflecting the conservation of mass, momentum, and energy in the Lagrangian context yields:

$$\frac{\mathbf{D}\rho}{\mathbf{D}t} + \rho \nabla \bullet \mathbf{v} = 0, \tag{2.8}$$

$$\frac{\mathbf{D}\mathbf{v}}{\mathbf{D}t} = -\frac{\nabla P}{\rho} + \mathbf{f}, \tag{2.9}$$

$$\frac{\mathbf{D}\epsilon}{\mathbf{D}t} + \frac{P}{\rho} \nabla \bullet \mathbf{v} = Q, \tag{2.10}$$

Lagrangian co-ordinates are suitable for arbitrary geometries, which make them ideal for our hydrodynamic study of both the spherical and aspherical SN ejecta-CSM interaction.

2.3 Smoothed Particle Hydrodynamics (SPH)

SPH is a Lagrangian method for solving the Euler equations by discretizing the fluid domain into a set of particles (Monaghan 2005). Mathematically, these particles can be thought of as interpolation points where fluid variables can be evaluated. In astrophysics, the SPH particles represent individual fluid parcels or elements with inter-particle forces designed to mimic the true pressure and other body forces of the fluid (Gingold & Monaghan 1977) (GM77 hereafter).

Lucy (1977) developed the earliest implementation of SPH and used it to study the motion of self-gravitating systems made of compressible gases. The term "smoothed particle hydrodynamics" was coined by GM77, where they independently spearheaded the development of the method to test its numerical ability to reproduce static and rotating stellar models. In both of these independent approaches, the numerical scheme they implemented was derived from the Monte Carlo theorem, which owes its origin to the need for estimating probability densities from sampled data by statisticians. GM77 made the assumption that at any time, the positions of the fluid elements are randomly distributed according to the material density. To recover the density from a known distribution is then equivalent to recovering the underlying probability distribution from a sample. They used a smoothing kernel technique, an interpolation method which represents any function in terms of the

values of a set of particles in a well defined domain, to achieve this.

Originally, SPH was designed for hydrodynamic problems for which simple exact or analytical solutions are known and solved for all fluid variables: density, entropy, energy, and velocity. Two steps are required for formulating the SPH equations: the kernel approximation and particle approximation step (Liu & Liu 2010). The kernel approximation step expresses an arbitrary function and its derivatives as a finite integral - sometimes called a continuous form. Thus the function and its derivatives are estimated by evaluating the smoothing kernel and its derivatives at a point of interest. In the particle approximation step, the discretization of the computational domain is done by representing the simulation volume in terms of an initial distribution of particles whose field variables are then estimated by summing up the values of the nearest neighbouring particles using the smoothing kernel (Liu & Liu 2010).

2.3.1 Kernel approximation

At its heart, the kernel approximation method uses an integral to represent a field quantity, $A(\mathbf{r})$, as a function of the spatial coordinates, $\mathbf{r} = (x, y, z)$, by adopting a trivial identity as given by Liu & Liu (2010),

$$A(\mathbf{r}) = \int_V A(\mathbf{r}')\delta(\mathbf{r} - \mathbf{r}')\, d\mathbf{r}', \tag{2.11}$$

where V is the volume of the integral that contains $\mathbf{r}$. Similarly, $\mathbf{r}'$ is a dummy variable ranging over V, $d\mathbf{r}'$ is a differential volume element and $\delta(\mathbf{r} - \mathbf{r}')$ is the Dirac delta function given by

$$\delta(\mathbf{r} - \mathbf{r}') = \begin{cases} 1, & \text{for } \mathbf{r} = \mathbf{r}', \\ 0, & \text{for } \mathbf{r} \neq \mathbf{r}'. \end{cases} \tag{2.12}$$

As long as $A(\mathbf{r})$ is defined and continuous in V, equation 2.12 ensures that the finite integral in equation 2.11 is exact. The Dirac delta function collapses to a point, hence it would be difficult to use for discrete numerical models. By replacing the Dirac delta function with a smoothing kernel, $W(\mathbf{r} - \mathbf{r}', h)$ of finite width, h, the kernel approximation of any continuous scalar or vector field quantity, $A(\mathbf{r})$, is defined by convolving $A(\mathbf{r})$ with $W(\mathbf{r} - \mathbf{r}', h)$ through

$$A_s(\mathbf{r}) = \int_V A(\mathbf{r}')\, W(\mathbf{r} - \mathbf{r}', h)\, d\mathbf{r}', \tag{2.13}$$

where $A_s(\mathbf{r})$ denotes a smoothed field and h is known as the smoothing length. The smoothing length controls the size of support domain (or smoothing area) V over which the smoothing kernel is spread. The smoothing kernel reduces to a Dirac delta function in the limit $h \to 0$ when a sufficiently large number of particles N are used to describe a continuous system, i.e., as $N \to \infty$.

The kernel approximation step is second-order accurate, $O(h^2)$, due to the disorder of the random sample of particles (Liu et al. 2003). Thus, in full form, equation 2.13 should be rewritten as

$$A_s(\mathbf{r}) = \int_V A(\mathbf{r}')\, W(\mathbf{r} - \mathbf{r}', h)\, d\mathbf{r}') + O(h^2), \tag{2.14}$$

where the error in the integral depends on the condition that the smoothing kernel is an even function with respect to $\mathbf{r}$ and satisfies the compact condition requirements discussed later in section 2.3.2. It is essential that a differentiable $W(\mathbf{r} - \mathbf{r}', h)$ can be constructed such that the gradient of a scalar field, $\nabla A(\mathbf{r}')$, is derived by taking the spatial derivative of equation 2.14 at $\mathbf{r}'$, and applying the smoothing kernel. Thus the first derivative of the kernel approximation is obtained by replacing $A_s(\mathbf{r})$ with its derivative,

$$\nabla A_s(\mathbf{r}) = \int_V \nabla \left[A(\mathbf{r}')\, W(\mathbf{r} - \mathbf{r}', h)\, d\mathbf{r}') + O(h^2) \right], \tag{2.15}$$

where the divergence in the integral is operated with respect to the primed coordinate. Using integration by parts with the divergence theorem, while enforcing the compact support condition and neglecting residual boundary terms, Liu & Liu (2010) showed that a gradient of a smoothed field quantity can be written as

$$\nabla A_s(\mathbf{r}) = \int_V A(\mathbf{r}')\, \nabla W(\mathbf{r} - \mathbf{r}', h)\, d\mathbf{r}') + O(h^2). \tag{2.16}$$

Since second-order derivatives are needed in the Euler equations, kernel approximations for second derivatives can be obtained provided a higher-order smoothing kernel is applied. By substituting $A_s(\mathbf{r})$ with its second derivative $\nabla^2 A_s(\mathbf{r})$, in a similar argument to equation 2.16, the second derivatives of the kernel approximation yields a divergence of a scalar gradient field,

$$\nabla^2 A_s(\mathbf{r}) = \int_V A(\mathbf{r}')\, \nabla^2 W(\mathbf{r} - \mathbf{r}', h)\, d\mathbf{r}') + O(h^2), \tag{2.17}$$

and similarly, these second derivatives are also second-order accurate.

2.3.2 Smoothing kernel selection

In SPH, selecting the smoothing kernel is crucial since it determines the quadrature for interpolating the integral, and also defines the radius of the support domain for a particle of interest. Morris (1996) studied the stability properties of SPH using several smoothing kernels; for equation 2.13 to converge and be valid, $W(\mathbf{r} - \mathbf{r}', h)$ should satisfy certain elementary conditions:

1. **Normalization condition** - This states that the smoothing kernel must be normalized to one, that is

$$\int_V W(\mathbf{r} - \mathbf{r}', h)\, d\mathbf{r}' = 1. \tag{2.18}$$

It is also called the *Unity condition* because the integration of the smoothing kernel should yield unity.

2. **Compact support** - The smoothing kernel should be compactly supported, that is

$$W(\mathbf{r}-\mathbf{r}',h)=0 \quad \text{for } |\mathbf{r}-\mathbf{r}'|>\kappa h, \tag{2.19}$$

where κ is a constant related to the smoothing kernel shape for a particle at $\mathbf{r}$, and κh defines the effective non-zero area of the specified smoothing kernel.

3. **Positivity** - The smoothing kernel should be non-negative in the support domain. It follows that

$$W(\mathbf{r}-\mathbf{r}',h)\geq 0, \tag{2.20}$$

for any point at $\mathbf{r}'$ within the support domain of the particle at $\mathbf{r}$.

4. **Decay** - The value of the smoothing kernel should be monotonically decreasing with increasing distance between the particles, as a result, closer particles should have a bigger influence on the particle under consideration than those further away.

5. **Delta function property** - The smoothing kernel should satisfy the Dirac delta function condition as $h \to 0$, that is

$$\lim_{h\to\infty} W(\mathbf{r}-\mathbf{r}',h)=\delta(\mathbf{r}-\mathbf{r}'). \tag{2.21}$$

In practical computations, the smoothing length never goes to zero but this property exists to allow us to explicitly observe the approximation value converging to a function value, i.e., $A_s(\mathbf{r})=A(\mathbf{r})$.

6. **Symmetric property** - A smoothing kernel should be an even function. This implies that particles which are equidistant but at relatively different positions from the particle under consideration should exert the same influence on that particle, hence,

$$W(\mathbf{r}-\mathbf{r}',h)=W(\mathbf{r}'-\mathbf{r},h). \tag{2.22}$$

7. **Smoothness** - A smoothing kernel must be sufficiently continuous for the approximation function and its derivatives to yield accurate results.

A function obeying any of the above criteria generally qualifies as an SPH smoothing kernel. The best way to assign a physical meaning to the SPH equations is often attributed to GM77, who assumed that the smoothing kernel to be a Gaussian function. This is because the Gaussian smoothing kernel is continuous over the entire domain, even for high order derivatives and it is expressed as

$$W(\mathbf{r}-\mathbf{r}',h)=\frac{\sigma}{h^D}e^{-q^2}, \tag{2.23}$$

where D is the number of spatial dimensions, σ is a normalization factor given by $\sigma = \left[\frac{1}{\sqrt{\pi}}, \frac{1}{\pi}, \frac{\pi}{\sqrt{\pi}}\right]$ in 1D, 2D and 3D, respectively, and q is the relative distance between two particles at positions $\mathbf{r}$ and $\mathbf{r}'$ given by

$$q = \frac{r}{h} = \frac{|\mathbf{r} - \mathbf{r}'|}{h}. \tag{2.24}$$

It is commonly chosen for its stability and accuracy especially for disordered particles (GM77). Although this smoothing kernel approaches zero quickly, it never goes to zero theoretically and as a result it is not fully compact. The computational cost scales as $O(N^2)$, where N is the number of particles in the simulation, therefore it is better to use a Gaussian-like smoothing kernel with full compact support in which the computational cost scales as $O(N\,N_{\mathrm{NGB}})$ (Cossins 2010), where N_{NGB} is the number of neighbour particles within the spherical smoothing volume of radius κh about any one particle used to compute smoothed estimates.

Substantial work has been invested in constructing accurate smoothing kernels that fit the above criteria (1-7); we adopt a standard cubic B-spline smoothing kernel, which was originally used by Monaghan & Lattanzio (1985), for this work. The cubic B-spline smoothing kernel (or cubic-spline kernel) belongs to a family of functions based on the work of Schoenberg (1946) called the M_n splines or B-spline functions. B-spline functions are piece-wise continuous polynomial functions with compact support and have continuous first and second derivatives (each M_n function is continuous up to $(n-2)th$ derivatives). Since the cubic-spline kernel only depends on the absolute value of $|\mathbf{r} - \mathbf{r}'|$ as described in equation 2.24, it is categorized as a "radial" kernel (Monaghan 2005). The M_4 or cubic-spline smoothing kernel is the lowest order B-spline commonly used for SPH application, defined as

$$M_4(x,h) = W(\mathbf{r} - \mathbf{r}', h) = \frac{\sigma}{h^D} \begin{cases} 1 - \frac{3}{2}q^2 + \frac{3}{4}q^3, & \text{if } 0 \le q < 1, \\ \frac{1}{4}(2-q)^3, & \text{if } 1 \le q < 2, \\ 0, & q \ge 2, \end{cases} \tag{2.25}$$

where σ is a normalization constant with values $\sigma = \left[\frac{2}{3}, \frac{10}{7\pi}, \frac{1}{\pi}\right]$ in one, two and three dimensions, respectively (Monaghan 1992). It has a Gaussian-like shape but with narrower compact support. Thus, only particle interactions within $2h$ of the central particle contribute to the smoothing and exactly zero contribution for particles at $\ge 2h$. It has continuous first- and second-order derivatives for all q, making it insensitive to local particle disorder. The gradient of the cubic-spline kernel is spherically symmetric and well defined for all values of q, such that

$$\nabla W(\mathbf{r} - \mathbf{r}', h) = \frac{\sigma}{h^{D+1}} \begin{cases} \frac{9}{4}q^2 - 3q, & \text{if } 0 \le q < 1, \\ -\frac{3}{4}(2-q)^2, & \text{if } 1 \le q < 2, \\ 0, & q \ge 2. \end{cases} \tag{2.26}$$

These combined attributes result in a great computational advantage in terms of speed. However, even though the cubic-spline kernel is the preferred smoothing kernel in SPH, its second derivative is a piece-wise linear function. As a consequence, its stability properties are not as good as those of smoother kernels (Morris 1996). For large N_{NGB}, the cubic-spline kernel has also been shown to be subject to a clumping instability (Valdarnini 2012), in which pairs of particles with inter-particle distance, $q < \frac{2}{3}$, remain close together because the cubic-spline kernel gradient tends to zero below this threshold distance (Read et al. 2010).

To overcome this, higher-order B-spline functions such as quartic- and quintic-spline smoothing kernels that are more stable and even more Gaussian-like are used. In our work, we focus on the quintic-spline smoothing kernel,

$$M_6(x,h) = W(\mathbf{r}-\mathbf{r}',h) = \frac{\sigma}{h^D}\begin{cases}(3-q)^5 - 6\,(2-q)^5 + 15\,(1+q)^5\,, & \text{if } 0 \le q < 1,\\ (3-q)^5 - 6\,(2-q)^5\,, & \text{if } 1 \le q < 2,\\ (3-q)^5\,, & \text{if } 2 \le q < 3,\\ 0, & q \ge 3,\end{cases} \tag{2.27}$$

where the support domain is truncated at $3h$ with normalization constant $\sigma = \left[\frac{1}{120}, \frac{7}{478\pi}, \frac{1}{20\pi}\right]$ in one, two and three dimensions, respectively (Price 2012). It is clear from Figure 2 of Price (2012) that one can obtain smoother kernel summations by progressing to higher-order B-spline kernels, thereby increasing N_{NGB} without changing the smoothing length. On the contrary, by increasing the N_{NGB} under the cubic spline only stretches the cubic spline to enclose a larger N_{NGB} and it is equivalent to changing the ratio of h to the inter-particle spacing. On account of their accuracy, both cubic- and quintic-spline smoothing kernels are second-order accurate, $O(h^2)$.

Second derivatives of the smoothing kernel strongly dictate the stability properties of SPH, and as such, sufficiently continuous smoothing kernels generally yield stable SPH equations. The quintic-spline function discuss earlier has sufficiently smooth second order derivatives than the linear piece-wise second order derivative of the cubic-spline function (see Price et al. (2018) for comparison) and the results are identical to that of a Gaussian for most problems, implying that even though the kernel goes to zero as $q \to 0$, the quintic-spline should be consistently stable compared to the cubic-spline kernel. However, these higher-order kernels come at a cost – since the region of contributing N_{NGB} is larger, the computations are more expensive. So the application of interest will dictate whether using higher order kernels is worth the computational cost.

2.3.3 Particle approximation

The particle approximation step is a way of discretizing the simulation volume into a series of N particles where field variables are estimated from this set of particles (Liu & Liu 2010).

The initial configuration of these particles represents the state of the system and they can also be used for carrying out the numerical integration. By this convention, a particle, i, occupies a volume element, ΔV_i, in the problem domain and has mass, m_i, and density, ρ_i. Each particle also has position, $\mathbf{r}_i$, and velocity, $\mathbf{v}_i$, with thermodynamic field variables such as specific internal energy, ϵ_i, or entropy, S_i. A discretized form of a continuous field quantity $A_s(\mathbf{r})$ in equation 2.13 is obtained by interpolating the summation over the neighbouring particles near a given point. Equation 2.13 is then written in terms of discrete summations as

$$A_s(\mathbf{r}_i) \approxeq \Sigma_{j=1}^{N}\, A(\mathbf{r}_j) W(\mathbf{r}_i - \mathbf{r}_j, h) \Delta V_j, \tag{2.28}$$

where ΔV_j is the volume element of the jth particle (Liu & Liu 2006). The volume element can be estimated from the corresponding mass-density ratio, $\frac{m_j}{\rho_j}$, where m_j and ρ_j are mass and density of particle j, respectively, therefore,

$$A_s(\mathbf{r}_i) \approxeq \Sigma_{j=1}^{N} \frac{m_j}{\rho_j}\, A(\mathbf{r}_j) \cdot W(\mathbf{r}_i - \mathbf{r}_j, h). \tag{2.29}$$

According to equation 2.13, the summation should be over all N particles in the problem domain. In practice, a smoothing kernel with compact support is employed, thus $W(\mathbf{r}_i - \mathbf{r}_j, h)$ effectively vanishes beyond a finite distance κh. Hence in equation 2.29, the summation is over the nearest neighbouring j particles that are enclosed by the spherical kernel radius of a given particle i at some time t. Particle approximation ensures that the finite values of a field quantity for one particle can be approximated by taking the average value of the field quantities of the particles inside the support domain and weighting them by a smoothing kernel (Liu & Liu 2010). This establishes the basis of all SPH frameworks.

Similarly, the derivative of equation 2.29 can be obtained by taking the ordinary differential of $A_s(\mathbf{r}_i)$ as $\nabla \cdot A_s(\mathbf{r}_i)$ at $\mathbf{r}_i$,

$$\nabla \cdot A_s(\mathbf{r}_i) \approxeq \Sigma_{j=1}^{N} \frac{m_j}{\rho_j}\, A(\mathbf{r}_j) \cdot \nabla W(\mathbf{r}_i - \mathbf{r}_j, h), \tag{2.30}$$

and the gradient of the smoothing kernel as

$$\nabla W(\mathbf{r}_i - \mathbf{r}_j, h) = \frac{\mathbf{r}_i - \mathbf{r}_j}{r_{ij}}\, \frac{\partial W(\mathbf{r}_i - \mathbf{r}_j, h)}{\partial r_{ij}}, \tag{2.31}$$

evaluated with respect to the coordinates of particle i where $r_{ij} = |\mathbf{r}_i - \mathbf{r}_j|$. A symmetric, higher accuracy gradient estimate is often used in SPH to ensure that the derivative of the approximated function vanishes if it is constant (Monaghan 2005), and equation 2.30 takes the form

$$\nabla \cdot A_s(\mathbf{r}_i) \approxeq \rho_i \left[\Sigma_{j=1}^{N}\, m_i \left(\frac{A(\mathbf{r}_j)}{\rho_j^2} + \frac{A(\mathbf{r}_i)}{\rho_i^2} \right) \cdot \nabla W(\mathbf{r}_i - \mathbf{r}_j, h) \right]. \tag{2.32}$$

Physical processes such as diffusion or thermal conduction require second-order derivatives which can be obtained by taking a derivative of equation 2.32. The particle approximation

step introduces the mass and density of the particle into the SPH formulation, which is essential for hydrodynamic problems where density is a key field. Suppose $A_s(\mathbf{r}_i)$ is a density field, $\rho(\mathbf{r}_i)$. The smoothed density for particle i with spatial coordinates, $\mathbf{r}_i$, is estimated everywhere by

$$\rho_i = \Sigma_{j=1}^{N_{\rm NGB}} m_j W(\mathbf{r}_i - \mathbf{r}_j, h), \tag{2.33}$$

where the summation includes the contribution of particle i itself. Equation 2.33 shows how the mass of j particles is smoothed to produce the estimated density, ρ_i. Other smoothed field quantities that depend on density are naturally derived from equation 2.33.

2.3.4 Variable smoothing length (h)

For fluid models in which there is no compression or rarefaction, a constant smoothing length, h, is sufficient. Indeed, in the early formulation of SPH, GM77 employed a spatially constant smoothing length, though it was allowed to change with time relative to the densest part of the calculation. However, current astrophysical models have near vacuum-like conditions where particle interactions are negligible, or may undergo shock compression where a large number of particles are so close together that they are found within a smoothing length, hence h should be varied accordingly. The natural choice of setting h is to relate it to the local number density, $n(\mathbf{r}_i)$, of particles,

$$h \propto n(\mathbf{r}_i)^{-\frac{1}{D}}, \tag{2.34}$$

hence, it is sometimes called the "resolution length". For equal mass particles, h is a variable that is implicitly defined by

$$\eta(\kappa h)^D \rho_i = N_{\rm NGB}\, m_i, \tag{2.35}$$

where D is the number of spatial dimension, η is a parameter specifying h in units of mean particle separation, $(\frac{m_i}{\rho_i})^{1/D}$, with $\eta = 1, \pi, \frac{4\pi}{3}$ for $D = 1, 2, 3$ (Valdarnini 2012). The restriction to equal mass particles means that the resolution strictly follows mass (Price et al. 2018). The smoothing length is therefore determined by solving for h in equation 2.35 in terms of the units of mean inter-particle separation (making h proportional to the density itself)

$$h = \eta \left(\frac{m_i}{\rho_i}\right)^{\frac{1}{D}}, \tag{2.36}$$

so that $N_{\rm NGB}^{1D} = 2(\kappa\eta)$, $N_{\rm NGB}^{2D} = \pi(\kappa\eta)^2$ and $N_{\rm NGB}^{3D} = \frac{4\pi(\kappa\eta)^3}{3}$. $N_{\rm NGB}$ particles can take any arbitrary values, provided η is used as the fundamental parameter in determining it. This means the $N_{\rm NGB}$ parameter only characterizes the mean number of neighbours and there can be strong fluctuations around this mean (i.e., in strong density gradients). For a cubic-spline kernel, which is zero for $\kappa h > 2$, $N_{\rm NGB}$ is 5 in 1D, 21 in 2D, and 57 in 3D (default setting for η is 1.2) (Morris 1996). By enforcing the relation in equation 2.35, we

equivalently limit the mass inside the support domain to be a constant, such that in 3D,

$$M^i_{\rm tot} = \int_V \rho dV = \Sigma_{j=1}^{N_{\rm NGB}} m_j \approx \frac{4}{3}\pi(\kappa h)^3 \rho_i \ . \tag{2.37}$$

For equation 2.36 to hold, $M_{\rm tot}$ can be rewritten by defining $M_{\rm tot} = m_i N_{\rm NGB}$, which implies that the $N_{\rm NGB}$ should also be approximately constant. This shows that the mass inside the support domain is conserved exactly, but if h is allowed to vary, the integral does not sum up to exactly $M_{\rm tot}$, however, the total mass carried by the particle is conserved. In SPH, resolving both the dense and sparse regions of the domain evenly proves advantageous, thus keeping the ratio of h to the mean local inter-particle separation constant (Price 2012).

There are many ways to dynamically change h such that the $N_{\rm NGB}$ is kept relatively constant. Here we adopt a more reliable and optimal technique for setting h employed by Hopkins (2013). To allow for a dynamic smoothing length, h_i, a mathematical relation which makes it differentiable is required. This amounts to enforcing the condition 2.34 on the effective $N_{\rm NGB}$, ("close to, but not necessarily equal to, the discrete number of neighbors inside h_i") (Hopkins 2015). By setting h such that the compact smoothing kernel centered at each particle encloses a relatively small $N_{\rm NGB}$, makes the resolution naturally adaptive with respect to number density. As a result, we do not set a particle-centered $h_i = h(\mathbf{r})$ to enclose a definite $N_{\rm NGB}$ (introducing discontinuities in h), but rather it is determined by particle number density, $n(\mathbf{r}_i) \equiv n_i$, at that region. By choosing h this way, we constrain it to depend only on the particle positions which eliminates discontinuous forms of h.

2.3.5 Numerical errors in SPH

The SPH method has been successfully applied to model many astrophysical environments, however, it suffers from known numerical weaknesses, e.g., lack of zeroth-order consistency, or the E_0 error (Hopkins 2015). This means that the interpolation of a constant pressure field or field with a complicated, higher-order shape is not guaranteed for non-uniform point distributions (Frontiere et al. 2017). Another issue is that the prescription of artificial viscosity ($\alpha_{\rm AV}$), which is required to numerically capture hydrodynamic shocks, still introduces numerical dissipation in any shocked flows, which result in non-physical behaviour in the solution. Various corrections of $\alpha_{\rm AV}$ have been proposed and the one used for this work follow the prescription given by Cullen & Dehnen (2010) (CD10 hereafter) as implemented in `GIZMO` (Hopkins 2015).

2.3.6 Artificial viscosity ($\alpha_{\rm AV}$)

In order to simulate discontinuities found in shock problems, the addition of an $\alpha_{\rm AV}$ term is required and must be treated with rigour. The first important property of $\alpha_{\rm AV}$ is that, it must never act as a false pressure, it should always be dissipative and must transfer kinetic energy into internal energy (Caramana et al. 1998). Force associated with $\alpha_{\rm AV}$ should be

Galilean invariant and vary depending on compression and expansion of the system, where it is zero for the latter (Caramana et al. 1998). In addition, the $\alpha_{\rm AV}$ should discriminate a shockwave from adiabatic compression, and not generate unwanted entropy when only adiabatic compression is present. In a system undergoing uniform stretching and/or a rigid rotation, $\alpha_{\rm AV}$ should turn off completely, and produce no effect along the direction tangential to the to a convergent shock front where velocity vector is directed inwards. (Caramana et al. 1998).

Since $\alpha_{\rm AV}$ does not naturally come with the original governing fluid equations, it is explicitly added to the momentum equation such that it acts only on shocks. SPH has two well-known formulations of $\alpha_{\rm AV}$, the classical von Neumann-Richtmyer-Landshoff (vNRL) $\alpha_{\rm AV}$, which is based on the discretized estimate of the $\nabla \cdot v$ term, where v is the flow velocity vector field, and the more widely used $\alpha_{\rm AV}$ formulation based on the pair-wise relative velocity of particles (Hosono et al. 2016). Both of the aforementioned formulations causes non-physical oscillations in the numerical results around the shocked regions. To suppress this effect, several prescriptions (switches) exist to add the correct amount of dissipation at discontinuities while effectively turning it off elsewhere. The two prescriptions we tested in this work are the well-known Balsara switch, which allows entropy generation across shocks and stops particle inter-penetration (Balsara 1995, Cartwright & Stamatellos 2010), and the state-of-the-art adaptive $\alpha_{\rm AV}$ switch proposed by CD10 which uses the total time derivative of the velocity divergence as a shock indicator while discriminating between pre-shock and post-shock regions.

Another important term that works in tandem with $\alpha_{\rm AV}$ is artificial conductivity ($\alpha_{\rm AC}$) proposed by Price (2008). This term introduces artificial heat conduction in the SPH equations with the purpose of smoothing thermal energy at contact discontinuities. The entropy at contact discontinuities is smoothed by enforcing pressure continuity and removing the effect of artificial surface tension which inhibits the growth of Kevin–Helmholtz and Richtmyer–Meshkov instabilities at fluid interfaces (Valdarnini 2012).

2.4 New meshless methods

The stationary-grid method predates all numerical schemes mentioned in this chapter so far and Teyssier (2015) gives a detailed review of their applications in astrophysics. This method is a precursor to the two cutting-edge meshless methods that are discussed later in this section. Grid-based methods discretizes the domain volume into cells and the fluid equations are solved across the cell boundaries (Hopkins 2015). The earlier formulation of the stationary-grid method was purely Eulerian. After decades of development in computational fluid dynamics, the most popular approach to non-stationary grid-based methods is using the finite-volume Godunov integration scheme developed by S. K. Godunov in 1959. As originally presented, this scheme involved a Lagrangian step followed by an Eulerian

remapping step. This method is a conservative finite-volume scheme which solves exact, or approximate Riemann problems at each cell interface (Murante et al. 2011).

2.4.1 Meshless finite volume (MFV) and Meshless finite mass (MFM)

Unlike stationary-grid methods where individual elements are connected by a mesh, meshless methods use field nodes to represent the simulation domain and its boundaries. These "field nodes" do not connect to form a traditional mesh grid, meaning no prior information is required on the relationship between the field nodes themselves or the approximation of the unknown fluid variables. These methods build on the numerical framework put forward by Lanson & Vila (2008). Meshless algorithms for hydrodynamics are still in their developing stages, but there has been a tremendous effort to incorporate them into astrophysics studies. A first attempt to implement a fully conservative and self-consistent variant of a meshless method into an astrophysical context was presented by Gaburov & Nitadori (2011), where a heuristic derivation of the meshless equations for scalar conservation laws was obtained. In this work, we focus on Meshless Finite Volume (MFV) and Meshless Finite Mass (MFM) methods and their implementation in `GIZMO` (Hopkins 2015, 2017).

In MFV/MFM methods, fluid particles move in a Lagrangian manner, the resolution adapts continuously with the fluid, no artificial dissipative terms are required, and angular momentum is conserved. Their numerical implementation eliminates velocity-dependent truncation errors, naturally couple to N-body gravity algorithms, allow for isotropic fluid flow, and have been shown to capture shocks, shear flows and fluid instabilities with high accuracy (Hopkins 2015). MFV/MFM are governed by a system of hyperbolic partial differential equations in a frame moving with velocity, $\mathbf{v}_{\rm frame}$, of the form

$$\frac{\partial \mathbf{U}}{\partial t} + \nabla \cdot (\mathbf{F} - \mathbf{v}_{\rm frame} \otimes \mathbf{U}) = 0, \tag{2.38}$$

where $\mathbf{U}$ is any conserved scalar field in the absence of a source term, $\mathbf{F}$ is its flux in the frame moving with $\mathbf{v}_{\rm frame}$, ∇ is the gradient operator, and the scalar conservation equations are given by,

$$\mathbf{U} = \begin{pmatrix} \rho \\ \rho\,\mathbf{v} \\ \rho\,\epsilon_{\rm tot} \end{pmatrix} = \begin{pmatrix} \rho \\ \rho\,\mathbf{v} \\ \rho\,\epsilon + \frac{1}{2}\,\rho\,|\mathbf{v}|^2 \end{pmatrix} = \begin{pmatrix} \rho \\ \rho\,v_x \\ \rho\,v_y \\ \rho\,v_z \\ \rho\,\epsilon + \frac{1}{2}\,\rho\,|\mathbf{v}|^2 \end{pmatrix}, \tag{2.39}$$

where ρ is mass density, $\epsilon_{\rm tot}$ is total specific internal energy, ϵ is specific internal energy, and the last equality extends $\mathbf{v}$ to 3D space, and the flux of conserved variables, $\mathbf{F}$, is

$$\mathbf{F} = \begin{pmatrix} \rho\,\mathbf{v} \\ \rho\,\mathbf{v}\otimes\mathbf{v} + P\,\mathcal{I} \\ (\rho\,\epsilon + P)\,\mathbf{v} \end{pmatrix}, \tag{2.40}$$

where P is the pressure, and $\mathcal{I}$ is the identity tensor. To deal with the non-linear discontinuous flows, Hopkins (2015) and Gaburov & Nitadori (2011) determined the weak solution to the conservation equation following integration by parts of the term $\phi\nabla\cdot\mathbf{F}$ to obtain,

$$0 = \frac{d}{dt}\int_\Omega \mathbf{U}(\mathbf{r},\,t)\,\phi\;d^\nu\mathbf{r} - \int_\Omega \mathbf{F}(\mathbf{U},\,\mathbf{r},\,t)\cdot\nabla\,\phi\;d^\nu\mathbf{r}, \tag{2.41}$$

where the test function, $\phi = \phi(\mathbf{r},\,t)$, is any arbitrary ifferentiable function integrated over the entire space-time domain of the problem, Ω (such that $d\Omega = d^\nu\mathbf{r}$, where ν is the number of spatial dimensions). Assuming the fluxes and/or ϕ vanish at infinity, the Lagrangian function ($d\phi/dt = 0$) is an advective derivative (see Hopkins (2015) and Lanson & Vila (2008) for a complete derivation).

As in the SPH method, the meshless schemes use the smoothing kernel to estimate the smoothed fluid quantities, albeit is a different framework. The smoothing length, h_i, of all the nodes is calculated based on the number density, n_i, as described by condition 2.34. In order to represent the domain volume with a set of N nodes with coordinates, $\mathbf{r}_i$, a method of partitioning the volume among N_i nodes is required. The SPH kernel, $W(\mathbf{r}-\mathbf{r}_i, h(\mathbf{r}))$ is used to calculate the fraction of a volume element, $d^\nu\mathbf{r}$, that is assigned to node i (Hopkins 2015). A function, $\phi_i(\mathbf{r})$, is associated with the fractional volume, $d^\nu\mathbf{r}$, for a node i according to

$$\phi_i(\mathbf{r}) \equiv \frac{1}{\omega(\mathbf{r})}\,W(\mathbf{r}-\mathbf{r}_i,\,h(\mathbf{r})), \tag{2.42}$$

$$\text{for} \tag{2.43}$$

$$\omega(\mathbf{r}) \equiv \sum_j W(\mathbf{r}-\mathbf{r}_j,\,h(\mathbf{r})), \tag{2.44}$$

where $h(\mathbf{r})$ is the smoothing length that enters W. Thus, the smoothing function is responsible for partitioning the volume at any point, $\mathbf{r}$, among the volumes "associated with" the nodes i. In principle, W is any arbitrary function that has compact support and the weights are normalized by the term $\omega(\mathbf{r})^{-1}$ such that the total volume always sums correctly (i.e., fractional weights must always sum up to unity at every point). Second-order accuracy, linear and angular momentum conservation, and locality of operations are guaranteed by the function $W(\mathbf{r}-\mathbf{r}_i,\,h(\mathbf{r}))$ obeying the elementary conditions of a smoothing kernel given in section 2.3.2. The smoothing function, $W(\mathbf{r}-\mathbf{r}_i,\,h(\mathbf{r}))$, ensures a configuration of particles that share the partitioned volume in a similar manner to SPH, resulting in particles

with overlapping fuzzy volume elements (see Fig. 2.1) (Hopkins 2015). A mathematically rigorous look at Voronoi-based moving-mesh methods show that they are a special case of the MFM/MFV methods, where the function W approaches the limit of a delta function and the volume integral is evaluated exactly.

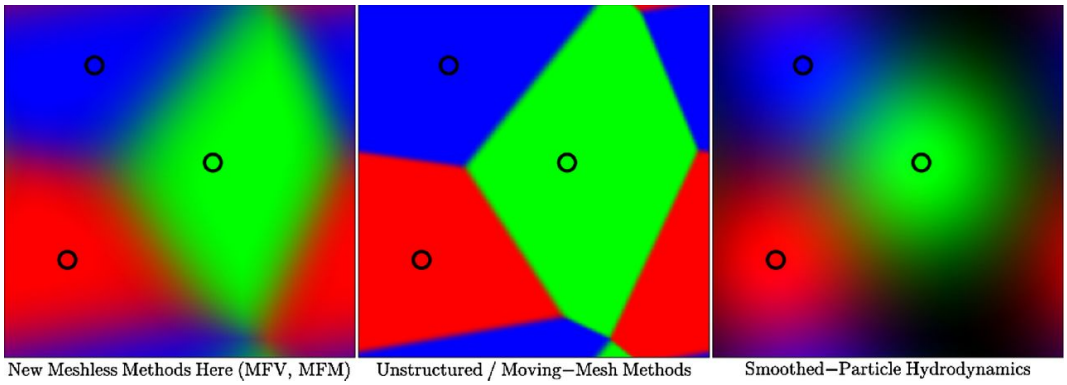

Figure 2.1: Various definitions of volume partitions as given by the smoothing kernel function at each point between Meshless, Mesh and SPH particles. Figure and caption taken from Fig. 1 of Hopkins (2015).

In summary, MFV incorporates features of both SPH and finite-volume schemes where a second-order Godunov approach is used to calculate particle interactions (exchanging mass, momentum and energy) but weighted with a smoothing kernel. It solves the Reimann problem for positions across a plane that is fixed relative to the mesh nodes (Hopkins 2015). It follows a quasi-Lagrangian formulation which computes mass fluxes between neighbouring particles for complicated fluid flows, and the relative particle motion which changes with the domain leads to higher-order corrections. The MFM method is the practical result of eliminating the mass fluxes between particles that occur in the MFV method. It is also based on the same Godunov finite-volume scheme where the Reimann problem is solved across the Lagrangian cell interface that deforms relative to the complicated fluid flow. MFM conserves particle masses only if the particles move with the velocity field, otherwise, the MFM method gives rise to zero-order errors (Hopkins 2015). The nodes in MFV and MFM are just cells moving with the fluid flow and these cells have a definite volume partition. It is rather straightforward to show that, for a smooth flow, the MFV and MFM methods will become exactly identical, thus the only difference is the order of accuracy. Contrary to SPH, in which h defines the volume encompassing the nearest neighbouring particles and W is used to estimate the field quantity such as density, MFV/MFM methods have well-defined volume partitions where the velocity at the cell interface is used in solving a 1D Riemann problem to compute the interface fluxes between a particle i and its neighbours j.

2.5 Initial condition (IC) generation

Depending on the numerical method used, obtaining optimal initial conditions (ICs) can be a trivial task, as in the case of early finite-element methods, or a very complicated procedure, as in the case of meshless methods (SPH, MFV, MFM). In 3D, the ICs should contain a complete description of particle density, $\rho(\mathbf{r})$, velocities, $v(\mathbf{r})$, and specific internal energy, $\epsilon(\mathbf{r})$, as a function of position ($\mathbf{r} = x, y, z$). Since all the numerical schemes considered here employ a smoothing kernel to calculate smoothed fluid quantities at the location of a particle from the contribution of all neighbouring particles, ICs whose interpolation properties are accurate as possible are required.

The simplest construction of the ICs is to arrange particles on a three dimensional lattice. Several lattice configurations exist that could be employed to produce ICs, the simplest of which is a cubic lattice. However, the cubic lattice structure is in an unstable equilibrium and has strong preferred directions along the simulation axes (Diehl et al. 2012). Thus it is crucial for the initial particle configurations to fulfill two key requirements to be considered optimal ICs for meshless methods:

- **Isotropy**: Particle arrangement must be isotropic, both at a local and global scale. This requirement ensures that shocks propagating in the simulation domain behave the same way in all directions.
- **interpolation accuracy**: The configuration of particles should be uniform at a local scale, so as to minimize noise during kernel weighted density calculations. Any deviations from uniformity should also be isotropic.

To avoid geometrical effects, e.g., carbuncle instability seen in Fig. 13 of Hopkins (2015), and to reduce irregularity of the random sampling, ICs are perturbed and then relaxed into a low energy configuration by applying a dampening force that is proportional to, but directed against, the particle velocities. For the Sedov-Taylor blastwave test, we need a spatially uniform particle distribution to simulate a constant density CSM. The best set-up for such a distribution is by generating a gravitational glass. In this work we adopt the implementation of a gravitational glass commonly used in cosmology simulations as provided in the cosmological simulation code, `Gadget-2` (Springel 2005). This method simply reverses the sign of particle-on-particle gravitational forces and dampens the motion of particles, allowing them to settle into an equilibrium configuration as shown in Fig. 2 of Diehl et al. (2012). The distribution of particles in a glass IC settle on a quasi-hydrostatic equilibrium, resembling an arrangement of molecules in a physical glass which poses a low energy state. While the distribution itself is non-regular, the interparticle distances in a confined volume help reduce noise (Arth et al. 2019).

For more complex IC geometries and profiles, we use the Weighted Voronoi Tesselations ICs (WVTICs) code by Diehl et al. (2012) to generate glass-like ICs. WVTICs assumes a metric

(a Euclidean distance) and a set of k points in a given domain, such that $\mathbf{z}_i,\ i = 1, 2, ...k$, is a "generator", a Voronoi tessellation of the domain such that the ith region contains all of the points closer to $\mathbf{z}_i$, according to the chosen metric, than to any other generator (Diehl et al. 2012). A weight is then applied to the distance from each generator, where each particle within a chosen h contributes to the calculation of a displacement in each iteration (Diehl et al. 2012).

WVTICs is wrapped around the generic SPH framework, ensuring the correct interpolation properties. Thus, the initial set of particles is constructed by sampling random positions following the underlying density distribution $\Phi(\mathbf{r}) \propto h(\mathbf{r})^{-3}dV$ for a volume, dV, with the corresponding smoothing length, h. The aim is to produce a relaxed, low energy glass-file for an arbitrary desired physical model. WVTICs then couples the random sampling method with the relaxation method to create more complex particle distributions. In each relaxation step, a summation over the neighbouring particles near a given point is calculated, followed by a repulsive force to push each particle pair apart. The force computation is weighted by the distance between the particle pairs and the target h in order to converge to a desired density model whist settling on a glass-like configuration. In addition, the magnitude with which the particles move is decided by the scaling factor which depends on the mean inter-particle distance. The initial uniform random distribution is then iteratively evolved through these steps towards the desired distribution. The net displacement of particle i due to particle j is then given by

$$\Delta\mathbf{r}_i = C \cdot h_{ij} \cdot W\left(|r_{ij}|, h_{ij}\right) \cdot \frac{r_{ij}}{|r_{ij}|}, \tag{2.45}$$

with the symmetrized form of h given by

$$h_{ij} = \frac{h_i + h_j}{2}. \tag{2.46}$$

The value of C in equation 2.45 dictates the fraction of h_{ij} the particles should move during each iteration step. Equation 2.46 means that the push from a neighbour on one side and one on the opposite end should cancel each other out. The relaxation step stops as soon as most of the particles are moved less than a small fraction of the inter-particle distance.

WVTICs therefore generates a glass-like distribution of particles with a desired density model settled in a local potential energy minimum. This potential energy minima is defined by the pairwise inter-particle force. Since the SPH kernel weighting operates on the local neighbouring particles, a global force term is used to improve global convergence and avoid a local energy minima. To compute this global force term, a global redistribution step is carried out every few relaxation steps by the code. The redistribution involves displacing particles from regions with $\rho > \rho_{\mathrm{model}}$ into regions with $\rho < \rho_{\mathrm{model}}$. To ensure that less particles are redistributed as the density calculations approach the model solution, an upper

limit to the amount of sampled particles is enforced. To accept a particle i for redistribution, the code checks if a random number r_i fulfils

$$r_i \in [0,1] < \left(\frac{\rho_i - \rho_{\text{model}}(x_i)}{\rho_{\text{model}}(x_i)} \right). \tag{2.47}$$

Equation 2.47 favours particles with large density errors to be redistributed and more particles are probed as the calculation of density approach the desired density model. In addition to choosing the initial distribution, an upper limit on the maximum number of iterations to further reduce computational cost is set. Tests conducted by Diehl et al. (2012) has shown that the symmetrized version of the h gives much better convergence towards model solution globally, which results in lower density errors. To improve the rate of convergence, one can change the initial state of the particle distribution by changing the random number distribution of the density function itself. This is done using the Von Neumann rejection sampling method and it forms part of a broad class of computational algorithms called the Monte Carlo methods. Instead of starting with a random uniform distribution of particle positions, this approach ensures that the particle density distribution already follows the desired model without changing other properties of the distribution.

2.6 Numerical methods summary

The equations of fluid dynamics, closed by the gas EOS, establish the governing laws of most hydrodynamic models. SPH, MFV, and MFM are Lagrangian hydrodynamic schemes used to discretize a simulation domain and numerically solve the fluid equations. Parameters such as N_{NGB} and α_{AV} play a major role in how well a meshless method performs at a particular problem and should be thoroughly explored. Since meshless methods are sensitive to the ICs, glass-like ICs are a requirement as they ensure a relaxed, low energy state. Each numerical method comes with advantages and disadvantages depending on the problem being addressed, hence, in the words of George E.P Box "essentially all models are wrong but some are useful"; we explore this further in the next chapter.

Chapter 3

Sedov-Taylor Blastwaves

Computer models are only approximate representations of the physical system or process being studied. Thus, a simulation code should be verified and validated to the degree needed for the model's intended application. Verification and validation of computational models is conducted either during code development or when applying an existing code to a new problem as we do in this work. With advances in computational fluid dynamics leading to increased confidence in numerical modelling of realistic problems, model verification and validation methodology has grown into a discipline of its own (Roache 1998, Kamm et al. 2008). In computational fluid dynamics, verification and validation are technical terms reserved for unique descriptions when modelling a problem, thus, we adopt the definitions of Committee et al. (1998);

- **Verification** is a process of demonstrating whether a code or model implementation accurately represents the conceptual model and the analytic solution to that particular model.
- **Validation** is a method of examining the degree of how much a model accurately describes the physical system from which it is intended to be used.

While verification testing involves comparing the simulation results with exact solutions to simple problems and quantifying the error in the simulations, in validation testing, one compares the results from a numerical simulations to laboratory test data or quantifiable observations asses the credibility and applicability of the governing equations and their numerical framework (Calder et al. 2002). Astrophysical environments are complicated and often subject to complex interplay of physical processes (e.g. radiation transport, nuclear burning, transitions to low and high Mach numbers), each of which required thorough testing. Thus, a validation of a simulation code for an observed astrophysical event is not a trivial process, more especially when the observed event is too far away to resolve. Since validation is much broader in scope than verification and requires testing the fundamental assumptions and model equations that go into a model (Calder 2005), this section focuses only on verification and we briefly discuss validation of our models in section 3.3.

Verification testing requires problems that have strong exact solutions, i.e., either (i) expressible in closed-form or (ii) the equations are rigorously simplified to forms that can be solved accurately (Roache 1998). An example of the former is the Sedov-Taylor blastwave problem with its algebraically simple solution (Sedov 1959). In order to demonstrate that `GIZMO` is a reliable code for investigating the Sedov-Taylor phase of SN blastwave, we identify a range of parameters that gives the best agreement with the Sedov-Taylor analytic solution and describe our efforts at assessing whether the numerical results of the discretized hydrodynamic schemes implemented in `GIZMO` provides accurate solutions of the corresponding continuum equations.

3.1 Sedov-Taylor analytic solution

There are many code verification tools for constructing the Sedov-Taylor analytic solution. In this work we adopt a robust implementation of the code written by Frank Timmes, along with James Kamm, who solved the Sedov-Taylor problem for generic coordinate systems (spatial dimension D) with a generic external ambient density profile, $\rho(r) = Ar^{-\omega}$, where r is the radius from the center point, A is a positive dimensional constant and ω is the density power-law exponent (Kamm 2000). To keep the total mass finite within the domain, Kamm (2000) constrained ω according to $0 \leq \omega \leq D$.

Our Sedov-Taylor explosion starts with a uniform pressure-less, static fluid of mass density, $\rho_0 = 1.0\,\mathrm{g\,cm^{-3}}$, into which a point explosion source of energy, $E_0 = 1.0 \times 10^{51}$ erg, at the center is introduced. This large input of energy is in the form of thermal energy at time, $t = 0$. This imparts extremely high temperatures at the explosion point accompanied by the propagation of a strong leading shock wave that expands outwards. The propagation of the initial shock wave is so rapid that the gas directly behind the leading shock front is not in pressure equilibrium with the gas further behind the shock wave (Frontiere et al. 2017). The shock wave moves radially outwards with energy,

$$E_0 = \int \left[\frac{1}{2}\rho v^2 + \frac{P}{\gamma - 1} \right] dV, \tag{3.1}$$

where ρ is the mass density, v is the velocity, P is the pressure, γ is the adiabatic index and dV is the spherical volume element (Singleton et al. 2016). The integration runs over the volume behind the shock ($0 \leq r \leq r_{\rm sh}$), where $r_{\rm sh}$ is the radial position of the shock at time t, and dV takes the form, $dV = 4\pi r^2 dr$ for $D = 3$. Since the total energy released should be constant throughout the motion, the Sedov solver should be able to convert internal energy into kinetic energy according to the energy integral given in Eq 3.1. Thus, to evolve this integral in time, a numerical integration method is required. We also take the adiabatic index to be $\gamma = \frac{5}{3}$ and adopt the mean molecular weight for the shocked gas of $\mu = \frac{\bar{m}}{m_p} = 1.25$, as prescribed by Immler & Lewin (2003).

The initial gas pressure, $P(r,0) = 6.9032 \times 10^{-13}\,\mathrm{g\,cm^{-1}\,s^{-2}}$, and specific internal energy $\epsilon(r,0) = 9.8618 \times 10^{11}\,\mathrm{erg\,g^{-1}}$, are evaluated from the ideal gas equation of state by assuming the ambient gas temperature of a hot, diffuse hydrogen and helium plasma at $T = 10\,000\,\mathrm{K}$.

Using these initial conditions, we adopt the publicly available `FORTRAN` source code (`http://cococubed.asu.edu/research_pages/sedov.shtml`) developed by Kamm & Timmes (2007) (KT07, hereafter) to generate the analytical solution shown in Fig. 3.1. An algorithmic procedure for evaluating the Sedov-Taylor self-similar analytic solution in terms of prescribed initial parameters and the fluid equations in closed-form is outlined in Chapter 3 of Kamm (2000). In the appendix A.1.1, we briefly highlight the method used by the `FORTRAN` code to obtain the Sedov-Taylor analytic solution. For the standard case we consider here, Eq. 3.1 is isolated into two energy integrals, J_1 and J_2 defined in A.1.1, which are then evaluated using Romberg's method. We then used the parameters and boundary conditions given in Table 3.1 required by the `FORTRAN` code, to calculate the one dimensional solutions for a Sedov-Taylor blastwave propagating through a uniform, constant density medium.

KT07 improved the original `FORTRAN` solver by implementing a quad precision (128 bit) floating point operation to accurately calculate similarity variables at small radii. In Fig. 3.1, the shock arrives at $r_{\mathrm{sh}} = 1.2240\,\mathrm{pc}$ at our desired final time, $t = 20\,\mathrm{yr}$. The pressure asymptotes to a non-zero value at the origin, and since the density vanishes there, the specific internal energy grows indefinitely. In addition to the solution of an array of spatial points at the desired time point, the Sedov solver also provides an output of all post-shock quantities and their energy integral parameters (see Table 3.2).

Description	Parameter	Value
Number of interpolation points	**nstep**	500
Total amount of energy deposited at the origin at $t = 0$	**eblast**	$1.0 \times 10^{51}\,\mathrm{erg}$
Geometry, 1=planar, 2=cylindrical, 3=spherical	**xgeom**	3.0
Initial density power-law exponent,	**omega**	0.0
Lower domain boundary	**zlo**	$0.0\,\mathrm{pc}$
Upper domain boundary	**zhi**	$6.0\,\mathrm{pc}$
Desired final time	**time**	$20.0\,\mathrm{yr}$
Initial ambient density	**rho0**	$1.05 \times 10^{-24}\,\mathrm{g\,cm^{-3}}$
Initial ambient velocity	**vel0**	$0.0\,\mathrm{km\,s^{-1}}$
Initial ambient pressure	**pres0**	$6.9032 \times 10^{-13}\,\mathrm{g\,cm^{-1}\,s^{-2}}$
Initial ambient sound speed	**cs0**	$10.4678\,\mathrm{km\,s^{-1}}$
Initial ambient specific internal energy	**ener0**	$9.8618 \times 10^{11}\,\mathrm{erg\,g^{-1}}$
Specific heat ratio, $\gamma = c_p/c_v$	**gamma**	1.6666

Table 3.1: All the assumed initial values and parameters required by the KT07 `FORTRAN` code to obtain the Sedov-Taylor analytic solution.

Description	Parameter	Value
Post-shock density	ρ_1	$4.2 \times 10^{-24}\,\mathrm{g\,cm^{-3}}$
Post-shock velocity	v_1	$17952.7\,\mathrm{km\,s^{-1}}$
Post-shock specific internal energy	ϵ_1	$1.6114 \times 10^{18}\,\mathrm{erg\,g^{-1}}$
Post-shock pressure	p_1	$4.51 \times 10^{-6}\,\mathrm{g\,cm^{-1}\,s^{-2}}$
Post-shock sound speed	Cs_1	$13381.15\,\mathrm{km\,s^{-1}}$
Shock position	r_1	$1.2240\,\mathrm{pc}$

Table 3.2: Table containing the output of the KT07 `FORTRAN` code describing all the physical post-shock quantities.

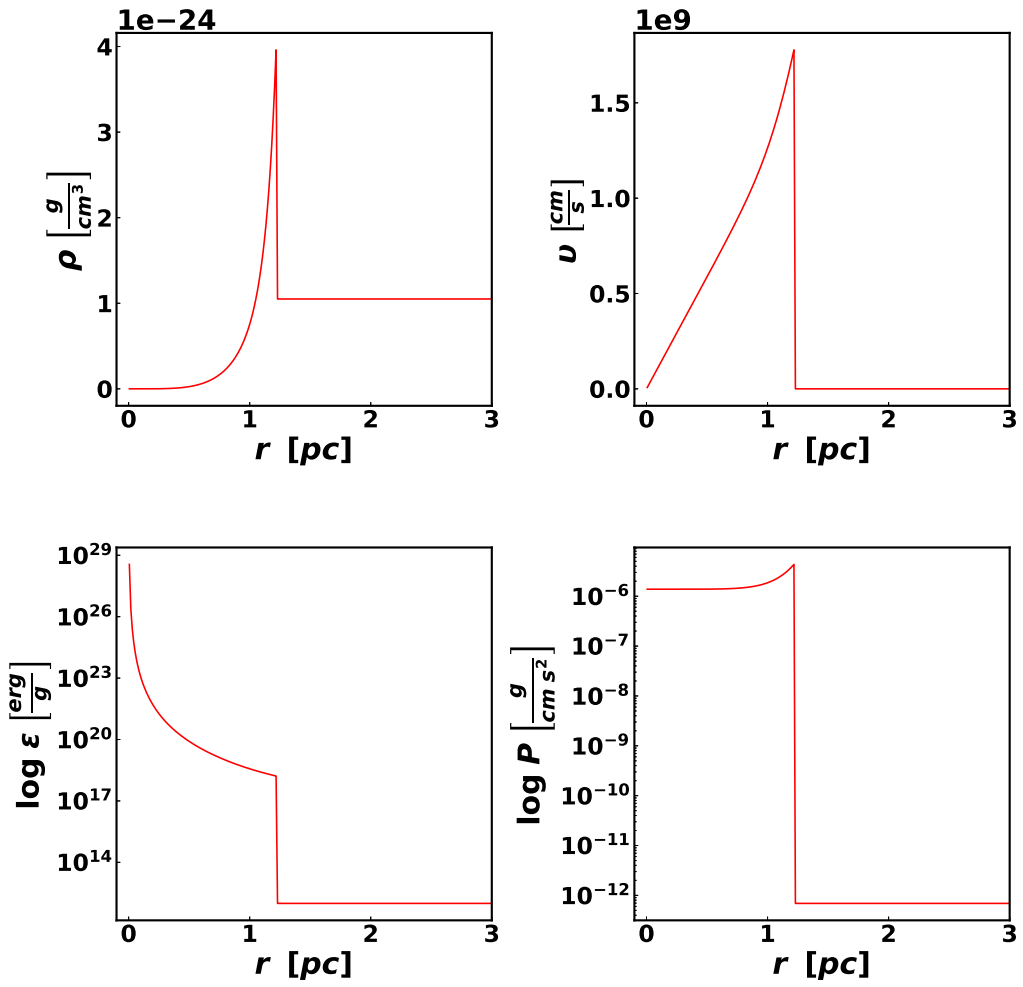

Figure 3.1: Radial profiles of the Sedov-Taylor blastwave analytic solution for mass density (*upper left*), material velocity (*upper right*), specific internal energy (*lower left*), and pressure (*lower right*) evaluated at time $t = 20\,\mathrm{yr}$.

3.2 Sedov-Taylor blastwave simulations

For our particular problem of a SN explosion inside a CSM, a point explosion with a large March number is a powerful test of code accuracy, code conservation, and how well the code captures shock jumps and preserves symmetry in three dimensions (Hopkins 2015). Since `GIZMO` uses adaptive time-steps, this test also checks the integration stability of the code.

3.2.1 Sedov-Taylor initial conditions

A SN explosion is typically initiated by injection of kinetic energy of the blast as thermal energy into the central-most particles and allowing a pressure gradient to launch a shocked flow into the surroundings (Greif et al. 2007). Similarly, Springel & Hernquist (2002) used a cartesian grid to initialize a particle distribution and deposited an explosion energy of unity into a single central particle as shown in Fig. 3.2a. This model is called a thermal energy bomb model and is mostly relevant for explosions in HII regions where densities are quite low and early radiative loses are insignificant (Aufderheide et al. 1991, Tominaga et al. 2013). In practice, a SN explosion initiated in this way causes the temperatures to skyrocket to tens of billions of Kelvin, thereby driving energy loses through thermal bremsstrahlung and inverse-compton before the pressure gradient can launch any shocked flows (Whalen et al. 2008, Kitayama & Yoshida 2005).

Standard SPH formulations are not suited for dealing with strong explosions because the direct neighbours of the explosion seed are quickly driven to non-physical negative temperatures (Springel & Hernquist 2002). According to Saitoh & Makino (2009), the individual time-step method in SPH also gives rise to integration errors when dealing with the multiphase nature of a strong point explosion. The alternative approach is the one employed by Valdarnini (2012), in which energy is deposited in a smoothed fashion, thereby avoiding the need to use the asymmetric form of the thermal energy equation to correct for the strong violation of energy conservation in the standard SPH formalism. Following this approach, one selects a point particle nearest to the defined center of the domain and all particles comprised within the support domain of the central particle of choice are given a fraction of the initial thermal energy, such that the total injected energy is unity.

For our study, we initialize a large domain in an octant, $0 < x, y, z < 6\,\mathrm{pc}$, with equal mass gas particles, $M_p = 6.6634 \times 10^{26}$g in a glass distribution (see Chapter 2). In this domain, the gaseous medium has a constant number density of $n_0 = 0.5$ particles per cm^{-3}. These particles behave like an ideal gas with adiabatic index, $\gamma = \frac{5}{3}$, and are subject to negligible gas pressure of 1.38×10^{-13} Pa, with gas temperature of $T = 10\,000\,\mathrm{K}$. We performed three simulations at different resolutions, i.e., 5×10^5 particles, 1×10^6 particles, and 1×10^7 particles, and enhanced the central 16, 32, and 64 particles with a fraction of the total thermal energy, $E_0 = 1.0 \times 10^{51}$ erg, respectively.

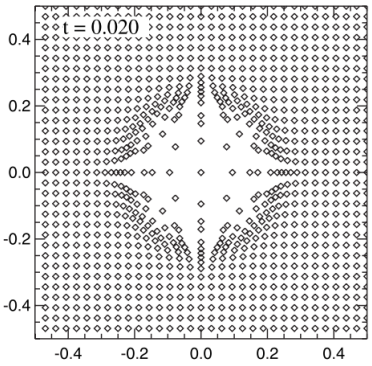

(a) Figure and caption taken from Figure 2 of Springel & Hernquist (2002).

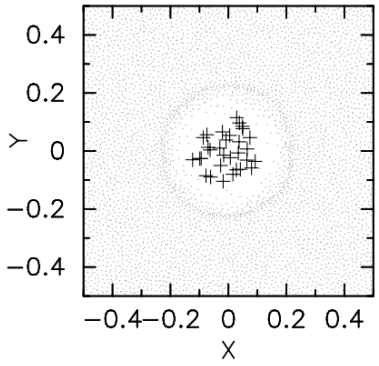

(b) Figure and caption taken from Figure 3 of Saitoh & Makino (2009).

Figure 3.2: (*a*) Delivering an explosion energy, $E = 1$, into a single particle at $t = 0.02$. The particles are initially distributed on a cartesian grid. Credit: Figure and caption taken from Springel & Hernquist (2002). (*b*) A point explosion energy, $E = 1$, shared across 32 central particles at time $t = 0.02$. The round dots are SPH ambient medium particles initially in a glass distribution and the crosses are the SPH particles initially heated by the thermal energy injection. Credit: Figure and caption taken from Saitoh & Makino (2009).

The top row of Fig. 3.3 shows the initial uniform radial density distribution of particles with constant density (top-left) while their initial velocities are set to zero (top-right). The bottom row of Fig. 3.3 shows the enhanced thermal energy particles in the inner radii in terms of their specific internal energy (bottom-left), and as a consequence of the equation of state, the pressure of these explosive energy infused particles is also amplified with respect to the negligible pressure of the ambient medium.

We compared the results of `GIZMO`'s implementation of SPH, MFV and MFM method at the final time, $t = 20\,\mathrm{yr}$, under different run-time parameters. All the run-time parameters and models we investigated are shown in Table 3.3. Particles in the initial conditions are assigned particle-type zero attribute, so that `GIZMO` interprets them as gas particles. The initial conditions file itself is written in HDF5 format and the simulation output is also in the same format. While SPH simulations do not require boundary conditions, MFM and MFV were evolved with periodic boundaries. We set the mesh motion for MFV to "fully Lagrangian", ensuring that it is conservative.

3.2.2 Radial profiles from 3D data

Our simulations of the Sedov-Taylor blastwave test are in 3D, however the Sedov-Taylor analytic solution is a simple 1D closed-form solution. For comparison purposes, we azimuthally averaged our 3D data into a radial profile. This is done by subdividing the domain into 500 concentric shells of equal thickness from the center of the domain to its boundaries. These

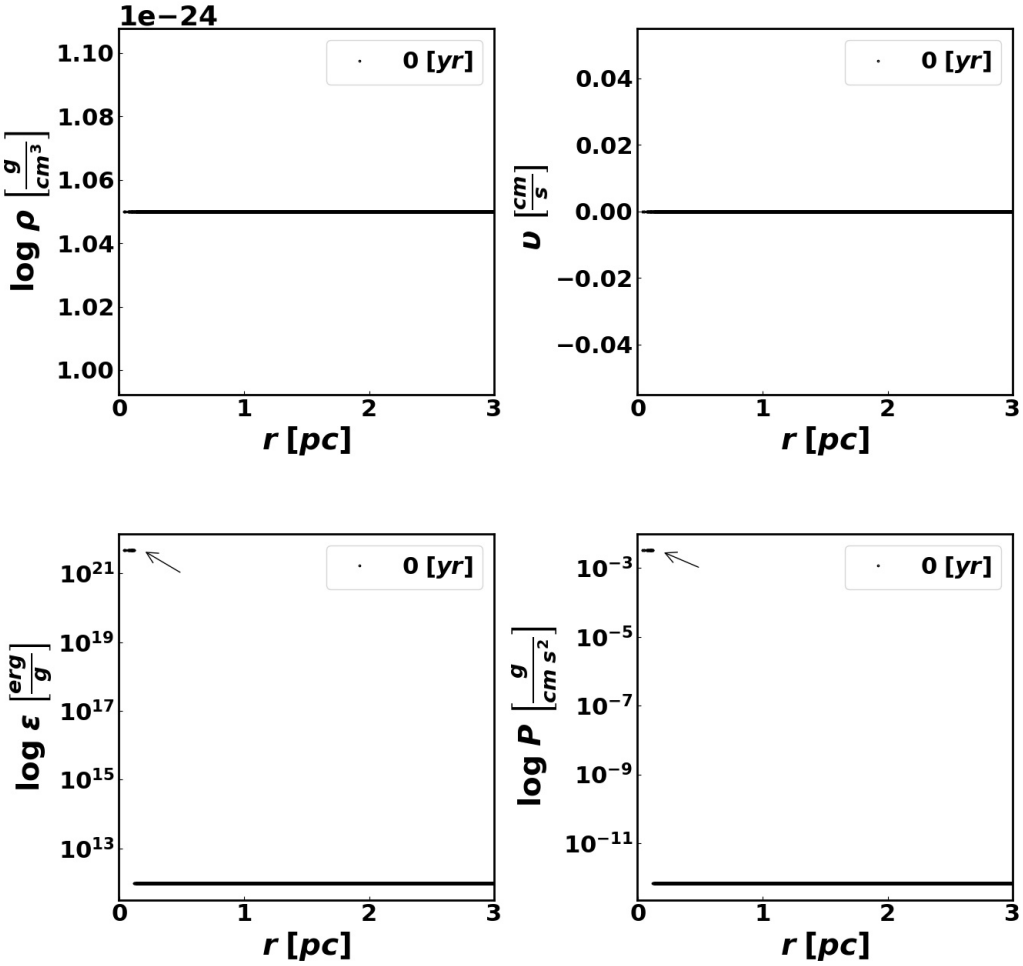

Figure 3.3: The initial setup of each hydrodynamic quantity; mass density (*upper left*), material velocity (*upper right*), specific internal energy (*lower left*), and pressure (*lower right*) required by the simulation. These initial conditions are the same for all simulations except for the number of particles. The black arrows indicate the energy injection point.

concentric shells have outer radii that correspond to the radial bins of the radial profile.

The mean of each hydrodynamic quantity (ρ, υ, ϵ, and P) is then calculated from all particles that fall within each radial bin. Ideally these summations would be done over the smoothing kernel, however, this would be more computationally expensive. A `python` routine called `scipy.stats.binned_statistic` was used to compute binned values for density, velocity, temperature and pressure. This routine allows the computation of the sum, mean,

Model	Solver	**G**	W	$N_{\rm NGB}$	$(PM)\,\alpha_{\rm AC}$	$\alpha_{\rm AV}$	$N_{\rm p}$
SPH_$\rm G_{ON}$	SPH	ON	M_4	57	0.5	$CD_{\alpha_{\rm AV}} = 1$	5e5
SPH_$\rm G_{OFF}$	SPH	OFF	M_4	57	0.5	$CD_{\alpha_{\rm AV}} = 1$	5e5
SPH_$\rm CD10_{AV}1$_$\alpha_{\rm AC}0$	SPH	OFF	M_4	57	0	$CD_{\alpha_{\rm AV}} = 1$	5e5
SPH_$\rm CD10_{AV}1.5$_$\alpha_{\rm AC}0$	SPH	OFF	M_4	57	0	$CD_{\alpha_{\rm AV}} = 1.5$	5e5
SPH_$\rm CD10_{AV}1.5$_$\alpha_{\rm AC}0.25$	SPH	OFF	M_4	57	0.25	$CD_{\alpha_{\rm AV}} = 1.5$	5e5
SPH_$\rm BS_{AV}1$_$\alpha_{\rm AC}0.5$	SPH	OFF	M_4	57	0.5	$BS_{\alpha_{\rm AV}} = 1$	5e5
SPH_$\rm BS_{AV}1$_$\alpha_{\rm AC}0$	SPH	OFF	M_4	57	0	$BS_{\alpha_{\rm AV}} = 1$	5e5
SPH_$\rm BS_{AV}1.5$_$\alpha_{\rm AC}0$	SPH	OFF	M_4	57	0	$BS_{\alpha_{\rm AV}} = 1.5$	5e5
SPH_$N_{\rm NGB}128$_M_6	SPH	OFF	M_6	128	0.5	$CD_{\alpha_{\rm AV}} = 1$	5e5
SPH_$\rm N_p$1e6	SPH	OFF	M_4	57	0.5	$CD_{\alpha_{\rm AV}} = 1$	1e6
SPH_$\rm N_p$1e7	SPH	OFF	M_4	57	0.5	$CD_{\alpha_{\rm AV}} = 1$	1e7
MFV_$\rm G_{ON}$	MFV	ON	M_4	57	N/A	N/A	5e5
MFV_$\rm G_{OFF}$	MFV	OFF	M_4	57	N/A	N/A	5e5
MFV_$N_{\rm NGB}128$_M_6	MFV	ON	M_6	128	N/A	N/A	5e5
MFV_$\rm N_p$1e6	MFV	ON	M_4	57	N/A	N/A	1e6
MFV_$\rm N_p$1e7	MFV	ON	M_4	57	N/A	N/A	1e7
MFM_$\rm G_{ON}$	MFM	ON	M_4	57	N/A	N/A	5e5
MFM_$\rm G_{OFF}$	MFM	OFF	M_4	57	N/A	N/A	5e5
MFM_$N_{\rm NGB}128$_M_6	MFM	OFF	M_6	128	N/A	N/A	5e5
MFM_$\rm N_p$1e6	MFM	OFF	M_4	57	N/A	N/A	1e6
MFM_$\rm N_p$1e7	MFM	OFF	M_4	57	N/A	N/A	1e7

Table 3.3: The models and run-time parameters for the Sedov-Taylor blastwave. The abbreviations are as follows; **G** is for self-gravity, W is the choice of smoothing kernel with M_4 representing the cubic-spline kernel and M_6 representing the quintic-spline kernel, $N_{\rm NGB}$ is the number of neighbours, $\alpha_{\rm AC}$ is the artificial conductivity and "PM" is the Price (2008) and Monaghan (1997) formulation of artificial conductivity, $\alpha_{\rm AV}$ is the artificial viscosity and "CD" is the Cullen & Dehnen (2010) adaptive artificial viscosity prescription and "BS" is the traditional Balsara Switch, and $N_{\rm p}$ is for the number of particles in the simulation domain.

median or other statistics within each bin. Radial profiles are then plotted using the values of the binned averages and the radial bins for each hydrodynamic quantity.

We conducted a systematic study of the simulation data to inspect how the choice of the number of bins affects the averaged radial profiles from the simulation. As shown in Fig. 3.4, using ≥ 1000, resulted in noisy radial profiles. The goal was to obtain a smooth average of the simulation data while retaining the important features of the Sedov-Taylor blastwave solution and this was achieved with 500 bins.

3.2.3 Effect of self-gravity

Several Sedov-Taylor blastwave tests were investigated in which the importance of self-gravity of the gas was determined. We performed six simulations, two for each numerical method for particle self-gravity ON and OFF, i.e., models SPH_$\rm G_{ON}$, SPH_$\rm G_{OFF}$,

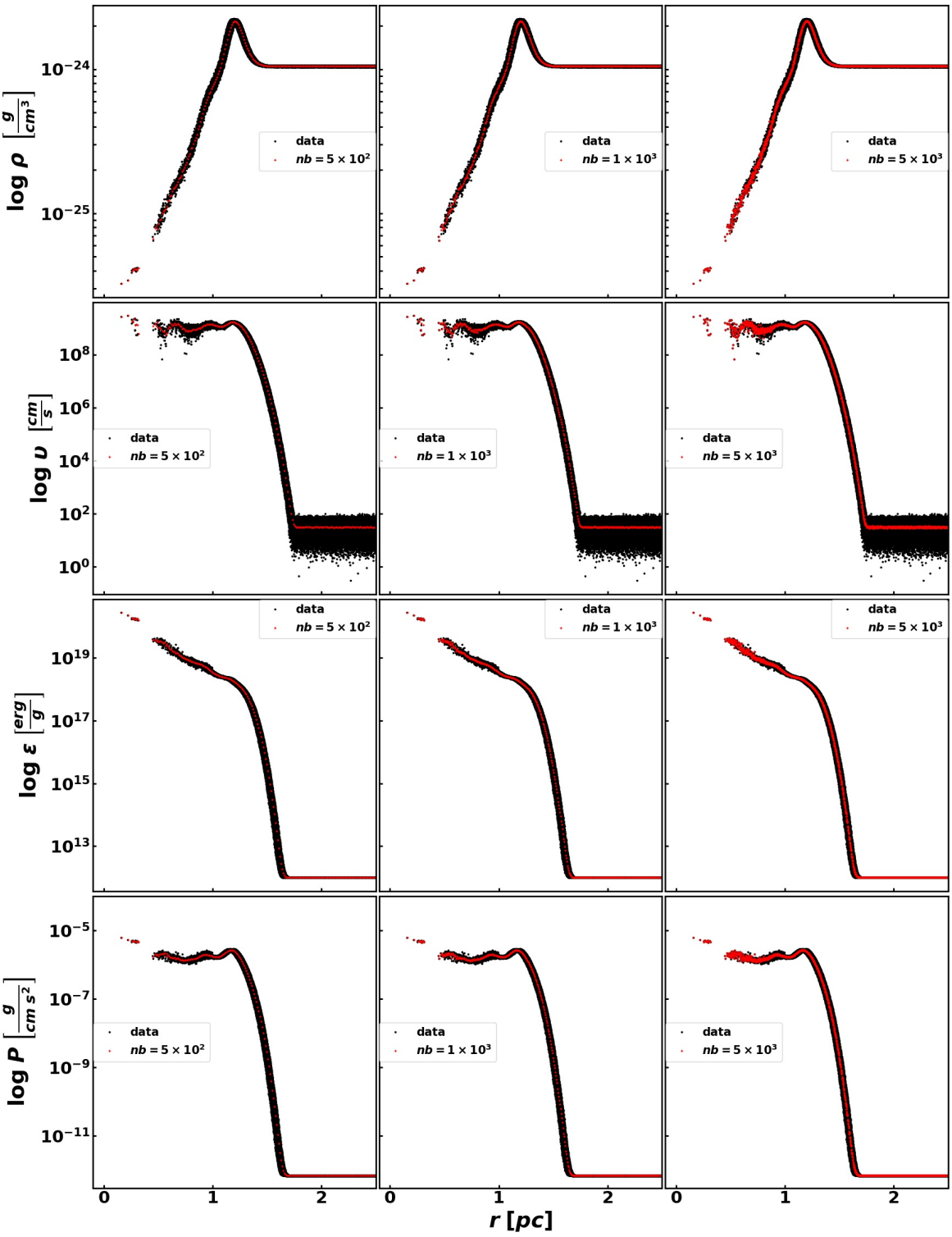

Figure 3.4: A series of radial density *(1st row)*, velocity *(2nd row)*, specific internal energy *(3rd row)* and pressure *(4th row)* profiles showing binned averages (red crosses) over-plotted on top of simulation data (black squares). The number of bins (nb) used to subdivide the radius increases from left to right. It is clear that for a low-resolution ($N_{\rm p} = 5 \times 10^5$) simulation, using 500 bins still retains all the Sedov-Taylor blastwave features and thus is an optimal choice for the number of bins.

MFV_G_{ON}, MFV_G_{OFF}, MFM_G_{ON} and MFM_G_{OFF} in Table 3.3. We employed the cubic-spline (M_4) kernel with $N_{NGB} = 57$ for all six tests and used the CD10 adaptive artificial viscosity (α_{AV}) prescription in conjunction with the artificial conductivity (α_{AC}) term introduced by Price (2008) for SPH simulations. We also set the mesh motion of the MFV method to be fully Lagrangian, so as to take advantage of its naturally conservative properties. To run viable simulations with gravity, `GIZMO` employs a variable gravitational softening length (ε_g, scaled with local inter-element separation) for gas particles. The radial density and velocity profiles in Fig. 3.5 exhibit a peak at the shock front location, which occurs at approximately $r \sim 1.22$ pc, in accordance with the analytic solution.

A visual inspection of Fig. 3.5 and Fig. 3.6 shows that there is no difference between SPH simulation with self-gravity (SPH_G_{ON}, orange diamonds) compared to that without self-gravity (SPH_G_{OFF}, blue triangles). As shown in Fig. 3.5a, both model SPH_G_{ON} and SPH_G_{OFF} estimated the shock density jump to be 51.2%, and the shock position at 98.6% of the analytic solution, respectively. The maximum shock velocity is estimated at 93.9% of the analytic solution, as shown in Fig. 3.5b. These results are in agreement with previous investigations conducted by Valdarnini (2012), where they found a density jump of ~ 2, instead to the expected value of 4. The radial velocity (Fig. 3.5b), specific internal energy (Fig. 3.6a) and pressure profiles (Fig. 3.6b) also consistently show identical results for both model SPH_G_{ON} and SPH_G_{OFF}.

Model MFV_G_{ON} and MFM_G_{ON} captured 59.0% and 54.1% of the shock density jump, respectively, and estimated 88.3% and 96.2% of the shock velocity, respectively, with respect to the analytic solution. Model MFV_G_{OFF} and MFM_G_{OFF} improved the shock density jump by 1.6%, and 2.2%, with respect to model MFV_G_{ON} and MFM_G_{ON}. The shock velocity is also improved by 3% and 3.8% in model MFV_G_{OFF} and MFM_G_{OFF}, respectively, relative to model MFV_G_{ON} and MFM_G_{ON}. Model MFV_G_{ON} overestimated the shock position by 1.1% compared to the negligible 0.3% for model MFV_G_{OFF} with respect to the analytic solution. Model MFM_G_{ON} estimated 97.7% of shock position with respect to the analytic solution, while this estimate is reduced by 0.8% in model MFM_G_{OFF} with respect to model MFM_G_{ON}. Based on these results, MFV and MFM method perform better at resolving the high density contrast of the shock fronts compared to the SPH method.

Whilst all models in this test captured the shock position considerably well, it is impossible to avoid the significant drawbacks evident in the radial profiles. All quantities are smoothed out at the shock position (with respect to the sharp shock front of the analytic solution) due to the inherent nature of the smoothing kernel interpolation at the heart of each method. Looking at the downstream particles right behind the shock front in Fig. 3.5b, SPH exhibits oscillatory scatter around the velocity solution resulting from the CD10 switch with some contribution from the α_{AC} term. While all models remain consistent with the density solution in the post-shock region, they completely diverge from the analytic solution

when one moves to smaller radii, $< 0.5\,\mathrm{pc}$, in the post-shock velocity, specific internal energy, and pressure.

All models underestimated the post-shock specific internal energy and overestimated the post-shock pressure at small radii as seen in Fig. 3.6a and Fig. 3.6b, respectively. SPH and MFV also overestimated the post-shock velocity at small radii, while MFM maintained its oscillatory behaviour all the way into the inner radii as seen in Fig. 3.5b. Although the shock density jump in model MFV_$\mathrm{G_{OFF}}$ is in good agreement with the analytic solution, it has some non-physical features at the shock front e.g., a large narrow drop at the shock front that plummets below the constant initial pressure and specific internal energy of the ambient gas. It is still not clear if this is due to a general numerical error in `GIZMO` or a result of the `gravtree` routine implementation with the MFV method.

In conclusion, the SPH method produced identical results with and without self-gravity of the gas. The MFM method has shown that excluding self-gravity resulted in good agreement with the analytic solution at the shock front, however, this comes at a small penalty of 0.8% in the shock position. For MFV, excluding self-gravity perfectly captured the shock position and significantly improved the estimates of the shock density jump and velocity. However, this does not translate well into specific internal energy and pressure, as it diverges from the solution with a sharp drop at the shock position. Thus, including self-gravity in MFV simulations is necessary as it ensures consistent agreement with the analytic solution across all quantities. Finally, post-shock velocity oscillations were evident due to irregular particle motions occurring at characteristic inter-particle separations $<< h$ arising from $\nabla \cdot v$ terms in the α_{AV} prescription (Monaghan & Gingold 1983).

3.2.4 Smoothing kernel and neighbour number test

The meshless methods considered here can employ different smoothing kernel functions and that can improve their accuracy. A common approach to get simulations to converge to an analytic solution is to increase the N_{NGB} and the total number of particles in the simulation so as to improve the kernel sampling. However, the M_4 kernel alone comes with difficulties unique to its property if one only increases the N_{NGB}. For a large N_{NGB}, the M_4 kernel is subject to a clumping instability which is highlighted in section 2.3.2

To address this issue, a higher order B-spline kernel function called the quintic-spline (M_6) kernel with $N_{\mathrm{NGB}} = 128$ is used. It retains the bell shape of the kernel, a feature which is necessary for good density estimates. A study by Zhu et al. (2015) showed that as the N_{NGB} increase, the distribution slowly approaches a Guassian-like distribution peaked at the estimated density value. Dehnen & Aly (2012) also demonstrated that using higher

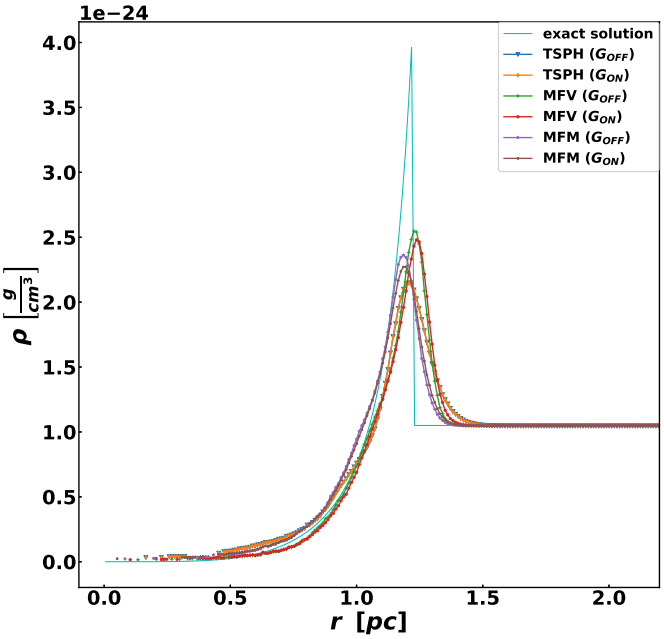

(a)

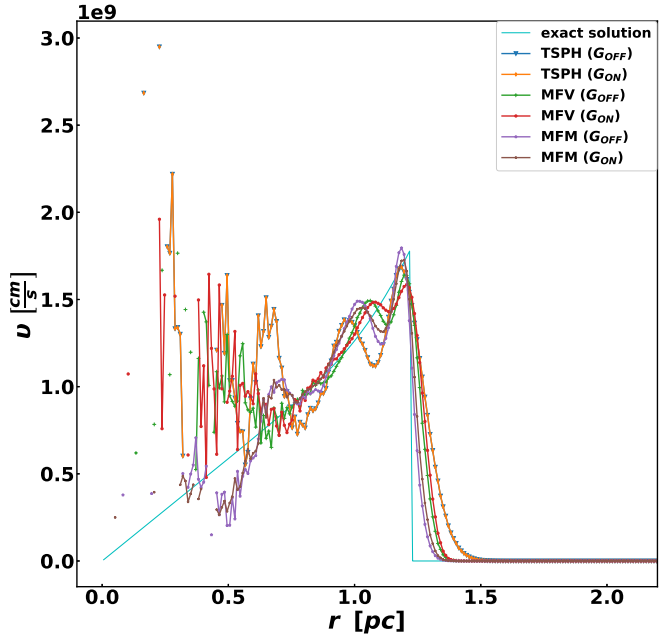

(b)

Figure 3.5: Radially averaged profiles of the Sedov-Taylor point explosion showing the effects of self-gravity on *(a)* density and *(b)* velocity for SPH, MFV and MFM. The simulation results and the analytical solution (cyan line) are given at time $t = 20\,\mathrm{yr}$. G_{ON} represents simulations with self-gravity turned ON, while G_{OFF} is for simulations with self-gravity turned OFF.

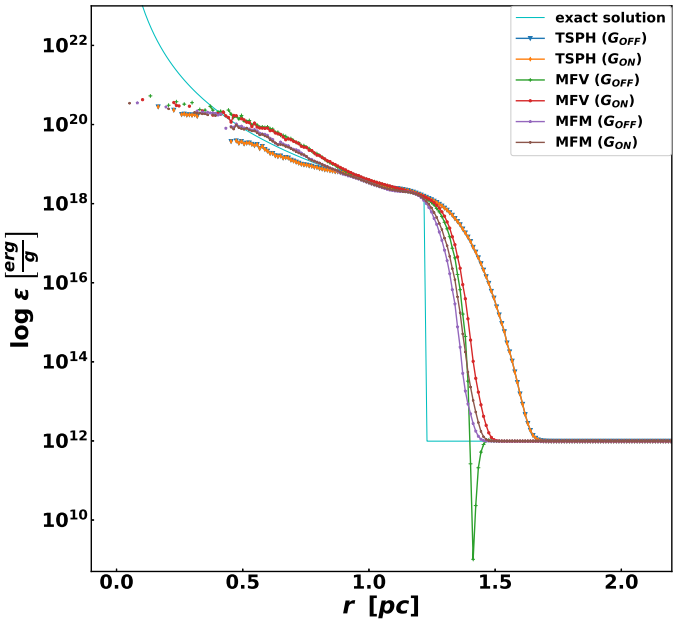

(a)

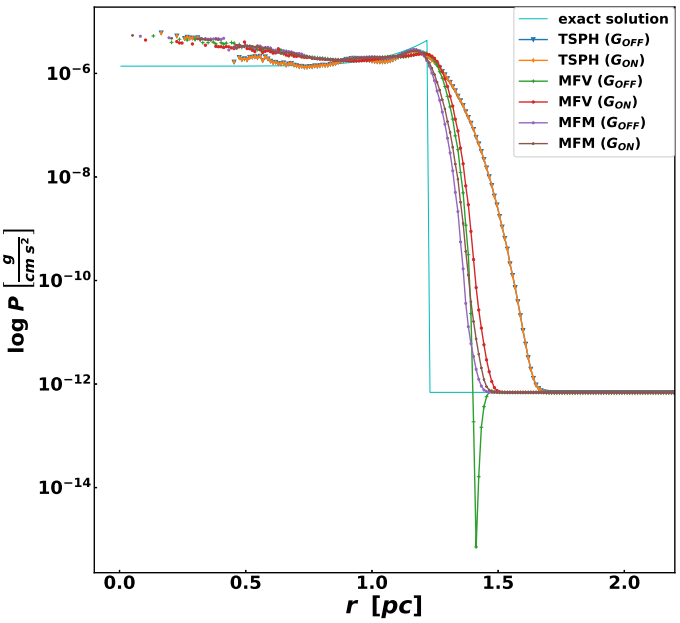

(b)

Figure 3.6: Same as Fig. 3.5 except for *(a)* specific internal energy and *(b)* pressure.

order smoothing kernels with larger $N_{\rm NGB}$ increases their convergence rate. In this test, all simulations were executed at the same resolution of $N_{\rm p} = 5 \times 10^5$ particles.

Since we have established that self-gravity does not have any significant effect in SPH and MFM, only the MFV simulations include self-gravity, so as to reduce computational cost and time. In this test we focused on models SPH_$\rm G_{OFF}$, SPH_$N_{\rm NGB}$128_M_6, MFV_$\rm G_{ON}$, MFV_$N_{\rm NGB}$128_M_6, MFM_$\rm G_{OFF}$ and MFM_$N_{\rm NGB}$128_M_6 and chose model SPH_$\rm G_{OFF}$ as our reference model. This is due to the fact that the parameter settings of model SPH_$\rm G_{OFF}$ are the default SPH parameters for Sedov-Taylor blastwave simulations as per `GIZMO` user guide (`http://www.tapir.caltech.edu/~phopkins/Site/GIZMO_files/gizmo_documentation.html`). Here models SPH_$\rm G_{OFF}$, MFV_$\rm G_{ON}$ and MFM_$\rm G_{OFF}$ all employ the cubic spline (M_4) kernel with $N_{\rm NGB} = 57$ and their details are discussed in section 3.2.3.

In model SPH_$N_{\rm NGB}$128_M_6, the shock density jump is reduced by 3.2% and shock velocity slightly improved by 0.9% with respect to the reference model, while the shock position remained unchanged. This trend is carried on to model MFV_$N_{\rm NGB}$128_M_6 and MFM_$N_{\rm NGB}$128_M_6, as their shock density jumps are reduced by 2.8% and 3.8%, respectively, relative to model MFV_$\rm G_{ON}$ and MFM_$\rm G_{OFF}$ while their estimated shock positions remain unchanged. Relative to the reference model, model MFV_$N_{\rm NGB}$128_M_6 and MFM_$N_{\rm NGB}$128_M_6 improved their shock density jump by 5% and 1.3%, respectively. While the shock velocity jump in model MFM_$N_{\rm NGB}$128_M_6 reduced by 2.1% relative to model MFM_$\rm G_{OFF}$, it is slightly reduced by 0.3% in model MFV_$N_{\rm NGB}$128_M_6, relative to model MFV_$\rm G_{ON}$. That translates to a 4% improvement and 5.3% reduction in the shock velocity estimates for model MFM_$N_{\rm NGB}$128_M_6 and MFV_$N_{\rm NGB}$128_M_6, respectively, compared to the reference model. The shock position is reduced by 2.6% in model MFM_$N_{\rm NGB}$128_M_6 and improved by 2.5% in model MFV_$N_{\rm NGB}$128_M_6, relative to the reference model.

Although the M_6 kernel with larger $N_{\rm NGB}$ is expected to perform better than the M_4 kernel with smaller $N_{\rm NGB}$, this requires a stronger scaling of $N_{\rm NGB}$ with particle resolution (Zhu et al. 2015). Thus, a combination of particle resolution, smoothing kernel and $N_{\rm NGB}$ are all crucial for optimizing the efficiency of the simulations. A visual inspection from all radial profiles shows that all models with a M_6 kernel and a larger $N_{\rm NGB}$ broadens the shock fronts, resulting in a reduced shock density jump as shown in Fig. 3.7 and Fig. 3.8. All the drawbacks of the SPH method and deviations from the analytic solution previously mentioned are still present in SPH simulations. Velocity profiles show a noisy behaviour in the post-shock region caused by reordering of particle positions after the particle distribution becomes anistropically compressed in the shock. However, using the M_6 kernel with $N_{\rm NGB} = 128$ reduced the noise in the post-shock velocity field.

One disadvantage of using the M_6 kernel with larger $N_{\rm NGB}$ is the increased computational cost. It should be noted that both MFV/MFM reliably capture the position and amplitude of the shock and perform better than SPH even with the M_6 kernel and $N_{\rm NGB} = 128$. The deviations from the analytic solution are present in the post-shock pressure and internal energy and in the oscillation around the velocity solution at smaller radii, regardless of the kernel used. This test has proven that using higher-order kernels and a larger $N_{\rm NGB}$ without increasing particle resolution does not dramatically improve the numerical solution. Since using the M_6 kernel with large $N_{\rm NGB}$ comes at a huge computational cost without improving the solution, the M_4 kernel is a better option for low resolution simulations.

3.2.5 Artificial viscosity and conductivity tests

In SPH, $\alpha_{\rm AV}$ is necessary for the correct treatment of shocks. One way to do this is by adding an appropriate viscous force in the momentum equation, but this often generates unwanted dissipation away from the shocks. Another long standing problem in SPH is the fact that it is unable to resolve mixing instabilities at fluid discontinuities. The solution to the local mixing instability problem in shocks is to introduce an $\alpha_{\rm AC}$ term with the purpose of smoothing thermal energy at fluid interfaces (Price 2008). This $\alpha_{\rm AC}$ term gives a smooth entropy transition at contact discontinuities (Valdarnini 2012). In this test we investigated how well the different prescriptions of $\alpha_{\rm AV}$, i.e., the CD10 switch (which uses total time derivatives of the velocity divergence as a shock indicator) and the traditional Balsara switch, manage to capture shocks in SPH. For this test we focused on models SPH_CD10$_{\rm AV}$1_$\alpha_{\rm AC}$0, SPH_CD10$_{\rm AV}$1.5_$\alpha_{\rm AC}$0, SPH_CD10$_{\rm AV}$1.5_$\alpha_{\rm AC}$0.25, SPH_BS$_{\rm AV}$1_$\alpha_{\rm AC}$0.5, SPH_BS$_{\rm AV}$1_$\alpha_{\rm AC}$0 and SPH_BS$_{\rm AV}$1.5_$\alpha_{\rm AC}$0 as shown in Table 3.3, and used model SPH_G$_{\rm OFF}$ as our reference model.

All simulations employ the M_4 kernel with $N_{\rm NGB} = 57$, while varying the values of $\alpha_{\rm AV}$ and $\alpha_{\rm AC}$. The resulting radial profiles are presented in Fig. 3.9 and Fig. 3.10. Since the CD10 switch is adaptive, $\alpha_{\rm AV}$ varies internally with time. Model SPH_CD10$_{\rm AV}$1_$\alpha_{\rm AC}$0 and SPH_CD10$_{\rm AV}$1.5_$\alpha_{\rm AC}$0 yield a shock density jump and shock velocity improvement of 7.3% and 8.1%, respectively, with respect to the reference model. However, the shock velocity remains unchanged relative to the reference model. Since the CD10 switch is adaptive, manually setting it to a higher value, $\alpha_{\rm AV} = 1.5$, like in model SPH_CD10$_{\rm AV}$1.5_$\alpha_{\rm AC}$0, does not affect the result of the numerical solution, as shown by the green crosses overlapping with the orange diamonds in all radial profiles, both of which had their $\alpha_{\rm AC}$ term disabled.

In model SPH_CD10$_{\rm AV}$1.5_$\alpha_{\rm AC}$0.25, the shock density jump and shock velocity increased by 2.3% and 2%, respectively, compared to the reference model, while the estimated shock position remained unchanged. Although reducing $\alpha_{\rm AC}$ to 0.25 or turning it off completely

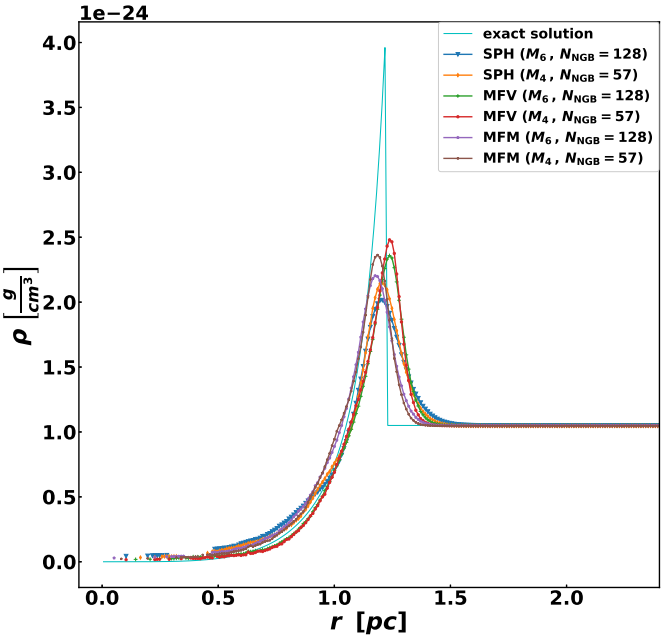

(a)

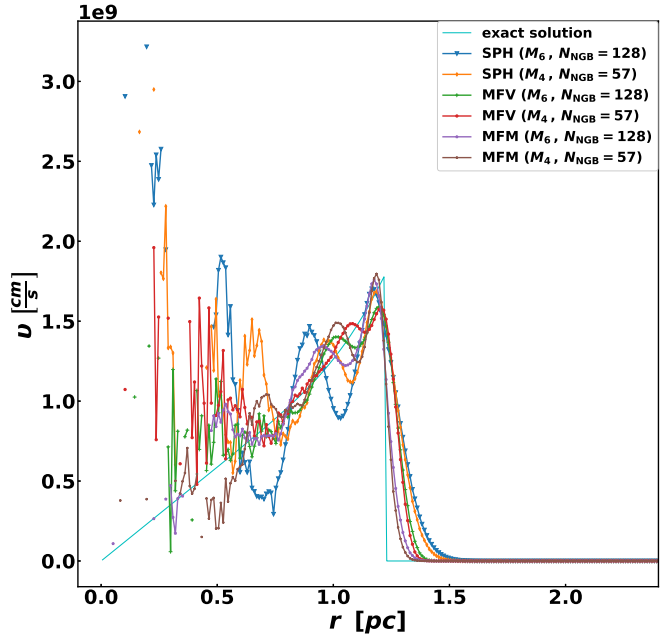

(b)

Figure 3.7: Radial profiles showing the effects of adopting a higher-order kernel and larger $N_{\rm NGB}$ on *(a)* density and *(b)* velocity for SPH, MFV and MFM simulations. The simulation results and the analytical solution (cyan line) are evaluated at time $t = 20\,\mathrm{yr}$. M_4 and M_6 stands for the cubic- and quintic-spline kernels, respectively.

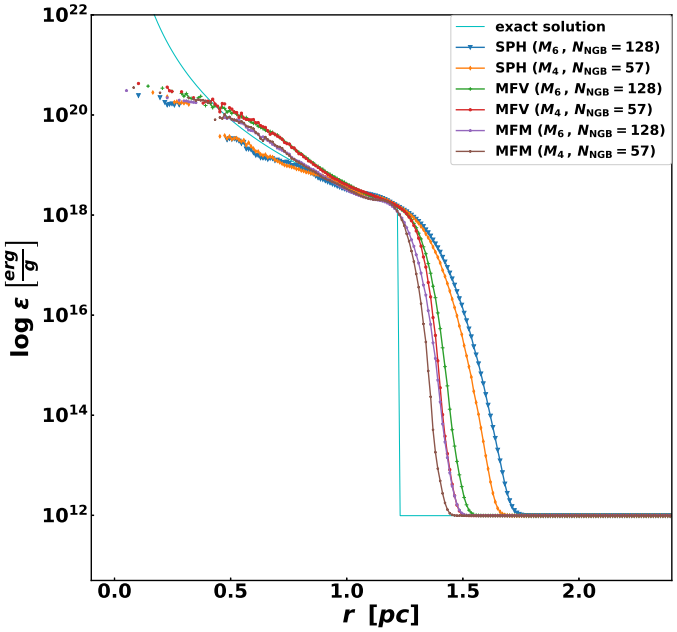

(a)

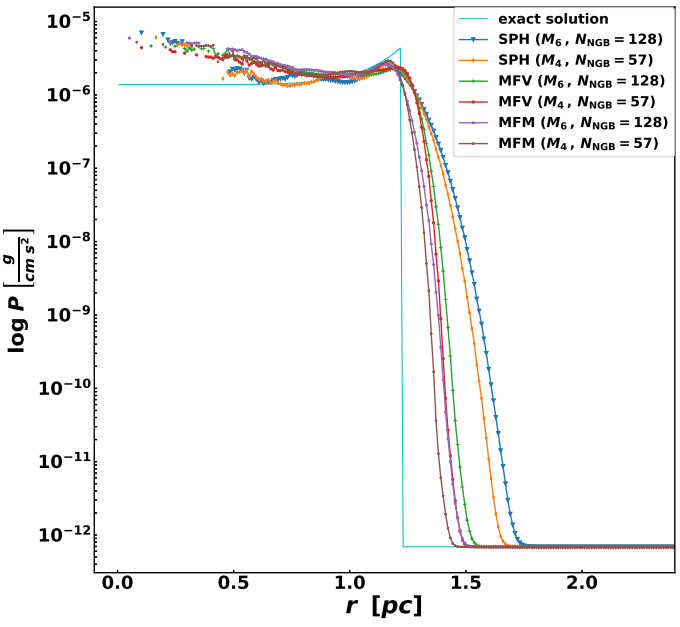

(b)

Figure 3.8: Same as Fig. 3.7 except for *(a)* specific internal energy and *(b)* pressure.

improved the amplitude of the density jump, it generates noise in the post-shock velocity estimates, especially at smaller radii. This is also observed in the radial specific internal energy (Fig. 3.10a) and pressure (Fig. 3.10b) profiles.

Model SPH_$BS_{AV}1$_$\alpha_{AC}0.5$ resulted in a 4.8% and 5.3% increase in shock density jump and shock velocity, respectively, compared to the reference model while, the estimated shock position remained unchanged. In model SPH_$BS_{AV}1$_$\alpha_{AC}0$ and SPH_$BS_{AV}1.5$_$\alpha_{AC}0$, $\alpha_{AV} = 1.5$ was changed from 1 to 1.5, respectively, while α_{AC} is disabled. The results showed that the shock density jump increased by 13.4% and 8.7%, respectively, while the shock velocity is overestimated by 5.7% and 3.1% respectively, with respect to the reference model. The minor reduction in the shock position is barely noticeable at 0.9% for both model SPH_$BS_{AV}1$_$\alpha_{AC}0$ and SPH_$BS_{AV}1.5$_$\alpha_{AC}0$ with respect to the reference model.

Based on the collective results of this test, using the traditional Balsara switch with $\alpha_{AV} = 1$ and without α_{AC} captures shock jumps better than the recommended `GIZMO` settings. The post-shock ringing in the velocity field causes the largest deviation from the analytic solution for all values of α_{AV}. As discussed previously, it is due to viscous dissipation in regions of the flow that are not undergoing shocks and it is a well known effect that depends on the α_{AV} prescription. The Balsara switch with $\alpha_{AV} = 1$ and $\alpha_{AC} = 0.5$ minimizes the noise at small radii ≤ 0.5 pc, however, it overestimates the maximum velocity at the shock front. Even though the Balsara switch is better than the CD10 switch at capturing shocks, due to the spherical symmetry property discussed later in section 3.2.7, simulations using the CD10 switch are preferred over those using the Balsara switch.

3.2.6 Resolution test

In order to investigate the effect of varying resolution, simulations were carried out using 5×10^5, 1×10^6, and 10×10^6 particles in the simulation box. The tests clarify the difficulty of resolving the structure of a thin shock front in 3D accurately. To reduce the computational time for these tests, we evolved our simulations for 8 yr, and since the Sedov-Taylor solution is self-similar, we have the same features as at late times. We employed the M_4 kernel with $N_{NGB} = 57$ for all methods and focused on models SPH_G_{OFF}, SPH_N_p1e6, SPH_N_p1e7, MFV_G_{ON}, MFV_N_p1e6, MFV_N_p1e7, MFM_G_{OFF}, MFM_N_p1e6 and MFM_N_p1e7. SPH uses the CD10 switch with $\alpha_{AC} = 0.5$. Radial density profiles for 5×10^5, 1×10^6, and 10×10^6 particles at time $t = 8$ yr are shown in Fig. 3.11, Fig. 3.12 and Fig. 3.13.

For the Sedov-Taylor blastwave at 8 yr after the initial explosion, the shock position and shock density jump of the reference model (SPH_G_{OFF}) was estimated at 98.5% and 43.2%

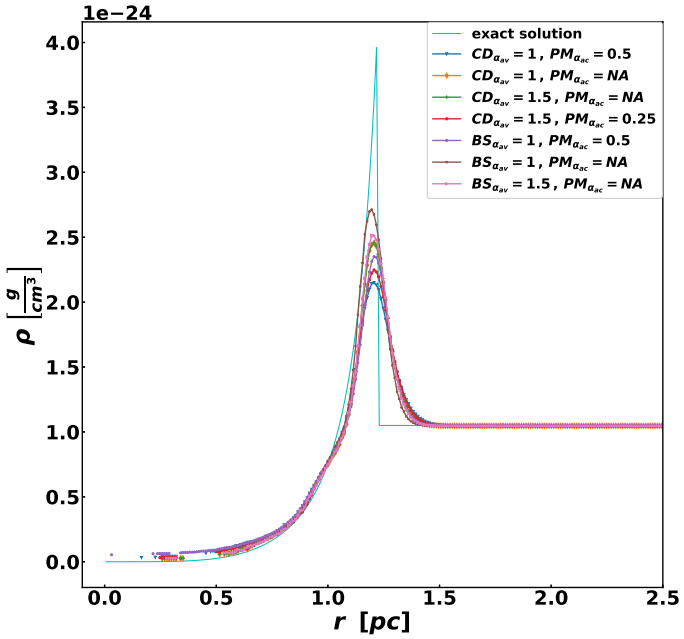

(a)

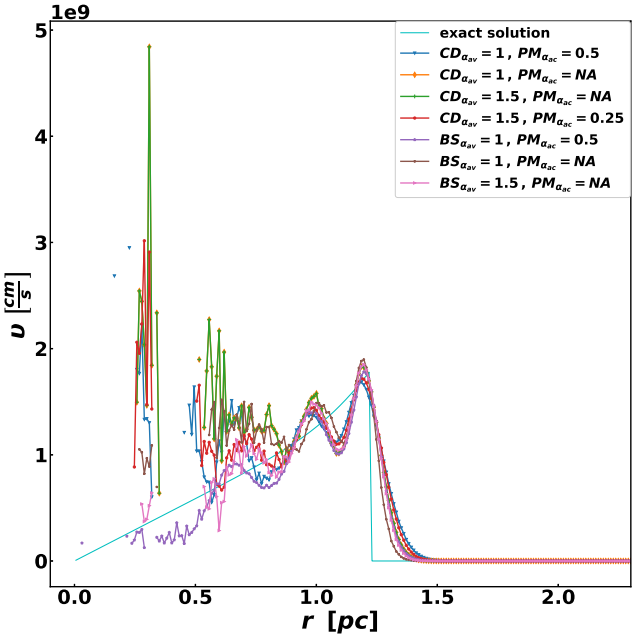

(b)

Figure 3.9: Radial profiles showing the effect of applying different prescriptions of $\alpha_{\rm AV}$ together with $\alpha_{\rm AC}$ on *(a)* density and *(b)* velocity for SPH simulations. The cyan line represents the Sedov-Taylor analytic solution at $t = 20\,{\rm yr}$. These simulations were run using the cubic-spline kernel with $N_{\rm NGB} = 57$, with $CD_{\alpha_{\rm AV}}$ representing the CD10 switch, $PM_{\alpha_{\rm AC}}$ representing Price (2008) $\alpha_{\rm AC}$ formulation and $BS_{\alpha_{\rm AV}}$ is the traditional Balsara switch.

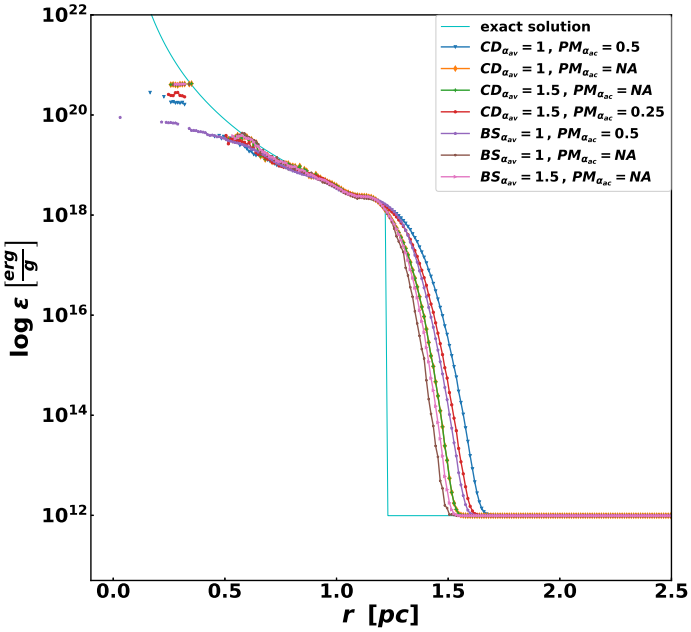

(a)

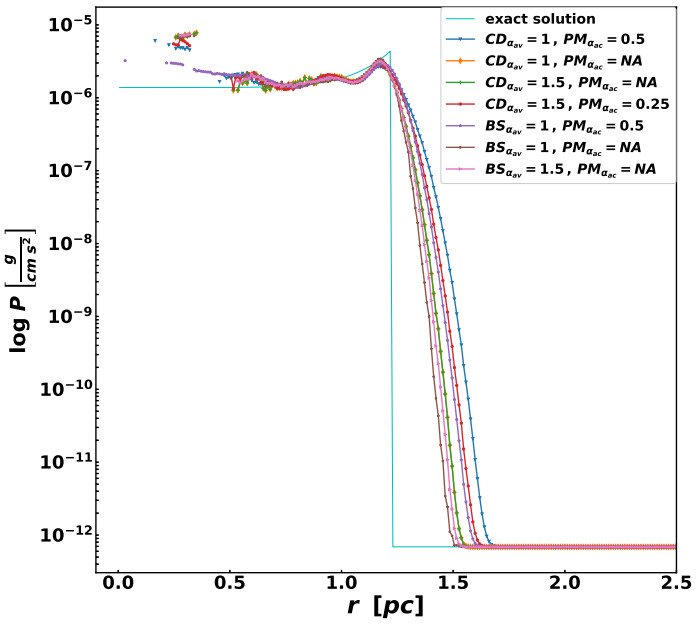

(b)

Figure 3.10: Same as Fig. 3.9 except for *(a)* specific internal energy and *(b)* pressure.

of the analytical value, respectively. The shock velocity was estimated at 93.2% of the analytic solution. In model SPH_N_p1e6 and SPH_N_p1e7, the shock density jump increased by 5.5%, and 23.0%, respectively, relative to model SPH_G_{OFF}. The corresponding shock position shows a minor increase of 0.3% and 0.6%, respectively, relative to model SPH_G_{OFF}. Models MFV_G_{ON}, MFV_N_p1e6 and MFV_N_p1e7 results also scale with increasing resolution. The density jump increased by 9.7%, 14.4%, 26.4%, respectively, and the shock position is overestimated by 0.9%, 1.2%, 1.6%, respectively, relative to model SPH_G_{OFF}. Finally, models MFM_G_{OFF}, MFM_N_p1e6 and MFM_N_p1e7 performed similar to models MFV_G_{ON}, MFV_N_p1e6 and MFV_N_p1e7, with density jumps increased by 8.3%, 9.8%, 24.5% relative to model SPH_G_{OFF}, while the shock position is reduced by 3.7% for model MFM_G_{OFF}, and increased by 0.9% and 0.6% for model MFM_N_p1e6 and MFM_N_p1e7, respectively, relative to model SPH_G_{OFF}. As shown in Fig. 3.11b, 3.12b and 3.13b the smoothing length of each particle decreases with resolution as expected especially in high density regions like in shocks where h decreases from 0.1404 pc to 0.1147 pc and finally 0.0480 pc.

The post-shock ringing in the velocity field is reduced significantly at higher resolutions, and the values remained consistent with the analytic solution even at smaller radii. The specific internal energy and pressure solutions have narrower shocks than their low resolution counterparts as expected. While SPH improves the density estimates at high resolution, it is still very noisy in the post-shock regions and the sporadic ringing of the post-shock velocity field make it a less accurate method for treating shocks.

Our results are consistent with those found in studies by Rosswog & Price (2007) and Springel & Hernquist (2002). The former has shown that increasing resolution from 50^3 to 100^3 particles for SPH simulations result in an increase in shock density amplitude from 2.1 to 2.67 with respect to the exact value of 4, consistent with a factor of 2 change in smoothing length, as seen in Fig. 6 of Rosswog & Price (2007). They further estimate that it would require using 41×10^6 particles to fully resolve the density jump in 3D. Rosswog & Price (2007) also found a maximum density jump of about 66.8% of the analytic solution for a simulation with 100^3 particles. Springel & Hernquist (2002) showed that with SPH, increasing the resolution improves the estimate on the shock density jump significantly, and they were able to improve the shock amplitude from ~ 1.5 to 2 relative to the exact value of 4 when increasing the particle resolution from 32^3 to 64^3. In particular, the smaller shock broadening found in our preceding investigations can be ascribed to a resolution effect. Springel & Hernquist (2002) pointed out that it is also possible to improve resolution by modifying the smoothing algorithm of SPH so that it locally adjusts to properties of the flow. `GIZMO` does this by being spatially adaptive so as to allow the smoothing length of each particle to decrease or increase depending on the local number density of particles (i.e adaptive smoothing).

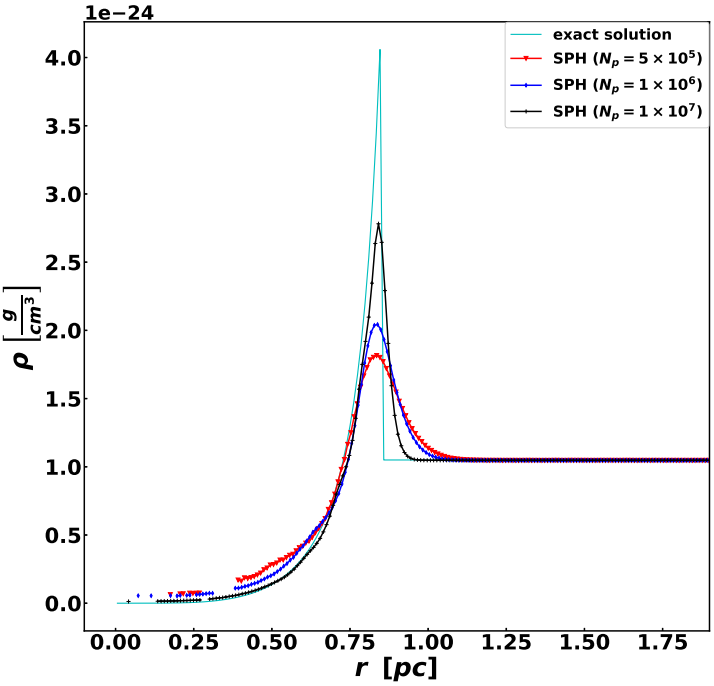

(a)

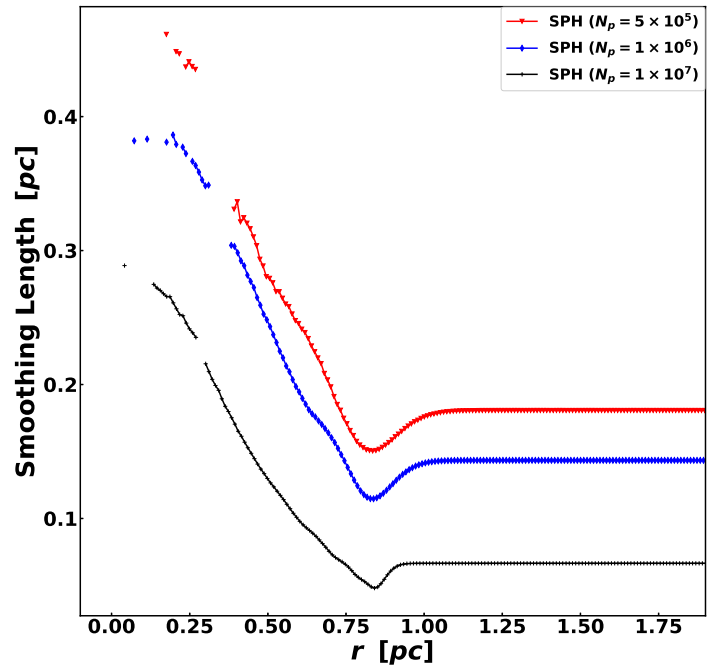

(b)

Figure 3.11: Radial density profiles (a) showing the effect of increasing the total number of particles, N_p, for the Sedov-Taylor blastwave SPH simulation which is compared to the exact solution given by the solid cyan line at $t = 8\,\mathrm{yr}$. The resolution adapts according to the local number density and this is shown in (b) as the smoothing length is the lowest at the position of the shock where the density is the highest.

3.2.7 Code symmetry test

Due to the property of self-similarity, the solution of the expanding Sedov-Taylor blastwave scales to larger radii during the temporal evolution of the blastwave. To test if the numerical methods preserve symmetry, one has to show that fields such as density and pressure preserve spherical symmetry. For SPH, the conservation of fluid quantities is independent of the geometry, meaning that problems involving complicated deformations are especially well suited to SPH simulation. MFM and MFV are Godunov-based schemes that rely on upwind Riemann solvers to exactly capture discontinuities. This results in low numerical dissipation, and a high level of robustness. However, such upwind Riemann solvers (both exact and approximate) have their own peculiar numerical instabilities, a well known example is the carbuncle phenomenon.

The carbuncle phenomenon is a numerical instability that affects the numerical accuracy of capturing shock waves (Shen et al. 2019). This phenomenon is more pronounced in compressible flows in the hypersonic regime (Agrawal & Srinivasan 2017). Although MFV and MFM use stable Reimann, low dissipative solvers, if the propagating shocks involve a carbuncle instability, both methods will violate the spherical symmetry of the expanding shock front. This will be indicated by low density bubbles at the shock front.

In this section we consider the results of SPH, MFV, and MFM Sedov-Taylor simulations using $N_{\rm p} = 5 \times 10^5$ particles with the M_4 kernel and $N_{\rm NGB} = 57$. For SPH runs we consider simulations that used the CD10 switch with $\alpha_{\rm AC} = 0.5$ and the Balsara switch with $\alpha_{\rm AV} = 1.5$ and $\alpha_{\rm AC} = 0$. In Fig. 3.14, Fig. 3.15 and Fig. 3.16, a 2D cross-section slice of density, pressure, and velocity along, $0.0 < x, y < 6.0$, are shown through $z = 3.0$ at $t = 20$ yr. Fig. 3.14a shows that SPH with the CD10 switch preserves spherical symmetry better than SPH with the Balsara switch, which shows an uneven surface of the shock (Fig. 3.14b). For SPH runs using the Balsara switch with $\alpha_{\rm AV} = 1.5$ and without $\alpha_{\rm AC}$, the solution is spherical on average, but the mild deformation of the shock front and the severe noise visible in the post-shock region means that if we allow the simulation to evolve to late times, the sphericity of the solution will be lost. In Fig. 3.14c and Fig. 3.14d the similarly smooth spherical shocks attest to the good preservation of symmetry by the MFM and MFV methods, respectively.

The pressure fields in Fig. 3.15 show complementary results to the density fields in Fig. 3.14. The mild deformation in the leading shock front is still present in Fig. 3.15b. The pressure field in Fig. 3.15a, Fig. 3.15c and Fig. 3.15d show a smooth, spherically expanding pressure wave on average and a flat, uniform solution for the post-shock material, while the Balsara switch shown in Fig. 3.15b still has mild deformation in the leading shock and cannot

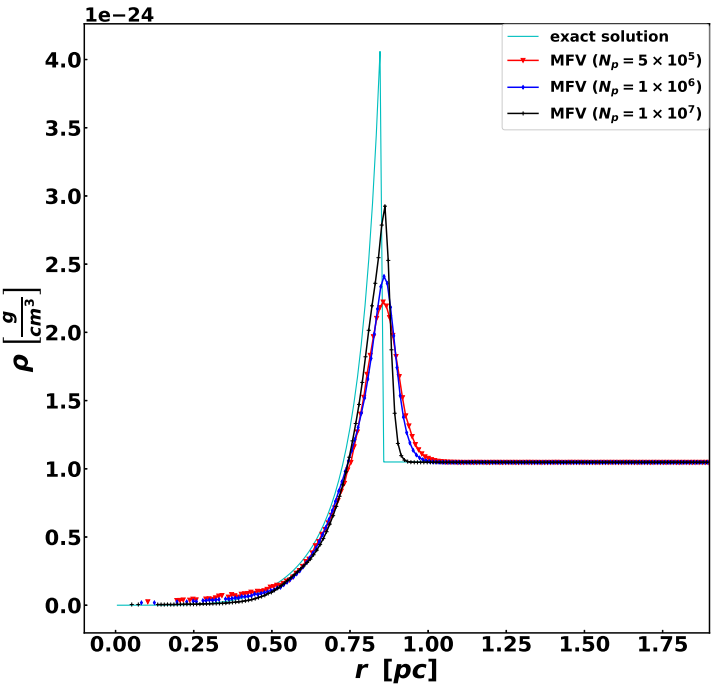

(a)

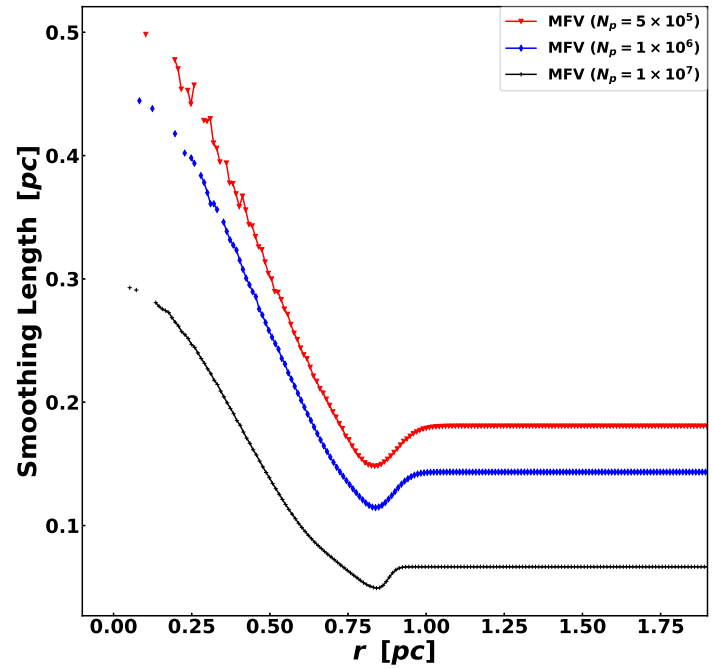

(b)

Figure 3.12: Same as Fig. 3.11 except for the MFV method.

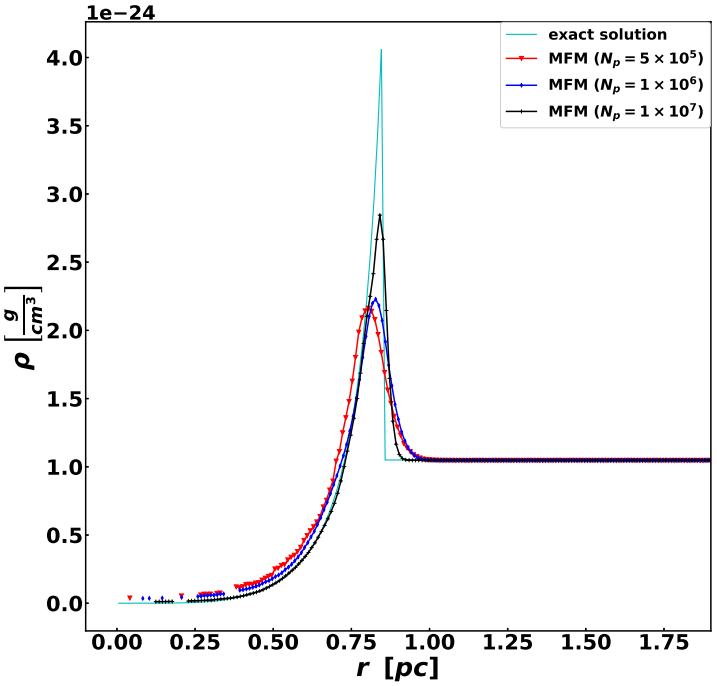

(a)

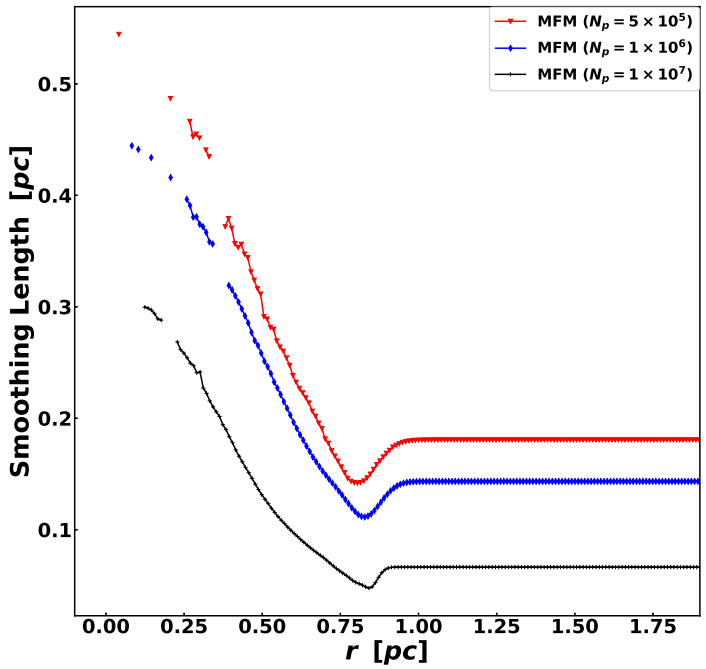

(b)

Figure 3.13: Same as Fig. 3.11 except for the MFM method.

maintain the flat solution in the post-shock material. MFM and MFV maintain excellent spherical symmetry and there are no carbuncle instabilities at the shock front that sometimes arise from Reimann solvers.

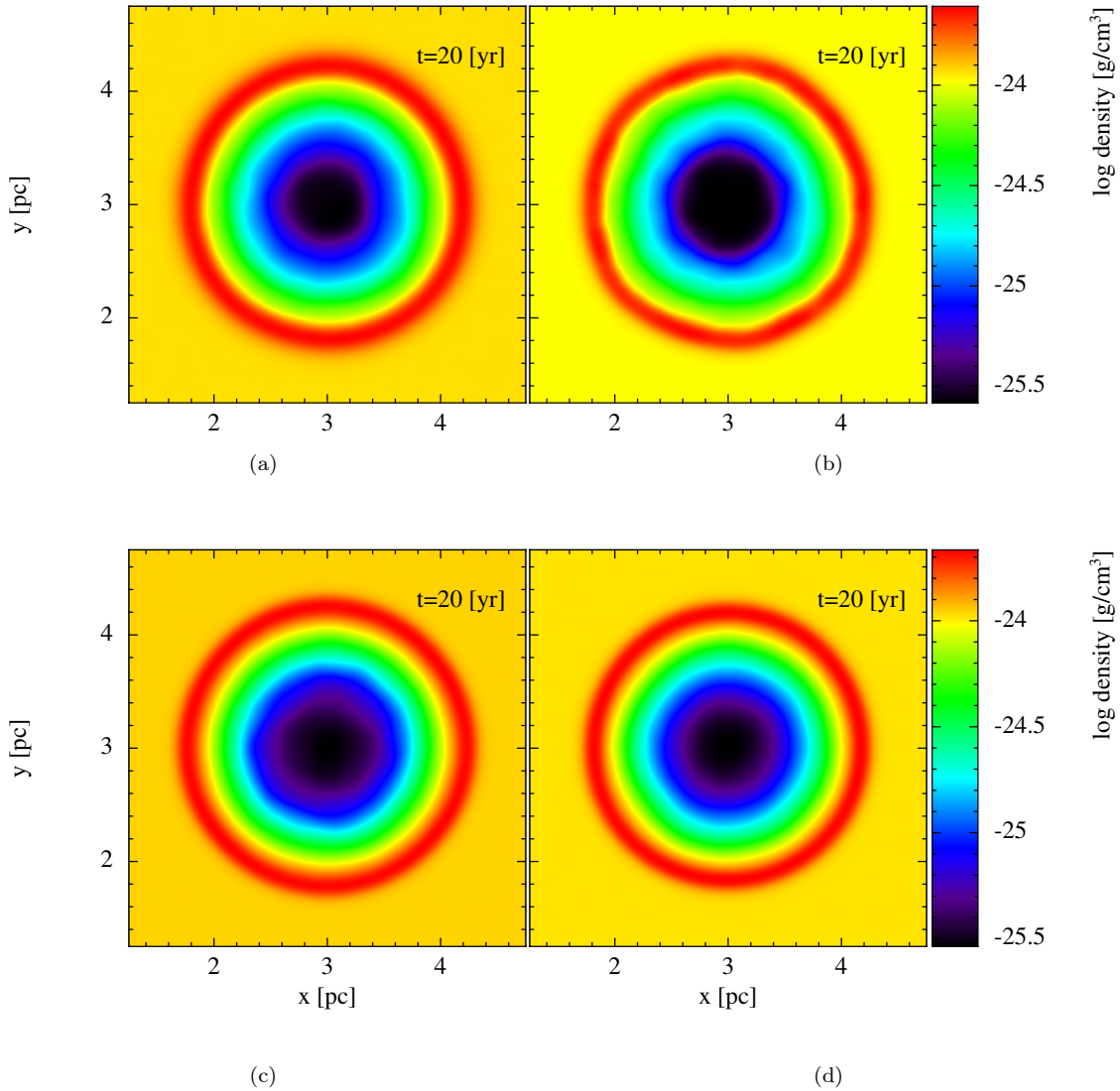

Figure 3.14: Density cross-sections along the z-axis for *(a)* SPH with CD10 switch and $\alpha_{\rm AC}$, *(b)* SPH with the traditional Balsarsa switch, *(c)* the MFV method, and *(d)* the MFM method.

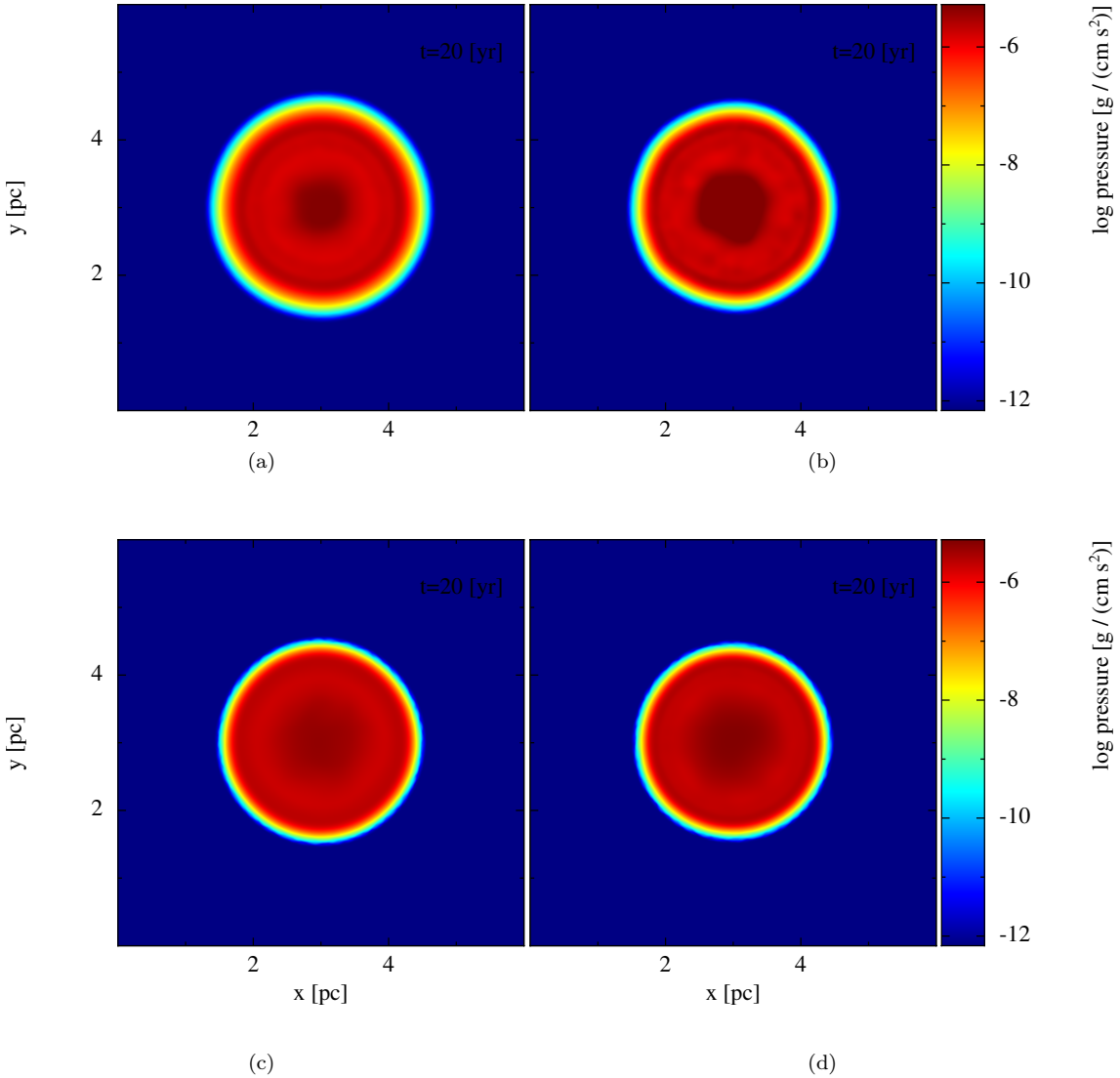

Figure 3.15: Pressure cross-sections along the z-axis for *(a)* SPH with CD10 switch and α_{AC}, *(b)* SPH with the traditional Balsarsa switch, *(c)* the MFV method, and *(d)* the MFM method.

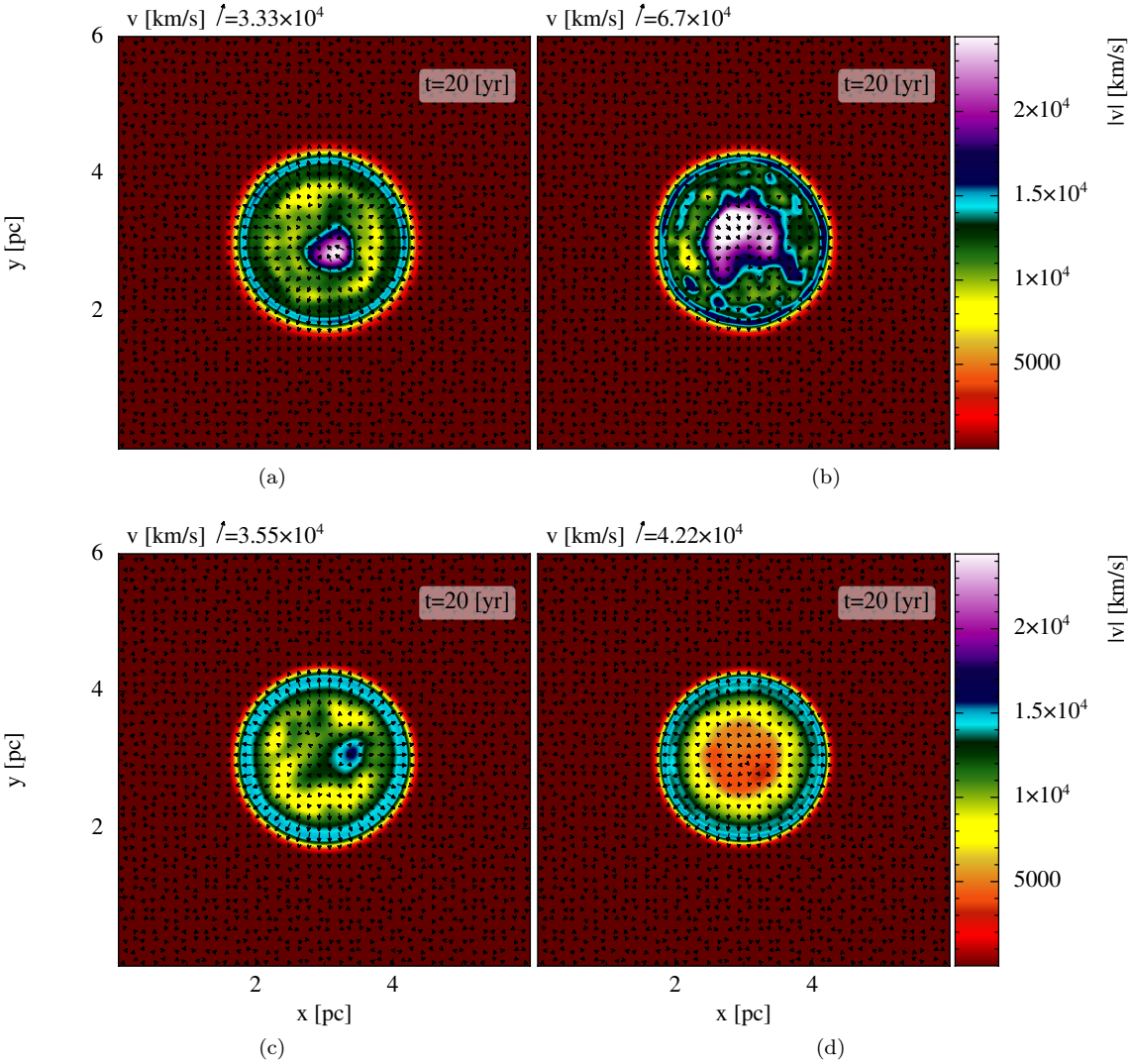

Figure 3.16: Velocity cross-sections in $\mathrm{km\,s^{-1}}$ along the z-axis for *(a)* SPH with CD10 switch and α_{AC}, *(b)* SPH with the traditional Balsarsa switch, *(c)* the MFV method, and *(d)* the MFM method.

3.3 Discussion

From an extensive, systematic study of the Sedov-Taylor blastwave test we demonstrated that the SPH results with particle self-gravity are identical to those without self-gravity. The shock density jump and velocity are better captured with MFM without self-gravity, while MFV without self-gravity slightly improves these estimates, but also diverges from the solution at the shock front with a significant, sharp drop in the pressure and specific internal energy profiles. The cause of the sharp drop at the shock front needs further numerical investigation, therefore it is necessary to include self-gravity in MFV simulations to guarantee consistent results across all hydrodynamic quantities. Self-gravity was excluded for SPH and MFM simulations to save computational time.

While keeping the particle resolution at $N_{\rm p} = 5 \times 10^5$ particles, using the quintic-spline smoothing kernel with $N_{\rm NGB} = 128$ did not improve the agreement with the exact solution compared to the cubic-spline smoothing kernel with $N_{\rm NGB} = 57$. In fact, employing a higher-order kernel with larger $N_{\rm NGB}$ without increasing particle the resolution resulted in reduced shock amplitudes and broader shock fronts for all methods compared to simulations with the cubic-spline smoothing kernel with $N_{\rm NGB} = 57$, as expected from the study of numerical convergence properties of SPH conducted by Zhu et al. (2015). Thus, since using the quintic-spline kernel did not significantly improve the overall solution and is also more computationally demanding, the cubic-spline smoothing kernel with $N_{\rm NGB} = 57$ was adopted.

Two artificial viscosity switches, CD10 and Balsara, were used for the treatment of shocks in SPH. The CD10 switch is adaptive and operates in the range $0.05 \leq \alpha_{\rm AV} \leq 2$. When $\alpha_{\rm AC}$ is reduced or turned off completely, CD10 significantly improved the shock density jump but overestimated the shock velocity. However, this resulted in a lot of noise generated in the post-shock velocity, pressure and specific internal energy at small radii, thus, a compromise value of $\alpha_{\rm AC} = 0.5$ is used to address this. These results are in agreement with CD10, in which they demonstrated that their switch is best for resolving shocks and preventing particle inter-penetration.

The Balsara switch with $\alpha_{\rm AV} = 1$ and without $\alpha_{\rm AC}$ resulted in more accurate shock density jump and sharp shock fronts compared to the CD10 switch, however, the shock front becomes less smooth and deforms at 20 yr. Both the Balsara and CD10 switch exhibit unphysical post-shock velocity oscillations arising from the artificial viscosity prescription. This is due to irregular particle motions centred around $\nabla \cdot v$ terms too small to be damped out at inter-particle distances much smaller than h (Monaghan & Gingold 1983). MFV and MFM do not require artificial dissipation terms and are shown to be less diffusive than the CD10 artificial viscosity switch in SPH, despite their use of a Riemann solver. Furthermore, both MFV and MFM conserve symmetry considerably well while Balsara fails to do so.

CD10 SPH simulations conserve spherical symmetry better than Balsara SPH, making the former better suited for the Sedov-Taylor blastwave simulations.

A major advantage of these Lagrangian methods is the resolution is spatially adaptive to the properties of the flow. As the smoothing length of each particle decreases or increases depending on the local number density of particles h is a minimum at the shock position. Increasing particle resolution significantly improved the capturing of the shock amplitude and resulted in sharper shock fronts. Our resolution study was in agreement with the results presented by Springel & Hernquist (2002). As expected, all the shock fronts are broadened due to the nature of the smoothing kernel implemented at the heart of each method. Using $N_{\rm p} = 1 \times 10^7$ particles, MFV had the sharpest shock front, with maximum shock density jump of 69.6%, whereas MFM and SPH with the CD10 switch and $\alpha_{\rm AC} = 0.5$ resulted in 67.7% and 66.2% of the analytical solution, respectively.

It is evident that Hopkins (2015) obtained a better numerical approximation using only $N_{\rm p} = 64^3$ particles for the MFV simulation of the Sedov-Taylor blastwave test compared to our model MFV_N$_{\rm p}$1e7 with $N_{\rm p} = 10^7$ particles. However, Hopkins (2015) used a relatively high injection energy for the SN explosion, $E_0 = 1.98 \times 10^{53}$ erg, delivered in a top-hat distribution to the central-most particle, and an assumed ambient gas density of 6.7×10^{-22} g cm^{-3} in a simulation box that spans 6 pc which we assumed from the GIZMO parameter file preset for Sedov-Taylor blastwave test. Compared to our initial condition setup, this would result in a stronger shock propagating in a higher density medium. They also excluded self-gravity in their model, which we have shown that it improves the shock density jump by 1.3% (see section 3.2.3) even though it leads to a sharp drop in pressure and specific internal energy at the shock fronts. MFM also minimized broadening at the shock front, while MFV overestimated the shock position. Thus, the configurations using the cubic-spline kernel with $N_{\rm NGB} = 57$ for MFV, MFM and SPH with the CD10 switch and $\alpha_{\rm AC} = 0.5$, are best suited for simulating the early phases of SN explosions.

The Sedov-Taylor blastwave problem has also been simulated using Eulerian adaptive mesh refinement (AMR) codes in previous studies. Using 100^3 particle/grid elements for the initial setup, Tasker et al. (2008) compared the AMR codes, i.e., `Enzo`(PPM) (Bryan et al. 2014) and `FLASH` (Fryxell et al. 2000)), with `Gadget2` SPH and found that they captured 8% more of the shock density jump than the latter. However, two levels of refinement was used for the AMR codes, which allow them to insert additional resolution elements at the region of the shock, instead of following number density as in SPH. Thus, it would require an initial static grid of 250^3 to reproduce a blastwave with similar resolution to an SPH simulation with 100^3 particles (Tasker et al. 2008). In our models, using $N_{\rm p} = 5 \times 10^5$ particles showed that MFV and MFM captured 9.7% and 8.3% more of the shock amplitude, respectively, with respect to SPH. This behaviour is less significant when we increase particle resolution to $N_{\rm p} = 1 \times 10^7$, where MFV and MFM only manages to capture 3.4% and 1.5% of more of

the shock than SPH, respectively. Note, although AMR codes are good at resolving shocks, they have other caveats, e.g., angular momentum in rotational flows is not conserved and non-Galilean invariant (Springel 2010).

Chapter 4

Supernova-Circumstellar Medium Interactions

Three dimensional simulations of SN explosions in meshless methods like SPH is a computationally demanding problem, primarily due to the challenges of capturing strong discontinuities and instabilities arising at the interaction region. In addition, one must set up a more realistic initial SN ejecta profile such that the remnant evolves in a manner that is representative of an SNR during the Sedov-Taylor period.

4.1 Initial conditions

4.1.1 Initial SN ejecta setup

In the early stages, SN ejecta in a free flowing CSM is effectively modelled by a cold freely expanding material where energy is kinetic rather than thermal – see thermal energy bombs in Chapter 3 (Perego et al. 2015). Due to the different phases of evolution and dynamic processes at play, modelling the expansion of the blastwave until it dissipates is numerically challenging. An accurate model of the initial ejecta in free expansion must constrain its hydrodynamic profile to be less than the radius encompassing more background circumstellar mass than the ejected mass. Relatively high densities of the ionized circumstellar gas in the vicinity of the central RSG have this radius on the order of 5×10^{-3} to 1×10^{-1} pc, but to evaluate the impact of the blastwave on the neighbouring circumstellar gas, the evolution of the blastwave must go out to tens of parsecs (Whalen et al. 2008). A Lagrangian form of the equations of hydrodynamics is adopted and the mass of the ejecta is therefore defined by

$$M_{\rm ej}(r,t) = \int_{r_{\rm min}}^{r_{\rm max}} 4\pi r^2 \rho(r,t) dr \ , \tag{4.1}$$

where, $M_{\rm ej}$, is the total mass of the ejecta in which the mass of the stellar remnant is excluded, r, is the radius, $r_{\rm min}$ and $r_{\rm max}$ are the minimum and maximum radii defining the

lower and upper bound of the SN ejecta shell, respectively, t, is the time and, ρ, is the gas density. This profile of the ejecta is established in the first few days after the explosion and corresponds to the state of the gas in the limit $t \to 0$, where a free flowing, cold ejecta of piece-wise density distribution expands into a slow moving, warm ambient medium (Truelove & McKee 1999). The corresponding velocity profile, $v(r,t)$, of the ejected material approaching free expansion, is

$$v(r,t) = \begin{cases} \frac{r}{t} & \text{if } r < R_{\rm ej}, \\ 0 & \text{if } r > R_{\rm ej}, \end{cases} \tag{4.2}$$

where $R_{\rm ej}$ is the maximum radius that defines the leading edge of the SN ejecta. A few days after the SN explosion prior to the interaction with the ambient medium, the early ejecta density profile in free expansion is constant in the inner region and decreases as a power-law, $\rho \propto v^{-n}$, in the outer region, where n is the power-law index of the expanding matter. Without the surrounding CSM, the surface radius of the freely expanding ejecta would be defined by $R_{\rm ej} = v_{\rm ej} \times t$, where $v_{\rm ej}$ is the maximum velocity of the SN ejecta. Here we assume that the density profile of the SN ejecta at a given time, t, is approximated by a flat inner core and steeply declining outer edge, as described in Whalen et al. (2008) and van Veelen et al. (2009):

$$\rho(v,t) = \begin{cases} Ft^{-3}, & \text{for } v \le v_{\rm core}, \\ Ft^{-3}\left(\frac{v}{v_{\rm core}}\right)^{-n} & \text{for } v_{\rm core} < v \le v_{\rm ej}, \\ 0 & \text{for } v > v_{\rm max}, \end{cases} \tag{4.3}$$

where $v_{\rm core}$ is the constant velocity of the ejecta at the transition between an inner, constant density core and the outer, power-law density profile with index, n. The density normalization constants, F, and $v_{\rm core}$ are determined from the ejecta mass, $M_{\rm ej}$, and energy, $E_{\rm ej}$. $E_{\rm ej}$ and $M_{\rm ej}$ are related to $v_{\rm ej}$ following Whalen et al. (2008),

$$E_{\rm ej} = \frac{1}{2} M_{\rm ej}(r,t) \times v_{\rm ej}(r,t)^2 = \int_{r_{\rm min}}^{r_{\rm max}} 4\pi r^2 \frac{1}{2} \rho(r,t)\, v_{\rm ej}(r,t)^2 dr\,. \tag{4.4}$$

To determine F and $v_{\rm core}$, the minimum radius, $r_{\rm min}$, of the free expansion has to be chosen. The parameter, t, is set to $t = t_{\rm max} = \frac{r_{\rm max}}{v_{\rm max}}$, the time by which the leading edge of freely expanding ejecta has self-similarly grown to the maximum radius, $r_{\rm max}$, in the free expansion phase. The analytical expression for the normalization constant, $v_{\rm core}$, is

$$v_{\rm core} = \left[\frac{10E_{\rm ej}(n-5)}{3M_{\rm ej}(n-3)}\right]^{1/2} . \tag{4.5}$$

Therefore $r_{\rm core} = v_{\rm core} t_{\rm max}$ for $r_{\rm min} \ll r_{\rm core} \ll r_{\rm max}$ and F can be expressed as

$$F = \frac{1}{4\pi n} \frac{[3(n-3)M_{\rm ej}]^{5/2}}{[10(n-5)E_{\rm ej}]^{3/2}} . \tag{4.6}$$

The energy of the SN explosion, $E_{\rm ej} = 10^{51}$ erg, is assumed to be entirely kinetic, thus the maximum velocity of the ejected matter is set to $3 \times 10^4\,{\rm km\,s^{-1}}$, which is an approximate value corresponding to the maximum observed velocity in SNRs resulting from CCSNe. We assume a $15M_\odot$ RSG progenitor and $10M_\odot$ is assigned to the ejecta, while the remaining mass accounts for the compact object that forms and the total mass lost during the RSG phase due to free streaming RSG winds. The temperature of the ejecta is set to 1000 K, and assumed to be nearly neutral (Whalen et al. 2008). Since it is relatively cool, its contribution to the energy of the explosion is negligible.

To obtain our desired density profiles, we adopt the shell template proposed by Fryer et al. (2006) for setting up the initial particle distribution. In a shell template, particle coordinates are generated by a HEALPix (Hierarchical Equal Area isoLatitude Pixelization) algorithm by first tessellating a surface of a unit sphere into points or particles (Pakmor et al. 2012, Górski et al. 2005). The spherical explosion source is constructed from the inside outward, where each HEALPix shell determines a radial positions of the particles in that shell. The volume of a spherical shell is defined by the difference between the inner and outer volume of the enclosing spheres, given by

$$V_{\rm shell} = \frac{4}{3}\pi(r_2^3 - r_1^3), \tag{4.7}$$

where r_1 is the radius of the inner sphere and r_2 is the radius of the outer sphere. Thus, the radius of each shell is given by,

$$r_2 = \left[\frac{3}{4\pi}\left(\frac{m_{\rm shell}}{\rho_{\rm shell}} + \frac{4}{3}\pi r_1^3\right)\right]^{\frac{1}{3}}\,, \tag{4.8}$$

where $m_{\rm shell} = m_p \times N_{\rm shell}$, is the mass of gas inside each spherical shell, defined by the product of particle mass, m_p, and number of particles in each shell, $N_{\rm shell}$, and the shell density, $\rho_{\rm shell}$, is given by

$$\rho_{\rm shell} = \frac{m_{\rm shell}}{V_{\rm shell}}. \tag{4.9}$$

Using this formulation, we generate 655 shells, each shell containing 3072 particles with identical mass of $m_p = 9.94 \times 10^{27}$ g. We randomly rotate each shell about the x, y, and z axes so that, even if the same shell template is used, the global particle distribution is random. This ensures that there are no preferred directions which would result in numerical artefacts (Diehl et al. 2012). The result is shown in Fig. 4.1. The total mass of all the shells is $M_{\rm ej} = 2.00 \times 10^{34}$ g ~ 10.0 M$_\odot$, equivalent to the assumed mass of the ejecta and the total number of ejecta particles is 2 012 160. As shown in Fig. 4.2a, the radial density profile of the ejecta has a flat inner core of constant density and a steeply declining outer core with a power-law, $\rho \propto v^{-n}$, density distribution. The radial velocity profile of the ejecta shown in Fig. 4.2b, shows the freely expanding ejecta at each shell radius. We chose the HEALPix method because it can produce any radial density profile with very small scatter

in the particle densities and pressures at a certain radius compared to the random sampling of the density profile.

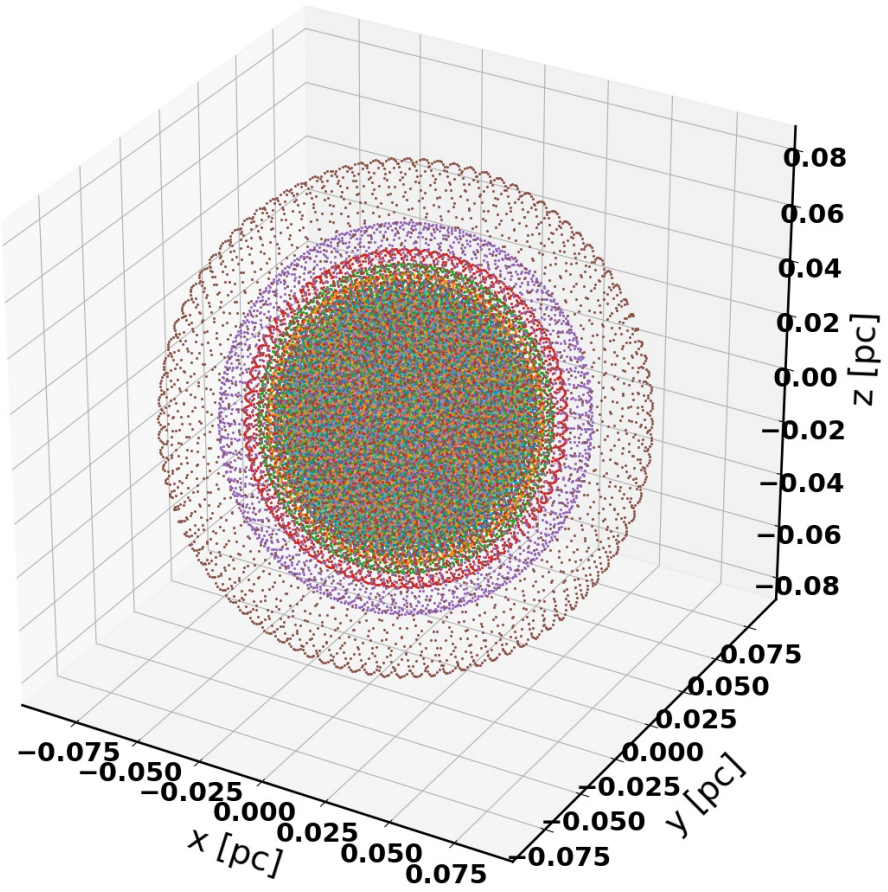

Figure 4.1: Spherical HEALPIX shells of SN ejecta are stacked on top of each other from the inside outward. The flat inner ejecta is signified by a constant density profile and the steeply declining outer ejecta has a power-law, $\rho \propto v^{-n}$, density profile (Whalen et al. 2008).

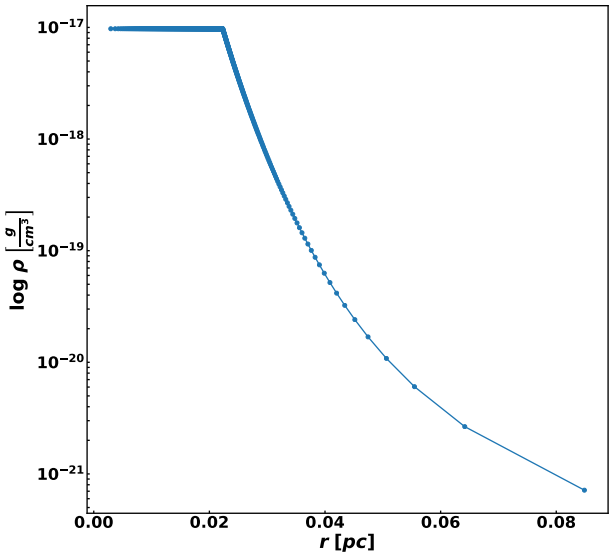

(a)

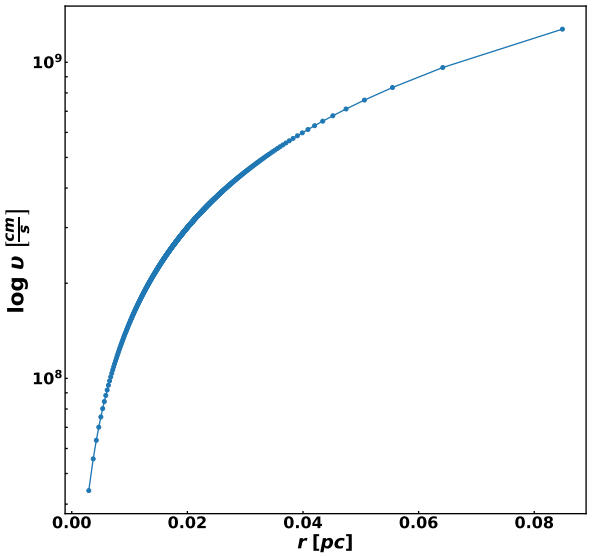

(b)

Figure 4.2: [*a*] SN ejecta radial density profile with a flat inner core and a steeply declining outer edge. The minimum radius is chosen to be typical for the surface of a RSG, $r_{\rm min} = 1730.25\,{\rm R}_\odot \sim 1.20 \times 10^{14}$ cm, and the maximum radius is $r_{\rm max} = 2.62 \times 10^{17}$ cm, sufficient to contain all the mass of the ejecta, $M_{\rm ej} = 10.06\,{\rm M}_\odot$, while minimizing the mass of the ambient gas. [*b*] The velocity profile of freely expanding ejecta evolves self-similarly into the CSM during the early ejecta-dominated stage with a maximum velocity of 9625.86 $\rm km\,s^{-1}$. Each point represents a shell.

4.1.2 Initial CSM Setup

Since we assume that the CSM is established by streaming stellar winds during the RSG phase, we constructed two radial density profiles with $1/r^2$ ($\rho - \mathrm{R2}$) and an axisymmetric torus ($\rho - \mathrm{TO}$) density distribution inspired by the RSG WOH G64 (see Chapter 1). There are several ways in which a particle distribution with spatially adaptive properties can be achieved. The first well known method proposed by Rosswog & Price (2007) is by radially compressing or stretching a uniformly distributed lattice. Every coordinate, $\mathbf{r}$, on the lattice is scaled by a scaling factor, q_r, that varies with radius to achieve the desired spherically symmetric distribution such that the stretched coordinates are given by $\mathbf{r}' = q_\mathrm{r}\mathbf{r}$. Rosswog & Price (2007) further relaxed the resulting configuration before using it in SPH simulations. The stretching process has its drawbacks as it results in a loss of regularity as shown in Figure 11 of Diehl et al. (2012).

To avoid the directional preference along the axes in the lattice configuration, a stretched glass method is used. Initially, one generates a gravitational glass of uniform density which is then radially stretched and compressed following the underlying density model. This process is not straight forward and it results in the glass transforming to a less relaxed state as shown in Figure 12 of Diehl et al. (2012). A final approach is to use the concentric shell method explained earlier in the modelling of the ejecta. While this technique works well for setting up spherical objects, it is not well suited for aspherical objects. Diehl et al. (2012) also pointed out the scatter in density at discrete radii arising within each shell that can lead to strong density perturbations and convection when the shock passes during the Sedov-Taylor blastwave test.

For the variable density initial conditions we considered in this chapter, we needed a more versatile approach for setting up initial conditions with arbitrary, spatially varying density requirements. For the purposes of generating these complex initial conditions, we used the Weighted Voronoi Tesselations (WVTs) code written by Arth et al. (2019) publicly available at `https://github.com/jdonnert/WVTICs`. First proposed by Diehl et al. (2012), the WVTs is a technique for generating initial conditions for meshfree simulations without any geometry restrictions. The algorithmic procedure of WVTs code is outlined in Chapter 2. The main purpose of using WVTs code is to produce relaxed, low energy, glass-like initial conditions for $\rho - \mathrm{R2}$ and $\rho - \mathrm{TO}$ CSM profiles with minimal error in the density estimates. There are number of initial states and parameters required in order to successfully generate the desired density model. A full suite of (analytical) test problems is included in the source code but we defined our own density model for the purposes of this work (see Chapter 2).

For the $\rho - \mathrm{R2}$ profile, we assumed that the RSG mass-loss rate, $\dot{M} = 6 \times 10^{-5}\,\mathrm{M}_\odot\,\mathrm{yr}^{-1}$, and wind velocity, $\upsilon_\mathrm{w} = 20\,\mathrm{km\,s}^{-1}$, are constant, and that the density is consistent with a

r^{-2} profile out to 6 pc. The density as a function of radius, r, is then given by

$$\rho_{\rm csm} = \frac{\dot{M}}{4\pi\upsilon_{\rm w} r^2}. \tag{4.10}$$

We created a $[6, 6, 6]$ pc box and set the maximum density to `Rho_Max` $= 2.46 \times 10^{-20}\,{\rm g\,cm^{-3}}$, sufficient for the dense inner parts of the CSM. For 2D simulations with $N_{\rm p} = 10^6$ particles in the CSM, we allowed for 512 relaxation steps with `MpsFraction` $= 5$. The combined number of ejecta-CSM particles in the final initial conditions setup is $N_{\rm p} = 2\,999\,708$. For 3D simulations with $N_{\rm p} = 10^7$ particles in the CSM, we allowed for 1024 relaxation steps with `MpsFraction` $= 0.35$, and the combined number of ejecta-CSM particles is $N_{\rm p} = 11\,885\,257$. After convergence, the WVTs method produced a smooth $\rho-$R2 profile with minimal scatter and minimum density of $1.19 \times 10^{-24}\,{\rm g\,cm^{-3}}$ in the CSM. The temperature of the CSM is set to be 10 000 K, assumed to be flash ionized by the initial SN explosion. The initial conditions of each physical quantity ($\rho\,, \upsilon\,, \epsilon$ and P) for the $\rho-$R2 profile are shown Fig. 4.3.

The most complex circumstellar density profile we considered is the $\rho-$TO model described in Ohnaka et al. (2008). This model assumes an equatorial torus with a bipolar cavity as shown in Fig. 4.4. The bipolar cavity has a lower density than in the torus, but non-zero, and the transition of density from the equatorial torus to the bipolar cavity (in direction of co-latitude) is smoothed as described by

$$\rho(r, \theta) \propto \left(\frac{r_{\rm in}}{r}\right)^2 \left[\frac{1}{e^{(|\theta|-\Theta)/\varepsilon}+1} + \frac{f}{e^{-(|\theta|-\Theta)/\varepsilon}+1}\right], \tag{4.11}$$

where r is the radial distance from the RSG and the polar angle, θ, measured from the equatorial plane is defined by

$$\theta = \arctan\left(\frac{z}{\sqrt{x^2+y^2}}\right), \tag{4.12}$$

in which $x\,, y\,, z$ are cartesian coordinates, $r_{\rm in}$ is the inner radius of the torus, Θ represents the half-opening angle subtended by the torus, ε is a smoothing constant that defines the transition of density from the equatorial torus to the bipolar cavity, and f is a constant defining the density ratio of the bipolar cavity to that of the equatorial torus. The proportionality constant in equation 4.11 is assumed to be,

$$A = \frac{\dot{M}}{4\pi\upsilon_{\rm w}}, \tag{4.13}$$

corresponding to the mass-loss parameter of the RSG. In our case, we assume a smooth ($\varepsilon = 0.3$) and steep ($\varepsilon = 0.03$) density drop with the ratio of the densities set to $f = 0.3$ and a half-opening angle of $\Theta = 60°$. The smooth ($\varepsilon = 0.3$) and steep ($\varepsilon = 0.03$) density drop is defined according to the change of density with respect to the polar angle, θ, defined in

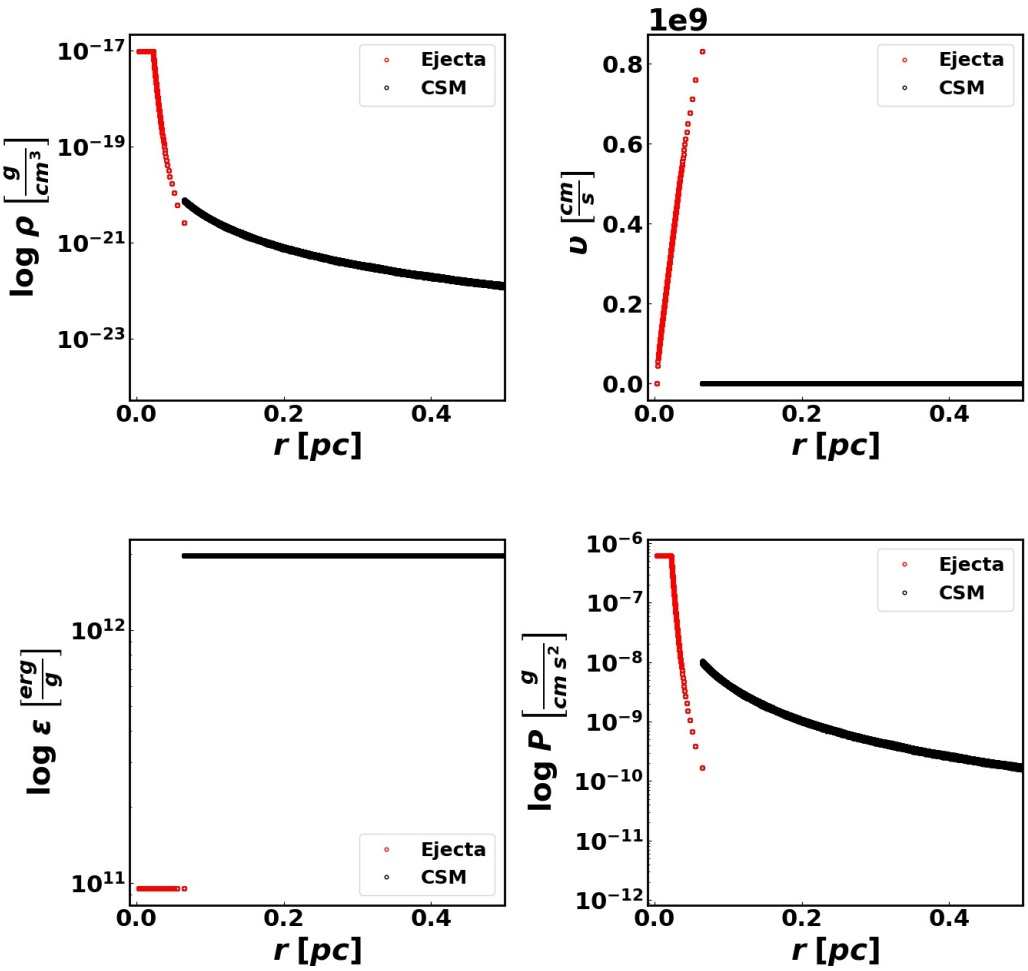

Figure 4.3: Radial density (ρ), velocity (υ), specific internal energy (ϵ), and pressure (P) profiles showing the initial conditions for the ρ – R2 CSM distribution. The red circles are the freely expanding ejecta and the black circles are the CSM. The temperature of the ejecta is set to 1000 K and the temperature of the CSM is 10 000 K.

equation 4.12. We chose these values to be consistent with the model parameters assumed for RSG circumstellar environment as derived by Ohnaka et al. (2008) for WOH G64. The density distribution is assumed to decrease with radius as r^{-2}, corresponding to a steady RSG wind with a constant velocity of 20 km s^{-1}. The radial distance of the inner and outer boundary of the torus are given by $r_{\rm in} = 0.085\,{\rm pc}$ and $r_{\rm out} = 1.0\,{\rm pc}$, respectively, assuming that the stellar radius of the underlying RSG is $R_\star = 1730.25\,{\rm R}_\odot$. We set the effective temperature to $T_\star = 3200\,{\rm K}$ for the central RSG.

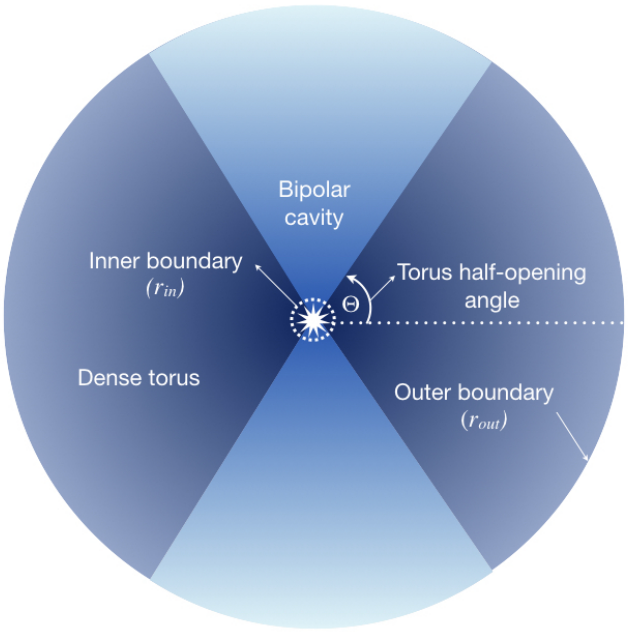

Figure 4.4: Schematic diagram of the torus model showing the dense torus, bipolar cavity, half-opening angle and the inner and outer radii (Ohnaka et al. 2008).

We assumed that the temperature of the CSM, $T_{\rm d}$, consisting of Fe-free silicate grains (see Chapter 1), is determined by the condition of radiative equilibrium,

$$T_{\rm d}(r) = T_\star \left(\frac{R_\star}{2r}\right)^{-\frac{4+\varphi}{2}} \quad \text{where} \quad \kappa_{\rm abs} \propto \lambda^{-\varphi}, \tag{4.14}$$

where φ is the absorption power-law coefficient. A full derivation is outlined in Appendix B of Bladh & Höfner (2012). For Fe-free silicates, the value for the power-law coefficient is assumed to be $\varphi \approx -0.9$. We generated 10^7 random particles positions inside a $[1, 1, 1]$ pc box and set the maximum density to `Rho_Max` $= 8.79 \times 10^{-20}\,\mathrm{g\,cm^{-3}}$, sufficient for the dense inner parts of the CSM. Since the WVTs method failed to converge with `Maxiter` $= 512$, we allowed for 1024 relaxation steps with `MpsFraction` $= 0.35$. The WVTs method converged to a $\rho - \mathrm{TO}$ radial density profile seen in Fig. 4.5. The combined number of ejecta–CSM particles in the final initial conditions setup is $N_\mathrm{p} = 11\,109\,117$. Fig. 4.5a and Fig. 4.5b show the difference in the density cross-section plots for a torus with a steep ($\varepsilon = 0.03$) and smooth ($\varepsilon = 0.3$) density drop, respectively. Both models result in a minimum density of $2.38 \times 10^{-25}\,\mathrm{g\,cm^{-3}}$ for the CSM.

The radial density profile of an axisymmetric torus with a steep density drop shows a narrower distribution as shown in Fig. 4.6a and the region separating the torus from the cavity is also much narrower. The radial density profile of an axisymmetric torus with a smooth density drop (Fig. 4.6b) is marked by a broad distribution with a prominent empty strip separating the dense torus from the bi-conical cavity.

Model	$\rho-$profile	Method	D	N_p	ε	f	Θ
RhoR2_MFV2D	$\rho - \mathrm{R2}$	MFV	2D	2999708			
RhoR2_MFM2D	$\rho - \mathrm{R2}$	MFM	2D	2999708			
RhoR2_SPH2D	$\rho - \mathrm{R2}$	SPH	2D	2999708			
RhoR2_MFV3D	$\rho - \mathrm{R2}$	MFV	3D	11885257			
RhoR2_MFM3D	$\rho - \mathrm{R2}$	MFM	3D	11885257			
RhoR2_SPH3D	$\rho - \mathrm{R2}$	SPH	3D	11885257			
RhoTOf03ε003_MFV3D	$\rho - \mathrm{TO}$	MFV	3D	11109117	0.03	0.3	60°
RhoTOf03ε003_MFM3D	$\rho - \mathrm{TO}$	MFM	3D	11109117	0.03	0.3	60°
RhoTOf03ε003_SPH3D	$\rho - \mathrm{TO}$	SPH	3D	11109117	0.03	0.3	60°
RhoTOf03ε03_MFV3D	$\rho - \mathrm{TO}$	MFV	3D	11113130	0.3	0.3	60°

Table 4.1: SN ejecta interaction models where D is the spatial dimension, N_p is the total number of particles, ε is a constant for the smoothing of the density drop from the torus to the bipolar cavity, f is the ratio of density in the cavity to that of the torus and Θ is the half-opening angle of the torus. Density profiles following a r^{-2} distribution are labelled $\rho - \mathrm{R2}$ with maximum density, $\rho_\mathrm{max} = 4.63\mathrm{e}{-21}$ [$\mathrm{g\,cm^{-3}}$], and CSM outer radius of $r_\mathrm{out} = 5.17$ [pc], and density profiles following a torus distribution are labelled $\rho - \mathrm{TO}$ with $\rho_\mathrm{max} = 1.75\mathrm{e}{-21}$ [$\mathrm{g\,cm^{-3}}$] and $r_\mathrm{out} = 0.86$ [pc]. All models used the cubic spline-kernel with $N_\mathrm{NGB} = 57$ and SPH used the CD10 switch with $\alpha_\mathrm{AC} = 0.5$.

4.2 2D hydrodynamic simulations

We performed 2D hydrodynamic simulations of the SN ejecta interacting with a $\rho - \mathrm{R2}$ CSM in order to investigate any differences between 2D and 3D using the different meshless methods implemented in `GIZMO`. As shown in Table 4.1, all 2D $\rho - \mathrm{R2}$ simulations presented

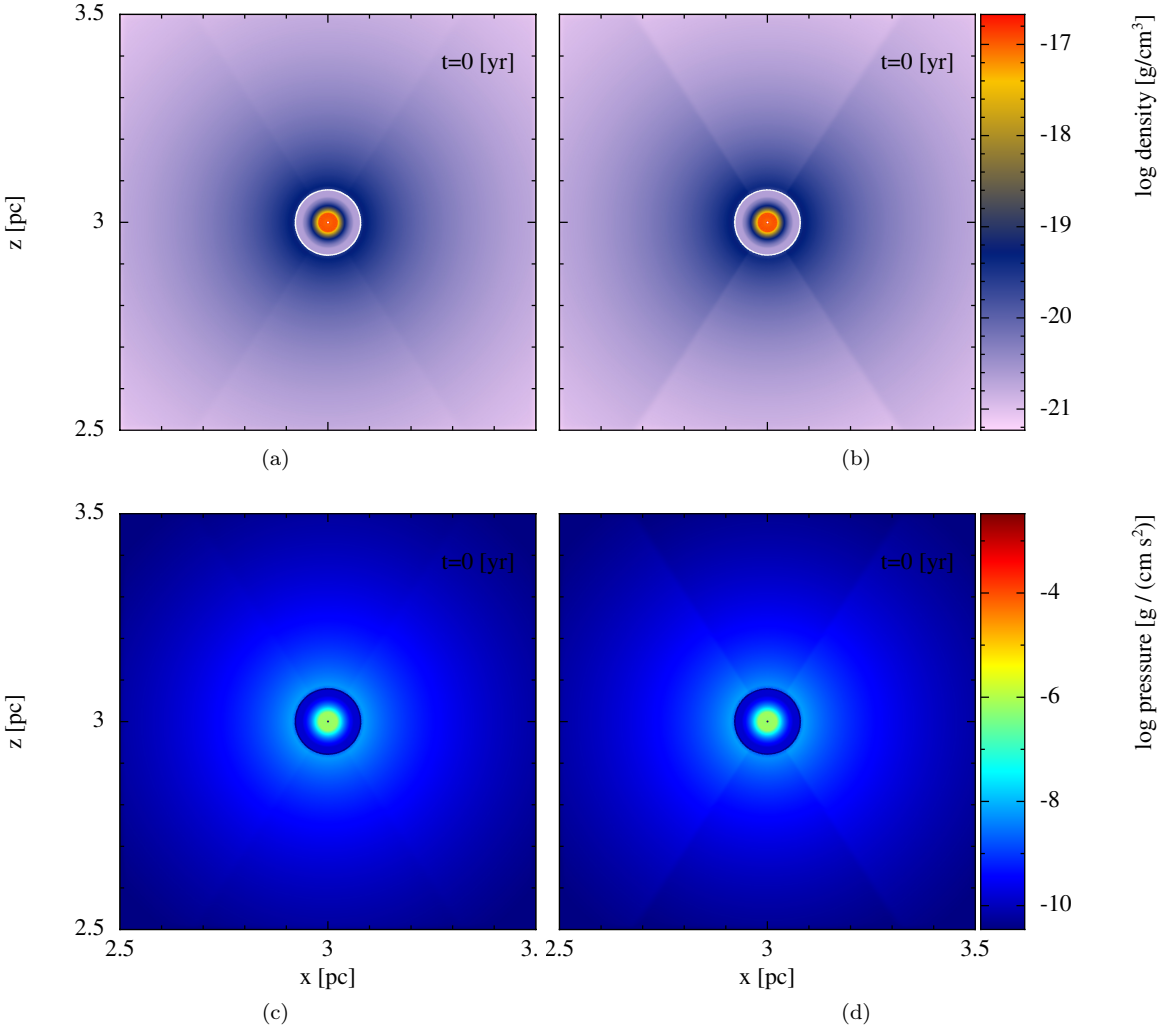

Figure 4.5: Density cross-sections across the y-axis showing the $\rho-\mathrm{TO}$ initial conditions for $[a]$ a steep density drop and $[b]$ smooth density drop with a half-opening angle of $\Theta = 60°$. The corresponding pressure cross-sections are shown in $[c]$ and $[d]$. The inner and outer radii of the CSM are set to $r_{\mathrm{in}} = 0.085\,\mathrm{pc}$ and $r_{\mathrm{out}} = 1.0\,\mathrm{pc}$, respectively.

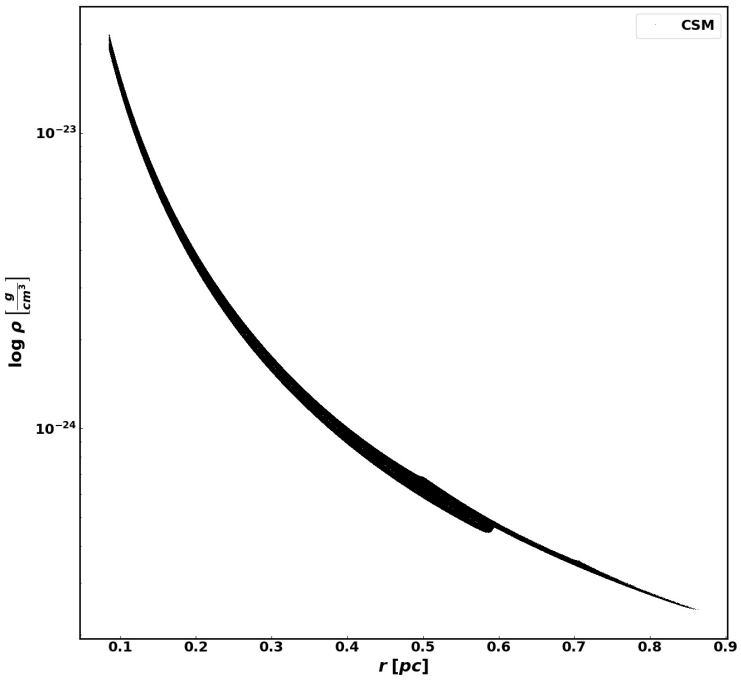

(a)

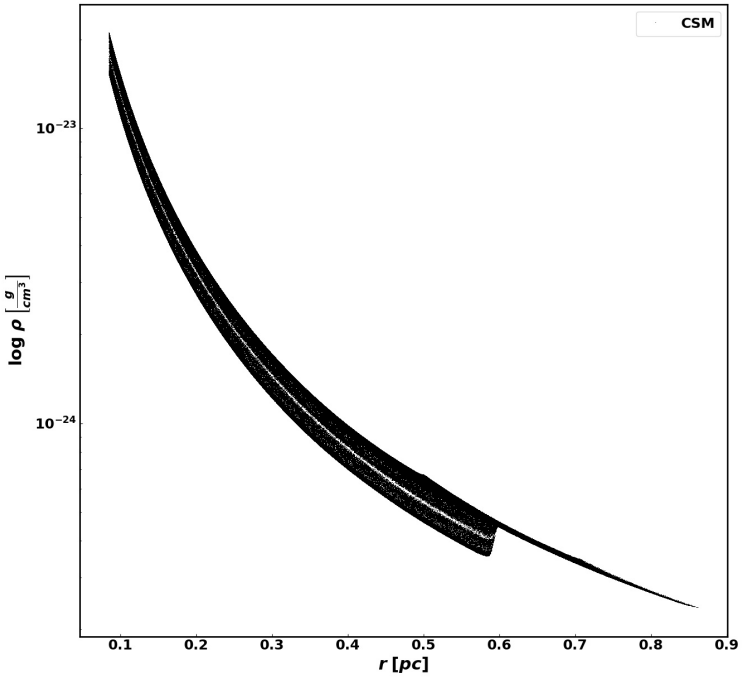

(b)

Figure 4.6: Comparison between the radial density distributions for the axisymmetric torus model with *(a)* steep density drop ($\varepsilon = 0.03$) , and *(b)* a smooth density drop ($\varepsilon = 0.3$). All the other range of free parameters, i.e., ratio of densities, f, half-opening angle, Θ, and the inner and outer boundary radius, $r_{\rm in}$ and $r_{\rm out}$, were fixed. All the CSM particles are plotted.

here employed the cubic-spline kernel with $N_{\rm NGB} = 57$ and we used a total number of 2 999 708 particles in the domain. That is, 2 012 160 particles for the spherically symmetric ejecta and 987 548 particles for the spherically symmetric CSM. For 2D simulations in `GIZMO`, gas self-gravity is turned off because the `GRAVTREE` algorithm is not designed to run in 2D. All the physical parameters and initial conditions of the 2D simulations remain identical to its 3D counterparts.

4.2.1 Ejecta interacting with a $\rho - \mathrm{R2}$ density CSM

We considered SN ejecta interacting with a $\rho - \mathrm{R2}$ distribution for three meshless methods, i.e., SPH, MFV and MFM to investigate how the discontinuities and instabilities develop and evolve. An obvious observation across all the cross-section plots is that, as expected, the expanding interaction shell grows in width and becomes increasingly unstable from 20 yr to 100 yr.

Results for model RhoR2_MFV2D in Table 4.1 are presented in Fig. 4.7 and Fig. 4.8. Starting from the center of the explosion inside the inner boundary in Fig. 4.7b, there are four successive regions, the fast moving unshocked ejecta, the reverse shock followed by the shocked ejecta, shocked CSM followed by the forward shock and lastly the unshocked CSM. The shocked ejecta and the shocked CSM are separated by a thin unstable layer called the contact discontinuity. The contact discontinuity is where the mixing of the ejecta with the CSM material and seeding of the Richtmyer-Meshkov instabilities occurs.

These Richtmyer-Meshkov instabilities are commonly found in fast moving interacting shells of SNRs due to ram-ram pressure. The instabilities are dense and pronounced compared to the enveloping shocked CSM. The unshocked $\rho - \mathrm{R2}$ CSM is almost stationary at $20\,\mathrm{km\,s^{-1}}$ with respect to the approaching forward shock. The passing forward shock increases the local density, temperature, pressure and velocity of the gas. The ejecta initially interacted with a higher density CSM in the inner regions, resulting in higher densities recorded in the shocked CSM region. Another consequence of initially interacting with a higher density CSM is that the expanding shell decelerates rapidly resulting in a significant decrease in its velocity at late times.

The leading shock front loses momentum as it evolves to large radii. This is evident when comparing Fig. 4.8c and Fig. 4.8d, as the velocity of the shocked CSM decreases to $\leq 3000\,\mathrm{km\,s^{-1}}$ at 100 yr, from $\sim 5000\,\mathrm{km\,s^{-1}}$ at 20 yr. As the SNR expands, it cools adiabatically because of the decreasing local gas pressure caused by volume expansion of the remnant. In the Sedov-Taylor phase, the post-shock temperature decreases with density via, $T_1 \propto \rho_0^{-\frac{2}{5}}$, hence Fig. 4.8b shows that the instabilities are cooler than the rest of the material in the shocked CSM. The instabilities grow larger with the expanding SNR which is consistent with what we expect for the growth timescale as a function of density. There are regions within the interacting shell with radial velocities greater than $3000\,\mathrm{km\,s^{-1}}$ and

these regions coincide with the locations of the instability filaments.

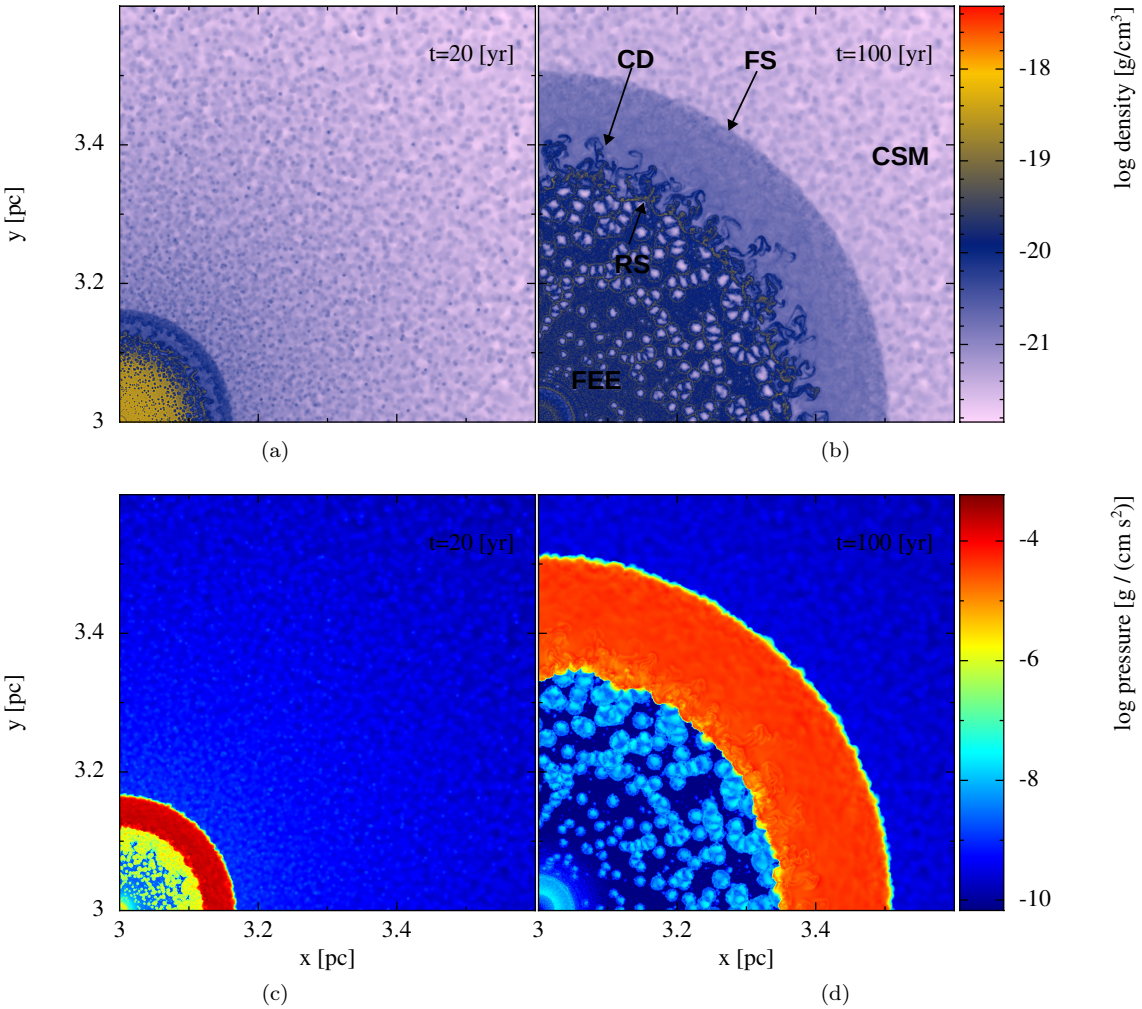

Figure 4.7: Cross-section plots of model RhoR2_MFV2D in Table 4.1 across the z axis for density at *(a)* 20 yr, and *(b)* 100 yr, and pressure at *(c)* 200 yr, and *(d)* 100 yr. These zoomed-in slices are focused on the first quadrant. The abbreviations are as follows; FEE-free expanding ejecta, RS-reverse shock, CD-contact discontinuity, FS-forward shock, CSM-circumstellar medium.

Results for model RhoR2_MFM2D in Table 4.1 are presented in Fig. 4.9 and Fig. 4.10. Judging by the morphology of the remnant at 100 yr, the cross-section plots of density (Fig. 4.9b) and velocity (Fig. 4.10d) show features similar to that of the MFV simulation, which is expected since both MFV and MFM use the same underlying Reimann solvers. There is no significant hydrodynamic difference between model RhoR2_MFV2D and model RhoR2_MFM2D simulations; their instabilities have similar sizes on average and are very turbulent, and the shocked CSM reaches a hot 8000 K in both cases. Their velocity fields (Fig. 4.8d and Fig. 4.10d) show that the instability filaments and the shocked CSM are the

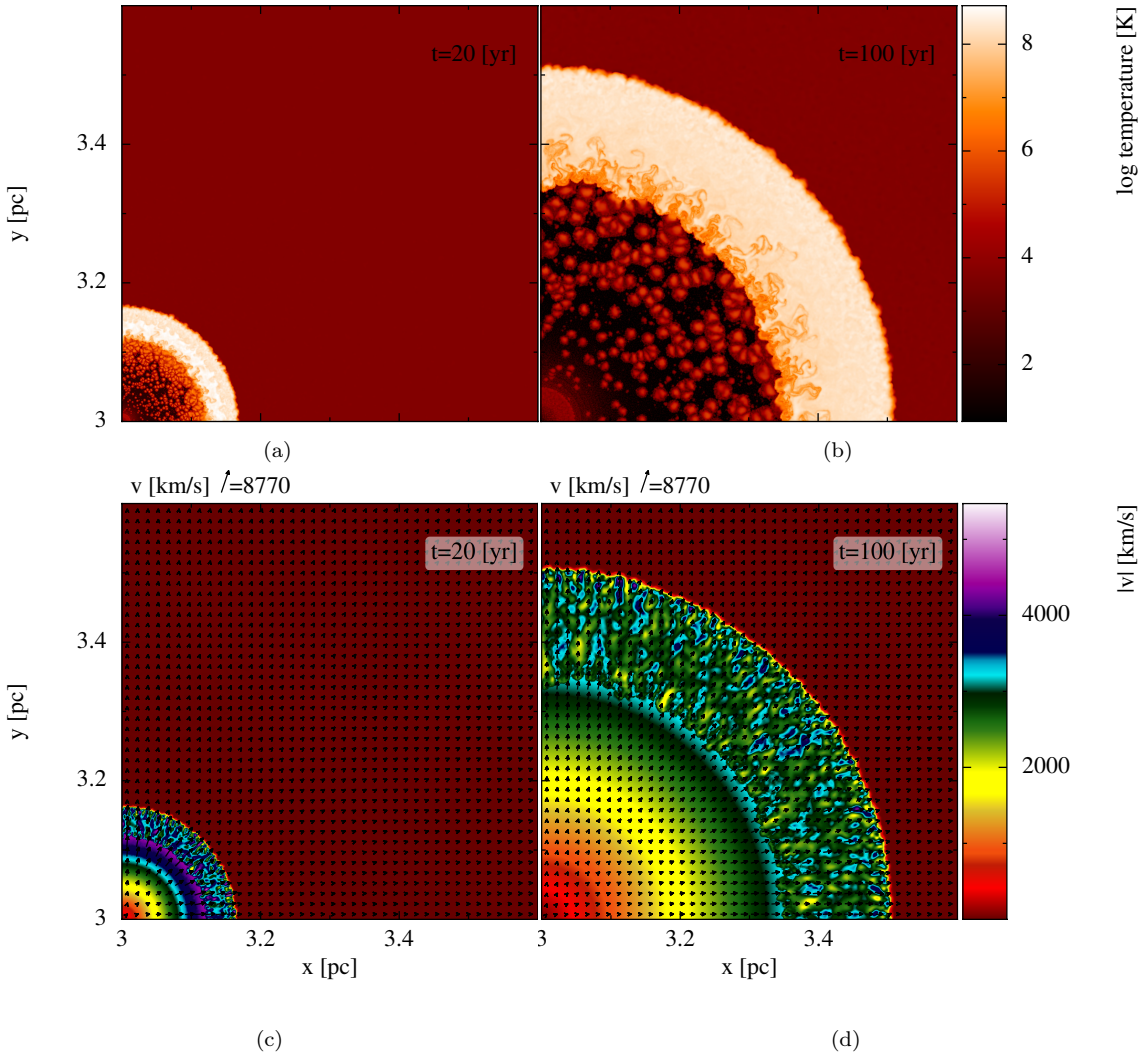

Figure 4.8: Same as Fig. 4.7 but for temperature [a, b] and velocity [c, d].

fastest moving material with a radial velocity of $\sim 4000\,\mathrm{km\,s^{-1}}$ at 100 yr.

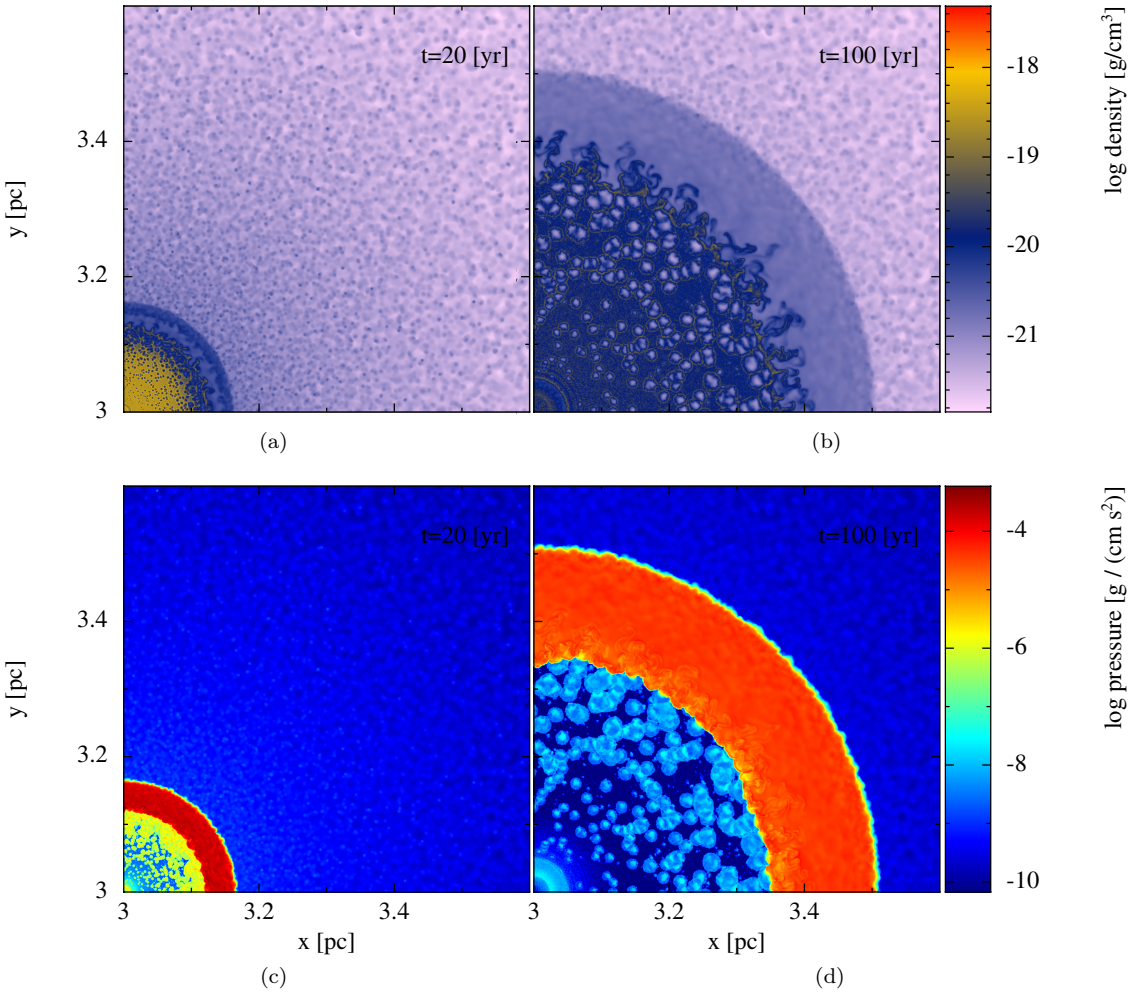

Figure 4.9: Same as Fig. 4.7 but for model RhoR2_MFM2D in Table 4.1.

For completeness, the results for model RhoR2_SPH2D in Table 4.1 are presented in Fig. 4.11 and Fig. 4.12. In this simulation, we employed the CD10 switch with $\alpha_{\mathrm{AC}} = 0.5$ for the treatment of discontinuities within the interaction region. Here the Richtmyer-Meshkov instabilities are less developed and smoothed out when observed at 100 yr as shown in Fig. 4.11b compared to models RhoR2_MFV2D and RhoR2_MFM2D. This is expected as instabilities are suppressed in SPH for large density contrasts (Read et al. 2010). The temperature and pressure of the shocked CSM and shocked ejecta is similar to the MFV and MFM case. As shown in Fig 4.12d, the maximum recorded velocity of the shocked CSM is $\sim 3000\,\mathrm{km/s}$, compared to $\sim 4000\,\mathrm{km/s}$ for the MFV and MFM models.

All models show that the cooler ejecta mixes with the shocked CSM resulting in cooler instabilities. A common feature that appears in all the 2D simulations is the prominent

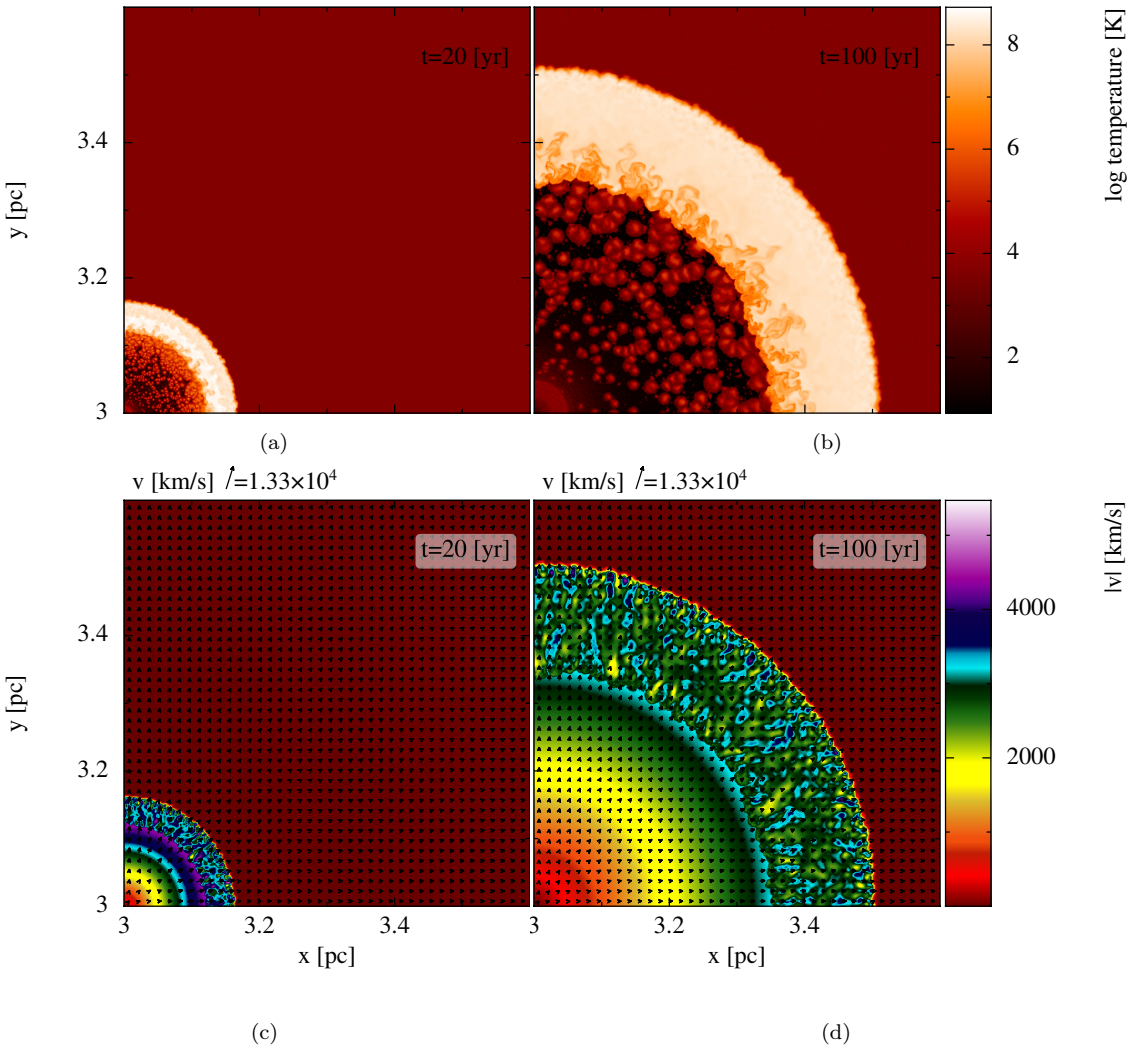

Figure 4.10: Same as Fig. 4.9 but for temperature [*a*, *b*] and velocity [*c*, *d*].

low density, hot granulation artefacts behind the reverse shock. As per private conversation with the primary code developer P. Hopkins, they might be seeded by our initial conditions when the inhomogeneity in the ejecta distribution lead to over–pressurized points. The other possibility is that it might be related to an `OPENMP` bug in `GIZMO` which is influencing all the numerical calculations to some extent. We conducted several tests (beyond the scope of this study) using the MFV method to investigate whether these artefacts are related to the numerical framework. We replaced the Riemann solver with a Kurganov-Tadmor flux limiter derived in Panuelos et al. (2020) which is said to be more diffusive, but smoother. We also tested the slope limiters by using a conservative slope-limiter designated for problems with sharp density contrasts in poor particle arrangements, as well as an aggressive slope-limiter to purposefully introduce numerical instability. Lastly, we enabled an energy-entropy switch as described in Hopkins (2015) implemented to deal with highly super-sonic flows in mesh-like methods. These approaches did not remove the granulation behind the reverse shock, we plan to resume this investigation in future work.

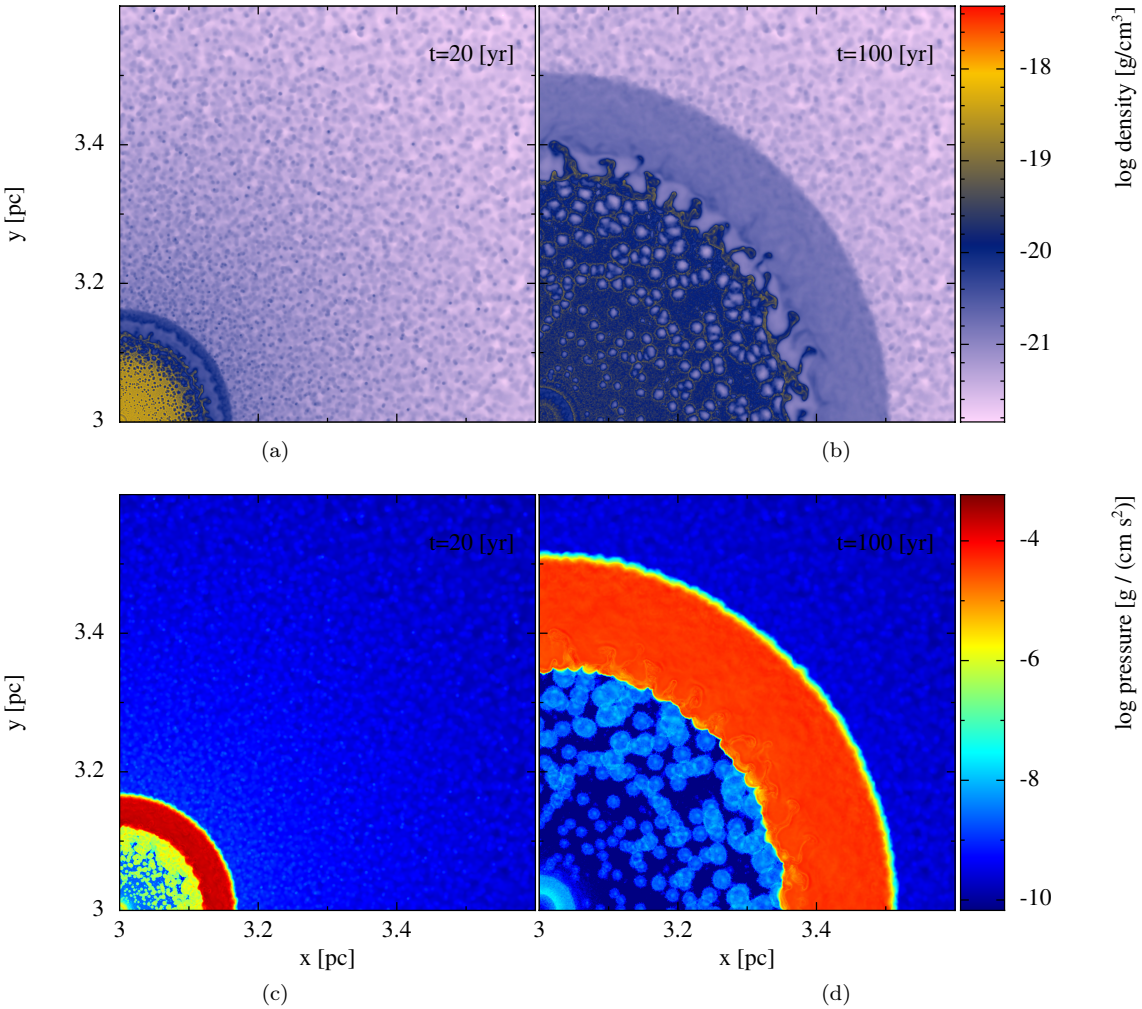

Figure 4.11: Same as Fig. 4.7 but for model RhoR2_SPH2D in Table 4.1.

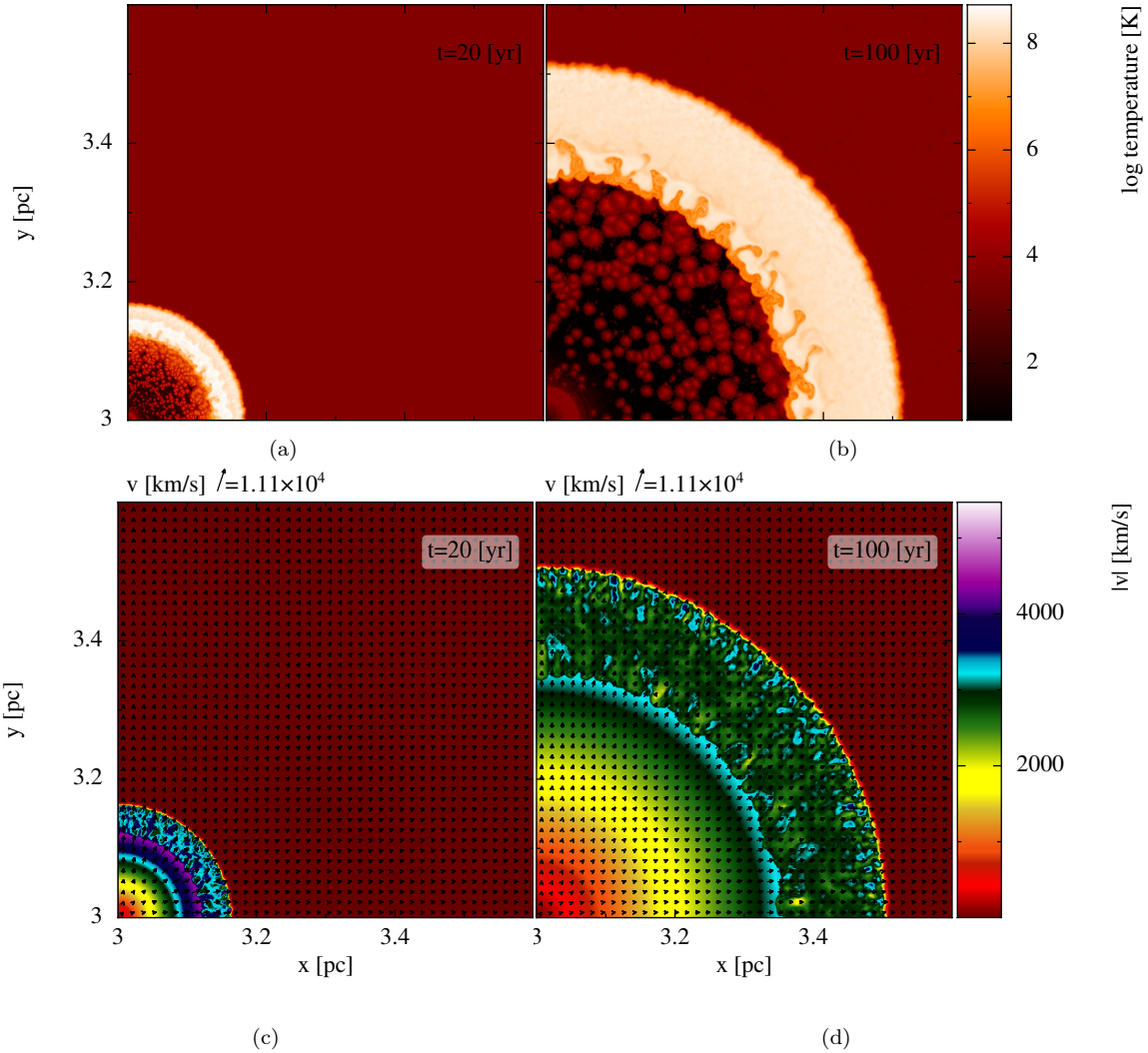

Figure 4.12: Same as Fig. 4.11 but for temperature $[a,\ b]$ and velocity $[c,\ d]$.

4.3 3D hydrodynamic simulations

We carried out 3D simulations of the SN ejecta interacting with $\rho-\mathrm{R2}$ and an $\rho-\mathrm{TO}$ CSM density distribution (see section 4.1.2). All simulations involved $N_\mathrm{p} = 11\,885\,257$ particles, that is $N_\mathrm{p} = 2\,012\,160$ particles for the ejecta and $N_\mathrm{p} = 9\,873\,097$ for the CSM. For the $\rho-\mathrm{R2}$ and $\rho-\mathrm{TO}$ models, the simulation box spans $0 \leq x, y, z \leq 6\,\mathrm{pc}$ and $2.5 \leq x, y, z \leq 3.5\,\mathrm{pc}$, respectively, with the point $x, y, z = (3, 3, 3)\,\mathrm{pc}$ taken as the reference centre. We used the MFV, MFM and SPH methods with a cubic-spline kernel and $N_\mathrm{NGB} = 57$ in order to investigate the development of discontinuities and instabilities in the interaction region as well as follow their hydrodynamic evolution from early-times (20 yr) to late-times (100 yr).

4.3.1 Ejecta interacting with a $\rho - \mathrm{R2}$ density CSM

The 3D simulations of SN ejecta interacting with a $\rho - \mathrm{R2}$ CSM profile showed the same general features as those in 2D. The interaction region is enclosed by the reverse and forward shock in which the former act as an interface between the free flowing ejecta and shocked ejecta, and the later is a boundary between the shocked CSM and the unperturbed CSM radially streaming away from the progenitor. These features are carefully labelled in the radial profiles shown in Fig. 4.13. For all computed radial profiles, the radius of each particle is computed using the Euclidean distance from the centre point $x, y, z = (3, 3, 3)$ pc, hence extending outwards from zero, while the cross-section plots, centred at point $x, y, z = (3, 3, 3)$ pc, zoom into the first quadrant of the spherical blastwave in order to show the details of the interaction region.

The radial number density, radial pressure, radial temperature and radial velocity profiles for model RhoR2_MFV3D in Table 4.1 at $20, 40, 60, 80$ and 100 yr after the SN explosion are presented in Fig. 4.14 and Fig. 4.15. The corresponding cross-section plots are presented in Fig. 4.16 and Fig.4.17. The reverse and forward shock are marked by a double peak structure in the radial number density (Fig. 4.14a) and velocity (Fig. 4.15b) profiles at 20 yr. As the shell evolves to larger radii, it grows in volume and as a consequence, the contact discontinuity dissipates and efficiently mixes the shocked ejecta with the shocked CSM. This is shown by the purple line at 100 yr in Fig. 4.14a, when the interaction region is completely mixed. This behaviour also applies to the temperature (Fig. 4.15a) and pressure (Fig. 4.14b) profiles as the interaction region evolves from being narrow at 20 yr to being broad at 100 yr. The maximum temperature remains unchanged at $\sim 10^8$ K, while the pressure decreases with time within the shell due to volume expansion.

Similar to the 2D simulations in the previous section, the Richtmyer-Meshkov instabilities grow as the remnant ages. Whereas in the 2D case all Richtmyer-Meshkov instabilities tend to be approximately the same size, the 3D Richtmyer-Meshkov instabilities are much more complex with a combination of large bubbles and filaments as shown in Fig. 4.16b. For the 3D case, only 2D cross-section plots of the 3D data are shown, however, the radial plots are calculated by including the z-coordinate in the Euclidean distance calculation. The radius at which the density is largest varies from 0.56 pc in 2D to 0.60 pc in the 3D case at 100 yr. The unshocked CSM is radially expanding at a velocity of $20\,\mathrm{km\,s^{-1}}$ relative to the approaching forward shock, while the shocked CSM decelerates from a velocity of $\sim 3800\,\mathrm{km\,s^{-1}}$ at 20 yr to a velocity of $\sim 2500\,\mathrm{km\,s^{-1}}$ at 100 yr as shown in Fig. 4.17d. The shocked CSM material is hot enough to emit in the near ultraviolet.

The radial profiles resulting from model RhoR2_MFM3D in Table 4.1 are shown in Fig. 4.18 and Fig. 4.19, and are similar to model RhoR2_MFV3D results in terms of the physical morphology of the interaction region both at 20 yr and 100 yr. However, while the reverse and forward shock are clearly defined, the contact discontinuity interface is significantly smoothed

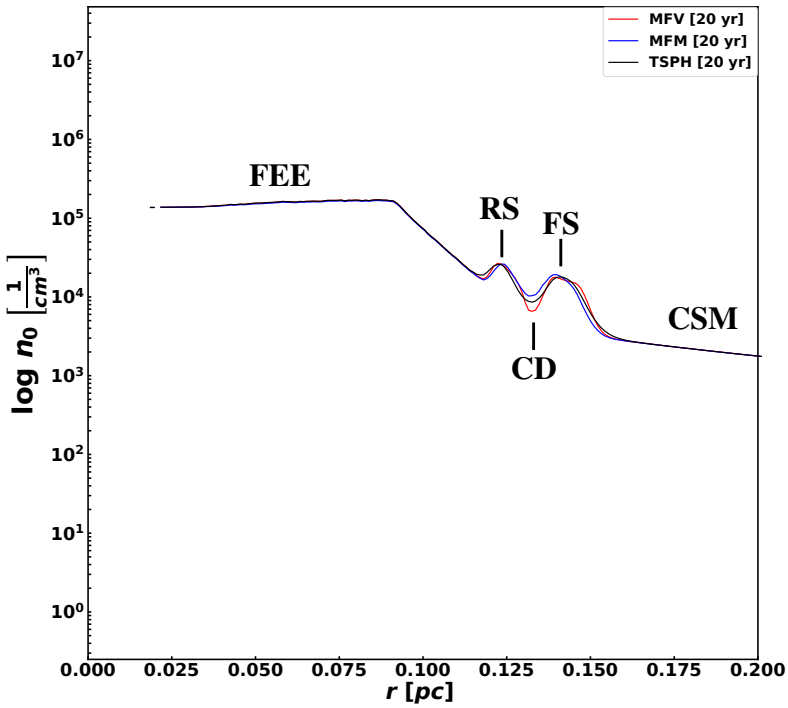

(a)

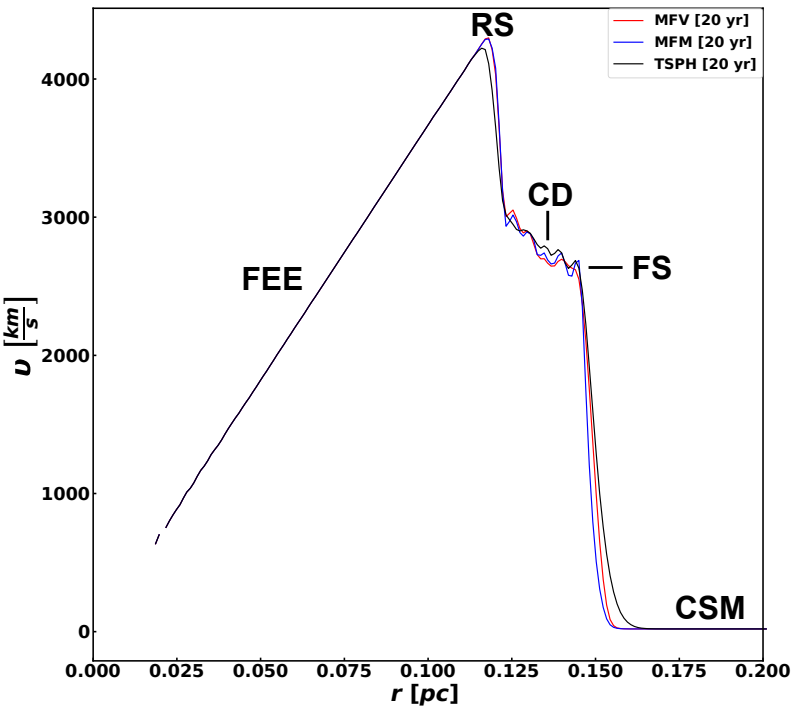

(b)

Figure 4.13: Comparison of radial number density [a] and velocity [b] plots for all methods at 20 yr. The data is azimuthally averaged into 5000 radial bins. The distinct regions of the remnant are as follows; FEE-free expanding ejecta, RS-reverse shock, CD-contact discontinuity, FS-forward shock, CSM-circumstellar medium.

out compared to the MFV simulation as shown Fig. 4.18a. This is further highlighted in the 3D simulations of $\rho - \mathrm{R2}$ (Fig. 4.13) where the MFV method shows more pronounced instabilities compared to the suppressed instabilities of the MFM method. The evolution of the flow from 20 yr to 100 yr is characteristic of the typical expansion of the remnant which adiabatically cools as the pressure decreases from $\sim 10^{-3}\,\mathrm{g\,cm^{-1}\,s^{-2}}$ to $\sim 10^{-4}\,\mathrm{g\,cm^{-1}\,s^{-2}}$ while the temperature of the shocked CSM barely changes as shown in Fig. 4.18b and Fig. 4.19a.

There is no significant difference between the maximum density and maximum temperature recorded in the instability bubbles for models RhoR2_MFV3D and RhoR2_MFM3D. The corresponding cross-section plots for model RhoR2_MFM3D are presented in Fig. 4.20 and Fig. 4.21. As previously observed with the MFV simulations, the growth of instabilities are much more complex in 3D as shown in Fig. 4.20b with large bubble-like structures, and the maximum density of these bubbles and filaments changes from $\rho \sim 10^{-19}\,\mathrm{g\,cm^{-3}}$ in the 2D case, to $\rho \sim 10^{-20}\,\mathrm{g\,cm^{-3}}$ in the 3D case. This is ten times lower than the density in the 2D case. Analysis of the radial velocity profile in Fig. 4.19b and velocity field in Fig. 4.21d affirm that the deceleration of the remnant is similar to that of model RhoR2_MFV3D.

Radial profiles for model RhoR2_SPH3D in Table 4.1 are presented in Fig. 4.22 and Fig. 4.23. Since this is an SPH simulation, we employed the CD10 switch with $\alpha_{\mathrm{AC}} = 0.5$ for the treatment of discontinuities. The corresponding cross-sections are shown in Fig. 4.24 and Fig. 4.25. An obvious outcome of SPH is that the contact discontinuity, the forward and reverse shock are significantly smoothed out when compared to model RhoR2_MFV3D, but the difference is not very large when compared to model RhoR2_MFM3D (see Fig. 4.13). Despite this, the characteristic morphology of a SN remnant is still visible in the radial density (Fig. 4.22a) profile, however, the radial velocity (Fig. 4.23b) profile loses the structure of the contact discontinuity completely and is replaced by the oscillatory behaviour in the shocked CSM. This post-shock ringing is a well known artefact of the α_{AV} prescription employed in SPH as discussed in Chapter 3.

As shown in Fig. 4.24b, the growth of instabilities are suppressed at late times. This results in a very smooth contact discontinuity and as a consequence, the pressure and temperature builds up on top of the reverse shock, leading to a sudden jump in pressure and temperature immediately behind the reverse shock as shown in Fig. 4.22b and Fig. 4.23a. Although the 2D simulations showed that the instabilities are suppressed, this effect is worse in 3D, thus SPH is not ideal for modeling the interaction region. For MFV and MFM methods, the interaction shell develops instabilities quickly and they become more complex due to the changes in density distribution. In all methods, moving from 2D to 3D results in the largest densities recorded at the instabilities varying by an order of magnitude from $10^{-19}\,\mathrm{g\,cm^{-3}}$ in 2D to $10^{-20}\,\mathrm{g\,cm^{-3}}$ in the 3D case. In the 2D simulation, the matter is spread out along a single axis, which means that density will decrease with radius of the instability. In the 3D simulation, the matter is spread out over surface area, which means that the local density

will decrease with the square of the radius.

4.3.2 Ejecta interacting with a $\rho - \mathrm{TO}$ CSM

We modelled the SN ejecta interacting with two different $\rho - \mathrm{TO}$ CSM profiles. The two axisymmetric torus profiles we modelled for the purposes of this study are; one with a steep density drop ($\varepsilon = 0.03$) and the other with a smooth density drop ($\varepsilon = 0.3$) from the torus to the bipolar cavity. We used the MFV, MFM and SPH methods with a cubic-spline kernel and $N_{\mathrm{NGB}} = 57$ to carry out these simulations. The simulation domain spans $2.5 < x, y, z < 3.5\,\mathrm{pc}$ with a total of $N_{\mathrm{p}} = 11113130$ and $N_{\mathrm{p}} = 11109117$ particles for a torus with a smooth and steep density drop, respectively. Due to the axisymmetric geometry of the remnant, we use radial line profiles instead of the azimuthally averaged radial profiles to quantitatively inspect the remnant's physical attributes. We used a data analysis software toolkit, `yt` (available at `http://yt.enzotools.org/`), developed by Turk et al. (2010). Using the `yt.LineBuffer` routine, we defined a starting and ending point in which we sampled 2^{16} data points and subsequently generated field (ρ, ϵ, υ and P) values along the sampling path.

Torus with a steep density drop

Cross-section slices for model RhoTO$f03\varepsilon003$_MFV3D in Table 4.1 are presented in Fig. 4.26 and 4.27. Although the evolution appears spherical at 20 yr, the forward shock progresses faster in the low density cavity compared to the torus. This is evident in Fig. 4.26b, as the remnant evolves into a prolate shape at 100 yr. The Richtmyer-Meshkov instabilities are also more pronounced at 100 years, and likewise they appear denser and cooler than the shocked CSM material ahead of them. Fig. 4.27d demonstrates the prolate geometry of the remnant as the shocked ejecta in the cavity is moving at velocities $> 1500\,\mathrm{km\,s^{-1}}$, while the shocked ejecta in the torus is moving at velocities $< 1500\,\mathrm{km\,s^{-1}}$.

Radial line profiles for all quantities in model RhoTO$f03\varepsilon003$_MFV3D are presented in Fig. 4.28 and Fig. 4.29 for different angles taken with respect to the xy-plane. The sharp vertical spikes at 0.01pc are the slowest moving shells in the freely expanding ejecta, which did not have sufficient velocity to move with the rest of the remnant. At 100 yr, the radial density and velocity line profiles (Fig 4.28a and Fig 4.29b) taken along the xy-plane ($\Theta = 0°$) and the z-axis ($\Theta = 90°$) shows characteristics of the reverse and forward shock separated by the contact discontinuity in the cavity and the torus, respectively. Their radial line profile along $\Theta = 60°$ shows more variation in density at radius 0.25 pc, indicative of the more pronounced instabilities and mixing. These features are observed across all quantities except for pressure, which appears to be smooth at the interaction region. Due to the sharp density contrast between the torus and the bipolar cavity with respect to the polar angle, there is no instability roll formed along the path defined by the half-opening angle.

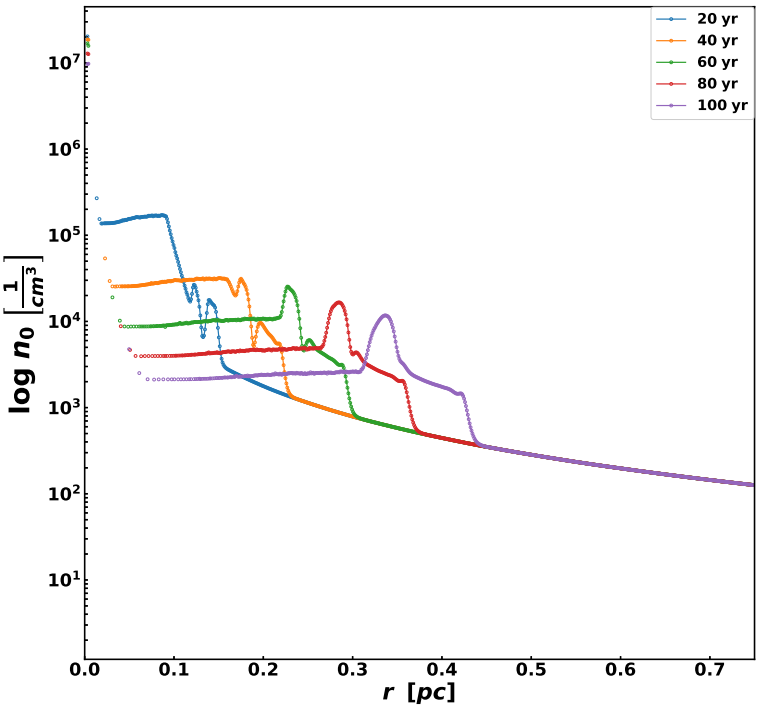

(a)

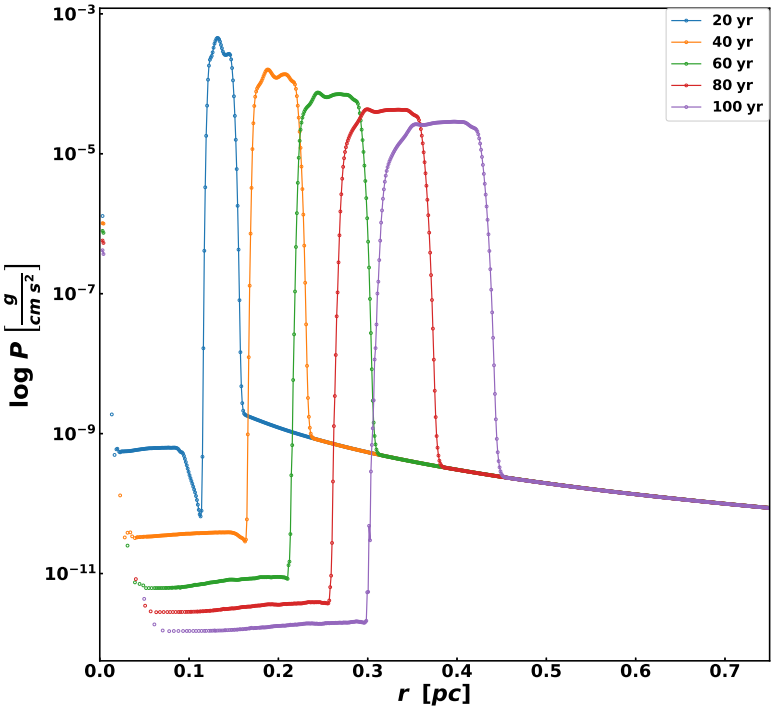

(b)

Figure 4.14: Radial density *(a)* and pressure *(b)* profiles for model RhoR2_MFV3D in Table 4.1 showing the evolution of the interaction region at various times of the Sedov-Taylor phase. The data presented here was azimuthally averaged into 5000 radial bins.

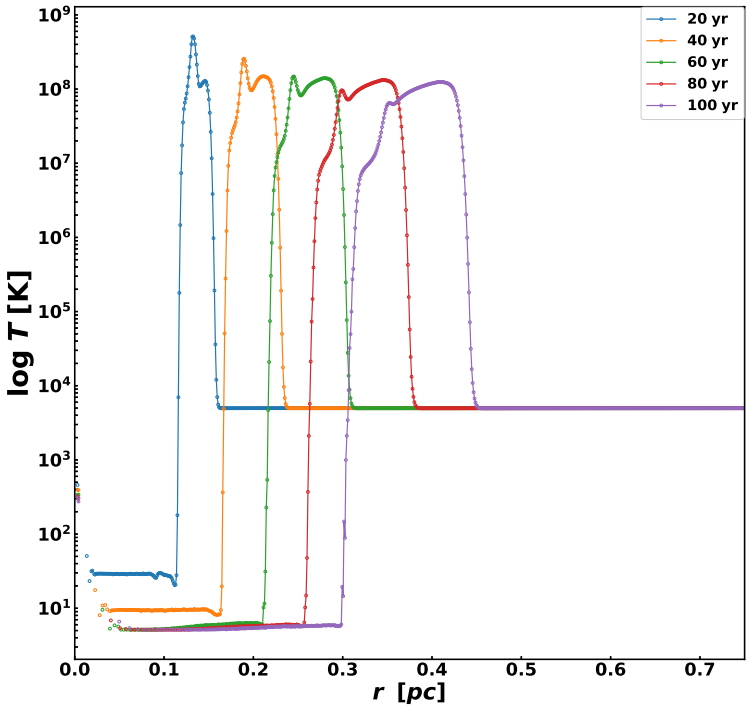

(a)

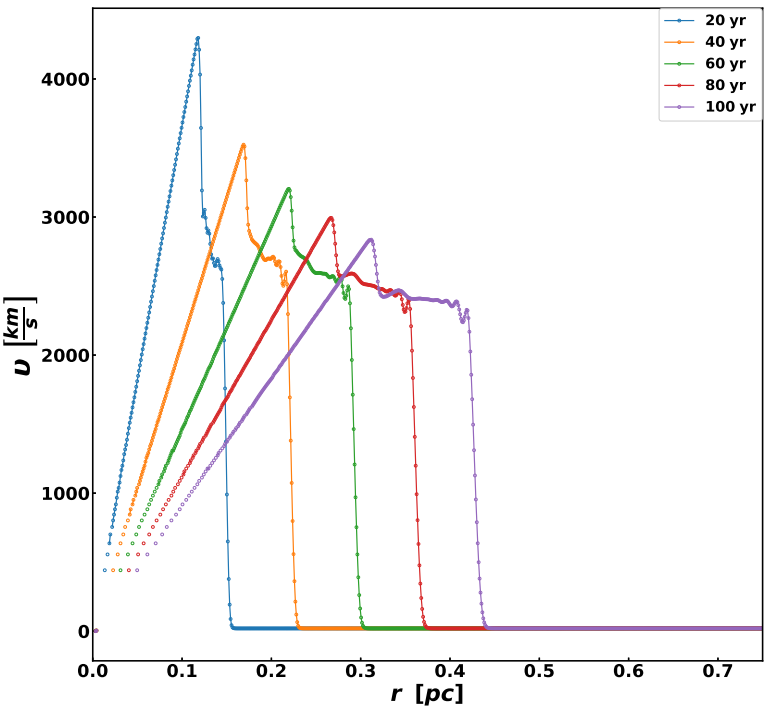

(b)

Figure 4.15: Same as in Fig 4.14 but for temperature (a) and velocity (b).

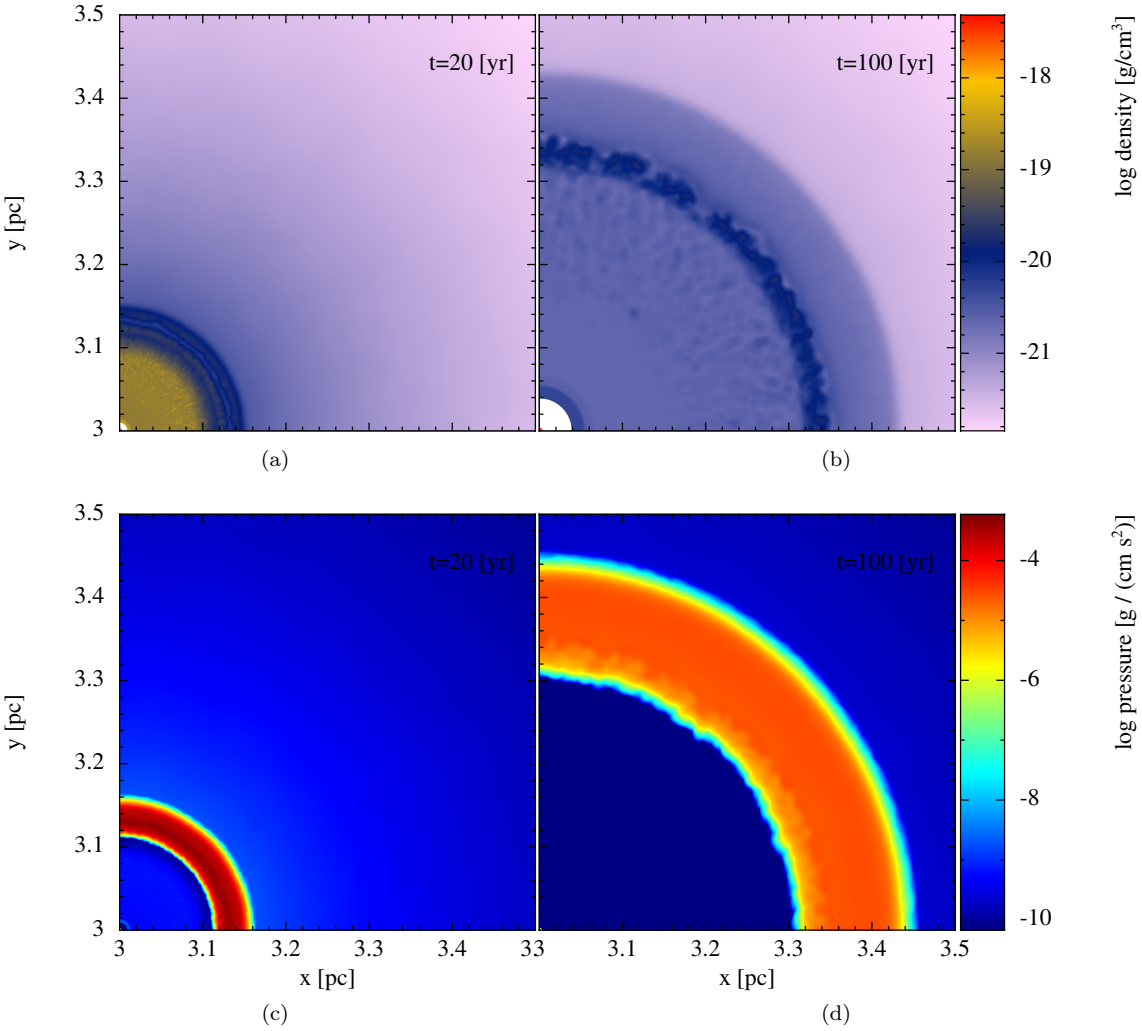

Figure 4.16: Cross-section slices for model RhoR2_MFV3D in Table 4.1 taken across the z-axis for density at *(a)* 20 yr and *(b)* 100 yr, and pressure at *(c)* 20 yr and *(d)* 100 yr.

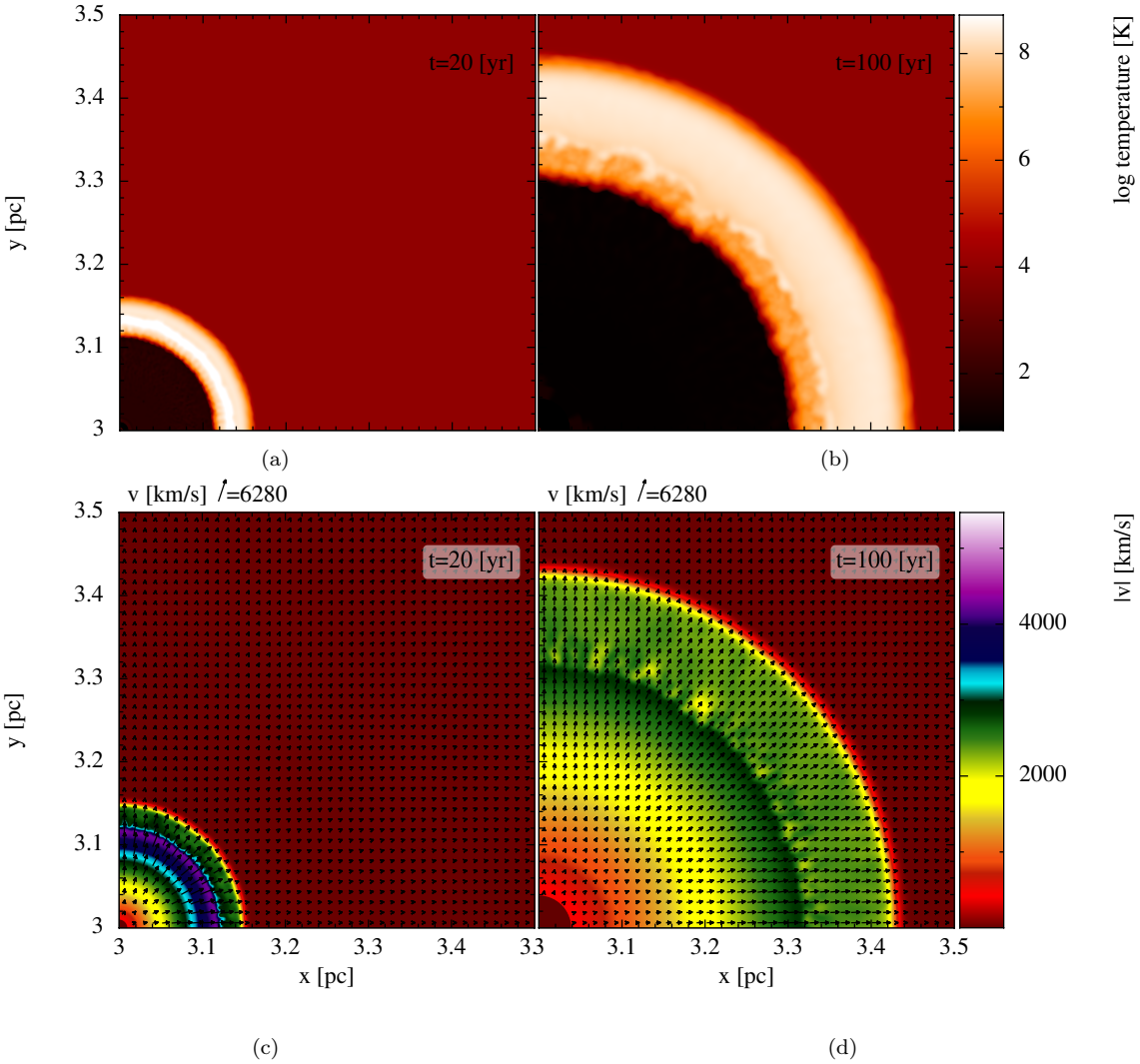

Figure 4.17: Same as in Fig 4.16 but for temperature (*a*, *b*) and velocity (*c*, *d*).

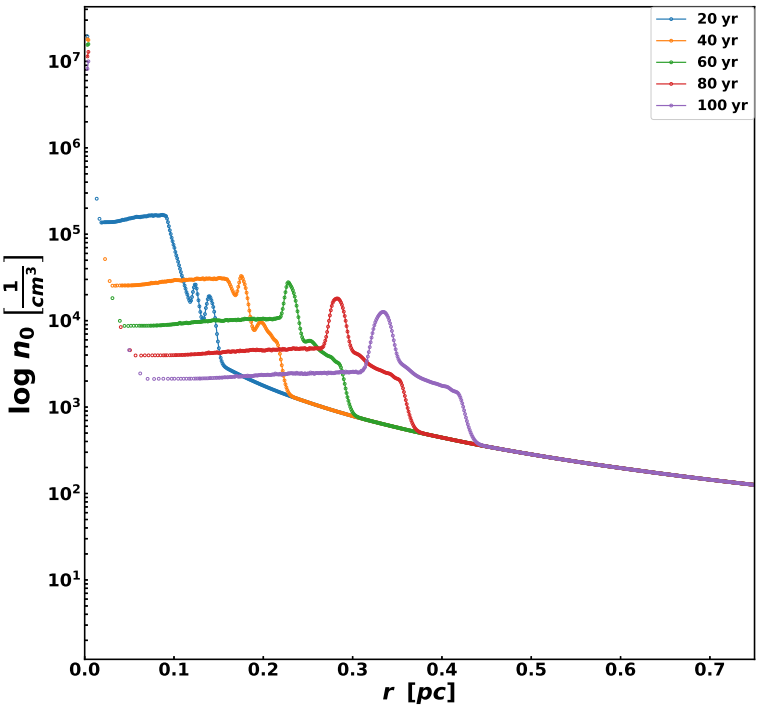

(a)

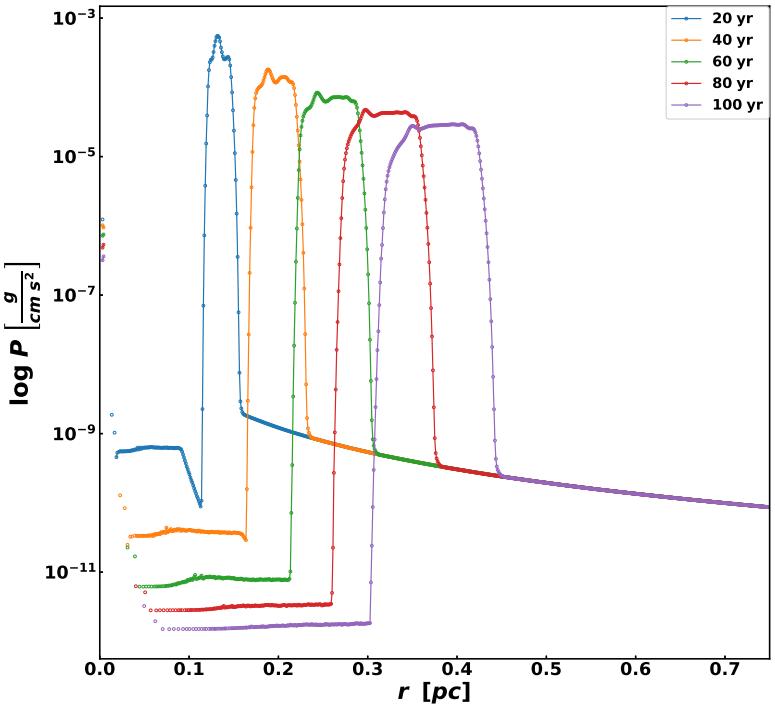

(b)

Figure 4.18: Radial density *(a)* and pressure *(b)* profiles for model RhoR2_MFM3D in Table 4.1 showing the evolution of the interaction region at various times of the Sedov-Taylor phase. The data presented here was azimuthally averaged into 5000 radial bins.

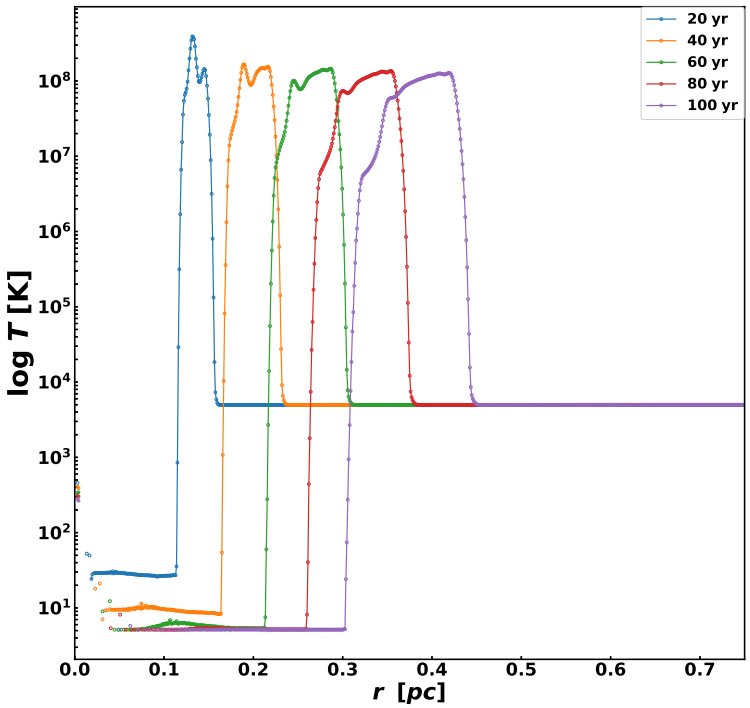

(a)

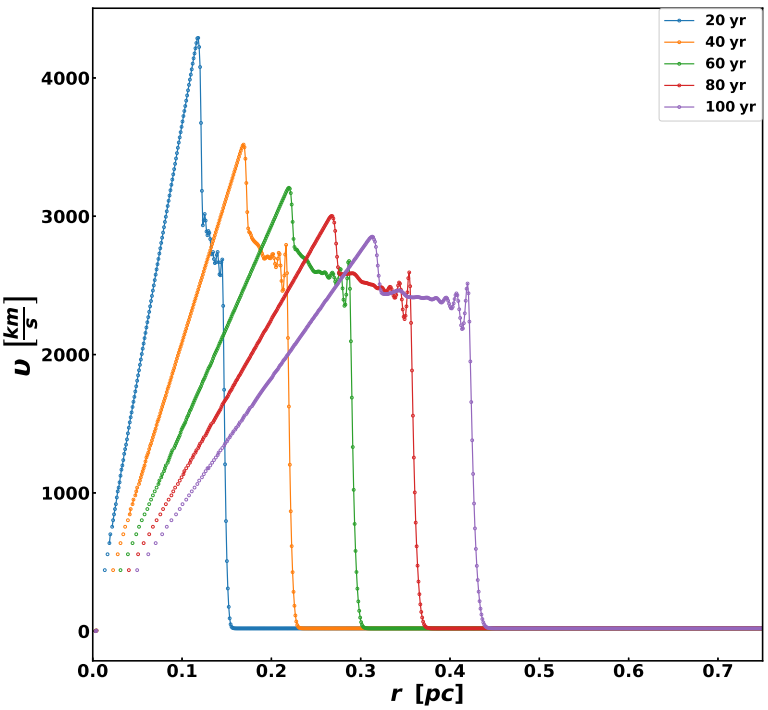

(b)

Figure 4.19: Same as in Fig 4.18 but for temperature (a) and velocity (b).

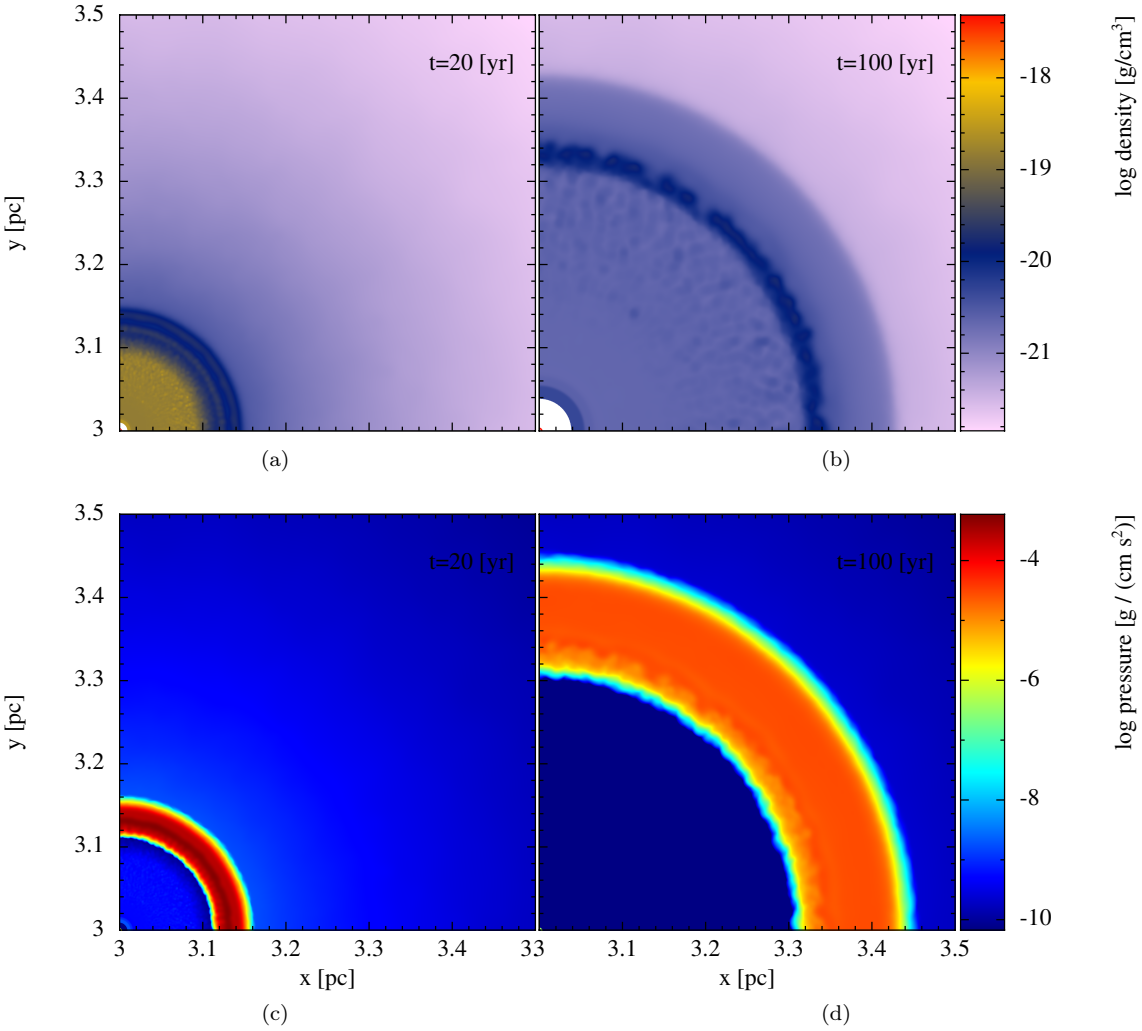

Figure 4.20: Cross-section slices for model RhoR2_MFM3D in Table 4.1 taken across the z-axis for density at *(a)* 20 yr and *(b)* 100 yr, and pressure at *(c)* 20 yr and *(d)* 100 yr.

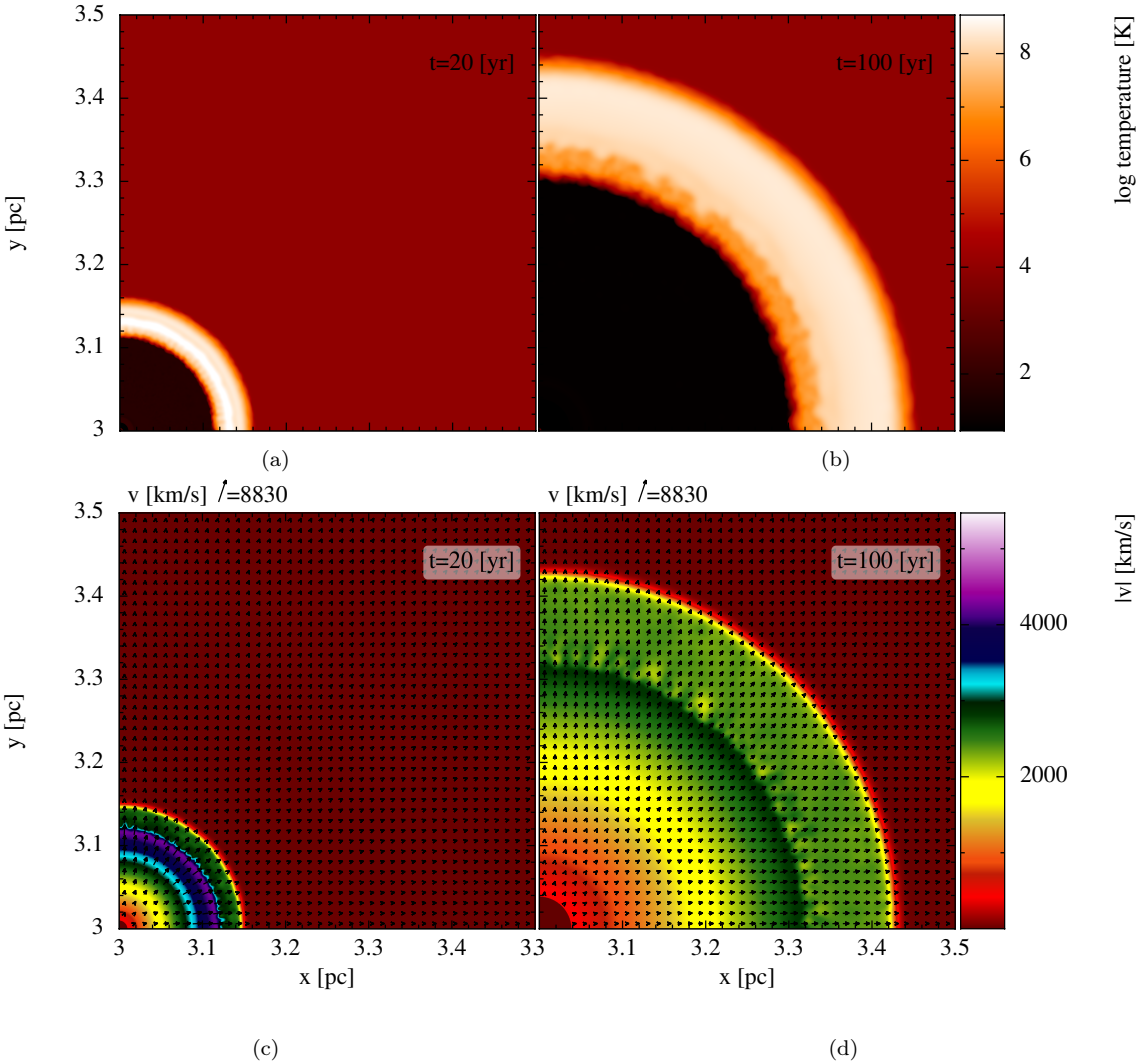

Figure 4.21: Same caption as in Fig. 4.20 but for temperature (*a*, *b*) and velocity (*c*, *d*).

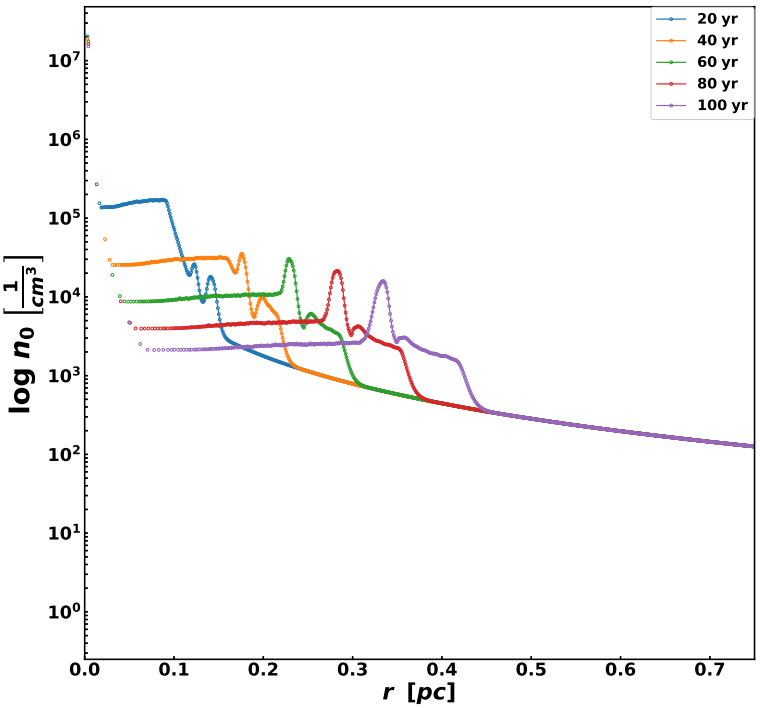

(a)

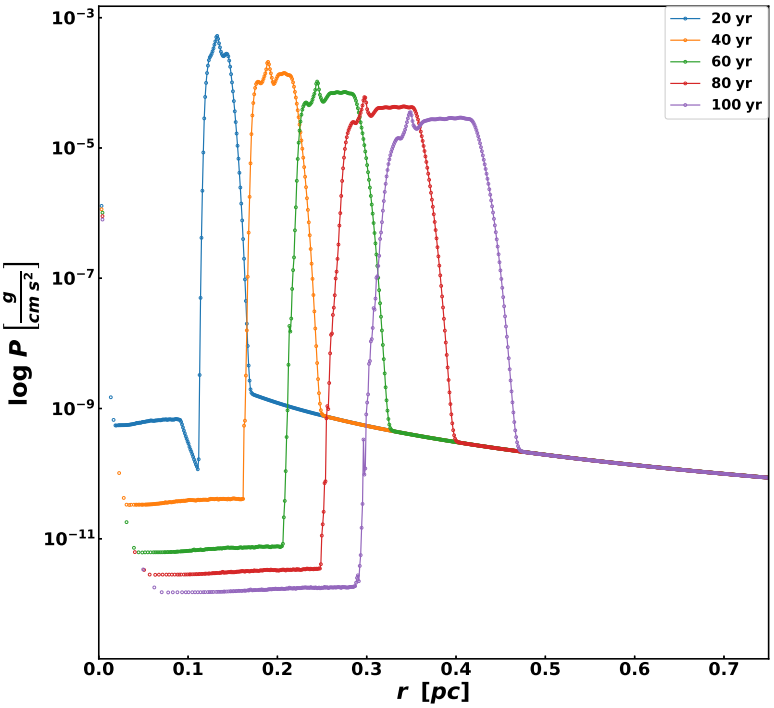

(b)

Figure 4.22: Radial density *(a)* and pressure *(b)* profiles for model RhoR2_SPH3D in Table 4.1 showing the evolution of the interaction region at various times of the Sedov-Taylor phase. The data presented here was azimuthally averaged into 5000 radial bins.

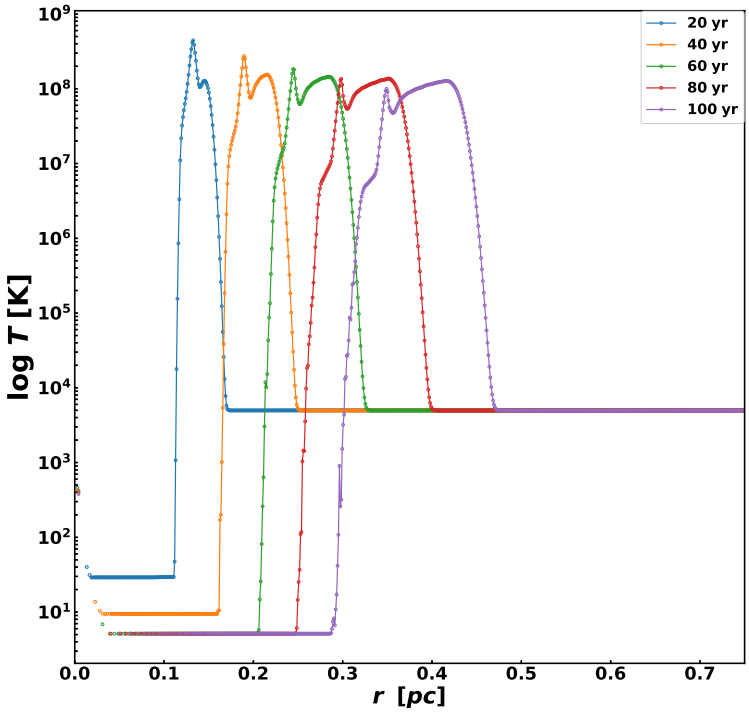

(a)

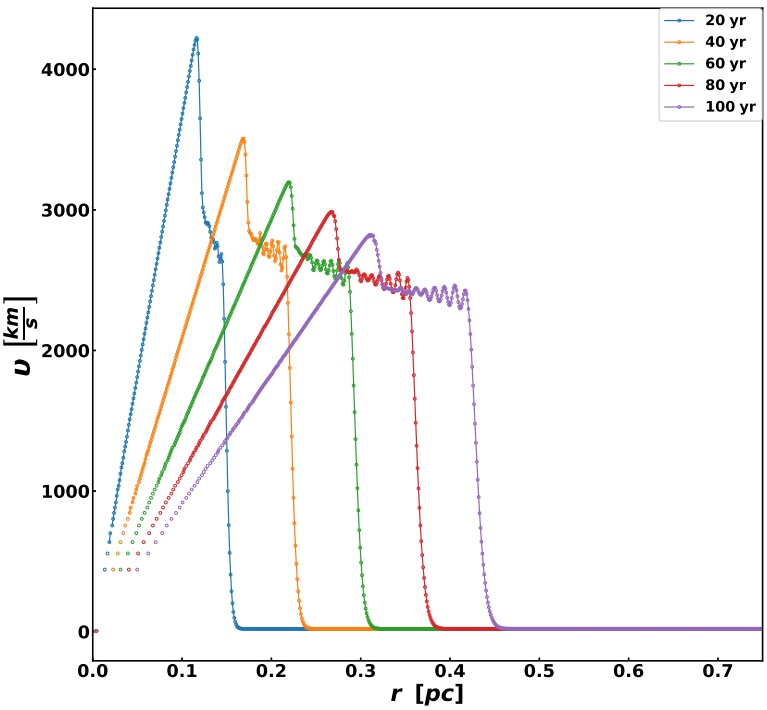

(b)

Figure 4.23: Same as in Fig 4.22 but for temperature (a) and velocity (b).

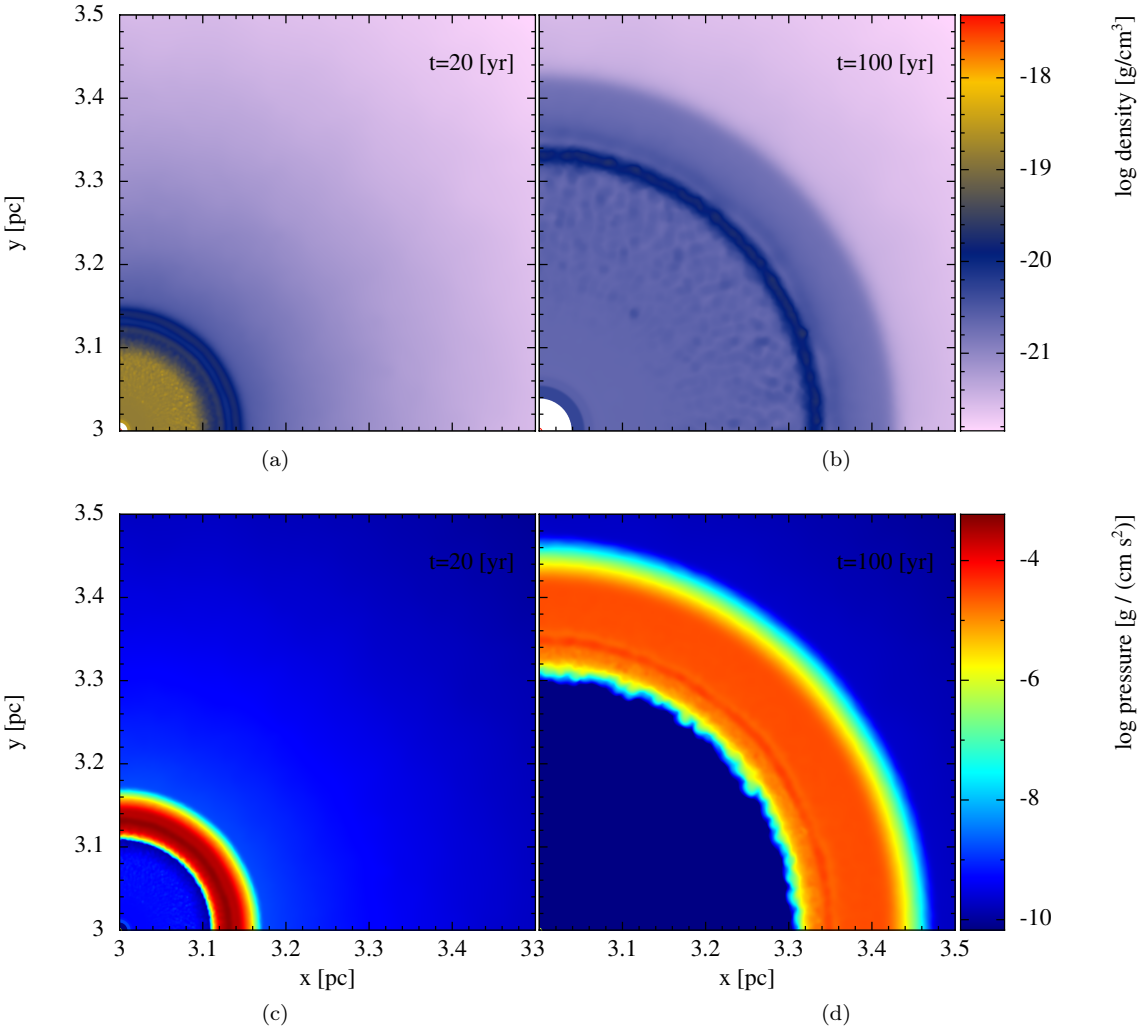

Figure 4.24: Cross-section slices for model RhoR2_SPH3D in Table 4.1 taken across the z-axis for density at *(a)* 20 yr and *(b)* 100 yr, and pressure at *(c)* 20 yr and *(d)* 100 yr.

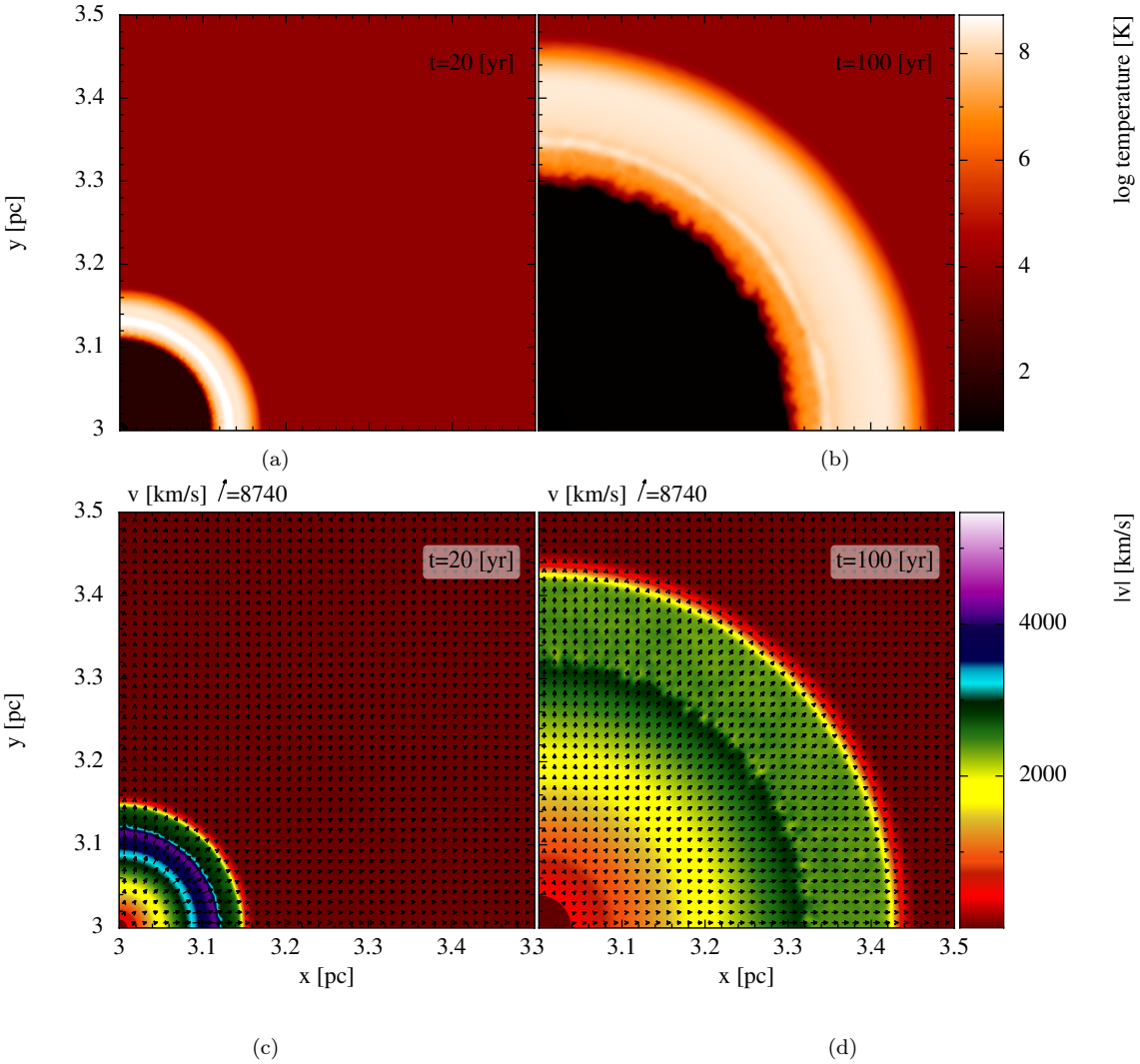

Figure 4.25: Same as in Fig. 4.24 but for temperature (*a*, *b*) and velocity (*c*, *d*).

The cross-section slice plots for model RhoTOf03ε003_MFM3D in Table 4.1 are shown in Fig. 4.30 and Fig. 4.31 and corresponding line profiles are plotted in Fig. 4.32 and Fig. 4.33. The radial line profiles in Fig. 4.32a and Fig. 4.33b show similar features of the interaction region as those seen in the MFV method. However, the instabilities are less pronounced, even along the $\Theta = 60°$ radial path. The pressure profile appears smooth, without any evidence of the presence of a contact discontinuity, and the temperature profile shows a small temperature variation at a radius of 0.25 pc like in model RhoTOf03ε003_MFV3D.

Lastly, results for model RhoTOf03ε003_SPH3D are presented in Fig. 4.34 and Fig. 4.35 and are accompanied by their radial line plots shown in Fig. 4.36 and Fig. 4.37. As expected from the SPH method, the shocks are smoothed out and instabilities are suppressed at late times. The suppression of these instabilities is further emphasized in the density line profile with a large density peak in the reverse shock at all angles. This is the only model that shows variation in pressure at a contact discontinuity as seen in Fig. 4.36b. The high temperature peak seen in Fig. 4.37a coincides with the radius of the contact discontinuity. The radial velocity of the shocked CSM in the dense torus and the bipolar cavity in all models (RhoTOf03ε003_MFV3D, RhoTOf03ε003_MFM3D and RhoTOf03ε003_SPH3D) is roughly the same $\sim 1500\,\mathrm{km\,s^{-1}}$ after 100 yr of the SN remnant's evolution, signifying the prolate geometry of remnant. These models have shown that the MFV method handles discontinuities and instabilities very well compared to the MFM and SPH method for the late-time SNR evolution.

Torus with a smooth density drop

Cross-section plots at 20 yr and 100yr for model RhoTOf03ε03_MFV3D in Table 4.1 are presented in Fig 4.38 and Fig 4.39. Due to the shallow density change from the torus to the bipolar cavity with respect to the polar angle, the prolate shape of the remnant forms early on as seen in Fig. 4.38a. In Fig. 4.38b, the instabilities are more pronounced, and an instability roll develops at the position where the dense torus interfaces with the nearly empty cavity. These instability rolls can also be seen in the temperature cross-section as the hot, shocked CSM gets enveloped by the cool, dense ejecta filaments (Fig. 4.39b). The density line profile along 60° reveals a significant drop in density at the contact discontinuity compared to other angles, signifying the very low density material in the instability roll. The shocked CSM in the cavity is moving at approximately $\sim 1800\,\mathrm{km\,s^{-1}}$ compared to less than $1500\,\mathrm{km\,s^{-1}}$ in the torus. Fig. 4.39c also shows that the instability rolls have the highest radial velocity compared to the rest of the remnant.

The corresponding line profiles are shown in Fig. 4.40 and Fig. 4.41 for all quantities at 100 yr. The sharp vertical spikes at 0.01 pc signifies a shell with insufficient initial velocity is still present in this simulation. In Fig. 4.40a, the line profile along the z-axis (green-line) reveals significantly lower densities than along the half-opening angle (orange-line) and the xy-plane (blue-line), as expected from the cavity of the torus. The evident features of shock

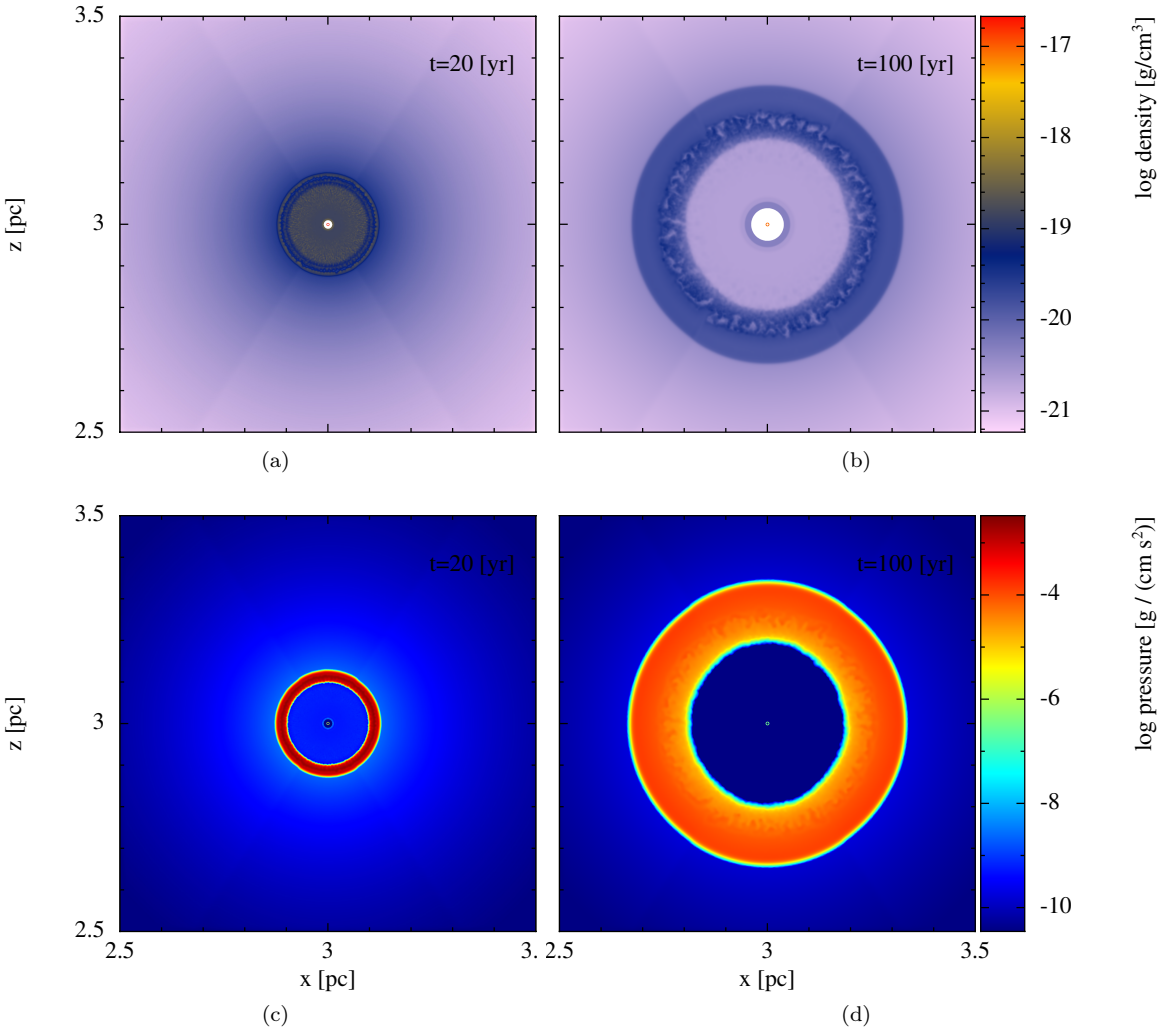

Figure 4.26: Cross-section slices for model RhoTOf03ε003_MFV3D in Tabel 4.1 taken across the y-axis for density at *(a)* 20 yr and *(b)* 100 yr, and pressure at *(c)* 20 yr and *(d)* 100 yr.

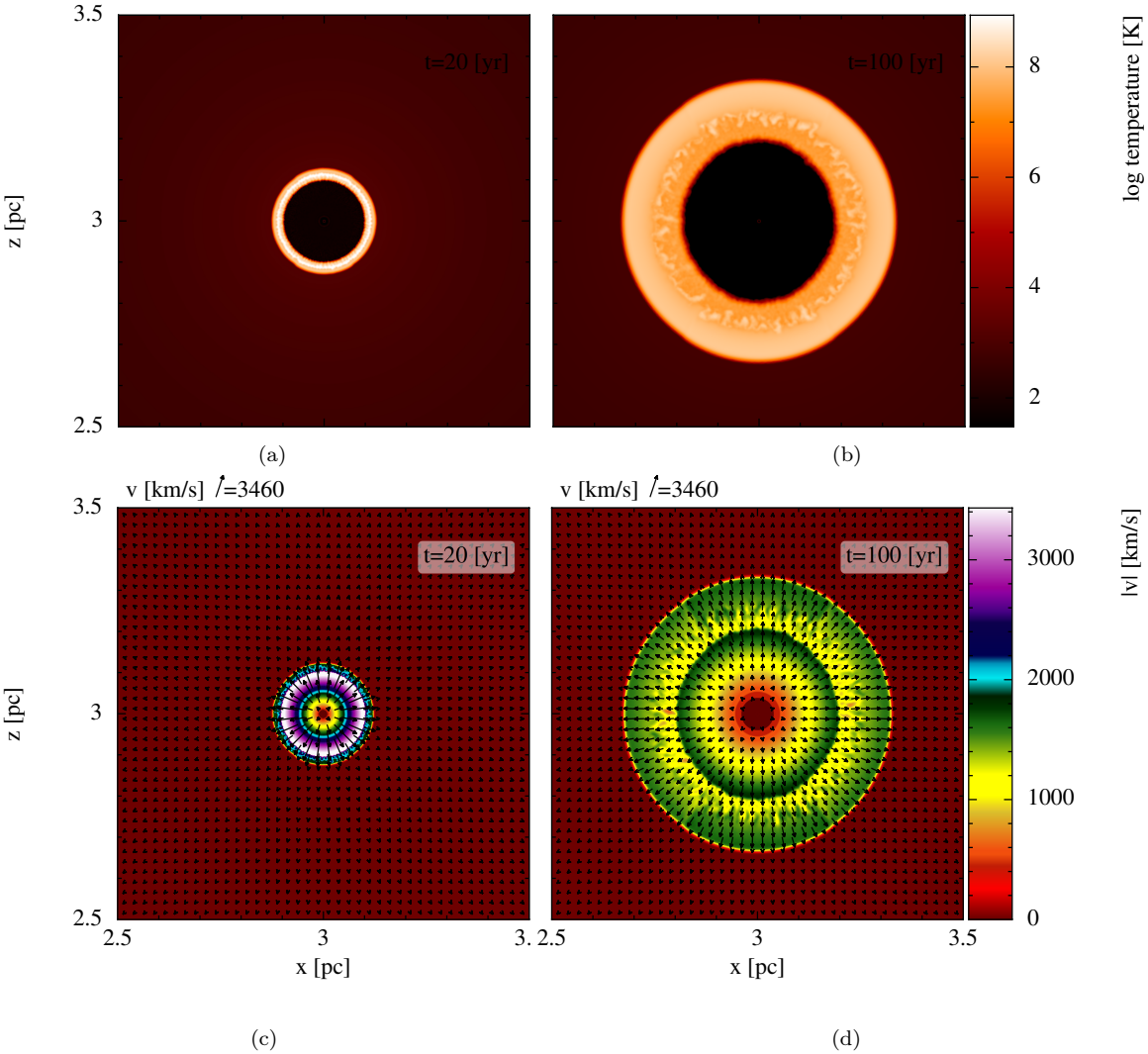

Figure 4.27: Same as in Fig. 4.26 but for temperature (*a*, *b*) and velocity (*c*, *d*).

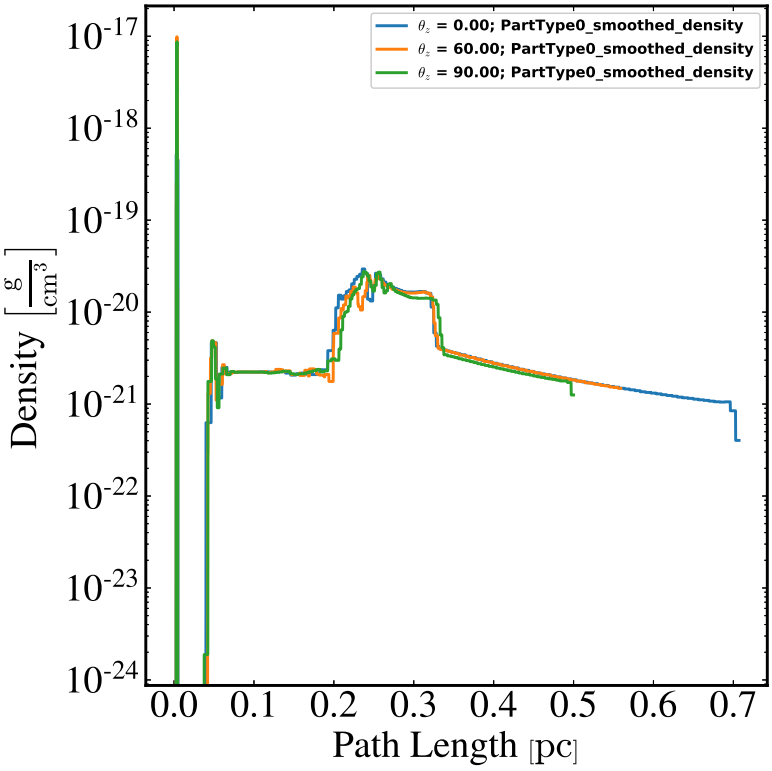

(a)

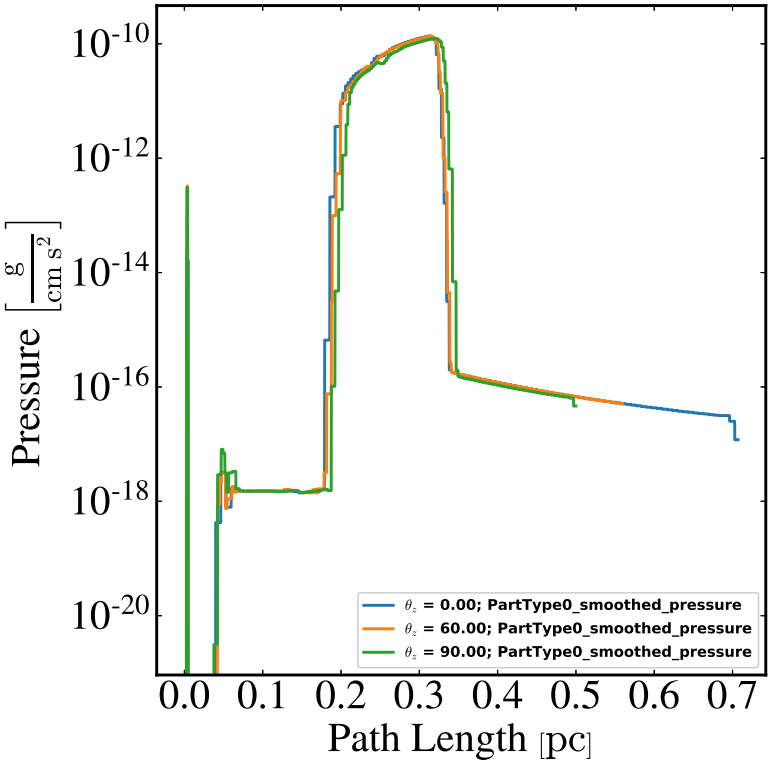

(b)

Figure 4.28: Radial line-plots for model RhoTOf03ε003_MFV3D in Table 4.1 measured at different angles for *(a)* density, and *(b)* pressure at 100 yr. $\Theta = 0°$ is along the xy-plane and $\Theta = 90°$ is along the z-axis.

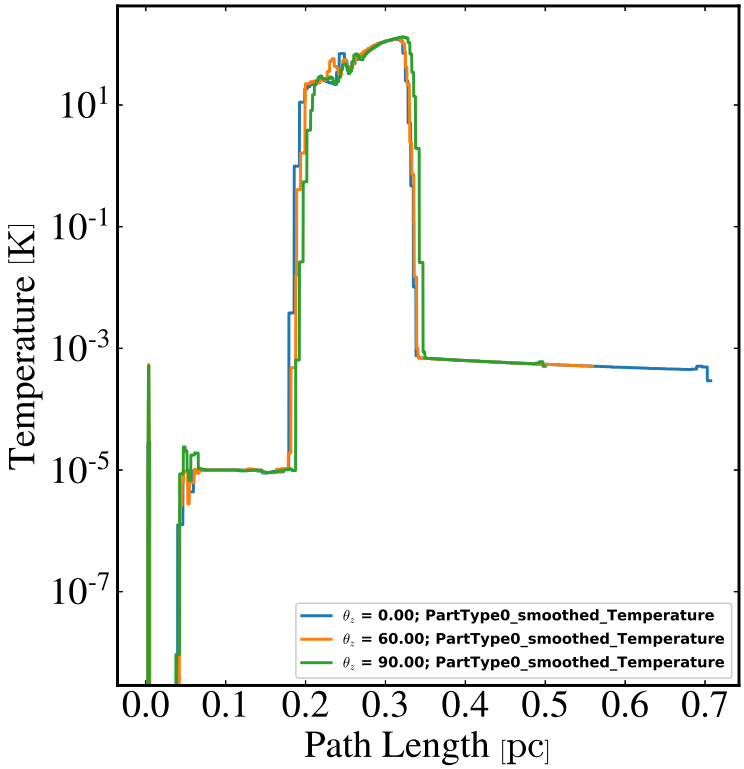

(a)

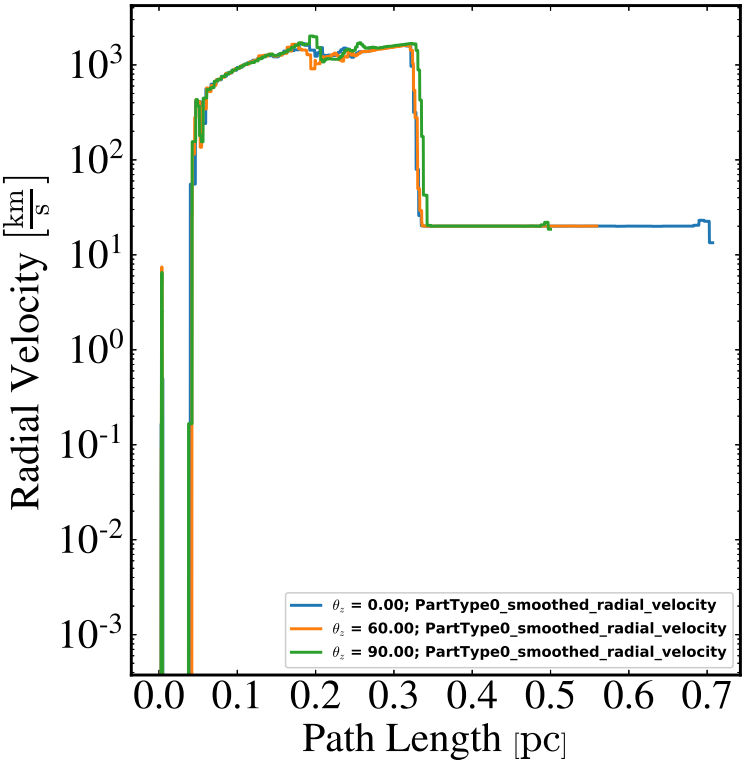

(b)

Figure 4.29: Same as in Fig. 4.28 but for temperature (a) and velocity (b).

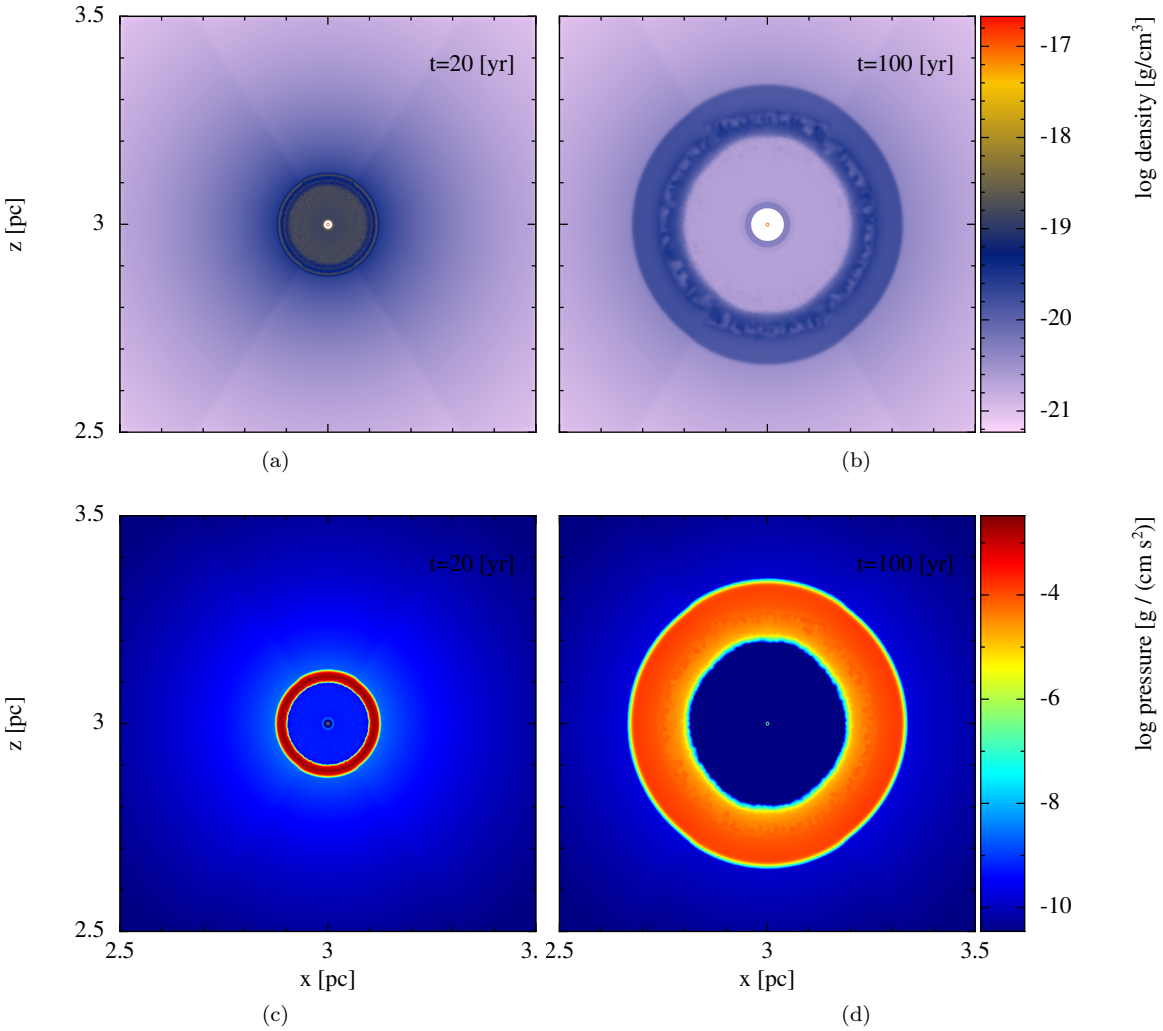

Figure 4.30: Cross-section slices for model RhoTOf03ε003_MFM3D in Table 4.1 taken across the y-axis for density at *(a)* 20 yr and *(b)* 100 yr, and pressure at *(c)* 20 yr and *(d)* 100 yr.

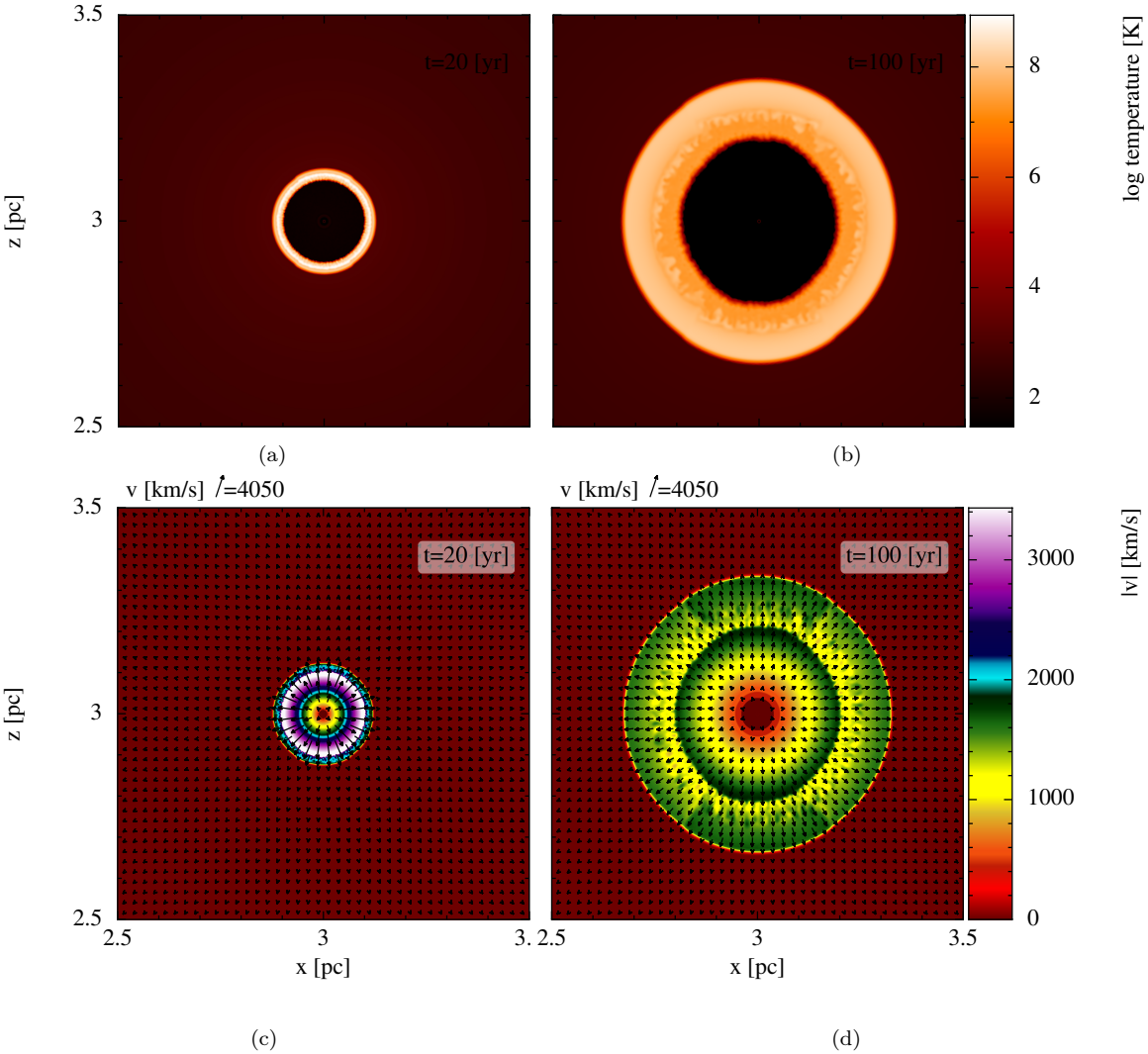

Figure 4.31: Same as in Fig. 4.30 but for temperature (*a*, *b*) and velocity (*c*, *d*).

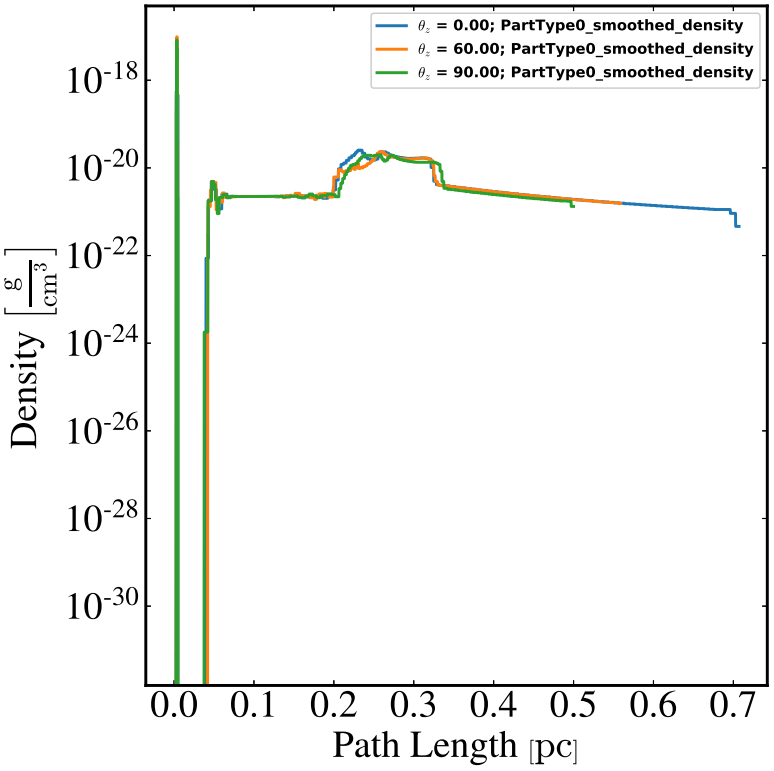

(a)

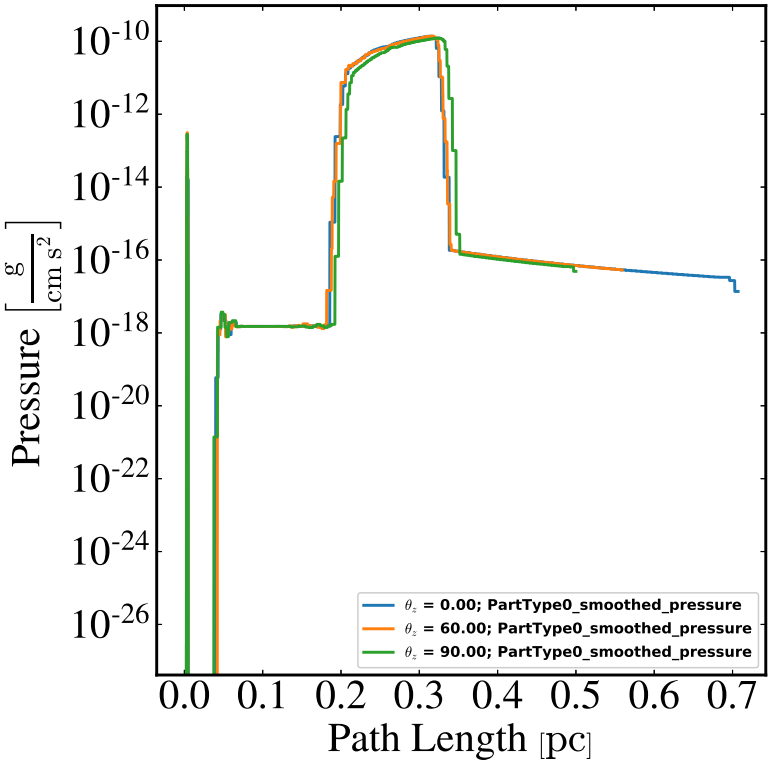

(b)

Figure 4.32: Radial line-plots for model RhoTOf03ε003_MFM3D in Table 4.1 measured at different angles for *(a)* density and *(b)* pressure at 100 yr. $\Theta = 0°$ is along the xy-plane and $\Theta = 90°$ is along the z-axis.

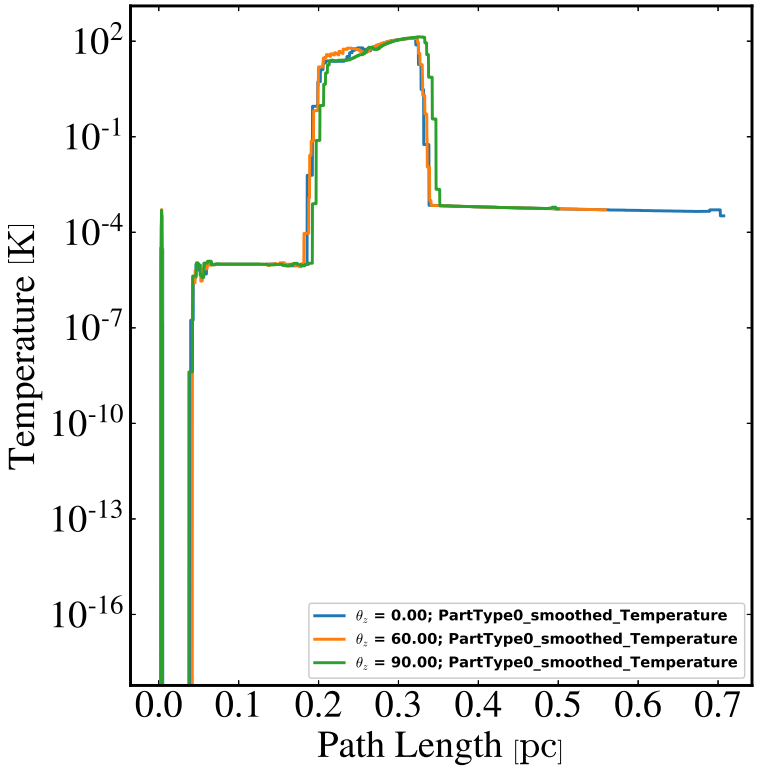

(a)

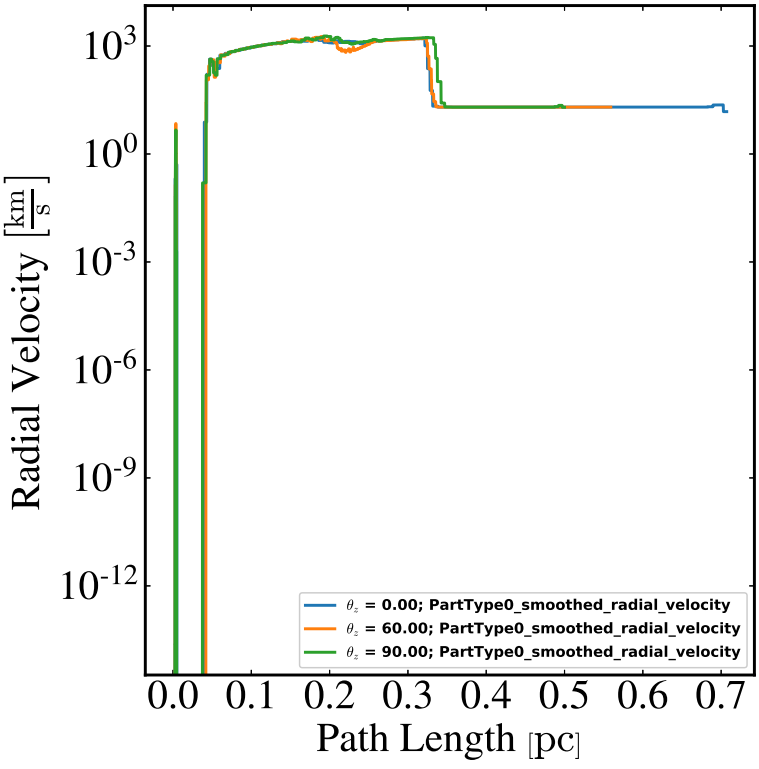

(b)

Figure 4.33: Same as in Fig. 4.32 but for temperature (a) and velocity (b).

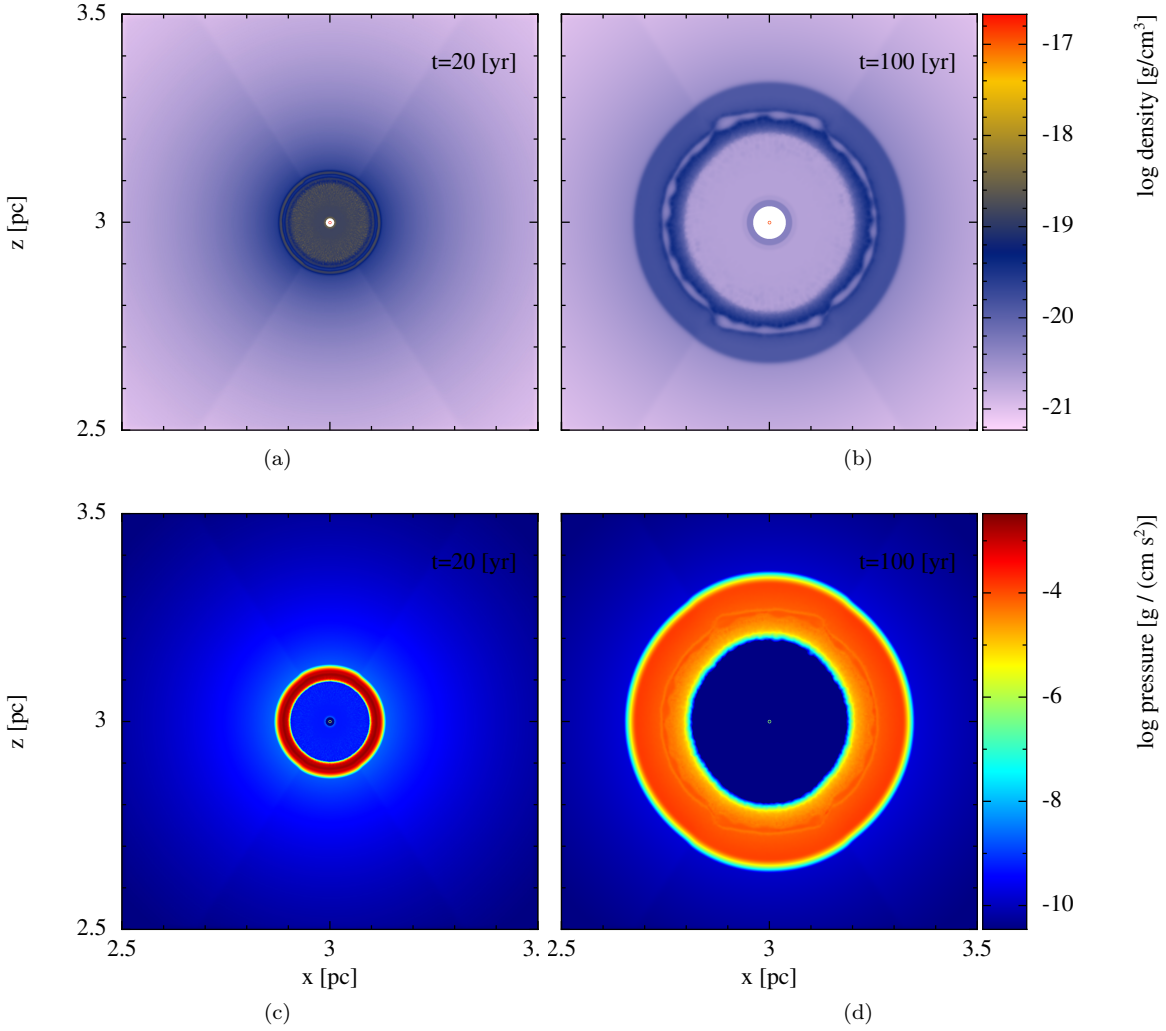

Figure 4.34: Cross-section slices for model RhoTOf03ε003_SPH3D in Table 4.1 taken across the y-axis for density at *(a)* 20 yr and *(b)* 100 yr, and pressure at *(c)* 20 yr and *(d)* 100 yr.

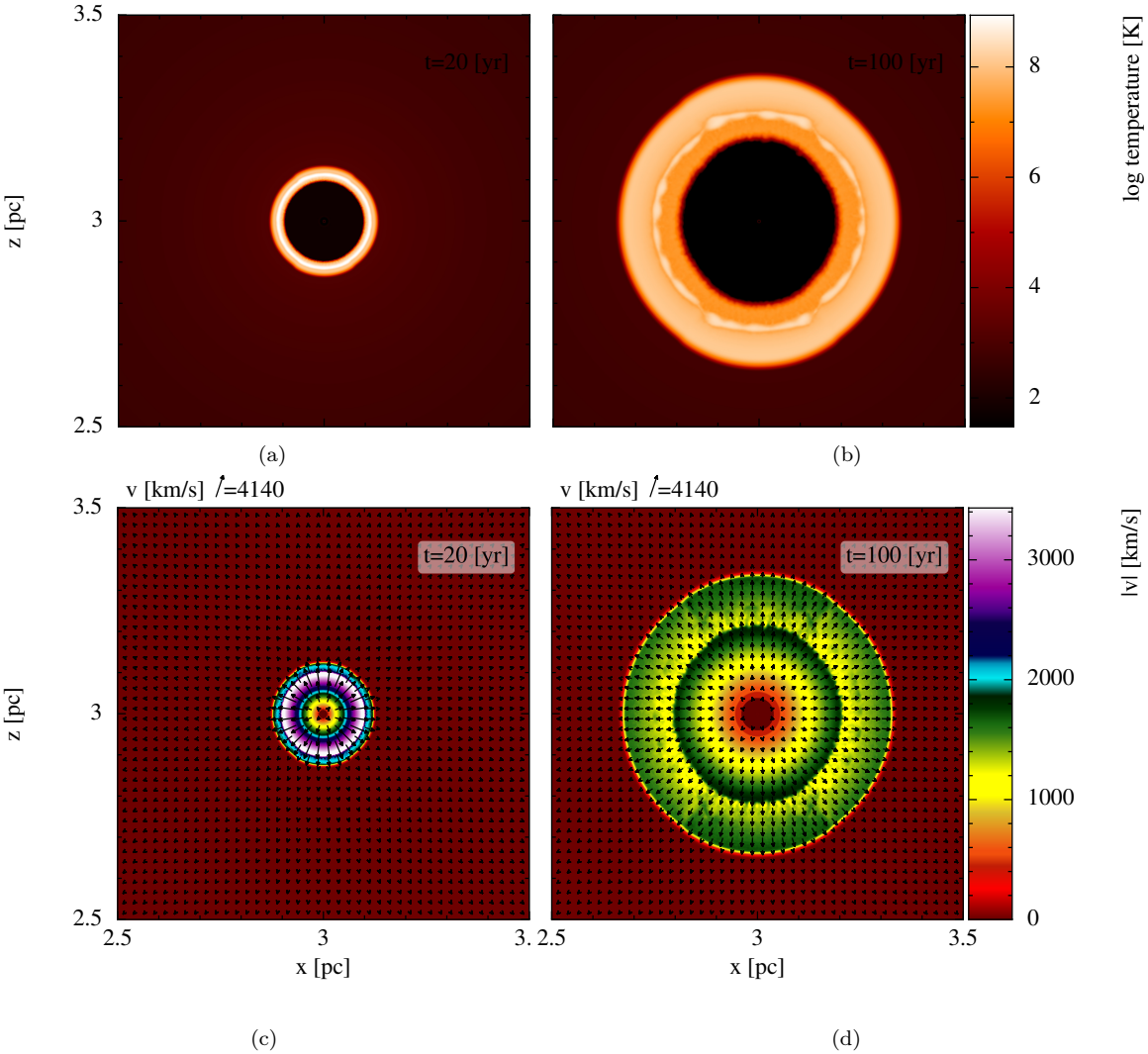

Figure 4.35: Same as in Fig. 4.34 but for temperature (*a*, *b*) and velocity (*c*, *d*).

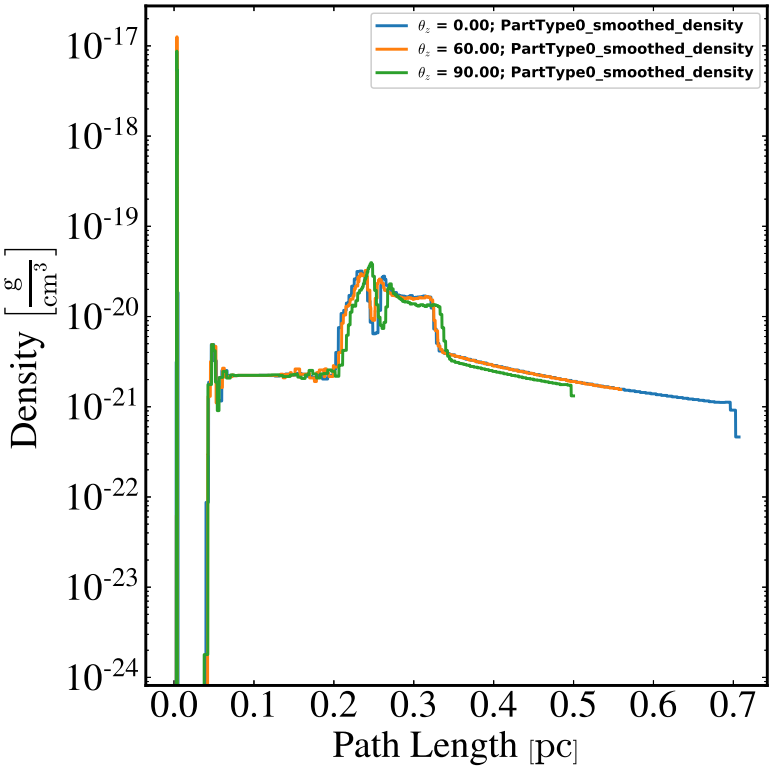

(a)

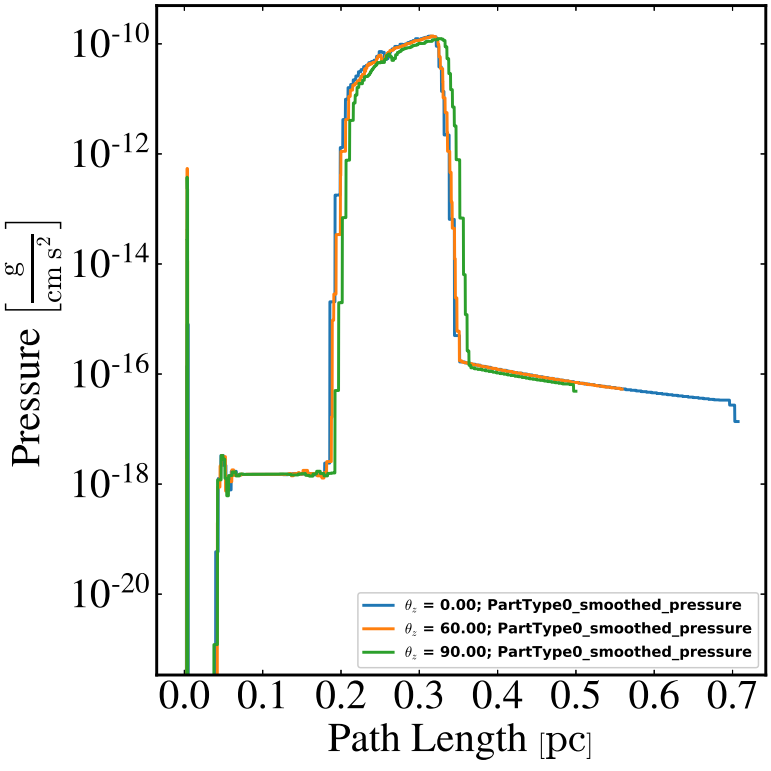

(b)

Figure 4.36: Radial line-plots for model RhoTOf03ε003_SPH3D in Table 4.1 measured at different angles for *(a)* density and *(b)* pressure at 100 yr. $\Theta = 0°$ is along the xy-plane and $\Theta = 90°$ is along the z-axis.

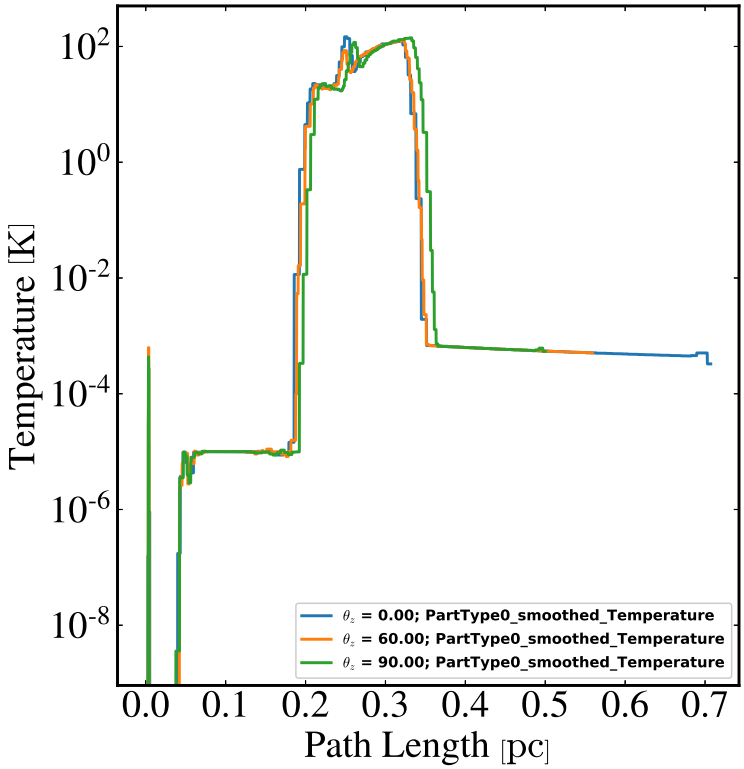

(a)

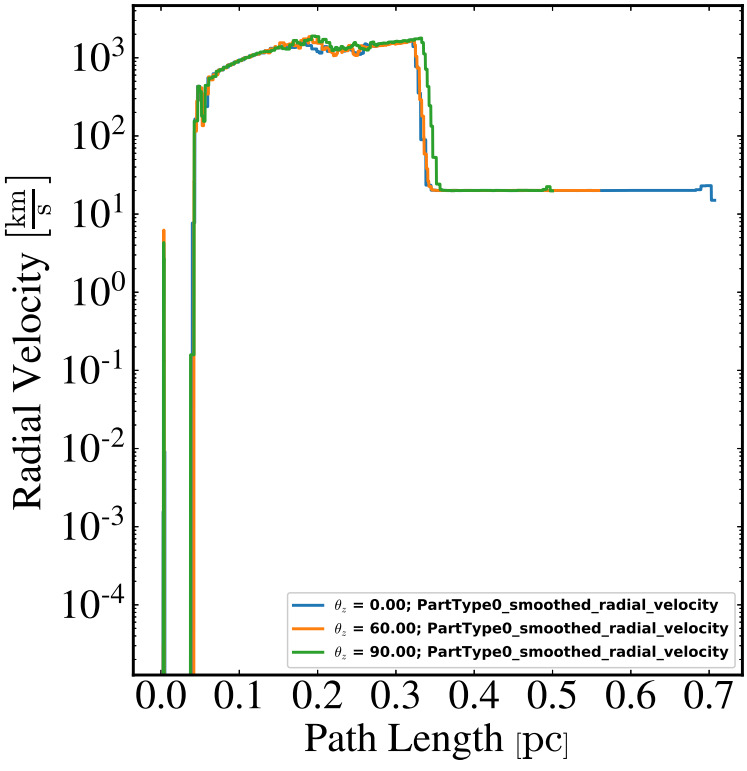

(b)

Figure 4.37: Same as in Fig. 4.36 but for temperature (a) and velocity (b).

interaction are highlighted by the pronounced reverse and forward shock separated by the contact discontinuity along the z-axis and the half-opening angle, while the xy-plane lacks a well defined contact discontinuity. This could be due to the fact that the shocked CSM and contact discontinuity along the xy-plane have roughly similar densities (10^{-20} g cm^{-3}) as the SN ejecta interacts with a much denser material in the torus. Taking line profiles along the xy-plane (blue-line) and half-opening angle (orange-line) produce similar densities on average, with the only difference being the unresolved contact discontinuity and higher densities along the xy-plane. In Fig. 4.41b, the velocity is shown to be erratic at radius 0.2 pc, owing to the turbulent motions at the contact discontinuity along the path of all angles. As previously observed in the $\rho - \mathrm{R2}$ simulations, the Richtmyer-Meshkov instabilities mix the cold ejecta with the hot shocked CSM, however, Fig. 4.41a reveals a sharp temperature increase along the half-opening angle, 60°, (orange-line), which is indicative of the hot gas in the instability roll and corresponds to the hot material at the centre of the roll in Fig 4.38.

4.4 Discussion

The collision between fast moving ejecta and slow moving circumstellar wind creates a moving interaction shell, which is driven outwards by the thermal pressure in a hot bubble of shocked, fast CSM. The Richtmyer-Meshkov instability is generally defined as a shock-induced Rayleigh-Taylor instability. However, unlike the Rayleigh-Taylor instability which occurs when a less dense fluid accelerates into a denser fluid and the growing perturbations are exponential with respect to time, a Richtmyer-Meshkov instability occurs regardless of the viewpoint of the propagating shock wave relative to the interface (i.e., from the tenuous or dense fluid point of view) and the perturbations initially grow linear with time (Kane et al. 1999). Formally, Richtmyer-Meshkov instabilities, are often regarded as pressure-driven rather than gravitationally-driven perturbations (Brouillette 2002)

In the 2D $\rho - \mathrm{R2}$ simulations of the interaction region, Richtmyer-Meshkov instabilities developed as early as 20 yr and are characterized by filament-like structures emerging from the contact discontinuity, whereas, in the 3D simulations the instabilities are made up of a combination of filaments that manifest into large bubbles. These instabilities are responsible for mixing of the cool ejecta material with the hot, shocked CSM. SPH suppresses the instabilities and further broadens the reverse and forward shock. SPH also showed ringing artefacts in the velocity of the shocked CSM, making it non-ideal for simulations of SNe interacting with the CSM. Moving from 2D to 3D showed that the instabilities arising from the contact discontinuity become less pronounced and on average the interaction shell expands more slowly in 3D. Whilst MFM performs similar to MFV when it comes to the pronounced nature of instabilities, it lacks the sharp reverse and forward shock characterizing the SN remnant morphology during the Sedov-Taylor phase. Similar behaviour was observed in both cases of the $\rho - \mathrm{TO}$ simulations, in which MFV resolved the SN interaction region

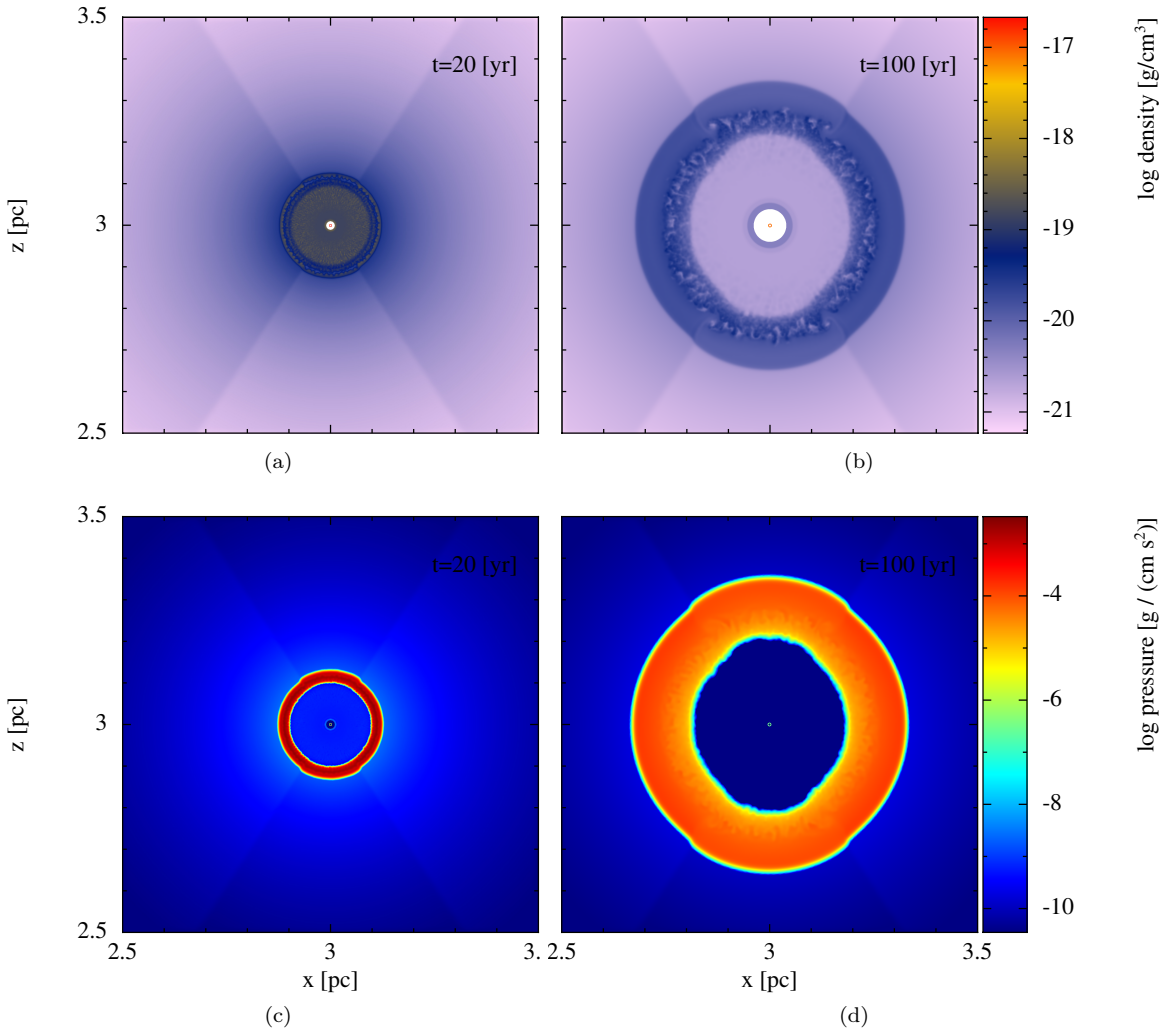

Figure 4.38: Cross-section slices for model RhoTOf03ε03_MFV3D in Table 4.1 taken across the y-axis for density at *(a)* 20 yr and *(b)* 100 yr, and pressure at *(c)* 20 yr and *(d)* 100 yr.

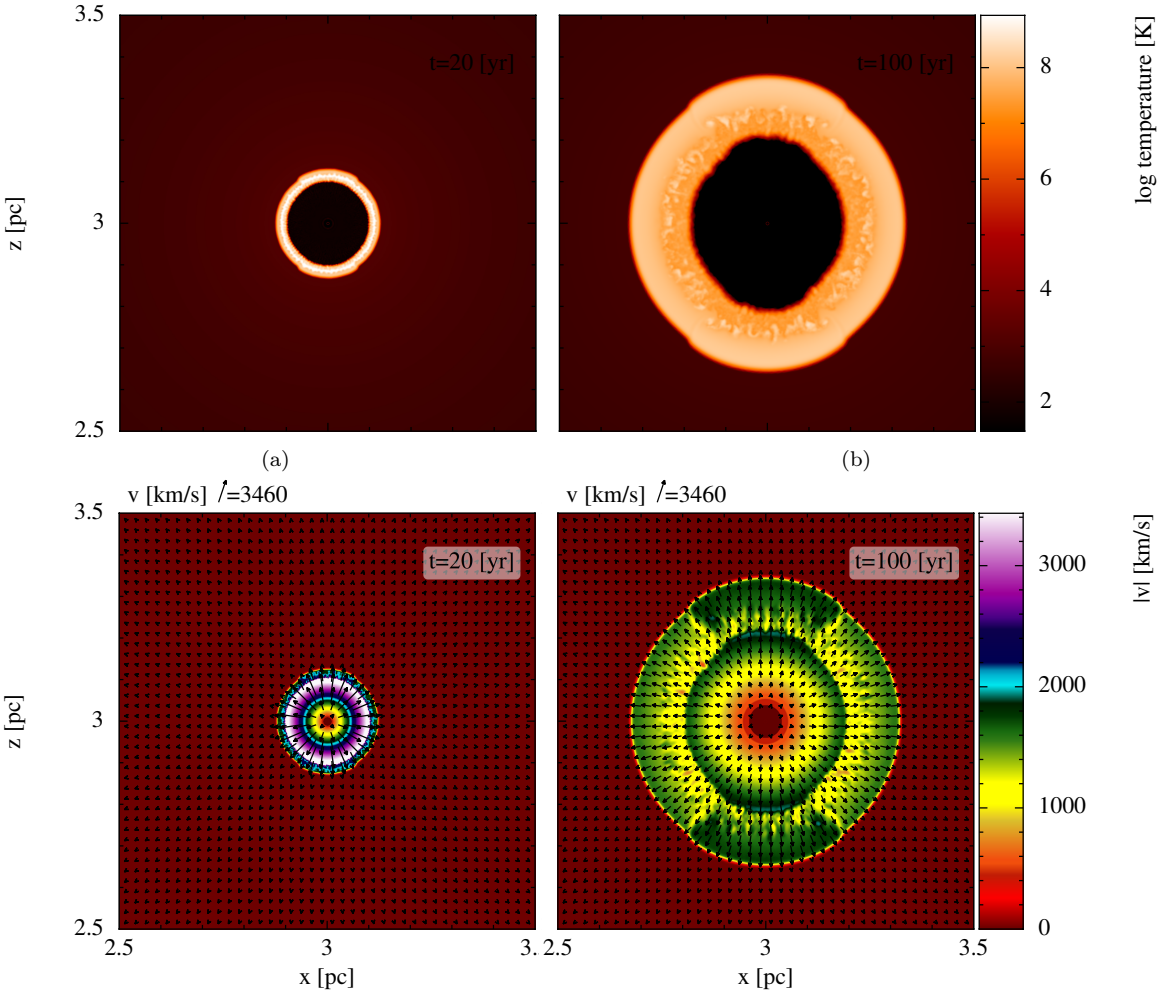

Figure 4.39: Same as in Fig. 4.38 but for temperature (a, b) and velocity (c, d).

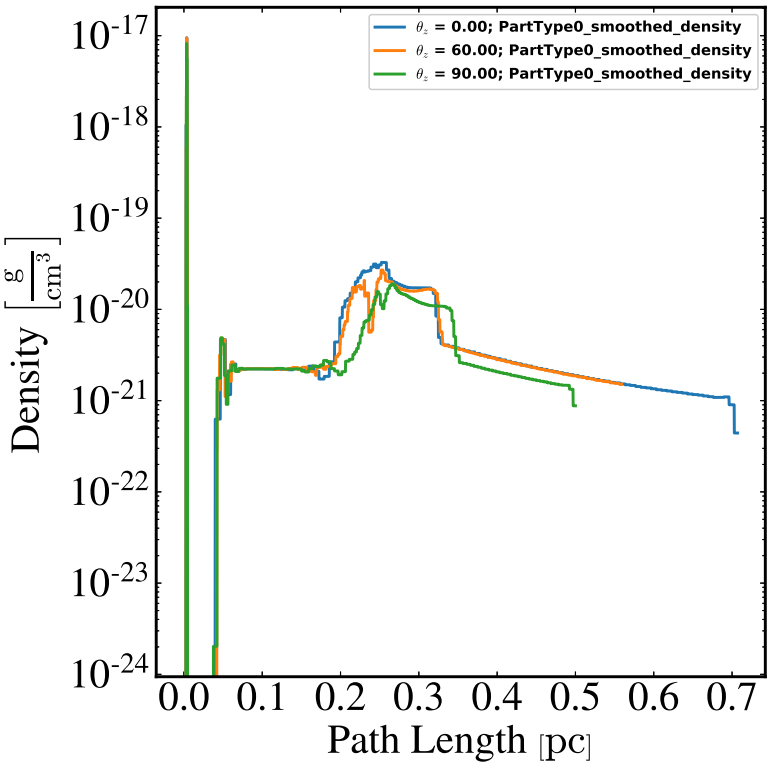

(a)

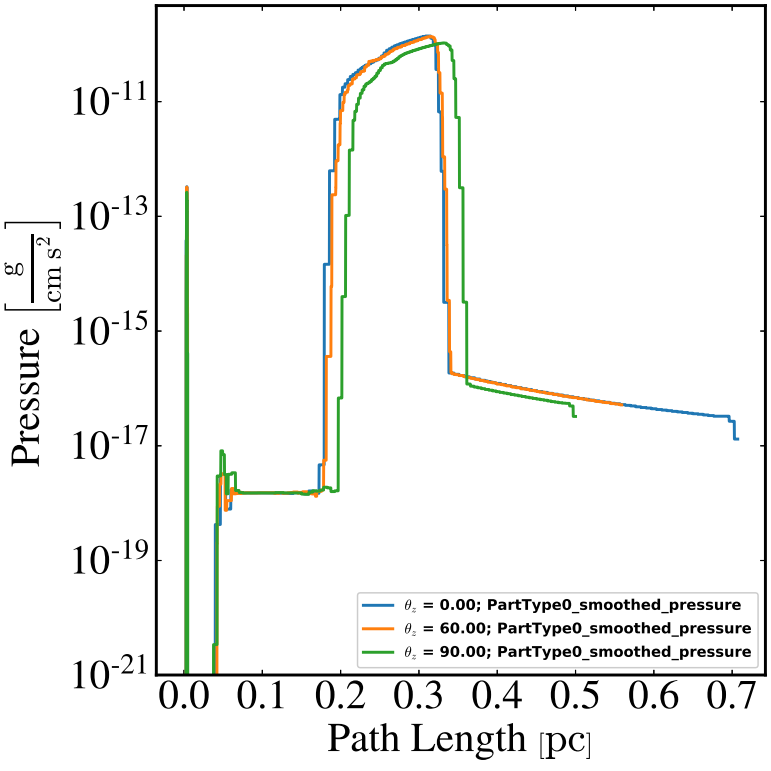

(b)

Figure 4.40: Radial line-plots for model RhoTOf03ε03_MFV3D in Table 4.1 measured at different angles for *(a)* density and *(b)* pressure at 100 yr. $\Theta = 0°$ is along the xy-plane and $\Theta = 90°$ is along the z-axis.

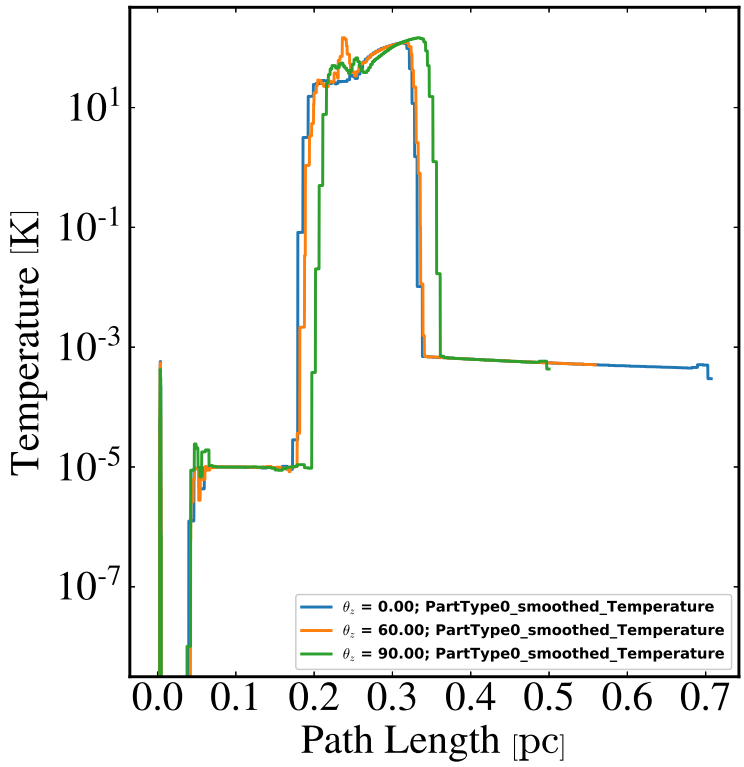

(a)

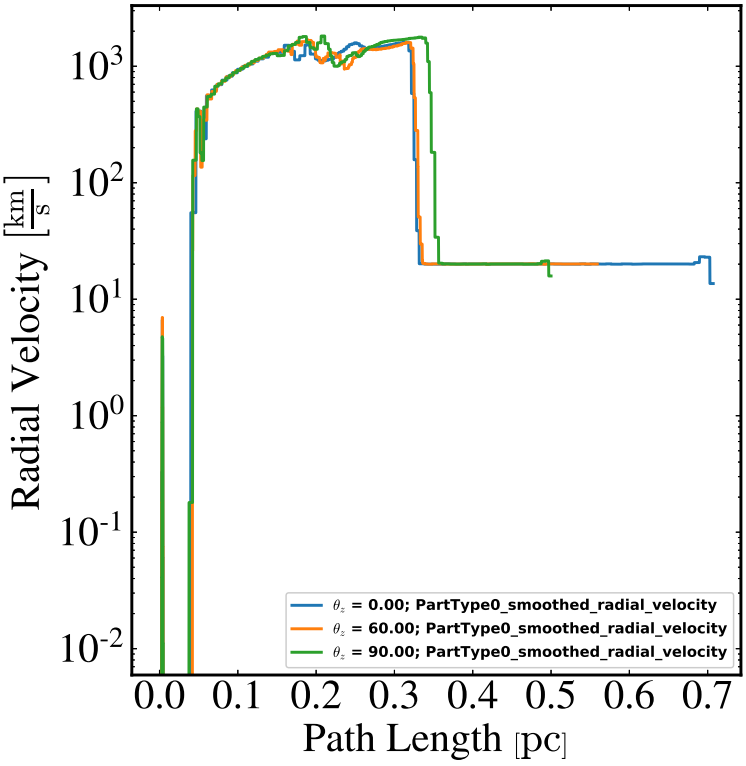

(b)

Figure 4.41: Same caption as in Fig. 4.40 but for temperature (a) and velocity (b).

better than MFM and SPH.

Simulations of young SN remnants performed by van Veelen et al. (2009) in 2D, evolved up to 335 yr for their model W0 (smooth $\rho - \mathrm{R2}$ profile), showed discontinuous jumps in density which marks the forward and reverse shock separated by the fingers of the Rayleigh-Taylor instabilities at the contact discontinuity. These instabilities are responsible for the mixing of the SN ejecta with the CSM as shown in Fig. 3 of van Veelen et al. (2009). Their results show that the shocked CSM is radially expanding at velocities exceeding $3500\,\mathrm{km\,s^{-1}}$ and has densities of approximately $10^{-22}\,\mathrm{g\,cm^{-3}}$. The radius of the forward and the reverse shock exhibit a relatively linear growth with time, and since the SN ejecta initially encounters a higher density CSM, the reverse shock initially moves slowly at approximately $2500\,\mathrm{km\,s^{-1}}$. Our 2D simulation results at 20 yr showed similar instabilities and remnant morphology to that of van Veelen et al. (2009). The shocked CSM density was recorded at $10^{-20}\,\mathrm{g\,cm^{-3}}$ with velocity $3200\,\mathrm{km\,s^{-1}}$ for our 2D MFV ejecta-CSM model, and MFM and SPH yield similar results. It is important to note that while our initial ejecta density structure is identical to that of van Veelen et al. (2009), we used $20\,\mathrm{km\,s^{-1}}$ instead of $4.70\,\mathrm{km\,s^{-1}}$ for the wind velocity, $6 \times 10^{-5}\,\mathrm{M_\odot\,yr^{-1}}$ instead of $1.54 \times 10^{-5}\,\mathrm{M_\odot\,yr^{-1}}$ for the mass loss rate and $\rho_{\max} = 10^{-21}\,\mathrm{g\,cm^{-3}}$ instead of $\rho_{\max} = 10^{-23}\,\mathrm{g\,cm^{-3}}$ for the dense inner regions of the CSM.

Our radial profile results for 3D MFV $\rho - \mathrm{R2}$ simulations of the interaction region are consistent with those of Whalen et al. (2008), in which they performed 1D grid based numerical calculations of SN ejecta interacting with neutral and ionized hydrogen gas clouds. Their results show the formation of the forward and reverse shock separated by a contact discontinuity in radial number density and velocity profile as early as 7.4 yr. This is characterized by a discontinuous double peak in number density ($\sim 10^6\,\mathrm{cm^{-3}}$) and a saw-tooth shape of the reverse ($\sim 3500\,\mathrm{km\,s^{-1}}$) and forward ($\sim 2500\,\mathrm{km\,s^{-1}}$) shock velocity for a $40\,\mathrm{M_\odot}$ progenitor. Our $15\,\mathrm{M_\odot}$ progenitor model resulted in similar features; our 3D MFV simulation of the interaction region have reverse and forward shock velocity of $\sim 4200\,\mathrm{km\,s^{-1}}$ and $\sim 3800\,\mathrm{km\,s^{-1}}$, respectively, at 20 yr after explosion and number density jumps of $\sim 10^4\,\mathrm{cm^{-3}}$ in both shocks.

Our study of the interaction of the SN ejecta with an axisymmetric torus with either a steep density drop or a smooth density drop from the torus to the bipolar cavity marks the first of its kind. In the steep density drop $\rho - \mathrm{TO}$ model, the remnant morphology assumes a prolate shape as early as ~ 20 yr. Since the torus is much denser than the cavity, the forward shock decelerates more rapidly in the equatorial region compared to the bi-polar cavity. The contact discontinuity is subject to Richtmyer-Meshkov instabilities as expected, but an additional pronounced instability roll develops along the half-opening angle of the torus, within $40 - 50$ yr in the smooth density drop model. The smooth density drop results in more pronounced instabilities, early onset of instability rolls and the prolate shape of the remnant is more defined, signifying an even faster moving forward shock in the cavity

relative to that in the torus. As the remnant ages in both scenarios, we expect the forward shock in the polar cavity to eventually sweep up enough material to decelerate, leading to a more spherical SN remnant at later times. The remnant overruns the simulation box before this stage in our study, therefore, a larger simulation box and more compute time would be required to investigate this further.

Observations of remnants in the early Sedov-Taylor phase are needed to capture the asymmetries and would also depend on the inclination of the remnant with respect to the line-of-sight; emission from face-on remnants would appear spherical as shown in Fig. 4.42. The torus model was inspired by observations of WOH G64 (Ohnaka et al. 2008). Radiative transfer modelling suggested that an opening angle of 60°, inner torus boundary radius of $r_{\rm in} = 15\,{\rm R}_{\star}$, outer torus boundary radius of $r_{\rm out} = 250 \times r_{\rm in}$, $f = 0.3$, $\varepsilon = 0.03$ and a fixed radial distribution following r^{-2}, characterizing a geometrically and optically thick torus viewed close to pole-on is the likely scenario for this RSG. This configuration is similar to our $\rho - {\rm TO}$ profile with a smooth density drop. Our results suggest that it would be difficult to directly observe the asymmetry produced by the eventual SN explosion–torus CSM interaction as the orientation is not very favourable.

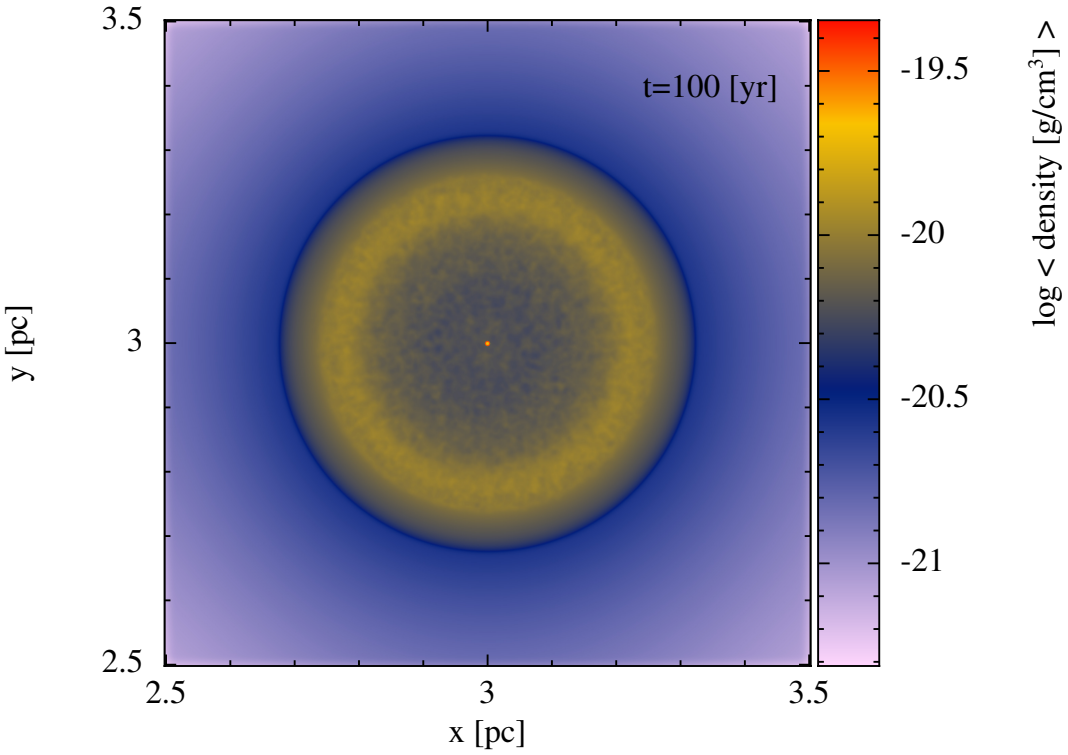

(a)

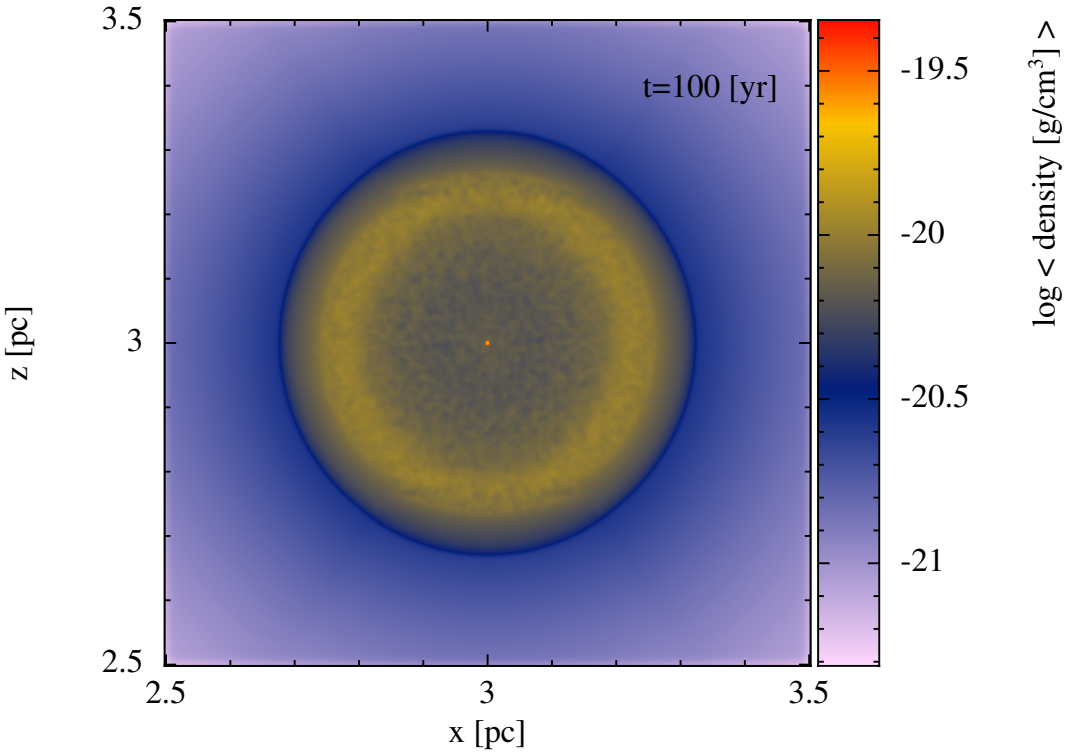

(b)

Figure 4.42: Projection plots of the torus model with a steep density drop ($\varepsilon = 0.03$) along (a) xy- and (b) zx-axis. This plot represents the normalized column density, $\int \rho dz$, along the projection.

Chapter 5

Summary and Future Work

The diversity of photometric light curves and spectra of CCSNe and a wide range of progenitor channels associated with their types leads to gaps in our understanding of the evolution of massive stars. Various mass-loss mechanisms in massive stars (metallicity, rotation, and binary interaction), can lead to different circumstellar density structures and geometries. By modelling the hydrodynamic evolution of young SNRs in complex circumstellar environments, we can establish a connection between the evolution of massive stars and their deaths. This is especially important for Type IIn SN that show signatures of an interaction with a dense circumstellar environment in their spectra. From these circumstellar interactions, mass-loss histories of different progenitor channels leading up to a SN and the mass of the progenitor before explosion can be constrained.

We have used the Sedov-Taylor blastwave test which has a known exact solution to determine how well the meshless methods (SPH, MFV, and MFM) in `GIZMO` capture and resolve strong shocks. These meshless methods are all Lagrangian and allow for continuous and adaptive resolution and deformation with the flow. The two new methods (MFV and MFM) belong to a sub-class of Lagrangian schemes called the Gudonov-type methods that behave like a moving-mesh code but without the underlying mesh.

We systematically investigated the options for various code parameters (e.g., self-gravity, smoothing kernel, $N_{\rm NGB}$, $\alpha_{\rm AV}$, $\alpha_{\rm AC}$, and resolution) specifically to find the best agreement with the Sedov-Taylor exact solution. For strong shocks, CD10 and Balsara SPH leads to unphysical post-shock ringing, which is present but minimal in MFV and MFM. The Balsara switch further causes asphericity of the shocks in SPH. While MFV captures the amplitude of the shock jump well, it poorly recovers the position of the shock front. The extent of the latter is by a small margin compared to the significant dampening and broadening of the shock density jumps in MFM and SPH.

After obtaining optimal parameters for each method, we presented meshless hydrodynamic

models of $1/r^2$ spherically symmetric and asymmetric SN remnants generated by the interaction of the ejecta with different CSM density profiles. In 2D and 3D, our results were in good agreement with previous numerical studies, both for Sedov-Taylor tests (e.g., Zhu et al. (2015), Springel & Hernquist (2002), Rosswog & Price (2007), Tasker et al. (2008)) and the interaction of SN ejecta with $1/r^2$ CSM profile (e.g., 1D and 2D models of Whalen et al. (2008), van Veelen et al. (2009), respectively). We studied the evolution of the interaction region and the development of instabilities; moving from 2D to 3D significantly changes the structure of instabilities from filaments to bubbles, and further makes the interaction region hot and unstable. Our novel simulations of SN ejecta interacting with a steep and smooth asymmetric torus profile were inspired by the observation of a dense, dusty circumstellar torus around the RSG, WOH G64 (Ohnaka et al. 2008). The asymmetry of the resulting prolate remnant may be observable at early times and with favourable viewing angles. A larger simulation box is required to further study the late-time morphological evolution of the remnant.

There are still some unresolved issues pertaining to the various numerical artefacts we encountered during this study. The sharp drop at the shock fronts in pressure and specific internal energy profiles when self-gravity is not included in MFV need to be investigated further. Another limitation was the $N_{\rm NGB}$ test at high resolution and with higher-order kernels. This test required more computational resources and we intend to carry out a thorough systematic study with varying particle resolution in future. We also encountered numerical artefacts in the form of hot, low density bubbles in the ejecta when running 2D simulations of SN ejecta interacting with the $1/r^2$ density profile. Future updates in `GIZMO` might address this issue, however, we plan to investigate the possible origin in the initial conditions as well.

For all the SN ejecta-CSM interaction models discussed in this work, we plan to also include additional physics, e.g., radiative transfer cooling, and allow the remnant to evolve through the radiative phase in which radiative losses of energy become significant. We will further investigate radio synchrotron emission coming from the interaction region, which is proposed by Chevalier (1982b) to be associated with the density of the CSM. Such studies as using high-resolution hydrodynamic simulations and radiation transfer has been shown to be in broad agreement with radio observations of young SNRs (Dwarkadas et al. 2010, Mioduszewski et al. 2001), however, more work is required to understand some unusual SNe, e.g., the variability exhibited by SN 1979C (Fig.1.6b). Such quantitative simulations would allow us to infer the density structure of the CSM, the evolution of the SN shock wave, the nature of the progenitor star that exploded and ultimately better understand the final stages of the evolution of massive stars.

Appendix A

Appendix

A.1 Problem of a strong explosion

If we assume that the gas is ideal, invicid and non-heat conducting, so that its motion does not involved any kind of physical or chemical change, the general fluid equations governing the flow of gas are the Euler equations, namely;
the continuity equation:

$$\frac{\partial \rho}{\partial t} + \frac{\partial(\rho \upsilon)}{\partial r} + (D-1)\frac{\rho \upsilon}{r} = 0, \tag{A.1}$$

the equation of motion:

$$\frac{\partial \upsilon}{\partial t} + \upsilon \frac{\partial \upsilon}{\partial r} + \frac{1}{\rho}\frac{\partial p}{\partial r} = 0, \tag{A.2}$$

and the entropy equation:

$$\frac{\partial (p\rho^{-\gamma})}{\partial t} + \upsilon \frac{\partial (p\rho^{-\gamma})}{\partial r} = 0, \tag{A.3}$$

where $D = (1, 2, 3)$ is the dimensionality of space for a plane flow; flow with cylindrical symmetry; and flow with spherical symmetry, respectively, and γ is the adiabatic index defined by the ratio of specific heats at constant pressure C_P and volume C_V:

$$\gamma = \frac{C_p}{C_v} = \frac{f+2}{f}, \tag{A.4}$$

where f is the number of degrees of freedom of a particle. Thus we observe that for a monoatomic gas, with 3 degrees of freedom, $\gamma = \frac{5}{3}$. All physical variables in the fluid equations depend on position and time, thus are a function of r and t. The Euler fluid equations lack the presence of a dimensional constant, and the initial conditions are the ones that introduce characteristic dimensions into the hydrodynamic problem.

Sedov (1959) showed that the initial conditions are only required to introduce two characteristic parameters of independent dimensions, for a unique similarity relationship between position and time coordinates to be constructed using dimensional analysis. Thus, each ba-

sic physical variable can be non-dimensionalized by multiplying them with their respective arbitrary dimensionless variables, V, Ω, and Π for velocity, density and pressure, respectively. The partial differential equations governing the fluid flow are then recast as ordinary differential equations in terms of V, Ω, and Π, resulting in a self-similar solution. An exact solution to this system ordinary differential equations can either be obtained in closed form or by a numerical quadrature as per our investigation (see Chapter 3). Adopting this mathematical description, Dokuchaev (2002) showed that the Sedov-Taylor self-similar spherical shock solution exists for an initial background medium with constant density. Korobeinikov (1991) generalized it to the case where initial density, ρ, depends on the radial coordinate, r, according to a power-law distribution,

$$\rho = \frac{A}{r^{\omega}}\ , \quad 0 \leq \omega < 3, \tag{A.5}$$

where A is a positive constant and ω is an arbitrary constant describing the density distribution (i.e. $\omega = 0$, for a uniform density medium). Book (1994) conducted an extensive survey that illustrates the significant effects of varying ω (with values for which the total mass in the region is finite) and γ (with values appropriate to ordinary gases) on the Sedov-Taylor self-similar solution for the case of a spherical explosion ($D = 3$). Furthermore, these self-similar solutions can also be obtained for both cases of isothermal and adiabatic flows of a spherical shock in a non-ideal gas (Naidu et al. 1983, Vishwakarma & Nath 2007). The stability properties of these solutions are well investigated by Cheng (1979).

If we consider a strong explosion occurring at a central point at time $t = 0$, within a pressure-less uniform background medium of constant density, ρ_0, a strong spherical shock-wave propagates through the initially undisturbed gas with an adiabatic index of γ, when $t > 0$. A finite amount of energy, E_0, is liberated instantaneously but the mass and dimension of the substance liberating the energy is neglected. Here we designate all values on the forward side of the shock surface (unperturbed gas) with subscript 0 (e.g. $\rho_0,\ P_0,\ \upsilon_0$), and the values behind the shock surface (shock cavity) with subscript 1 (e.g. $\rho_1,\ P_1,\ \upsilon_1$). The appropriate similarity assumptions for an expanding shock-wave are necessary for the derivation of the solution as well as determining if the solution is valid for a set of physical conditions:

- In the early period of expansion, thermal pressure behind the shock-wave, P_1, is significantly higher than the initial pressure of the external medium, P_0.
- The amount of energy radiated from the expanding shock is significantly less than the initial injected energy, E_0, (i.e energy remains constant).
- The background medium is a cold, uniform density ideal gas that is stationary with respect to the propagating shock-wave (i.e $\upsilon_0 = 0$).

The blastwave regime signifies the expansion phase during which energy remains constant. During the blastwave regime the shock velocity, $\upsilon_{\rm sh}$, shock density, $\rho_{\rm sh}$, and shock pressure,

$P_{\rm sh}$, are determined by the two initial parameters of the system (E_0 and ρ_0). These two parameters do not have unique expression to form a characteristic length scale and time scale of the problem. The solution for the expanding shock front thus requires a scale-free or self-similar solution. Thus, in a strong spherical explosion problem, three characteristic parameters with independent dimensions enter into the problem; initial pressure, P_0, initial gas density, ρ_0, with adiabatic index, γ, and the explosion energy, E_0, in addition to the radial coordinate, r, and time, t, (Sedov 1959).

Since the first condition assumes negligible initial gas pressure, this is marked by $P_0 \sim 0$, hence only two characteristic parameters with independent dimensions ($\rho_0,\ E_0$) are essential. Using general dimensional analysis, the goal is to determine a dimensionless variable, β, as a combination of r, t, E_0, ρ_0. Dimensions of the characteristic parameters that enter the problem are given in terms of the fundamental units of dimensions; mass, M, length, L, and time, T.

That is,

$$[r] = \mathrm{L}, \tag{A.6}$$

$$[t] = \mathrm{T}, \tag{A.7}$$

$$[\rho_0] = \frac{\mathrm{M}}{\mathrm{L}^3}, \tag{A.8}$$

$$[E_0] = \frac{\mathrm{ML}^2}{\mathrm{T}^2}, \tag{A.9}$$

Assuming that β will be given by some product of the four variables,

$$[\beta] = r\ t^k\ E_0^l\ \rho_0^m, \tag{A.10}$$

we can form a system of linear equations to solve for k, l, and m, by substituting the dimensions of every variable given by A.6 - A.9 into A.10. Using Gaussian elimination, the solution to the system of linear equations is

$$k = -\frac{2}{5},\ l = -\frac{1}{5},\ m = \frac{1}{5}\ . \tag{A.11}$$

Therefore, we can express β as

$$\beta = r\left(\frac{\rho_0}{E_0 t^2}\right)^{\frac{1}{5}}, \tag{A.12}$$

or alternatively we can express the radial position of the shock-wave at any time for a given external density and initial energy as

$$r = \beta\left(\frac{E_0 t^2}{\rho_0}\right)^{\frac{1}{5}}\ . \tag{A.13}$$

For spherical point explosions ($D = 3$) with monoatomic gas, $\gamma = \frac{5}{3}$, the self-similarity constant (computed to arbitrary precision) is $\beta(\gamma, D) = 1.15$ (Valdarnini 2012, Frontiere et al. 2017). As the solution is constant and dimensionless in β, we denote the position of the shock in the $\beta-$coordinate system by $\beta_{\rm sh}$. We can now determine the instantaneous radius of the shock, $R(t) = R_{\rm sh}$, using

$$R(t) = R_{\rm sh} = \beta_{\rm sh} \left(\frac{E_0 t^2}{\rho_0} \right)^{\frac{1}{5}} . \tag{A.14}$$

The instantaneous velocity of the expanding shock is then given by the rate of change of shock radius with respect to time:

$$\upsilon(t) = \upsilon_{\rm sh} = \frac{dR_{\rm sh}}{dt} = \frac{2}{5} \beta_{\rm sh} \left(\frac{E}{\rho_0 t^3} \right)^{1/5} . \tag{A.15}$$

From A.13 and A.14, we can determine a normalized similarity variable β_n defined as $\beta_n = \frac{\beta}{\beta_{\rm sh}} = \frac{r}{R_{\rm sh}}$. The conditions on the surface of the shock front are characterized by $\beta_n = 1$ (Masuyama et al. 2016). Replacing A.1 - A.3 by ordinary differential equations (ODE) with respect to β_n, the density, velocity, and pressure are assumed to depend on β_n through the dimensionless similarity functions, $\Omega(\beta_n)$, $V(\beta_n)$ and $\Pi(\beta_n)$, respectively. The solutions must take the form

$$\rho(r, t) = \rho_0 \Omega(\beta_n), \tag{A.16}$$

$$v(r, t) = \frac{r}{t} V(\beta_n), \tag{A.17}$$

$$p(r, t) = \rho_0 \frac{r^2}{t^2} \Pi(\beta_n). \tag{A.18}$$

These dimensionless variables are evaluated for the region $0 < r < R_{sh}$ where the factors ρ_0, r and t provide the proper dimensionality for the solutions. Using these variables, the Euler fluid equations are then rewritten in terms of the dimensionless ODEs which are then solved with respect to the derivatives of the dimensionless similarity functions (see Masuyama et al. (2016) for a full derivation). Since the solution of the spherical shock is self-similar, the physical quantities satisfy the boundary conditions at the strong shock front ($\beta_n = 1$), that is, the dimensionless similarity variables are given by (see Rankine-Hugoniot relations, equation A.20-A.24)

$$\Omega(1) = \frac{\gamma + 1}{\gamma - 1}, \; V(1) = \frac{2}{\gamma + 1}, \; \Pi(1) = \frac{2}{\gamma + 1}, \tag{A.19}$$

and they satisfy the normalization $\Omega(1) = V(1) = \Pi(1) = 1$. So far, we have found the radius of the shock front as a function of time and the dimensionless flow variables (ρ, υ, P) as a function of β_n with the appropriate physical quantities constructed out of E_0, ρ_0, r and t. However, the density, velocity, and pressure as a function of radius within the spherical shock front are not readily known. Assuming a very strong shock, the density, bulk velocity, pressure, and temperature, T, immediately inside the expanding shock front are determined

from the Rankine-Hugoniot jump conditions, given in Pfrommer et al. (2006) in the form

$$\frac{\rho_0}{\rho_1} = \frac{\gamma - 1}{\gamma + 1} + \frac{2}{(\gamma + 1)\mathcal{M}_0^2}, \tag{A.20}$$

$$\frac{\upsilon_1}{\upsilon_0} = \frac{\rho_0}{\rho_1}, \tag{A.21}$$

$$\frac{P_1}{P_0} = \frac{2\gamma\mathcal{M}_0^2}{\gamma + 1} - \frac{\gamma - 1}{\gamma + 1}, \tag{A.22}$$

$$\frac{T_1}{T_0} = \frac{\left[2\gamma\mathcal{M}_0^2 - (\gamma - 1)\right]\left[(\gamma - 1)\mathcal{M}_0^2 + 2\right]}{(\gamma + 1)^2\mathcal{M}_0^2}, \tag{A.23}$$

where $\mathcal{M}$ denotes the Mach number of the shock,

$$\mathcal{M} = \frac{\upsilon_{\rm sh}}{c_s}\,, \tag{A.24}$$

and c_s is the local speed of sound in the non-moving gas given by

$$c_s = \sqrt{\frac{\gamma P_0}{\rho_0}}\,. \tag{A.25}$$

These conditions are derived in the frame of reference that is moving with the shock by applying the principle of conservation of mass, momentum and energy across the shock (Krehl 2015). As such, υ_0 represents the velocity of the background medium with respect to the shock, thus it is non-zero. In the strong shock regime, the shock is expanding with a velocity that is much greater than the speed of sound in the background medium (i.e. $\mathcal{M}_0 >> 1 \longrightarrow \upsilon_{\rm sh} >> c_s$). It is in this limit that the Rankine-Hugoniot jump conditions simplify to

$$\rho_1 = \frac{\gamma + 1}{\gamma - 1}\rho_0, \tag{A.26}$$

$$\upsilon_1 = \frac{\gamma - 1}{\gamma + 1}\upsilon_0, \tag{A.27}$$

$$P_1 = \frac{2\gamma\mathcal{M}_0^2}{\gamma + 1}P_0, \tag{A.28}$$

$$\frac{T_1}{T_0} = \frac{2\gamma(\gamma - 1)\mathcal{M}_0^2}{(\gamma + 1)^2}. \tag{A.29}$$

If the background pressure is expressed in terms of the speed of sound,

$$P_0 = \frac{\rho_0 c_s^2}{\gamma}\,, \tag{A.30}$$

then the Mach number of the shock can be written as

$$\mathcal{M}_0^2 = \frac{\rho_0\upsilon_0^2}{\gamma p_0}, \tag{A.31}$$

where the pressure immediately behind the shock takes the form

$$P_1 = \frac{2}{\gamma+1}\rho_0 \upsilon_0^2 \,. \tag{A.32}$$

If we change the frame of reference of the Rankine-Hugoniot equations from the frame moving with the shock to the stationary frame of the background medium, it only affects the velocity terms, yielding new terms; $\upsilon_{\rm in} = \upsilon_{\rm sh} - \upsilon_1$ and $\upsilon_{\rm out} = \upsilon_{\rm sh} - \upsilon_0$ for the velocities inside and outside of the shock, respectively. The original assumption requires a stationary gas outside the approaching shock be zero ($\upsilon_{\rm out} = 0$), leading to $\upsilon_{\rm sh} = \upsilon_0$. Thus, substituting A.27 into $\upsilon_{\rm in}$ yields

$$\upsilon_{\rm in} = \upsilon_0 - \frac{\gamma-1}{\gamma+1}\upsilon_0 = \frac{2}{\gamma+1}\upsilon_0, \tag{A.33}$$

and the expression of the gas velocity behind the expanding shock becomes

$$\upsilon_1 = \frac{2}{\gamma+1}\upsilon_0 \,. \tag{A.34}$$

Outside the approaching shock-front ($r > \upsilon_{\rm sh}t$), the density remains at the initial constant of ρ_0, while in the interior post-shock region ($r < \upsilon_{\rm sh}t$) the density rapidly decays until it vanishes at the origin. Note that when the dissipative effects are ignored, the specific entropy, s, is conserved across the shock front (Goodman 1990). Hence A.3 is equivalent to

$$p = K(s)\rho^\gamma, \quad \frac{dK(s)}{dt} + \upsilon\frac{dK(s)}{dr} = 0 \,. \tag{A.35}$$

As a result of the strong shock jump conditions, the density ratio converges to some maximum value of

$$\frac{\rho_1}{\rho_0} = \frac{\upsilon_0}{\upsilon_1} = 4 \,, \tag{A.36}$$

and this ensures that the density and velocity at the surface of the shock front increases by a factor of four with respect to the constant background density. Since the temperature ratio in Eq. A.29 is proportional to $\mathcal{M}_0^2$, its values will grow arbitrarily large in the limit of a strong shock.

A.1.1 Sedov-Taylor algorithm

Since we are only interested in the standard case and assume a constant initial density medium, all expressions and relations hereafter are written such that the initial density power-law exponent, ω, is zero. The immediate post-shock velocity in the similarity variable, V_1,

$$V_1 = \frac{4}{(D+2)(\gamma+1)}, \tag{A.37}$$

and the location of a singular point of the fluid equations, V_*,

$$V_* = \frac{2}{D(\gamma-1)+2}, \tag{A.38}$$

that occurs along this similarity variable, are sufficient to determine the type of closed-form solution (standard, singular or vacuum) we seek. Of the three possible forms that exist, we employ the standard case with a spherical geometry ($D = 3$). In the standard case, a non-zero solution extends from the shock position to the origin, at which the pressure is finite. In particular, if $V_1 < V_* - \epsilon_o$, the solution type is standard. ϵ_o is a small ($\sim 10^{-4}$) numerical parameter assigned to avoid hard zeros and limit some of the exponents to be discussed below from becoming sufficiently large thereby leading to numerical overflow. According to Sedov (1959), there exists a unique solution curve that passes through the shock point and must satisfy a relation given by,

$$Z = \frac{\gamma-1}{2}\frac{V^2(V-\frac{2}{D+2})}{\frac{2}{(D+2)\gamma}}, \tag{A.39}$$

in all geometries ($D = 1, 2, 3$). The correct solution form then depends on the relation between the shock state and a singular point of the fluid equations that occurs along the curve given by equation A.39 (Kamm 2000). The four auxiliary functions for the closed-form solution with respect to the non-dimensional similarity variable V are;

$$\begin{aligned} x_1 &= aV, \\ x_2 &= b(cV-1), \\ x_3 &= d(1-eV), \\ x_4 &= b\left[1-\frac{cV}{\gamma}\right], \end{aligned} \tag{A.40}$$

where the parameters a, b, c, d, e are defined in terms of the physical parameters D, γ, and ω as,

$$\begin{aligned} a &= \frac{(D+2)(\gamma+1)}{4}, \\ b &= \frac{\gamma+1}{\gamma-1}, \\ c &= \frac{(D+2)\gamma}{2}, \\ d &= \frac{(D+2)(\gamma+1)}{(D+2)(\gamma+1)-2[2+D(\gamma-1)]}, \\ e &= \frac{2+D(\gamma-1)}{2}. \end{aligned} \tag{A.41}$$

Given the above definitions, all the self-similar functions (or Sedov functions); scaled position λ, scaled speed f, scaled density g and scaled pressure h can be calculated. Thus, the Sedov

solution assumes the following form:

$$\begin{aligned} \lambda &= x_1^{-\alpha_0}\, x_2^{-\alpha_2}\, x_3^{-\alpha_1}, \\ f &= x_1 \lambda, \\ g &= x_2^{\alpha_3}\, x_3^{\alpha_4}\, x_4^{\alpha_5}, \\ h &= x_1^{\alpha_0 D}\, x_3^{-2(\alpha_4+\alpha_1)}\, x_4^{1+\alpha_5}, \end{aligned} \tag{A.42}$$

where the α_i exponents in the above expressions are related to the physical parameters as

$$\begin{aligned} \alpha_0 &= \frac{2}{D+2}, \\ \alpha_1 &= \frac{(D+2)\gamma}{D+2(\gamma-1)} \left[\frac{2D(2-\gamma)}{\gamma(D+2)^2} - \alpha_2 \right], \\ \alpha_2 &= -\frac{\gamma-1}{2(\gamma-1)+D}, \\ \alpha_3 &= \frac{D}{2(\gamma-1)+D}, \\ \alpha_4 &= \frac{(D+2)D}{D(2-\gamma)}\alpha_1, \\ \alpha_5 &= -\frac{2D}{D(2-\gamma)}. \end{aligned} \tag{A.43}$$

The first derivatives of the auxiliary functions with respect to the similarity variable, V, are then used to compute the energy integral. The dimensionless shock speed, V_{sh},

$$V_{sh} = \frac{2}{(D+2)\gamma}, \tag{A.44}$$

and the dimensionless immediate post-shock speed, V_1, form the lower and upper limits of the energy integral, respectively. When a finite amount of energy is deposited, two energy integrals must be evaluated. One or both of these integrals usually have a singularity at the lower limit of integration, leading to too many iterations for numerical integration routines (Timmes et al. 2005). The non-dimensional form of equation 3.1 is derived in terms of the scaled position of two energy integrals, J_1 and J_2, as:

$$\alpha = (D-1)\pi \left(J_1 + \frac{2J_2}{\gamma-1} \right), \tag{A.45}$$

in part to isolate singularities that may occur at lower integration bounds (see Kamm (2000) for a full derivation of J_1 and J_2). These energy integrals are obtained explicitly from the

Sedov functions in terms of the similarity variable, V, as;

$$J_1 = \int_{V_{sh}}^{V_1} -dV \frac{\gamma+1}{1-\gamma} V^2 \left[\frac{\alpha_0}{V} + \frac{\alpha_2 c}{cV-1} - \frac{\alpha_1 e}{1-eV}\right]$$

$$\times \left[(aV)^{\alpha_0}(b[cV-1])^{\alpha_2}(d[1-eV])^{\alpha_1}\right]^{-(D+2)} \tag{A.46}$$

$$\times \left((b[cV-1])^{\alpha_3}(d[1-eV])^{\alpha_4}\left[b\left(1-\frac{cV}{\gamma}\right)^{\alpha_5}\right]\right),$$

$$J_2 = \int_{V_{sh}}^{V_1} -dV \frac{\gamma+1}{2\gamma} V^2 \left(\frac{cV-\gamma}{1-cV}\right)\left[\frac{\alpha_0}{V} + \frac{\alpha_2 c}{cV-1} - \frac{\alpha_1 e}{1-eV}\right]$$

$$\times \left[(aV)^{\alpha_0}(b[cV-1])^{\alpha_2}(d[1-eV])^{\alpha_1}\right]^{-(D+2)} \tag{A.47}$$

$$\times \left((b[cV-1])^{\alpha_3}(d[1-eV])^{\alpha_4}\left[b\left(1-\frac{cV}{\gamma}\right)^{\alpha_5}\right]\right).$$

A.2 Weighted Voronoi Tesselation parameters

The WVTICs code was used to create the CSM distributions with $1/r^2$ density and torus profiles; the detailed parameters for these cases are given in section 4.1.2. The techniques above result in initial conditions that are smooth (isotropic), relaxed and random (no preferred directions). All the code parameter settings we chose for WVT method are labelled in table A.1. The parameter, `MpsFraction`, controls a fraction of particles that are to be redistributed in each relaxation step and decreases with increasing number of particles and it also depends on the density model chosen (see `https://github.com/jdonnert/WVTICs`)

WVT parameter	**3D Models**
CMAKE_C_FLAGS	-std=c99 -O2 -Wall -fopenmp
SAVE_WVT_STEPS	ON
SPH_CUBIC_SPLINE	ON
REJECTION_SAMPLING	ON
OUTPUT_DIAGNOSTICS	ON
`Npart`	10^7
`Maxiter`	1024
`MpsFraction`	0.35
`Problem_Subflag`	X
`Problem_Flag`	6

Table A.1: Tabel containing runtime parameter for the WVT method. All the other parameters where turned off

Bibliography

Agrawal, A. & Srinivasan, B. 2017, Indian Academy of Sciences, 42, 741

Arcavi, I. 2017, Hydrogen-Rich Core-Collapse Supernovae, ed. A. W. Alsabti & P. Murdin, 239

Arth, A., Donnert, J., Steinwandel, U., Böss, L., Halbesma, T., Pütz, M., Hubber, D., & Dolag, K. 2019, arXiv e-prints, arXiv:1907.11250

Aufderheide, M. B., Baron, E., & Thielemann, F. K. 1991, The Astrophysical Journal, 370, 630

Baade, W. & Zwicky, F. 1934, Proceedings of the National Academy of Sciences, 20, 254

Balsara, D. S. 1995, Journal of Computational Physics, 121, 357

Beasor, E. R. & Davies, B. 2017, Monthly Notices of the Royal Astronomical Society, 475, 55

Beswick, R. 2006, in Proceedings of the 8th European VLBI Network Symposium, 51

Bladh, S. & Höfner, S. 2012, Astronomy and Astrophysics, 546, A76

Book, D. L. 1994, Shock Waves, 4, 1

Brouillette, M. 2002, Annual Review of Fluid Mechanics, 34, 445

Bryan, G. L., Norman, M. L., O'Shea, B. W., Abel, T., Wise, J. H., Turk, M. J., Reynolds, D. R., Collins, D. C., Wang, P., Skillman, S. W., Smith, B., Harkness, R. P., Bordner, J., hoon Kim, J., Kuhlen, M., Xu, H., Goldbaum, N., Hummels, C., Kritsuk, A. G., Tasker, E., Skory, S., Simpson, C. M., Hahn, O., Oishi, J. S., So, G. C., Zhao, F., Cen, R., & and, Y. L. 2014, The Astrophysical Journal Supplement Series, 211, 19

Calder, A. C. 2005, Astrophysics and Space Science, 298, 25

Calder, A. C., Fryxell, B., Plewa, T., Rosner, R., Dursi, L. J., Weirs, V. G., Dupont, T., Robey, H. F., Kane, J. O., Remington, B. A., Drake, R. P., Dimonte, G., Zingale, M., Timmes, F. X., Olson, K., Ricker, P., MacNeice, P., & Tufo, H. M. 2002, The Astrophysical Journal Supplement Series, 143, 201

Caramana, E. J., Shashkov, M. J., & Whalen, P. P. 1998, Journal of Computational Physics, 144, 70

Cartwright, A. & Stamatellos, D. 2010, Astronomy and Astrophysics, 516, A99

Cheng, A. 1979, The Astrophysical Journal, 227, 955

Chevalier, R. A. 1977, Annual Review of Astronomy and Astrophysics, 15, 175

Chevalier, R. A. 1982a, The Astrophysical Journal, 258, 790

—. 1982b, The Astrophysical Journal, 259, 302

Chevalier, R. A. & Fransson, C. 2003, in Lecture Notes in Physics, Berlin Springer Verlag, Vol. 598, Supernovae and Gamma-Ray Bursters, ed. K. Weiler, 171–194

Committee, S. et al. 1998, American Institute of Aeronautics and Astronautics, Reston, VA, AIAA Standard No. G-077-1998

Cossins, P. J. 2010, PhD thesis, -

Cullen, L. & Dehnen, W. 2010, Monthly Notices of the Royal Astronomical Society, 408, 669

da Silva, L. A. L. 1993, Astrophysics and Space Science, 202, 215

Dehnen, W. & Aly, H. 2012, Monthly Notices of the Royal Astronomical Society, 425, 1068

Diehl, S., Rockefeller, G., Fryer, C. L., Riethmiller, D., & Statler, T. S. 2012, arXiv e-prints, arXiv:1211.0525

Dokuchaev, V. I. 2002, Astronomy and Astrophysics, 395, 1023

Domínguez, I. & Khokhlov, A. 2011, The Astrophysical Journal, 730, 87

Dubner, G. & Giacani, E. 2015, The Astronomy and Astrophysics Review, 23, 3

Dwarkadas, V. V., Dewey, D., & Bauer, F. 2010, Monthly Notices of the Royal Astronomical Society, 407, 812

Edmunds, M. G. 2017, Supernovae and the Chemical Evolution of Galaxies, ed. A. W. Alsabti & P. Murdin (Cham: Springer International Publishing), 2455–2471

Franco, J., Miller, Walter Warren, I., Arthur, S. J., Tenorio-Tagle, G., & Terlevich, R. 1994, The Astrophysical Journal, 435, 805

Frontiere, N., Raskin, C. D., & Owen, J. M. 2017, Journal of Computational Physics, 332, 160

Fryer, C. L., Rockefeller, G., & Warren, M. S. 2006, The Astrophysical Journal, 643, 292

Fryxell, B., Olson, K., Ricker, P., Timmes, F. X., Zingale, M., Lamb, D. Q., MacNeice, P., Rosner, R., Truran, J. W., & Tufo, H. 2000, The Astrophysical Journal Supplement Series, 131, 273

Gaburov, E. & Nitadori, K. 2011, Monthly Notices of the Royal Astronomical Society, 414, 129

Gal-Yam, A. 2017, Observational and Physical Classification of Supernovae, ed. A. W. Alsabti & P. Murdin, 195

Gingold, R. A. & Monaghan, J. J. 1977, Monthly Notices of the Royal Astronomical Society, 181, 375

Goodman, J. 1990, The Astrophysical Journal, 358, 214

Górski, K. M., Hivon, E., Banday, A. J., Wand elt, B. D., Hansen, F. K., Reinecke, M., & Bartelmann, M. 2005, The Astrophysical Journal, 622, 759

Greif, T. H., Johnson, J. L., Bromm, V., & Klessen, R. S. 2007, The Astrophysical Journal, 670, 1

Heger, A., Fryer, C. L., Woosley, S. E., Langer, N., & Hartmann, D. H. 2003, The Astrophysical Journal, 591, 288

Hillebrandt, W. & Niemeyer, J. C. 2000, Annual Review of Astronomy and Astrophysics, 38, 191

Hopkins, P. F. 2013, Monthly Notices of the Royal Astronomical Society, 428, 2840

—. 2015, Monthly Notices of the Royal Astronomical Society, 450, 53

Hopkins, P. F. 2017, arXiv e-prints, arXiv:1712.01294

Hosono, N., Saitoh, T. R., & Makino, J. 2016, The Astrophysical Journal Supplement Series, 224, 32

Immler, S. & Lewin, W. H. G. 2003, X-Ray Supernovae, ed. K. W. Weiler (Berlin, Heidelberg: Springer Berlin Heidelberg), 91–111

Janka, H. T., Langanke, K., Marek, A., Martínez-Pinedo, G., & Müller, B. 2007, Phys. Rep., 442, 38

Janka, H.-T., Melson, T., & Summa, A. 2016, Annual Review of Nuclear and Particle Science, 66, 341

Jones, T. W., Rudnick, L., Jun, B.-I., Borkowski, K. J., Dubner, G., Frail, D. A., Kang, H., Kassim, N. E., & McCray, R. 1998, Publications of the Astronomical Society of the Pacific, 110, 125

Kamm, J. & Timmes, F. 2007, On Efficient Generation of Numerically Robust Sedov Solutions, Tech. Rep. LA-UR-07-2849, Los Alamos National Laboratory, Los Alamos, NM

Kamm, J. R. 2000, Evaluation of the Sedov-von Neumann-Taylor Blast Wave Solution, Tech. Rep. LA-UR-00-6055, Los Alamos National Laboratory

Kamm, J. R., Brock, J. S., Brandon, S. T., Cotrell, D. L., Johnson, B., Knupp, P., Rider, W. J., Trucano, T. G., & Weirs, V. G. 2008, Enhanced verification test suite for physics simulation codes, Tech. Rep. LA-14379, Los Alamos National Laboratory (LANL), Los Alamos, NM

Kane, J., Drake, R. P., & Remington, B. A. 1999, The Astrophysical Journal, 511, 335

Kitayama, T. & Yoshida, N. 2005, The Astrophysical Journal, 630, 675

Korobeinikov, V. 1991, Problems of Point Blast Theory, American Institute of Physics translation series (American Inst. of Physics)

Kotak, R. & Vink, J. S. 2006, Astronomy and Astrophysics, 460, L5

Krehl, P. O. K. 2015, European Physical Journal H, 40

Langer, N. 2012, Annual Review of Astronomy and Astrophysics, 50, 107

Lanson, N. & Vila, J.-P. 2008, SIAM Journal on Numerical Analysis, 46, 1935

Levesque, E. M. 2017, Astrophysics of Red Supergiants, 2514-3433 (IOP Publishing)

Liu, M. & Liu, G. 2006, Applied Numerical Mathematics, 56, 19

Liu, M., Liu, G., & Lam, K. 2003, Journal of Computational and Applied Mathematics, 155, 263

Liu, M. B. & Liu, G. R. 2010, Archives of Computational Methods in Engineering, 17, 25

Lucy, L. B. 1977, AJ, 82, 1013

Martin, R. G., Tout, C. A., & Lesaffre, P. 2006, Monthly Notices of the Royal Astronomical Society, 373, 263

Masuyama, M., Shigeyama, T., & Tsuboki, Y. 2016, Publications of the Astronomical Society of Japan, 68, 22

Mioduszewski, A. J., Dwarkadas, V. V., & Ball, L. 2001, The Astrophysical Journal, 562, 869

Monaghan, J. 1997, Journal of Computational Physics, 136, 298

Monaghan, J. & Gingold, R. 1983, Journal of Computational Physics, 52, 374

Monaghan, J. J. 1992, Annual Review of Astronomy and Astrophysics, 30, 543

Monaghan, J. J. 2005, Reports on Progress in Physics, 68, 1703

Monaghan, J. J. & Lattanzio, J. C. 1985, Astronomy and Astrophysics, 149, 135

Morris, J. P. 1996, Analysis of smoothed particle hydrodynamics with applications (Monash University Australia)

Murante, G., Borgani, S., Brunino, R., & Cha, S.-H. 2011, Monthly Notices of the Royal Astronomical Society, 417, 136

Naidu, G. N., Rao, M. P. R., & Yadav, H. L. 1983, Astrophysics and Space Science, 89, 77

Ohnaka, K., Driebe, T., Hofmann, K. H., Weigelt, G., & Wittkowski, M. 2008, Astronomy and Astrophysics, 484, 371

Ott, C. D., Schnetter, E., Burrows, A., Livne, E., O'Connor, E., & Löffler, F. 2009, in Journal of Physics Conference Series, Vol. 180, Journal of Physics Conference Series, 012022

Pakmor, R., Edelmann, P., Röpke, F. K., & Hillebrand t, W. 2012, Monthly Notices of the Royal Astronomical Society, 424, 2222

Panuelos, J., Wadsley, J., & Kevlahan, N. 2020, Journal of Computational Physics, 414, 109454

Perego, A., Hempel, M., Fröhlich, C., Ebinger, K., Eichler, M., Casanova, J., Liebendörfer, M., & Thielemann, F. K. 2015, The Astrophysical Journal, 806, 275

Pérez-Torres, M. A., Alberdi, A., & Marcaide, J. M. 2001, Astronomy and Astrophysics, 374, 997

Pfrommer, C., Springel, V., Enßlin, T. A., & Jubelgas, M. 2006, Monthly Notices of the Royal Astronomical Society, 367, 113

Pols, O. 2011, STELLAR STRUCTURE AND EVOLUTION, uRL: `https://www.astro.ru.nl/~onnop/education/stev_utrecht_notes/`. Last visited on 2020/07/22

Price, D. J. 2008, Journal of Computational Physics, 227, 10040

—. 2012, Journal of Computational Physics, 231, 759 , special Issue: Computational Plasma Physics

Price, D. J., Wurster, J., Tricco, T. S., Nixon, C., Toupin, S., Pettitt, A., Chan, C., Mentiplay, D., Laibe, G., Glover, S., Dobbs, C., Nealon, R., Liptai, D., Worpel, H., Bonnerot, C., Dipierro, G., Ballabio, G., Ragusa, E., Federrath, C., Iaconi, R., Reichardt, T., Forgan, D., Hutchison, M., Constantino, T., Ayliffe, B., Hirsh, K., & Lodato, G. 2018, Publications of the Astronomical Society of Australia, 35, e031

Pruzhinskaya, M. V. & Lisakov, S. M. 2016, Journal of Astronomical History and Heritage, 19, 203

Puls, J., Sundqvist, J. O., & Markova, N. 2015, in IAU Symposium, Vol. 307, New Windows on Massive Stars, ed. G. Meynet, C. Georgy, J. Groh, & P. Stee, 25–36

Putman, M., Peek, J., & Joung, M. 2012, Annual Review of Astronomy and Astrophysics, 50, 491

Read, J. I., Hayfield, T., & Agertz, O. 2010, Monthly Notices of the Royal Astronomical Society, 405, 1513

Reynolds, S. P. 2008, Annual Review of Astronomy and Astrophysics, 46, 89

Roache, P. J. 1998, Verification and validation in computational science and engineering, Vol. 895 (Hermosa Albuquerque, NM)

Rosswog, S. & Price, D. 2007, Monthly Notices of the Royal Astronomical Society, 379, 915

Saitoh, T. R. & Makino, J. 2009, The Astrophysical Journal, 697, L99

Sana, H., de Mink, S. E., de Koter, A., Langer, N., Evans, C. J., Gieles, M., Gosset, E., Izzard, R. G., Le Bouquin, J. B., & Schneider, F. R. N. 2012, Science, 337, 444

Schoenberg, I. J. 1946, Quarterly of Applied Mathematics, 4, 112

Sedov, L. 1959, in Similarity and Dimensional Methods in Mechanics, ed. L. Sedov (Academic Press), 146 – 304

Shen, Z., Ren, J., & Cui, X. 2019, Journal of Physics: Conference Series, 1290, 012026

Singleton, Jr., R., Israel, D. M., Doebling, S. W., Woods, C. N., Kaul, A., Walter, Jr., J. W., & Rogers, M. L. 2016, ExactPack Documentation, Tech. Rep. LA-UR-16-23260, Los Alamos National Laboratory (LANL)

Smartt, S. J. 2015, Publications of the Astronomical Society of Australia, 32, e016

Smartt, S. J., Vreeswijk, P. M., Ramirez-Ruiz, E., Gilmore, G. F., Meikle, W. P. S., Ferguson, A. M. N., & Knapen, J. H. 2002, The Astrophysical Journal, 572, L147

Smith, N. 2014, Annual Review of Astronomy and Astrophysics, 52, 487

Smith, N., Andrews, J. E., & Mauerhan, J. C. 2016, Monthly Notices of the Royal Astronomical Society, 463, 2904

Springel, V. 2005, Monthly Notices of the Royal Astronomical Society, 364, 1105

Springel, V. 2010, Monthly Notices of the Royal Astronomical Society, 401, 791

Springel, V. & Hernquist, L. 2002, Monthly Notices of the Royal Astronomical Society, 333, 649

Tasker, E. J., Brunino, R., Mitchell, N. L., Michielsen, D., Hopton, S., Pearce, F. R., Bryan, G. L., & Theuns, T. 2008, Monthly Notices of the Royal Astronomical Society, 390, 1267

Taylor, G. 1950, Proceedings of the Royal Society of London. Series A, Mathematical and Physical Sciences, 201, 159

Teyssier, R. 2015, Annual Review of Astronomy and Astrophysics, 53, 325

Thielemann, F.-K., Nomoto, K., & Hashimoto, M.-A. 1996, The Astrophysical Journal, 460, 408

Timmes, F. X., Gisler, G., & George, H. M. 2005, Automated Analyses of the Tri-Lab Verification Test Suite on Uniform and Adaptive Grids for Code Project A, Tech. Rep. LA-UR-05-6865, Los Alamos National Laboratory (LANL), Los Alamos, NM

Tominaga, N., Blinnikov, S. I., & Nomoto, K. 2013, The Astrophysical Journal, 771, L12

Truelove, J. K. & McKee, C. F. 1999, The Astrophysical Journals, 120, 299

Turk, M. J., Smith, B. D., Oishi, J. S., Skory, S., Skillman, S. W., Abel, T., & Norman, M. L. 2010, The Astrophysical Journal Supplement Series, 192, 9

Valdarnini, R. 2012, Astronomy and Astrophysics, 546, A45

van Veelen, B., Langer, N., Vink, J., García-Segura, G., & van Marle, A. J. 2009, Astronomy and Astrophysics, 503, 495

Vishwakarma, J. P. & Nath, G. 2007, Meccanica, 42, 331

Weiler, K. W., Panagia, N., Montes, M. J., & Sramek, R. A. 2002, Annual Review of Astronomy and Astrophysics, 40, 387

Weiler, K. W., Sramek, R. A., Panagia, N., van der Hulst, J. M., & Salvati, M. 1986, The Astrophysical Journal, 301, 790

Weiler, K. W., Van Dyk, S. D., Sramek, R. A., & Panagia, N. 2004, 48, 1377

Whalen, D., van Veelen, B., O'Shea, B. W., & Norman, M. L. 2008, The Astrophysical Journal, 682, 49

Woltjer, L. 1972, ARA&A, 10, 129

Young, T. R. 2004, The Astrophysical Journal, 617, 1233

Zhu, Q., Hernquist, L., & Li, Y. 2015, The Astrophysical Journal, 800, 6